The University of Sheffield

INVESTIGATION OF TORQUE PRODUCTION AND CONTROL STRATEGY FOR VARIABLE FLUX RELUCTANCE MACHINES

Beomseok Lee

A thesis submitted for the degree of Doctor of Philosophy

Department of Electronic and Electrical Engineering

University of Sheffield

Mappin Street, Sheffield, S1 3JD, UK

1 January 2017

ABSTRACT

This thesis is focused on the torque production and control strategies of variable flux reluctance machines (VFRMs).

Based on energy conservation, an instantaneous torque equation is developed and analysed, which reveals the contributions of harmonic currents and inductances to the torque production. By using Fourier series, all of the harmonics in the phase currents and winding inductances are considered. It was found that the average torque of a 6/4 VFRM is mainly produced by the dc, fundamental and second harmonic components of the phase currents. Based on the derived torque equation, magnitudes and phases of the current harmonics are optimised so that the average torque is maximised under a given rms current. Undesirable level of torque ripple was found, due to the inductance harmonics. The third harmonic torque ripple is dominant in the 6/4 VFRM, whilst the 6/7 VFRM has a lower magnitude sixth harmonic component. In order to reduce the torque ripple, a harmonic field current is injected. Since the torque ripple reduction method utilises the machine parameters, the influence of the parameter mismatch is investigated. The torque waveforms predicted by the derived torque equation are compared with the results directly calculated by 2D-finite element analysis (FEA). Additionally, the experimental results verify that the derived torque equations can predict the torque production of the VFRMs to a good degree of accuracy.

In order to improve the machine efficiency and extend the operating speed range, an integrated field and armature current control strategy has been proposed. The field and armature currents are injected into a single coil as a sinusoidal current biased by a dc offset, rather than a separate field and armature winding. In the integrated current control scheme, a zero sequence current generates a virtual rotor flux as the field current, whilst the three-phase sinusoidal currents produce a rotating stator field. The zero sequence current is generated by adjusting the on-time of zero vectors between two inverters. In the case of the 6/4 VFRM, an open winding configuration is utilised since the field and armature windings have the same polarity in each tooth winding. In contrast, a dual three-phase winding configuration having a neutral point is adopted for the 6/7 VFRM, due to the opposite polarity between the field and armature windings. For the vector control, the voltage and torque equations are derived in the synchronous *dq*-axis frame. With the aid of MATLAB/*Simulink*, these equations are also utilised for the dynamic simulation. The simulation and experimental results validate that the proposed strategy can effectively increase the efficiency and extend the operating speed range of the VFRMs. As an extended work, a torque ripple reduction method is also applied to the integrated current control by injecting harmonic components into the zero sequence current.

ACKNOWLEDGEMENTS

I would like to express the deepest appreciation to my supervisor Prof. Z. Q. Zhu. His technical guidance and professional constructive support are valuable and impressive throughout the whole Ph.D. study of this research work.

I am very grateful to all the Ph.D. students in the Electrical Machines and Drives Group at the University of Sheffield, especially the control guys who have spent the same generation. Additionally, I would like to express appreciation for the support provided by the staff in the Electrical Machines and Drives Group at the University of Sheffield.

Finally, I am very thankful for my wife Eunhye Kang's love, encouragement and faith throughout my Ph.D. course. Her understanding and strong support make me dedicate great efforts on the research work. I would like to also express gratitude my whole family for their endless care, especially my parents and my parents-in-law.

CONTENTS

LIST OF SYMBOLS

Symbol	Description	Unit
e_a, e_b and e_c	*abc*-axis back emf	V
e_d and e_q	*dq*-axis back emf	V
f_s	Switching frequency	Hz
i_a^*, i_b^* and i_c^*	*abc*-phase reference currents	A
i_d^* and i_q^*	*dq*-axis reference currents	A
i_f^*	Reference field current	A
i_a, i_b and i_c	*abc*-phase currents	A
i_d and i_q	*dq*-axis currents	A
i_f	Field current	A
i_0	Zero sequence current	A
I_m	Current magnitude at *m*th harmonic order	A
I_{max}	Maximum inverter current	A
I_s	Phase current magnitude	A
K_P	Proportional gain	-
K_I	Integral gain	-
K_R	Resonant gain	-
L_a, L_b and L_c	*abc*-axis self-inductances	H
L_d and L_q	*dq*-axis self-inductances	H
L_0^a	dc component of self-inductances in armature windings	H
L_0^f	dc component of self-inductances in field windings	H
L_n^a	Self-inductance magnitude of armature windings at *n*th harmonic order	H
L_n^f	Self-inductance magnitude of field windings at *n*th harmonic order	H
M_0^a	dc component of mutual inductances between armature windings	H

M_0^f	dc component of mutual inductances between field and armature windings	H
M_n^a	Mutual inductance magnitude between armature windings at *n*th harmonic	H
M_n^f	Mutual inductance magnitude between field and armature windings at *n*th harmonic	H
m	Harmonic order of currents	-
N	Encoder pulse number per rotation	-
n	Harmonic order of inductances	-
P	Number of rotor poles	-
R_s	Phase winding resistance	Ω
T_a, T_b and T_c	abc-axis switching on-time	s
T_0	Zero sequence switching on-time	s
T_e	Electromagnetic torque generated by machine	Nm
T_L	Load torque	Nm
T_s	Sampling period	s
v_a^*, v_b^* and v_c^*	*abc*-axis reference voltages	V
v_α^* and v_β^*	*αβ*-axis reference voltages	V
v_d^* and v_q^*	*dq*-axis reference voltages	V
v_a, v_b and v_c	*abc*-axis voltages	V
v_α and v_β	*αβ*-axis voltages	V
v_d and v_q	*dq*-axis voltages	V
v_f	Field voltage	V
V_{dc}	dc link voltage	V
V_{max}	Maximum inverter voltage	V
V_s	Phase voltage magnitude	V
V_0	Zero sequence voltage	V

α_n	Inductance angle at *n*th harmonic order	°
α_n^a	Self-inductance angle of armature windings at *n*th harmonic order	°
α_n^f	Self-inductance angle of field windings at *n*th harmonic order	°
β_m	Current angle at *m*th harmonic order	°
γ_n^a	Mutual inductance angle between armature windings at *n*th harmonic	°
γ_n^f	Mutual inductance angle between field and armature windings at *n*th harmonic	°
θ_e	Electrical rotor position	°
θ_m	Mechanical rotor position	°
ρ	Flux-weakening gain	-
ψ_a, ψ_b and ψ_c	*abc*-axis flux-linkages	Wb
ψ_m	Open-circuit flux-linkage produced by PM	Wb
ω_e	Electrical angular speed of rotor	rad/s
ω_m	Mechanical angular speed of rotor	rad/s

LIST OF ABBREVIATIONS

AC	Alternating current
AD	Analog to digital
ADC	Analog to digital converter
CPSR	Constant power speed region
DAC	Digital to analog converter
DC	Direct current
DFDSM	Doubly fed doubly salient machine
DSPM	Doubly salient permanent magnet
EMF	Electro-motive force
FEA	Finite element analysis
IGBT	Insulated-gate bipolar transistor
IPM	Interior permanent magnet
LPF	Low pass filter
MMF	Magneto-motive force
MTPA	Maximum torque per ampere
MTPV	Maximum torque per voltage
PI	Proportional integral
PIR	Proportional integral resonant
PM	Permanent magnet
PWM	Pulse width modulation
RPM	Revolutions per minute
RWFSM	Rotor wound field synchronous machine
SFPM	Switched flux permanent magnet
SPM	Surface-mounted permanent magnet
SRM	Switched reluctance machine

SVPWM	Space vector pulse width modulation
SWFSFM	Stator wound field switched flux machine
SynRM	Synchronous reluctance machine
VFPM	Variable flux permanent magnet
VFRM	Variable flux reluctance machine

CHAPTER 1

GENERAL INTRODUCTION

1.1 Introduction

The interest in non-permanent magnet (PM) machines has been increased continuously. With the advanced technologies in the power electronics devices and controls, the various machines have been utilised as an alternative to conventional electrical machines such as induction or brushless PM machines [HUS05], [JEO15], [ZHU14]. VFRMs are stator electrically field excited synchronous machines having a similar structure with switched reluctance machines (SRMs) [LIU13b], [ZHU14], [LIU14a]. The stator and rotor are doubly salient structure without any coil or magnet on the rotor. The field and armature windings are identically wound on the stator tooth using non-overlapping windings. As a result, the rotor is simple and robust, and the heat can be dissipated easily. Additionally, brushes or slip rings are not required to feed the dc excitation current. The VFRMs have the advantage of wide-range constant-power operation, since the dc field current can be controlled independently from the armature current when the input voltage is limited at a high speed region [MBA12]. The flux-linkage can be adjusted in order to improve the efficiency in the high speed range [SHI07]. Because of its capability of flux control by the field current adjustment, the doubly fed configuration can achieve a very wide range of flux regulation, which realises a high

starting torque at a low speed operation and maintains a constant output power over a wide speed range [CHU15]. Hence, these two features are highly desirable for the industrial applications for various purposes. Fig. 1.1 shows the category of the electric machines based on the PM usage, i.e. PM machines, hybrid PM machines, and non-PM machines.

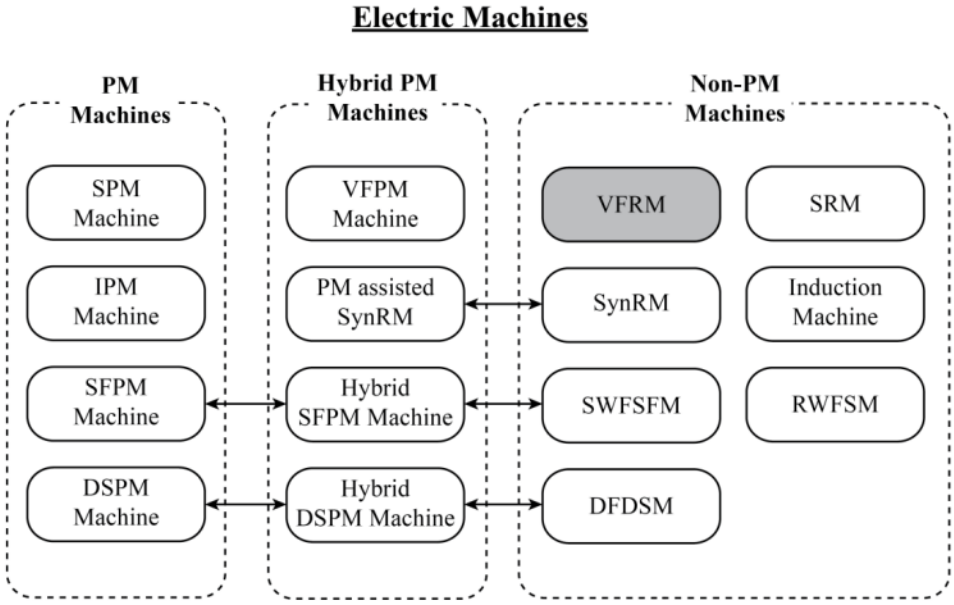

Fig. 1.1. Electric machines category based on the PM usage.

1.1.1 PM Machines

PM machines have been used in many applications such as automotive and industrial market sectors due to high torque/power density, high efficiency, high controllability and wide speed range operation [BIA01], [ZHU07], [CHA08], [DOR11]. Surface-mounted PM (SPM) and interior PM (IPM) machine types are both popular among the PM machines. The SPM machines are easier to be manufactured, whilst the IPM machines have a very good overload capability over the entire speed range. For a continuous torque production, both SPM and IPM machines exhibit practically the same performance at a given inverter rating and given size of

the mechanical parts [VAG10]. In terms of high speed losses, the SPM machines are mainly affected by PM losses, but the IPM machines are sensitive to slot harmonic losses [PEL12].

The PM machines can be classified into a different category depending on location of the PM excitation [LIA95]. Due to the PMs in the rotor, the SPM and IPM machines can be suffered from the possibility of irreversible demagnetisation by armature reaction or high temperature. Also, mechanical reliability may be degraded at high speed operation [CHE01]. When the PMs are placed on the stator side, the rotor geometry should be a salient pole, which is similar to that of switched reluctance machines (SRMs). Hence, it can have a potential for high speed operation due to its simple and robust rotor structure [CHE11], [ZHU11], [WU15]. Additionally, the temperature is easier to be managed with forced liquid cooling.

When the PMs are located between the stator teeth, it is switched flux PM (SFPM) machines [ZHU10]. The PMs can be also placed in the stator back-iron, which is known as doubly salient PM (DSPM) machines [CHE11]. As a major drawback of the DSPM machines, the torque density is relatively low due to its unipolar flux-linkage waveform. It can be overcome with the SFPM machines, which produces a bipolar phase flux-linkage waveform and more sinusoidal back electro-motive force (emf). As a result, the torque capability can be significantly improved due to its flux-focusing characteristic compared with that of the DSPM machines [ZHU10].

However, it becomes more important to consider the machines with less or no rare-earth magnet due to the relatively high PM material cost. Moreover, in order to extend the speed range a negative *d*-axis current is required for a flux weakening operation, which results in an

additional loss [JAH87], [MOR90], even demagnetisation in the PMs [SAR12]. Additionally, the flux weakening capability may be limited by an uncontrollable PM flux-linkage.

1.1.2 Hybrid PM Machines

Variable-flux PM (VFPM) machines are those which utilise some ways of changing the PM flux level [OWE11]. It allows flexibility in terms of optimising efficiency over a machine operating range. As examples, many VFPM machines have been researched including hybrid-excited machines with field windings [LUO00], which are one major category of the VFPM machines. A compromised design for the PM machines, which utilises the dc field winding in rotor [AMA09], has been developed for the SPM and IPM machines [AKE00]. Additionally, a mechanical structure is altered to adjust the flux level [ZHU15a], whilst the machines with other means of varying the PM flux have been used [SWA06]. Hybrid SFPM machines [OWE10], [AFI15] and hybrid DSPM machines [CHA03], [ZHA12] have been proposed, in which both dc field windings and PMs are utilised on the stator. Those machines can also utilise the coordinated operation between the PMs and field excitation current. From an integration of the topology between the PM machines and synchronous reluctance machines (SynRMs), a saliency ratio can be increased for the torque density enhancement [SOO95].

As a drawback of the hybrid PM machines, high magneto-motive force (mmf) from the field windings is required to change the flux density in air-gap produced by the PMs although it is relatively much easier to weaken the flux. It is because that magnetic saturation is significant and winding excitation is weaker compared with the PM excitations. Additionally,

the part of the stator should be occupied for the PMs, which reduces the area for the field and armature windings in the stator. In the case of the mechanically adjusted VFPM machines, it requires an extra actuation hardware which causes more complex system.

1.1.3 Non-PM Machines

SRMs have been applied to many applications since they have a simple and robust rotor structure [HUS05], [VIJ08], [TAK12]. They can be operated under high magnetic saturation and high temperature. Additionally, the SRMs exhibit inherent capability of fault tolerance [RAH00]. However, the SRMs also produce a large torque ripple and high noise and vibration. Induction machines are also one of the most used electric machines due to their ruggedness and availability for different applications [BEN00]. It can be commonly thought of a three-phase transformer whose shortened secondary winding is freely rotating forming an asynchronous machine [NAM10]. Additionally, the SynRM uses a rotating sinusoidal mmf and a reluctance concept [VAG98]. However, the rotor geometry design is quite complex, and numerous parameters are involved for an optimal design. More importantly, they exhibit relatively low torque density and low power factor.

Rotor wound field synchronous machines (RWFSMs) have been recently used for electric vehicle (EV) propulsion [JEO15]. Apart from the stator windings, they have the field windings on the rotors. As a main drawback of the RWFSMs, brushes or slip rings should be utilised for the field current excitation, which reduces mechanical reliability [SAN12].

In stator wound field (SWF) machines, it does not require any brush or slip rings for the field excitation since the field windings are placed on the stator [ZHU14]. For the

development of the non-rare earth PM machines, doubly-fed doubly-salient machines (DFDSMs) have been researched for electric vehicles and hybrid electric vehicles [FAN08], in which the PMs in the DSPM machines are replaced by the field excitation windings [LIA94]. Additionally, by substituting all of the PMs in the SFPM machines to the field windings, SWF switched flux machines (SWFSFMs) have been proposed [ZHU11]. The DSDFMs exhibit a simple and robust structure, which can save the cost of maintenance and manufacture. However, its phase flux-linkage waveforms are not identical between the phases since a flux path is asymmetric in the DFDSMs. It causes a high torque ripple and different amplitudes of each harmonic in the three-phase windings. Hence, the dc link voltage cannot be effectively utilised since the positive and negative peak voltages have different magnitudes [CHA02].

Compared with other DFDSMs, the VFRMs exhibit the short flux path, and the identical flux distribution for each phase since the field and armature windings are identically wound on the stator tooth [ZHU14]. This symmetrical flux distribution allows the identical back emf for all of the phases, which reduces the cogging torque and torque ripple. Unlike the SRMs or other non-PM machines, the main advantage of the VFRMs is the possibility of odd rotor pole numbers, whilst the doubly salient structure is maintained. For example, in the three-phase SRMs with 6-stator pole, odd rotor pole numbers cannot be applied [DES10]. However, the combinations of the stator/rotor pole in the VFRMs are no longer limited by the equations for the SRMs or doubly salient machines. Hence, the VFRMs with new stator/rotor pole combinations can be categorised as a new family of the reluctance machines [LIU13b], [LIU14a]. For example, in the 6-stator pole VFRMs, an odd rotor pole machine (5- or 7-rotor

pole) is applicable as well as an even rotor pole such as 4- or 8-rotor pole. However, the odd rotor pole number causes an unbalanced magnetic force (UMF). In order to avoid the UMF, a 12-stator-pole with either 10- or 14-rotor pole machines has been proposed by doubling the number of the stator and rotor poles together [LIU14a].

1.2 Variable Flux Reluctance Machines

1.2.1 Winding Configurations and Flux-Linkage

The VFRMs have the dc field windings identically wound in each stator tooth. It allows 5- or 7-rotor pole VFRM whose field flux can pass though the adjacent stator poles [LIU13b]. As a result, thinner back-iron can be achieved due to shorter field flux path compared with the SRMs and DFDSMs. Fig. 1.2 shows the cross sections and winding configurations of the 6-stator pole VFRMs with different rotor pole combinations. The initial position (θ_e = 0°) is defined, in which the centre of the rotor pole is aligned with one tooth wound by A1. Hence, if a constant current is excited in the A1 winding, the rotor will be aligned with the stator tooth wound by A1 winding. Fig. 1.3 shows the back emf vectors of each coil for the 6-stator pole VFRMs with different rotor pole combinations. Based on the coil back emf vectors, the winding configurations can be determined. In the 6/4 and 6/8 VFRMs, each coil of the armature windings in one phase has the same polarity. On the other hand, since the field and armature fluxes can pass through the adjacent stator teeth in the 6/5 or 6/7 VFRMs, each coil back emf of the same phase has an opposite polarity. It can be geometrically explained that the rotor pole is aligned with the stator tooth, whilst the rotor slot is align with the other stator

tooth simultaneously shown in Fig. 1.2. As a result, even order harmonics in the armature windings are cancelled due to its opposite polarity connection in the 6/5 and 6/7 VFRMs.

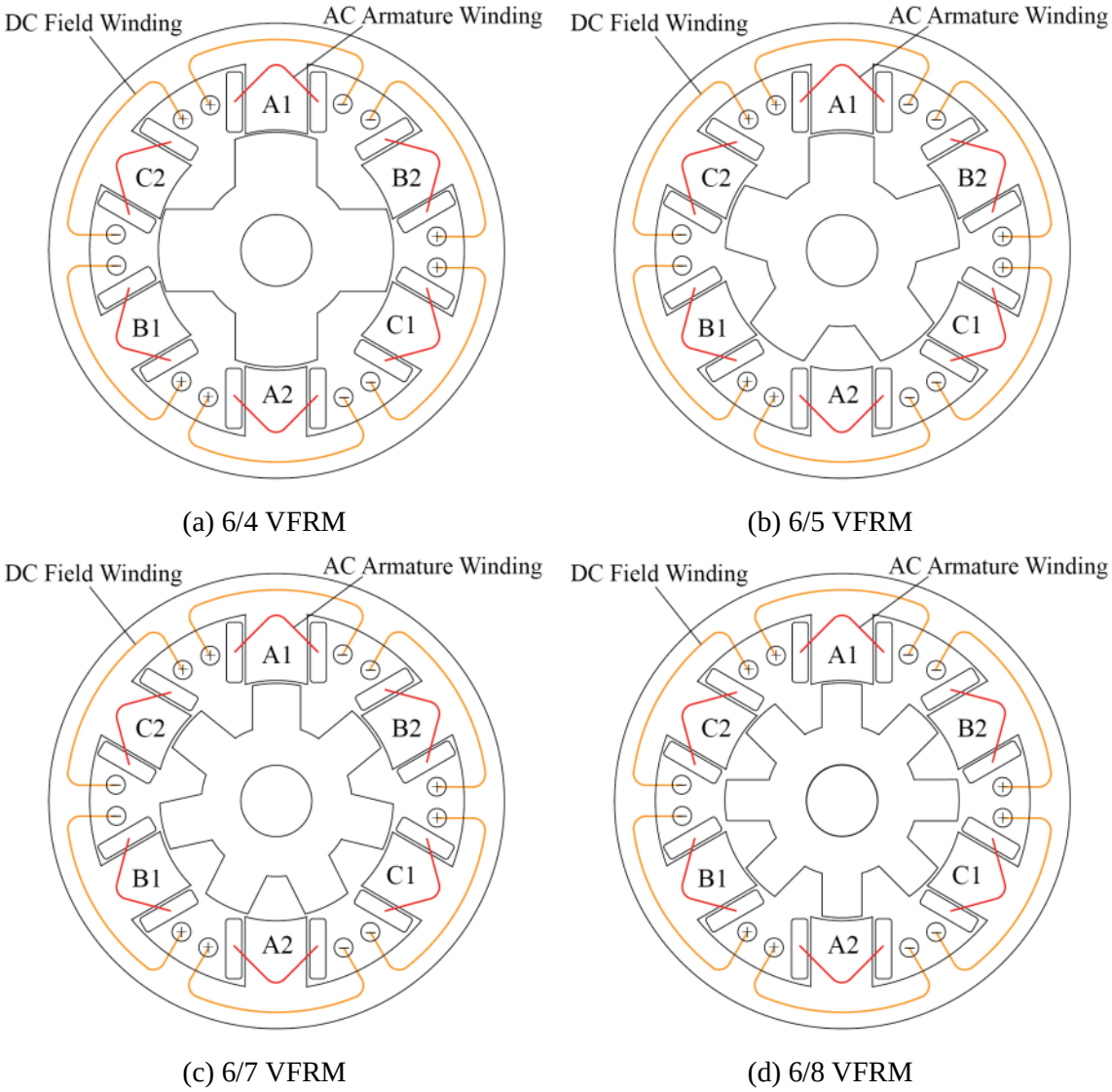

(a) 6/4 VFRM (b) 6/5 VFRM

(c) 6/7 VFRM (d) 6/8 VFRM

Fig. 1.2. Cross sections and windings of the 6-stator pole VFRMs with different rotor [LIU13b].

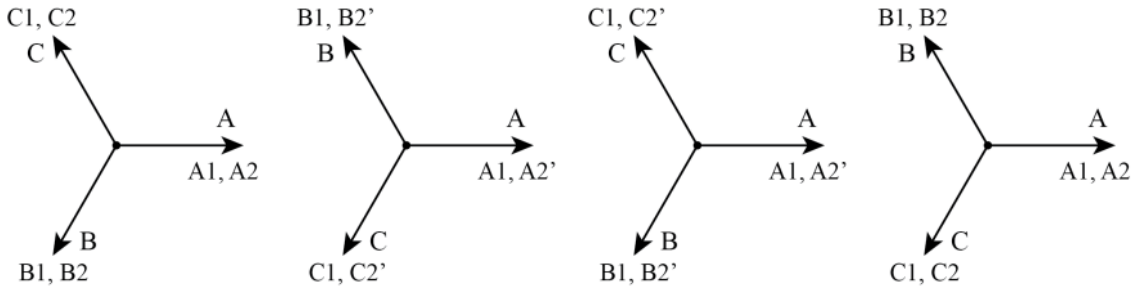

(a) 6/4 VFRM (b) 6/5 VFRM (c) 6/7 VFRM (d) 6/8 VFRM

Fig. 1.3. Coil emf vectors in the 6-stator pole VFRMs with different rotor poles [LIU13b].

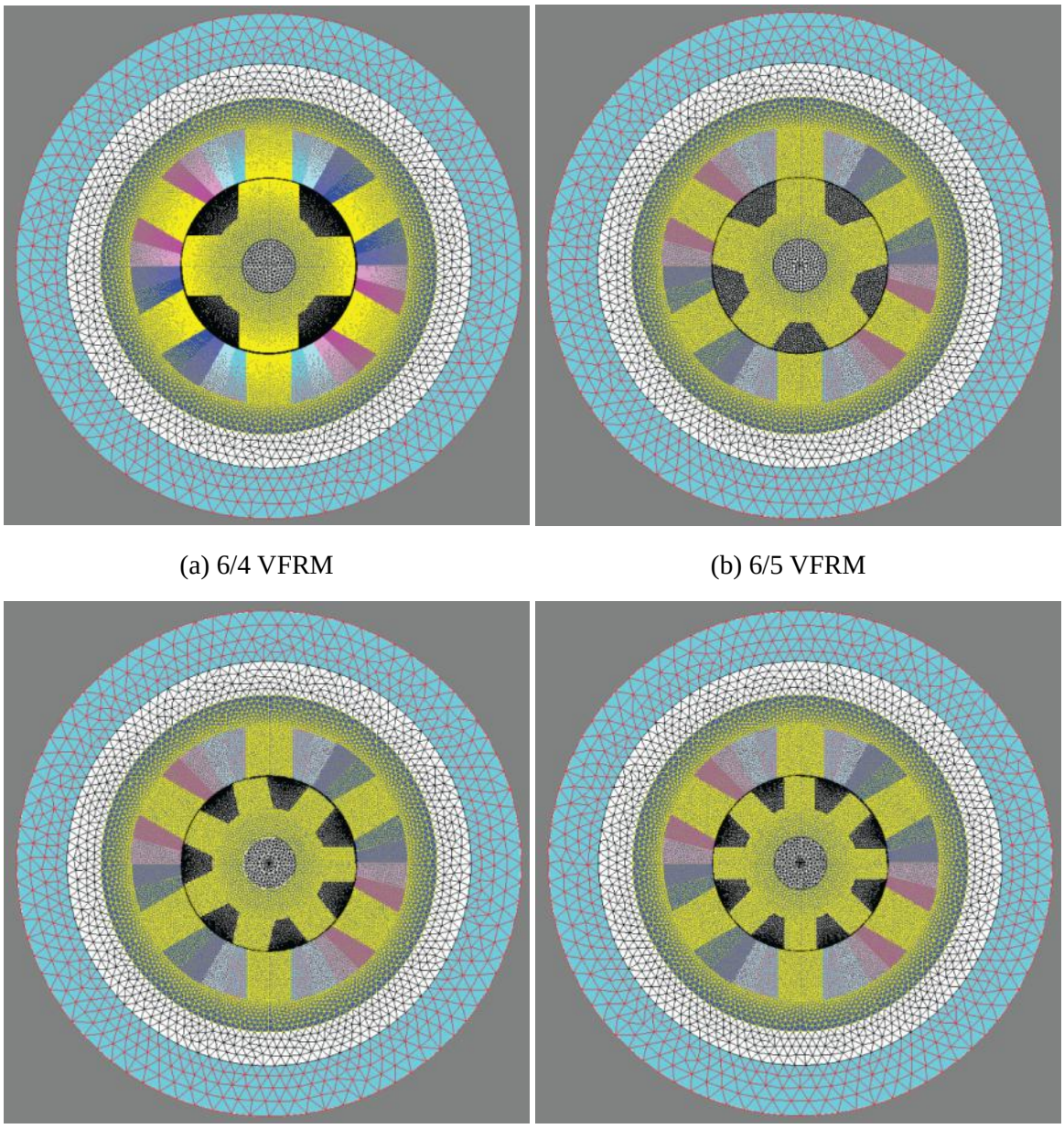

(a) 6/4 VFRM (b) 6/5 VFRM

(c) 6/7 VFRM (d) 6/8 VFRM

Fig. 1.4. Finite element meshes of the 6-stator pole VFRMs with different rotor pole numbers.

The entire cross section region is subdivided into triangular finite elements, in which the sides of the triangles coincide with the boundary of each material. In this thesis, Flux2D finite element software is utilized. The finite element subdivision meshes of the VFRMs are presented in Fig. 1.4. It can be seen that there is a higher concentration of elements near the air gap.

The flux-linkage waveforms and the harmonics are presented in Fig. 1.5. It shows that the dc component does not exist in the flux-linkage due to its opposite connection of the coils in the same phase in the 6/5 and 6/7 VFRMs. Additionally, the even and third harmonics in the 6/5 and 6/7 VFRMs are relatively less compared with the 6/4 and 6/8 VFRMs. Hence, more sinusoidal flux-linkage waveforms can be found in the 6/5 and 6/7 VFRMs.

Due to the short flux path through the adjacent stator teeth, the symmetrical field flux distribution can be achieved for each phase which provides the identical back emf for all of the phases. Fig. 1.6 shows the back emf waveforms and the corresponding harmonics for the VFRMs having different rotor pole combinations at 400 rpm and the field current of 2 A. It can be seen that the even order harmonics of the back emf are relatively small in the 6/5 and 6/7 VFRMs compared with the 6/4 and 6/8 VFRMs. Additionally, the third harmonic component is also negligible. This cancelation of the back emf harmonics can be also explained by the opposite connection and its flux-linkage cancelation, which cannot be obtained in the 6/4 and 6/8 VFRMs.

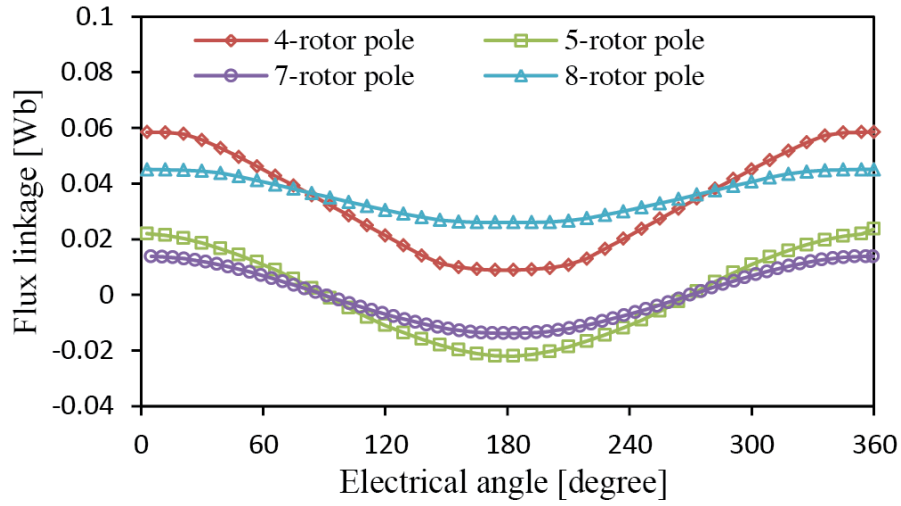

(a) Flux-linkage waveforms

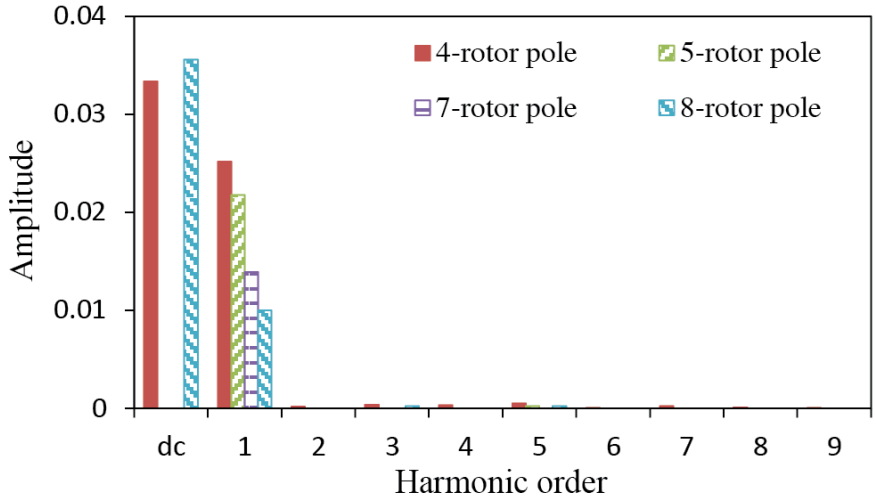

(b) Corresponding harmonics

Fig. 1.5. Flux-linkage waveforms and corresponding harmonic analysis of the 6-stator pole VFRMs with different rotor poles [LIU13b].

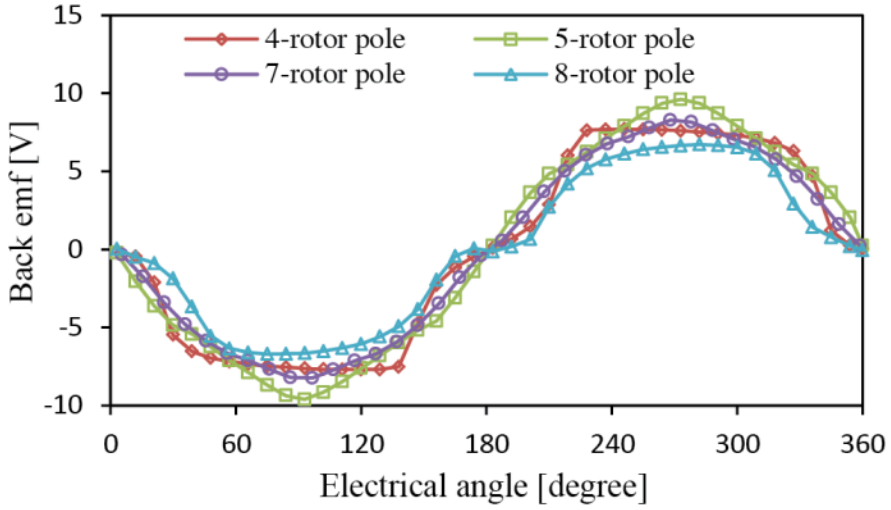

(a) Back emf waveforms

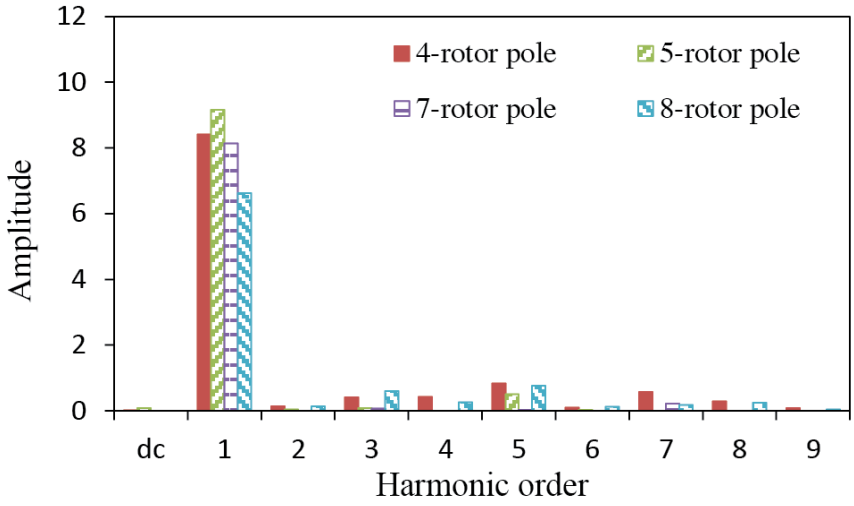

(b) Corresponding harmonics

Fig. 1.6. Back emf waveforms and corresponding harmonic analysis of the 6-stator pole VFRMs with different rotor poles [LIU13b].

1.2.2 Self- and Mutual Inductances

The self-inductance waveforms of the armature windings show a significant difference between the machines with different numbers of the rotor poles in Fig. 1.7(a). The 6/4 and 6/8 VFRMs exhibit the significant self-inductance variation, which is synchronous with one cycle

rotation. On the contrary, the self-inductance of the armature windings is almost constant in the 6/5 and 6/7 VFRMs due to the adjacent flux path. It is worth mentioning that the self-inductance variation is utilised for the average torque production in the SRMs, whilst it only contributes to torque ripple in the VFRMs [LIU13a]. Hence, it can be expected that the constant self-inductance waveforms of the armature windings in the 6/5 and 6/7 VFRMs will produce the low torque ripple compared with the 6/4 and 6/8 VFRMs.

Fig. 1.7(b) shows the self-inductance waveforms of the field windings. It can be found that the VFRMs exhibit the relatively constant waveforms in any rotor combinations. In the VFRMs, the field windings are configured in a series connection among all of the field coils. Hence, although each coil of the field windings may produce the variation, the variation component will be cancelled out except for a multiple of the third harmonic components due to the identical winding. From the field current control point of view, it is desirable to control the relatively constant inductance. The field current can be easily controlled, whilst a converter rating for the field current can be selected with less consideration about the inductance variation.

The mutual inductance waveforms between the field and armature windings are shown in Fig. 1.8(a). Unipolar inductance waveforms are observed in the 6/4 and 6/8 VFRMs, whilst bipolar mutual inductance waveforms are seen in the 6/5 and 6/7 VFRMs due to the opposite connection of the armature windings. More importantly, compared with the 6/4 and 6/8 VFRMs, the 6/5 and 6/7 VFRMs exhibit more sinusoidal waveforms. Since the average torque of the VFRMs is mostly produced by the mutual inductance between the field and armature

windings, it can be also expected that there is less torque ripple in the 6/5 and 6/7 VFRMs.

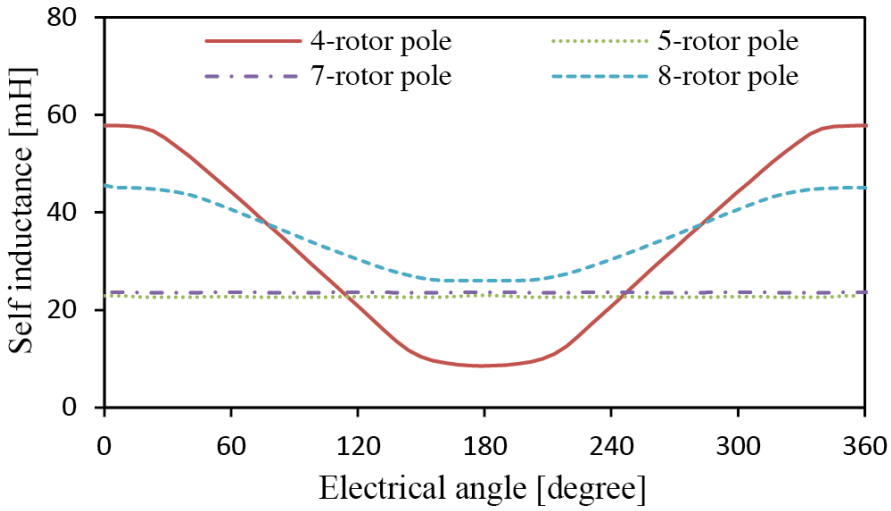

(a) Self-inductance waveforms of the armature windings

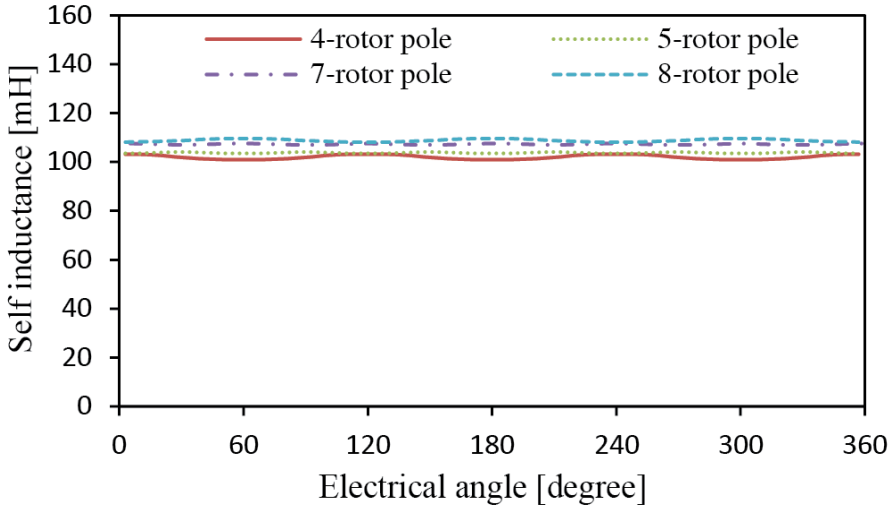

(b) Self-inductance waveforms of the field windings

Fig. 1.7. Self-inductance waveforms of the 6-stator pole VFRMs with different rotor poles [LIU13b].

Fig. 1.8(b) shows the mutual inductance between the armature phases. The mutual inductances are almost negligible in the 6/4 and 6/8 VFRMs, whilst the 6/5 and 6/7 VFRMs have almost constant mutual inductance waveforms. It confirms that the flux-linkage of the armature windings in the 6/5 and 6/7 VFRMs passes through the adjacent stator poles, which

results in a short flux path, whilst the 6/4 and 6/8 VFRMs have a long flux path. The negligible mutual inductance in the 6/4 and 6/8 VFRMs is the same as the SRMs. In contrary, the mutual inductance between the armature windings in the 6/5 and 6/7 VFRMs is given by the half of the self-inductance in the armature windings except for the leakage inductance. In the same principle of a synchronous machine such as the PM and induction machines, it is because that each phase winding is placed spatially by $2/3\pi$ and $\cos(2/3\pi) = -1/2$.

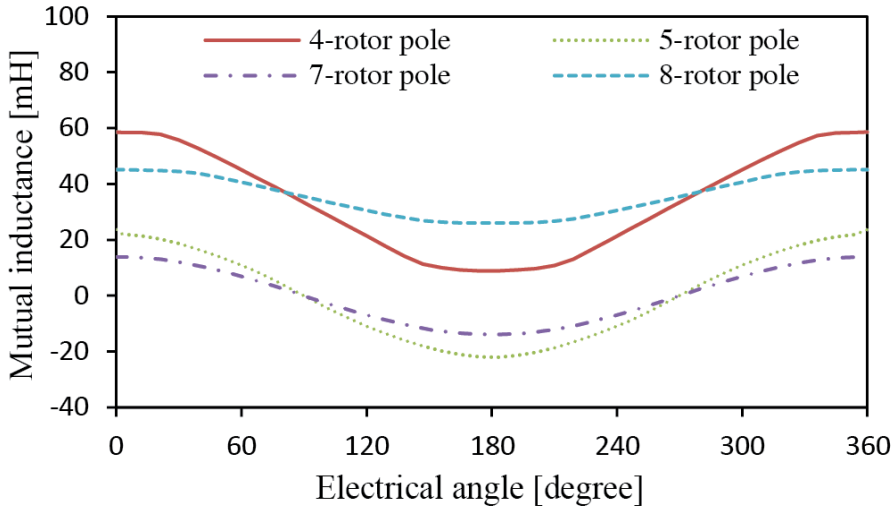

(a) Mutual inductance waveforms between the field and armature windings

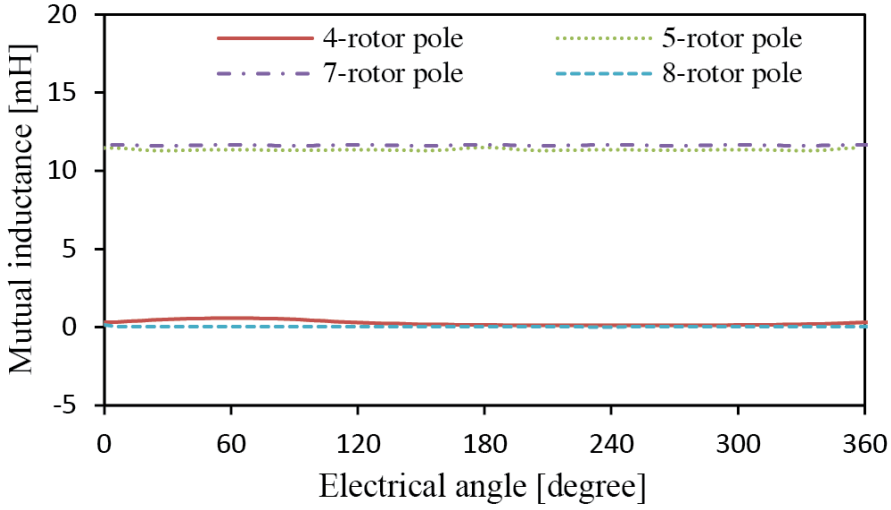

(b) Mutual inductance waveforms between the armature windings

Fig. 1.8. Mutual inductance waveforms of the 6-stator pole VFRMs with different rotor poles [LIU13b].

1.2.3 Torque Waveforms

Fig. 1.9 shows the torque waveforms of the VFRMs with different rotor pole combinations when the armature current is excited at 2 A and the field current is 1 A and 2 A. When the field current is excited at 2 A the average torque is almost doubled than that with 1 A of the field current in all of the stator/rotor pole combinations. However, a significant torque ripple can be observed in the 6/4 and 6/8 VFRMs. It is because that the self-inductance variation of the armature windings contributes to the torque ripple. Especially, the fundamental component of the self-inductance produces the third harmonic torque ripple. Hence, a significant reduction of the torque ripples can be obtained using the VFRMs having the odd rotor pole numbers, which has almost constant self-inductance [ZHU14].

The cogging torque waveforms of the VFRMs with different rotor poles at 2 A field current are shown in Fig. 1.10. In the PM machines, the cogging torque is produced by the interaction between the saliencies of the stator and the magnetised pole of the PMs [KOH03]. In the VFRMs, the cogging torque is defined as a torque at which the field current is only excited. Since the variation cycles of permeance are different depending on the stator/rotor pole combinations, the least orders of harmonic will also be different [LIU14a]. The least order harmonic of the cogging torque is 3 in the 6/4 and 6/8 VFRMs, whilst 6 in the 6/5 and 6/7 VFRMs. Additionally, a high field current will result in a higher cogging torque [LIU13b].

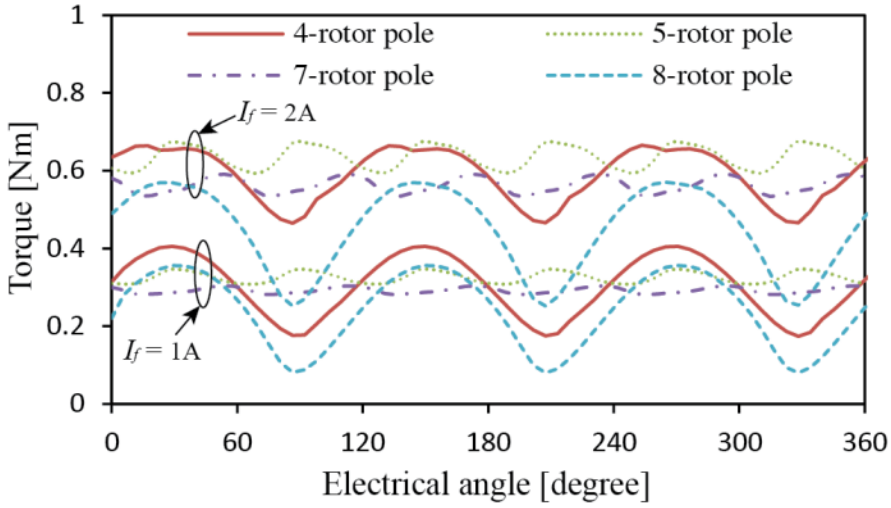

Fig. 1.9. Torque waveforms of the 6-stator pole VFRMs under I_a = 2 A [LIU13b].

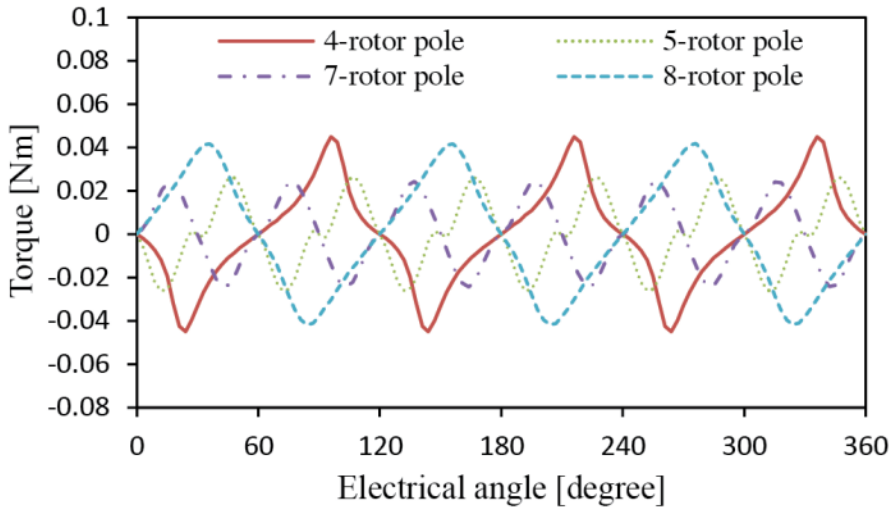

Fig. 1.10. Cogging torque waveforms of the 6-stator pole VFRMs under I_f = 2 A [LIU13b].

The torque generation in the VFRMs can be explained by the rotational force generated by the excited stator poles attracting the rotor poles. Fig. 1.11 shows the torque production of the 6/4 VFRM when the electrical rotor position is at 0°, 90°, 180°, and 270°, respectively. The diagram shows the flux path, excited current and directions of the torque production in the case of the excitation current shown in Fig. 1.12. For the simple explanation, the excited currents are presented as a summation of the field and armature currents since both windings

are wound on the same stator tooth.

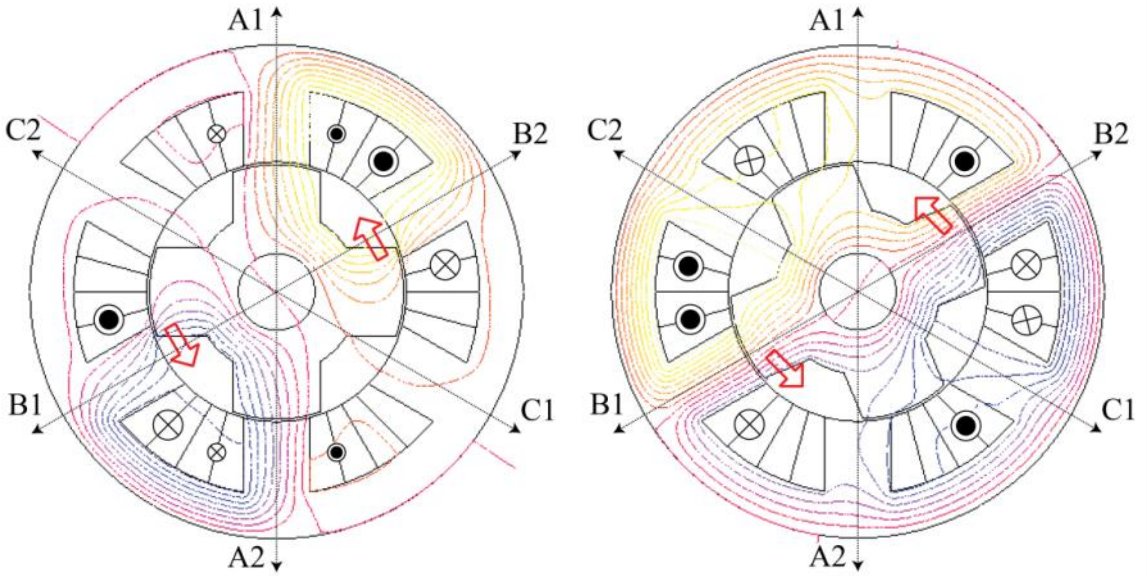

(a) $\theta_e = 0°$ (b) $\theta_e = 90°$

(c) $\theta_e = 180°$ (d) $\theta_e = 270°$

Fig. 1.11. Torque production of 6/4 VFRM at different rotor positions.

In this description, the field current is 2 A and the armature current is 3.83 A. The excited currents are presented in Fig. 1.11 as current symbols depending on the current magnitude and excitation direction. When the electrical rotor position is 0°, Phase B is excited at around 4.3 A, whilst Phase A is excited at 2 A. Due to the stator tooth excitation wound by Phase B, an

electromagnetic force is produced to minimize the reluctance on the main flux path. At θ_e = 90°, both Phase B and Phase C are excited followed by Phase C at θ_e = 180° and Phase A at θ_e = 270°.

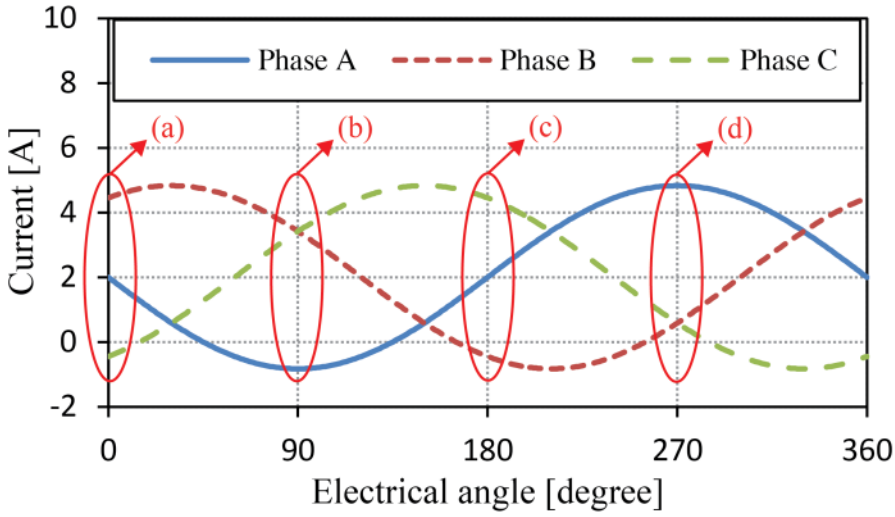

Fig. 1.12. Current waveforms of 6/4 VFRM.

The torque production in 6/5 or 6/7 VFRMs can be explained in the same manner with 6/4 VFRM torque production. As an example, torque production of 6/5 VFRM is presented in Fig. 1.13 with different electrical rotor positions. In 6/5 VFRM, one winding set has the same polarity between the field and armature windings, whilst the other winding set has different polarity. Hence, the excitation currents in stator tooth have six balanced waveforms shown in Fig. 1.14. When the electrical rotor position is located at 0°, Phase B1 and Phase C2 are excited. In order to minimise the reluctance on the main flux path, the rotor rotates with counter clockwise. At θ_e = 90°, Phase A2, Phase B1, and Phase C1 are excited, which leads to the torque production in the same direction. However, the torque is produced on only one side. It is different from 6/4 VFRM, in which the torque is generated by both sides. Hence, 6/5 or 6/7 VFRMs produce the unbalanced magnetic force (UMF). It should be noted that it can be

overcome by doubling the numbers of stator and rotor poles [REF].

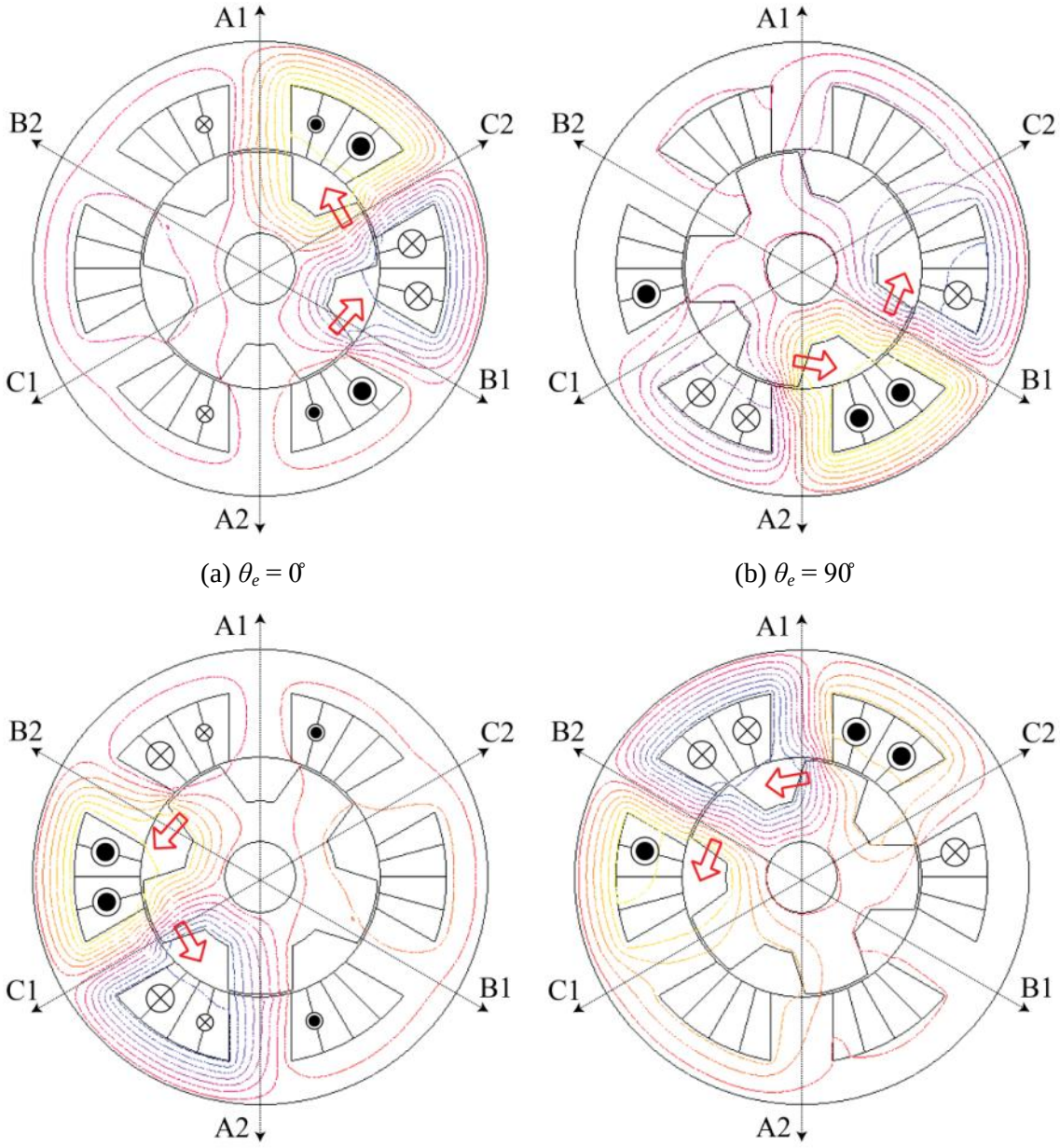

(a) $\theta_e = 0°$ (b) $\theta_e = 90°$

(c) $\theta_e = 180°$ (d) $\theta_e = 270°$

Fig. 1.13. Torque production of 6/5 VFRM at different rotor positions.

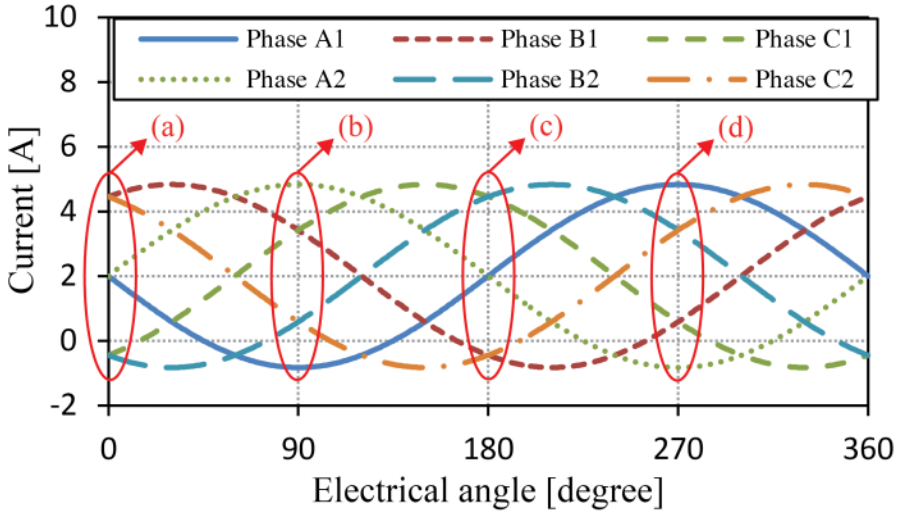

Fig. 1.14. Current waveforms of 6/5 VFRM.

1.3 Torque Production

1.3.1 Switched Reluctance Machines

In a general way, when the mutual inductance is neglected, the voltage equation for Phase A can be written as [MIL01]

$$v_a = Ri_a + \frac{d\gamma_a}{dt} = Ri_a + \frac{d\left(L_a i_a\right)}{dt} = Ri_a + L_a \frac{di_a}{dt} + w_e i_a \frac{dL_a}{dq_e}. \tag{1.1}$$

The instantaneous power *vi* of Phase A is

$$v_a i_a = Ri_a^2 + L_a i_a \frac{di_a}{dt} + w_e i_a^2 \frac{dL_a}{dq_e}. \tag{1.2}$$

The supplied energy, W_e, into the windings can be presented with the two parts, mechanical energy W_m and stored energy in magnetic circuits W_f. The mechanical energy only contributes to the torque production, whilst the stored energy in magnetic circuits does not affect the torque.

$$W_e = W_m + W_f. \tag{1.3}$$

At any instant, the change rate of magnetic stored energy is

$$\frac{d}{dt}\left(\frac{1}{2}L_a i_a^2\right) = \frac{1}{2}i_a^2\frac{dL_a}{dt} + L_a i_a \frac{di_a}{dt}. \tag{1.4}$$

Based on energy conservation, the converted mechanical power can be obtained by subtracting the resistive loss Ri^2 and the rate of change of the magnetic stored energy from the input power vi. Then, the instantaneous electromagnetic torque of Phase A is

$$T_e = \frac{1}{2}i_a^2\frac{dL_a}{d\theta_e}. \tag{1.5}$$

The torque of the SRMs is generated by the tendency of the rotor pole to align with the stator pole so that the flux-linkage distance is shortened. When the phase current is excited in the stator winding, the stator poles generate the flux-linkage. Then, the nearest rotor pole is pulled to align with the excited stator poles, in which the phase inductance increases. Fig. 1.15 shows the diagram of the phase inductance, phase current and the rotor position. When the edge of the rotor pole starts to be overlapped with the edge of the stator pole at θ_o, the phase inductance starts to increase. When the rotor pole is aligned with the stator pole at θ_{al}, the phase inductance reaches to the maximum inductance, L_{al}. Then, the aligned rotor pole and stator pole will be separated due to the rotor rotation. When the rotor pole is aligned with the centre of the stator slot opening at θ_u, the phase inductance is at the minimum L_u. θ_{on} is the rotor position, which is starting point of the phase current conduction, whilst θ_{off} is the end point of the phase current conduction. It is worth mentioning that θ_{on} is placed between θ_u and θ_o so that the phase current increases to its maximum quickly under the lowest phase inductance.

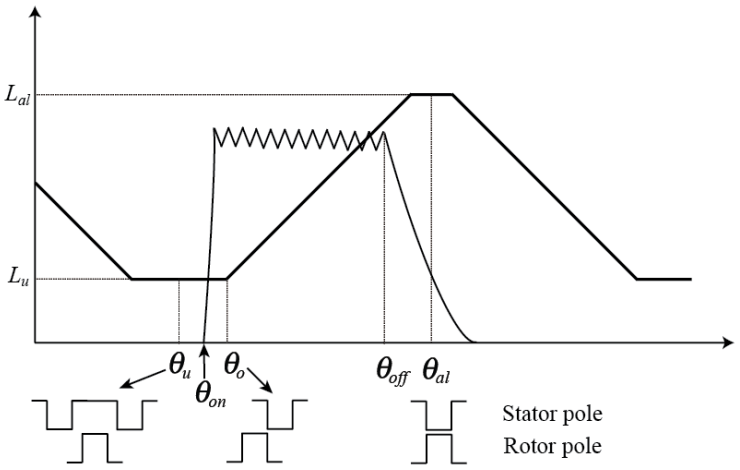

Fig. 1.15. Diagram of the phase inductance, current and rotor positions [MIL01].

Fig. 1.16 illustrates the torque production of the ideal phase inductance under a constant phase current. When the slope of the phase inductance is positive, it generates positive torque at $+T_{ph}$, whilst the negative inductance slope produces negative torque at $-T_{ph}$. It can be seen that the constant inductance does not produce any torque. In order to obtain a continuous positive torque, the phase current should be excited only at the positive slope of the phase inductance. In a three-phase SRM, the phase current can be consecutively excited so that all of the phase currents utilise the positive slope of each phase inductance. Then, resultant torque will be close to a constant torque ideally.

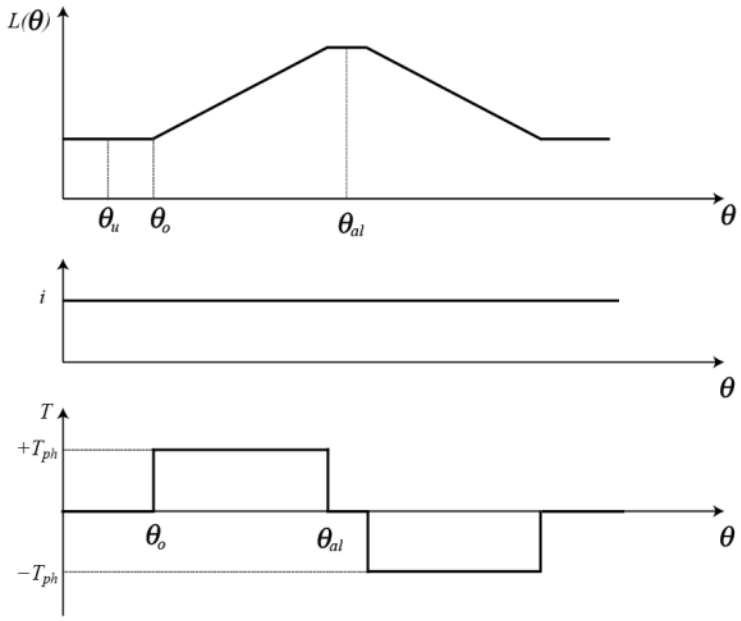

Fig. 1.16. Ideal torque production under a constant phase current [MIL01].

1.3.2 Permanent Magnet Synchronous Machines

The terminal voltages of the PM machines can be written with the phase currents and the flux linkages as

$$\begin{bmatrix} v_a \\ v_b \\ v_c \end{bmatrix} = R \begin{bmatrix} i_a \\ i_b \\ i_c \end{bmatrix} + \frac{d}{dt} \begin{bmatrix} \psi_a \\ \psi_b \\ \psi_c \end{bmatrix} \tag{1.6}$$

where ψ_a, ψ_b and ψ_c are the *abc*-axis flux-linkages, respectively. These flux-linkages can be defined in terms of the inductances, phase currents and flux-linkages by the rotor as follows

$$\begin{aligned} \psi_a &= L_{aa} i_a + L_{ab} i_b + L_{ac} i_c + \psi_{ar} \\ \psi_b &= L_{ba} i_a + L_{bb} i_b + L_{bc} i_c + \psi_{br} \\ \psi_c &= L_{ca} i_a + L_{cb} i_b + L_{cc} i_c + \psi_{cr} \end{aligned} \tag{1.7}$$

where ψ_{ar}, ψ_{br} and ψ_{cr} are the flux-linkages produced by the PMs on the rotor. The open-circuit back emfs can be presented as

$$e_a = \frac{d\psi_{ar}}{dt}, \quad e_b = \frac{d\psi_{br}}{dt}, \quad e_c = \frac{d\psi_{cr}}{dt} \tag{1.8}$$

Then, the electromagnetic torque can be calculated as [LIU13a]

$$T_e = \frac{1}{\omega_m}\left(e_a i_a + e_b i_b + e_c i_c\right) + \frac{1}{2}\left(i_a^2 \frac{dL_a}{d\theta_e} + i_b^2 \frac{dL_b}{d\theta_e} + i_c^2 \frac{dL_c}{d\theta_e}\right) + i_a i_b \frac{dL_{ab}}{d\theta_e} + i_b i_c \frac{dL_{bc}}{d\theta_e} + i_a i_c \frac{dL_{ac}}{d\theta_e}. \tag{1.9}$$

The first term of (1.9) is the synchronous torque, which is generated by the interaction between the phase current and flux-linkage generated by the PMs. Fig. 1.17 illustrates how a PM machine produces a constant power. With a balanced three-phase winding, having three-phase sinusoidal emfs, resistances, and inductances, three-phase sinusoidal currents produce a positive power. Then, the total electrical power is a constant value. The torque can be given by dividing the obtained power by a machine speed. The second and third terms are the reluctance torque, which is proportional to the change rate of the inductance with the rotor position. In the IPM machines, the inductance of any phase has two maxima and two minima in one electrical cycle rotation, representing a double-frequency harmonic variation. The mutual inductance between any two phases exhibits a similar characteristic. These inductance variations contribute to the reluctance torque produced by rotor saliency of the machine.

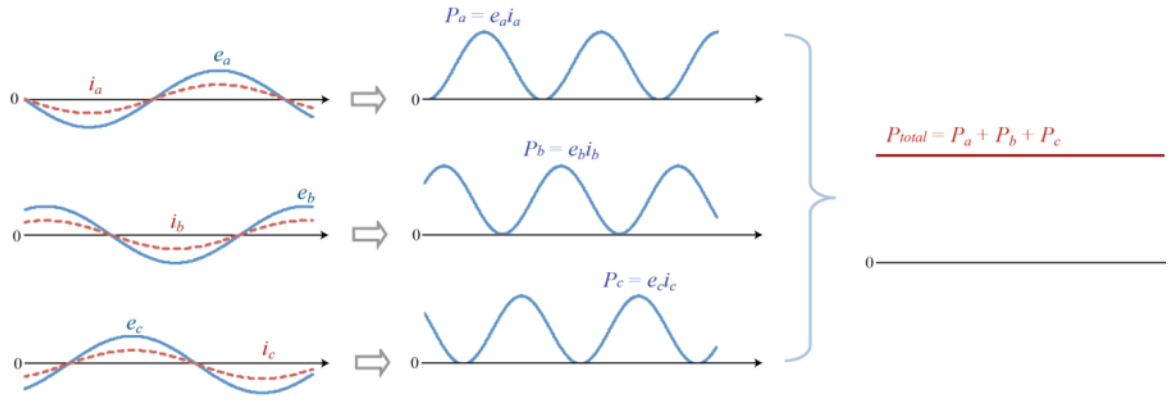

Fig. 1.17. Constant power generated from three-phase sinusoidal currents and back emfs [NAM10].

1.3.3 Variable Flux Reluctance Machines

Based on (1.5), the instantaneous torque production is extended to the 6/4 and 6/8 VFRMs as presented [LIU12b]

$$T_e = \frac{P}{2}\left(i_a^2 \frac{dL_a}{dq_e} + i_b^2 \frac{dL_b}{dq_e} + i_c^2 \frac{dL_c}{dq_e} \right) + \frac{P}{2}\left(i_f^2 \frac{dL_f}{dq_e} \right) + P\left(i_a i_f \frac{dM_a}{dq_e} + i_b i_f \frac{dM_b}{dq_e} + i_c i_f \frac{dM_c}{dq_e} \right). \quad (1.10)$$

It is shown that the instantaneous torque of the 6/4 VFRM is generated by three components. Firstly, the self-inductance variation of the armature windings produces the torque component. The torque production principle resulted from the self-inductance in the 6/4 VFRM is the same as that of the 6/4 SRM. It is proportional to the square of the armature current magnitude, but not related to its polarity. Under a sinusoidal armature current and constant field current condition, the self-inductance of the armature windings contributes to the torque ripple in the 6/4 VFRM, whilst it generates the average torque in the SRMs [LIU13b]. Secondly, the self-inductance of the field windings generates the torque ripple. This component can be regarded as a cogging torque as mentioned earlier. Lastly, the mutual inductance variation between the field and armature windings interacts with the field and armature currents and generates torque. The principle of the torque generation with the mutual inductance is similar to that of the PM machines having PM flux-linkage, where the torque is generated by the interaction between the flux-linkage and armature current. The relationship between the field current and the mutual inductance generates flux-linkage, and the flux-linkage contributes to the torque production with the armature current. Since the flux-linkage of the armature winding is varying over one periodic cycle with respect to the rotor rotation, the maximum torque generation can be achieved by using the armature current in phase. Under the

sinusoidal phase current and constant field current, the average torque is mostly produced by the mutual inductance between the field and armature windings [LIU13a].

On the other hand, the instantaneous torque production of the 6/5 and 6/7 VFRMs is

$$T_e = \frac{p}{2}\left(i_a^2\frac{dL_a}{dq_e} + i_b^2\frac{dL_b}{dq_e} + i_c^2\frac{dL_c}{dq_e}\right) + p\left(i_a i_b\frac{dM_{ab}}{dq_e} + i_b i_c\frac{dM_{bc}}{dq_e} + i_c i_a\frac{dM_{ca}}{dq_e}\right) + \frac{p}{2}\left(i_f^2\frac{dL_f}{dq_e}\right) + p\left(i_a i_f\frac{dM_{fa}}{dq_e} + i_b i_f\frac{dM_{fb}}{dq_e} + i_c i_f\frac{dM_{fc}}{dq_e}\right). \quad (1.11)$$

Unlike the 6/4 VFRM, the 6/5 and 6/7 VFRMs have the mutual inductance component between the armature windings. Hence, this mutual inductance component contributes to the torque production, which is presented in the second component of (1.11).

The VFRMs can be divided into two categories based on the winding configurations of the armature windings [LIU13b]. As a first category, the 6/4 and 6/8 VFRMs have a significant fundamental component of the self-inductance in the armature windings since the armature windings in each phase are connected with the same polarity. Based on the torque production in the SRMs, the self-inductance can be utilised for the additional average torque generation with the harmonic current injection. In contrast, the 6/5 and 6/7 VFRMs have a relatively constant self-inductance due to the opposite connection of the armature windings. This characteristic is similar with the SPM machines, which does not have a saliency between *dq*-axis inductances in a synchronous reference frame. Hence, the maximum average torque can be obtained by a maximum torque per ampere (MTPA) control, in which *q*-axis current is maximised with zero *d*-axis current control [NAM10].

1.4 Control Strategies

1.4.1 Switched Reluctance Machine Control

Typically, the SRM is excited by the unipolar excitation using an asymmetric bridge inverter [WAN05]. Although the SRMs have a simple and robust structure, they have some issues to be improved, i.e. high torque ripple, acoustic noise and vibrations. In order to improve a performance of the SRMs, many methods have been proposed, mainly for the torque ripple reduction. From the control point of view, the methods can be categorised into the following groups.

1.4.1.1 Current Waveform Shaping

This method is a conventional technique to reduce the torque ripple of the SRMs. The phase current waveforms are modified so that a smooth torque can be achieved by using a precedent calculation [MIK13]. The similar concept can be accomplished based on the flux-linkage waveform modification instead of the phase current [RUS98]. During the process of the current calculation, the torque sharing profile, optimisation, or overlapping angle between the phase currents have been utilised for the torque ripple reduction [HUS96]. Additionally, both voltage and current waveforms have been optimised to avoid the spike voltage since high peak current can be excited at the rotor position having a low inductance [STA99]. A modulated unipolar current waveform has been proposed and compared with a bipolar excitation current in terms of torque/current ratio and motor efficiency [NAK12]. The torque ripple was minimised by a combination of machine design and control strategy

[MIK13]. Through a simulation, the required current profiles were found and the resultant current harmonics were given based on the Fourier series. For the elimination of the third harmonic component in the sum of radial forces of the stator teeth, the acoustic noise and vibration reduction method has been proposed based on the utilisation of the dc, fundamental, second and third harmonic currents [TAK15]. As an extended study, a general case is derived by exploring optimised solutions, which considers not only the minimisation of the acoustic noise and vibration, but also copper loss, peak current or torque ripple [BAY16].

1.4.1.2 Feedback Method

For the torque ripple reduction, the operating conditions including machine parameters are fed back to a controller either directly or indirectly. A hysteresis torque controller has been utilised, in which the reference currents are calculated by comparing the directly measured torque and the reference torque [FUE05]. Instead of the direct torque measurement, the torque is estimated based on the measured phase currents and rotor position due to its high cost [KIM01]. Additionally, co-energy is employed for the torque calculation [LUK04], whilst the flux-linkage feedback is utilised for the torque estimation from the phase current and rotor position in a linear condition [BAR98].

1.4.1.3 Advanced Control Method

Since the current shaping technique and feedback methods are still complex, advanced control strategies have been proposed. The current profiles for the torque ripple reduction have been provided from an iterative learning controller [SAH01], whilst fuzzy logic provides a

turn-off angle for the same purpose [ROD01]. The fuzzy logic is also implemented in the current loop for the reference current generation [MIR99], and in the speed loop [SIN98]. Additionally, a neural network is adopted in a learning process of the torque estimation [LIN06]. However, the advanced control strategies have a slow dynamic response due to their high computation overloads.

1.4.1.4 Bipolar Current Excitation

A conventional three-phase inverter has been used for a sinusoidal current excitation to reduce a noise emission and vibration due to its smooth phase current excitation [AHN99], and torque ripple reduction [MOR12]. However, as a drawback of the sinusoidal current excitation, the torque density is inevitably decreased since some harmonic currents contributing to the average torque production are not utilized [LIU10]. One of the challenges for the modern SRM drives is the achievement of the torque density with smooth current excitation. In order to improve the torque density, a bipolar non-sinusoidal current excitation has been proposed by using different current excitations. The bipolar excitation of the SRM phases can result in a short flux path magnetic circuit, and lead to generating a higher torque with less pulsation, in addition to the efficiency and power quality improvement [EDR05]. The sinusoidal current biased by a dc offset was applied to each circuit, which provides the precise torque control and MTPA control. Although this method utilised the virtual rotor flux and rotating stator field, the fundamental component of the phase currents and inductances are only considered [NAK14]. Space vector control from a synchronous machine control has been adopted for the SRM drives [CHE02]. This scheme has a major advantage, which requires

neither the torque nor current profile.

1.4.2 Permanent Magnet Synchronous Machine Control

In general, the machine control methods can be categorised to three types, i.e. scalar control and vector control, which have been widely utilised for various machines [LIP96], and more recently direct torque control (DTC) [TAK89]. In this chapter, vector control and direct torque control are briefly reviewed.

1.4.2.1 Vector Control

The vector control allows an induction machine or synchronous machine to be controlled like a separately excited dc machine. The basic concept of the vector control is to transform three-phase quantities to two equivalent dc components called *dq*, in which *d* and *q* are two perpendicular axes [PAR29]. This allows the torque and flux to be decoupled and controlled separately [NAM10]. In vector control, the rotor position should be known in order to transform the machine quantities.

Generally, the operation conditions of the vector control are a constant torque and flux weakening region. These operations are determined due to the physical limitation of the machine and inverter [MOR90]. MTPA control and flux weakening control have been widely utilised. The MTPA control produces a maximum torque of the machine under a given current condition by maintaining a particular current angle [NAM10]. On the other hand, the objective of the flux weakening control is to increase the machine speed above the base speed [MOR90]. The basic concept is to reduce the flux-linkage in the air-gap by injecting a demagnetising

armature current in the synchronous machine drive. In this thesis, the vector control will be utilised, and more detailed control strategies will be given in Chapter 2.

1.4.2.2 Direct Torque Control (DTC)

The basic concept of the DTC is to control the torque and flux-linkage directly by using lookup tables with voltage vectors [TAK89]. The DTC employs two hysteresis controllers typically, in which one is to correct torque error and the other one is for flux-linkage error correction [FRE96]. The torque controller maintains the estimated torque within a hysteresis band, whilst the flux controller makes the rotating stator flux following a reference trajectory. The DTC has many advantages compared with the vector control. Of all the machine parameters, the stator winding resistance is only required for the DTC. Since the DTC utilises the reference voltage from a lookup table, the computation time of the control system can be reduced. Additionally, because it controls the torque and stator flux-linkage directly, a faster torque response is achieved compared with the vector control.

However, the main drawback of the DTC method is high torque ripple and stator flux-linkage ripple due to hysteresis controller [CAS00]. The DTC scheme is incorporated with space vector pulse width modulation (SVPWM) for the induction machines. It reduces the torque, flux, current, speed ripples in steady state as well as the acoustic noise [LAS00]. Additionally, since the switching frequency varies with operating conditions including the machine speed, load torque, and bandwidth of the controllers, a modified DTC has been proposed for the torque and flux ripple reduction at almost fixed switching frequency [TAN03]. Meanwhile, when the stator flux-linkage is estimated based on an integration of

voltage, it may lead to a long estimation time for both flux-linkage and torque [BOS97]. The compensation for the dc offset error has been utilised in the IPM machine drives [RAH04]. Since the flux-linkage estimation is mainly depended on the stator resistance, the resistance variation can cause a mismatch in the estimation. Especially at low speed operation, the variation of the stator resistance can significantly affect the integration process due to the low back emf. Hence, the stator resistance estimation scheme has been applied by using proportional and integral (PI) controllers based on the error in the flux-linkage [HAQ01].

1.4.3 Variable Flux Reluctance Machine Control

1.4.3.1 External Field Current Control

For the VFRM drives, the external field excitation current control scheme has been utilised as shown in Fig. 1.18 [LIU12a], [FUK12]. For the armature current control, the three-phase bridge inverter can be employed, which has been commonly used in the PM machine and induction machine drives. The dc field excitation current can be obtained by using a separated current source or additional inverter bridge.

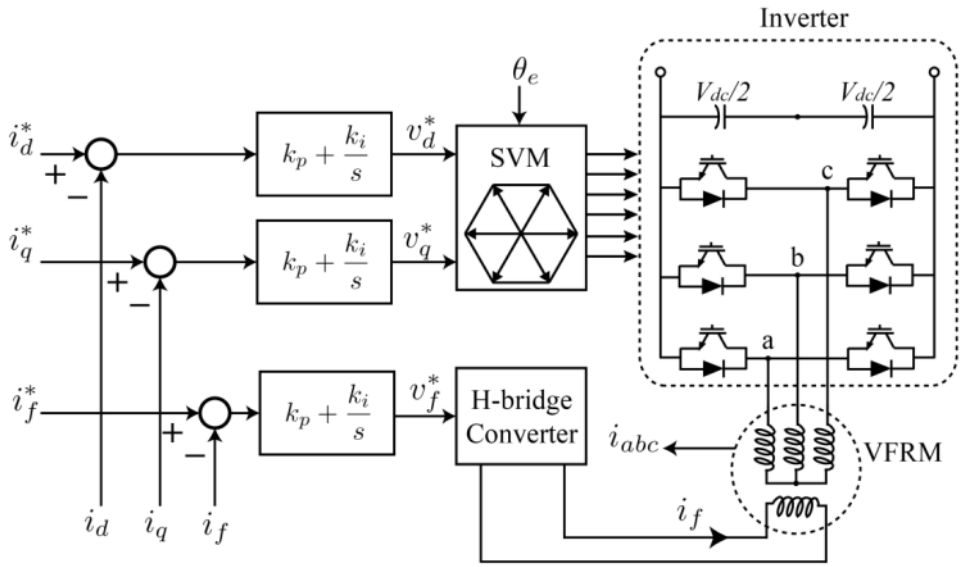

Fig. 1.18. External field current control method for VFRM drives [LIU12a].

1.4.3.2 Harmonic Current Injection

The current shaping techniques in the SRM drives can be regarded as a harmonic current injection into the phase currents. It was shown that the second harmonic current injection into the armature winding could contribute to the average torque in the 6/4 SRM [LIU12b]. However, the principle of the average torque production resulted from the second harmonic current was not fully explained, and the optimal excitation current was obtained from the numerical calculation [BAY16]. Since the 6/4 VFRM has the same structure as the SRMs except for the divided field and armature windings, the contribution of the harmonics will be investigated by using the 6/4 SRM. The derived torque equation is able to evaluate the torque productions for all of the current harmonics in the SRMs.

In contrast, the main source causing the torque ripple can be divided into three parts based on the torque production mechanism of the VFRMs. Firstly, the self-inductance of the armature windings produces the third harmonic torque ripple. Different from the 6/5 or 6/7

VFRMs, the 6/4 VFRM produces the significant third harmonic torque ripple, which is proportional to the square of the phase current magnitude [LIU13b]. In the IPM machines, the self-inductance of the phase windings changes at twice frequency per one rotor revolution, which results in a reluctance torque. However, the 6/4 VFRM has only one periodic change in the self-inductance with respect to the electrical rotor position. This fundamental component of the self-inductance generates the significant torque ripple having the third harmonic component in the 6/4 VFRM. Secondly, the harmonic components of the mutual inductances cause the torque ripple, which is similar with the harmonics in the back emf in the PM machines. Lastly, the cogging torque exists when only the field current is applied in the VFRMs. The interaction between the stator slot openings and the field excitation current causes cogging torque, which is independent of stator armature currents. Hence, in order to reduce such torque ripples the harmonic field current injection scheme can be applied to the VFRMs.

For the torque ripple reduction, many investigations have been researched over the past few decades based on the harmonic current injection. The torque ripple was minimised by selecting the appropriate current harmonics [LEH86]. A series of specific harmonic currents were added into the *q*-axis reference current to suppress the torque ripple. The additional torque components was generated to counteract the fundamental and second harmonic components of the cogging torque for the SFPM machines [JIA10], and PM machines [LEE08]. These prior works were extended to consider the inverter limitations including the finite supply voltage and the finite *di/dt* capability [HAN94]. Since these schemes were

studied under the assumptions that all of the three phases have identical back emf waveforms and have 120° elec. phase shift, the optimised reference phase current waveforms were calculated considering three-phase unbalanced conditions [PAR00]. In [NAK12], the enhanced half sinusoidal phase current has been proposed to achieve the smooth torque production when the excited phase is switched over the adjacent phase. In [BAY15], a numerical solution has been proposed by using the combinations of the harmonic components in the phase currents in order to reduce the acoustic noise and torque ripple.

1.5 Integrated Current Control for VFRMs

There is a possibility to inject the field and armature currents together into a single coil as sinusoidal current biased by a dc offset as shown in Fig. 1.19 [LIU12b], which is named as an integrated field and armature current. Since both field and armature windings are wound on the same stator tooth in the VFRMs, the field and armature windings can be connected in parallel to integrated phase windings as shown in Fig. 1.20. Then, the three-phase currents having dc offset can be injected into the integrated phase windings.

Generally, the phase winding resistance is proportional to the winding length, whilst it is inversely proportional to the cross section area of the winding. Since the integrated current control allows using field and armature windings in a parallel connection, the cross section area becomes double compared with that of the external field excitation control, and it leads to the half of the winding resistance. As a result, the copper loss can be decreased by half. Meanwhile, the number of turns per phase is the same between the external field excitation

current and the integrated current control. Thus, the static and varying components of the phase inductance in both current control methods are maintained at the same because the inductance is proportional to the square of the number of turns. The output torque is only related to the winding inductance components rather than the winding resistance. As a result, the torque can be maintained in both control method if the current condition is the same. It should be noted that the derived voltage and torque equations are still applicable when the integrated current control is adopted.

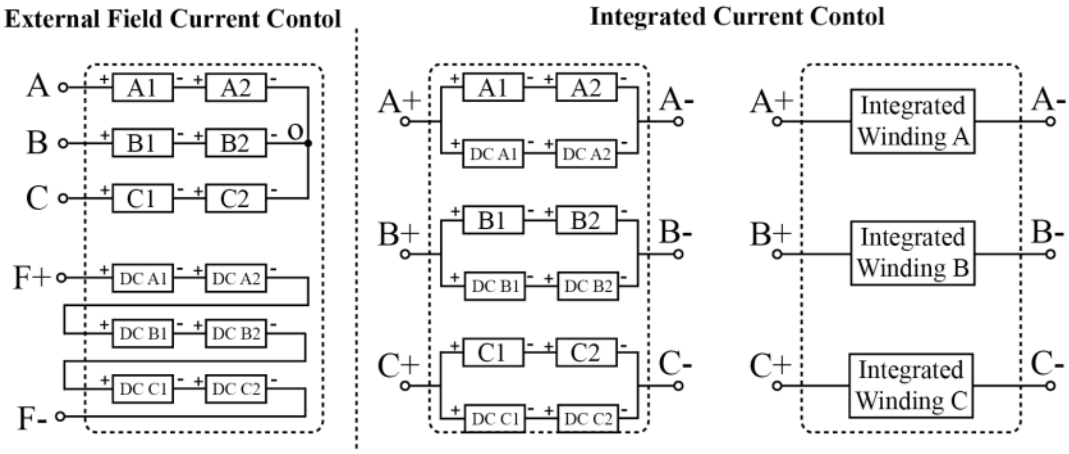

(a) 6/4 and 6/8 VFRMs

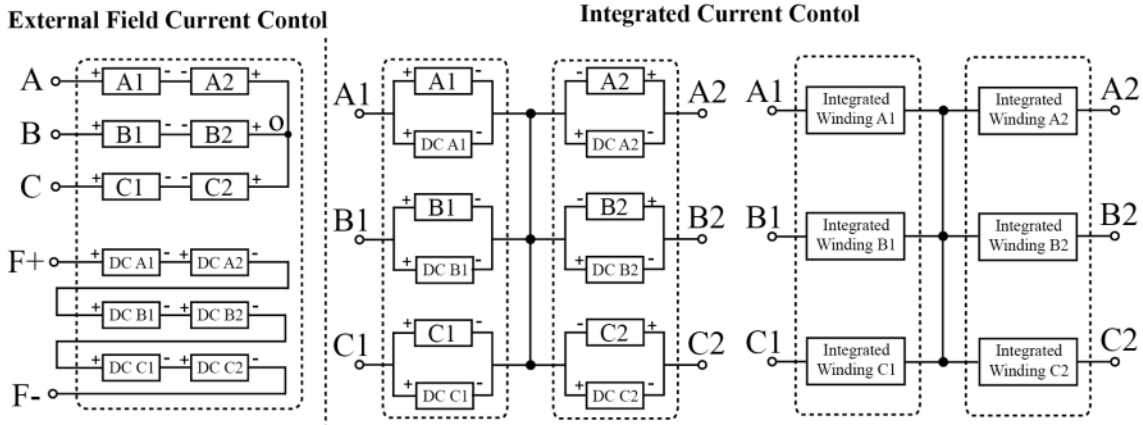

(b) 6/5 and 6/7 VFRMs

Fig. 1.19. Winding configurations of external field current and integrated current control.

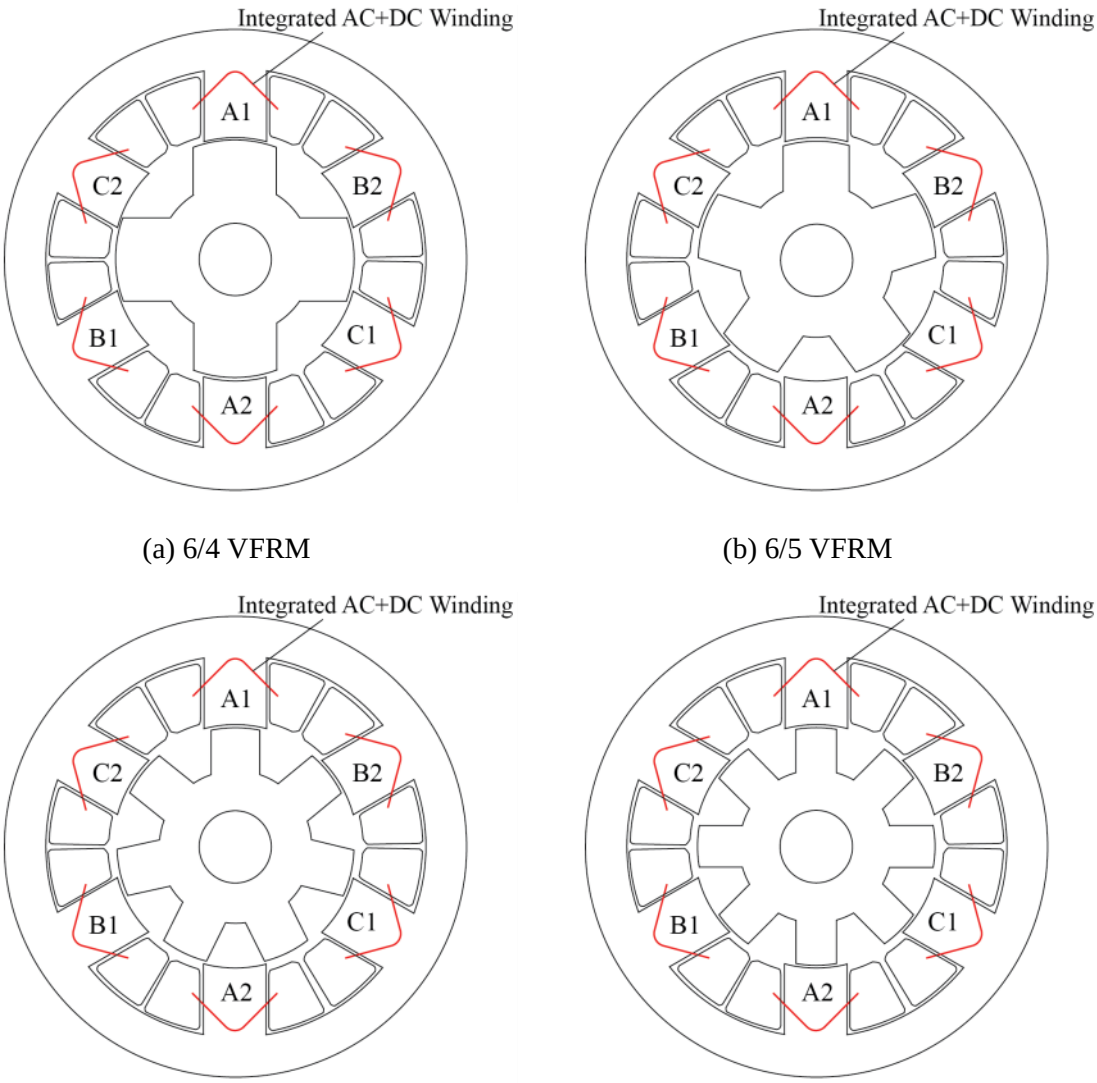

(a) 6/4 VFRM (b) 6/5 VFRM

(c) 6/7 VFRM (d) 6/8 VFRM

Fig. 1.20. Cross sections and windings of the 6-stator pole VFRMs with different rotor poles.

1.5.1 6/4 Variable Flux Reluctance Machine

For the sinusoidal phase current control with dc offset, the zero sequence current control has been utilised by using an asymmetric H-bridge inverter in Fig. 1.21 [NAK14]. In this method, the dc component of the phase current produces a virtual rotor flux, whilst the sinusoidal phase current generates a rotating stator field. In order to generate the dc component of the zero sequence current, an open winding inverter topology can be used, in

which two three-phase inverters are connected to the terminals of the open winding machine in Fig. 1.22 [TAK89], [MUN00]. Although it requires an additional inverter set compared with the conventional three-phase inverter, the increased output voltage leads to an extended operating speed range [KIM04], [PAN14].

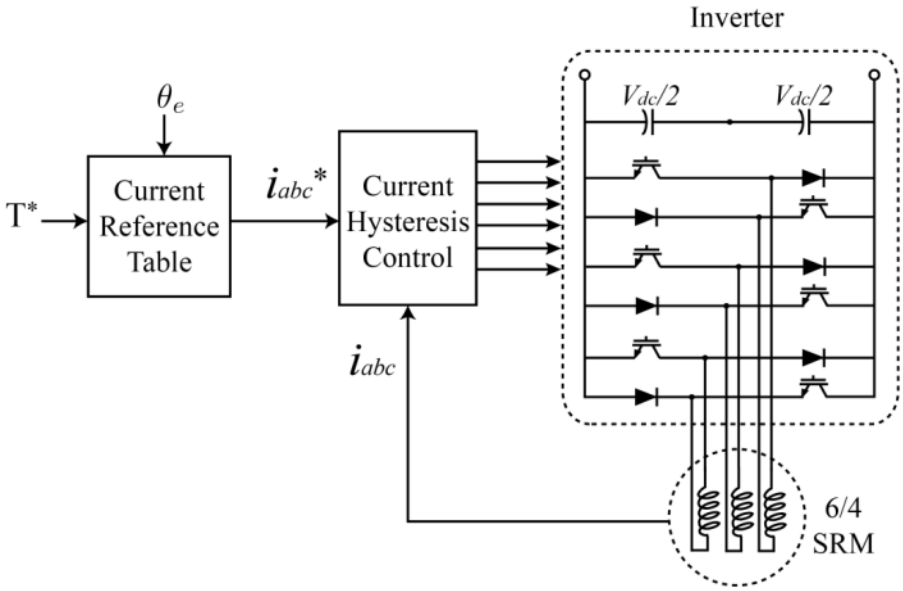

Fig. 1.21. Asymmetric H-bridge inverter [MIL01].

In the open winding inverter using two isolated dc link voltage sources, there is no zero sequence current path for the dc component in Fig. 1.22(a) [STE93], [LEV12], [SRI13]. Hence, it cannot generate the zero sequence current across the machine windings. On the other hand, the open winding inverter can be implemented with a single voltage source in Fig. 1.22(b) [BAI04], in which this configuration allows the current flowing through a common mode loop. However, it also generates the alternating zero sequence current through the machine windings depending on the inverter switching patterns, which may cause the undesirable losses and decrease the efficiency [CHE06], [SOM13]. Therefore, the schemes reducing the alternating components in the zero sequence should be paid to the open winding

inverter with a common dc link voltage source.

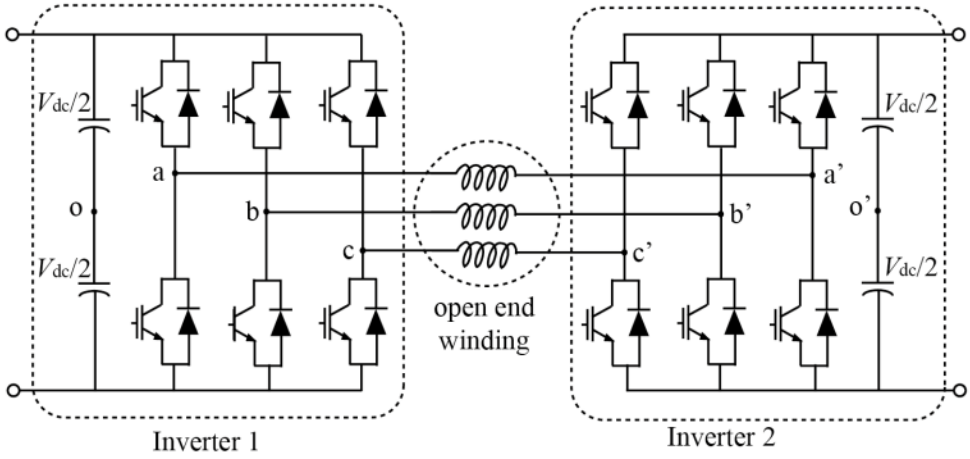

(a) Open winding inverter with two isolated voltage sources [SRI13]

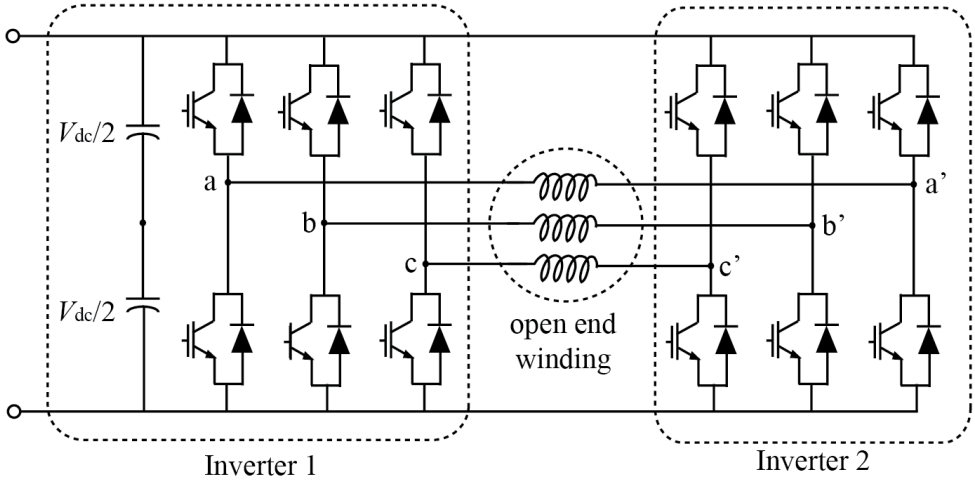

(b) Open winding inverter with a common voltage source [BAI04]

Fig. 1.22. Open winding inverter topology.

To suppress the alternating zero sequence current in the open winding configuration, a common mode voltage elimination has been proposed [BAI04]. The zero sequence voltage can be avoided by utilising the certain switching pattern in order to obtain the same common mode voltage between the two inverters. Also, 120° phase shift method based on the SVM has been introduced [SOM02]. Additionally, the optimal control scheme of switching angles in the two inverters has been proposed for the minimisation of the zero sequence component and

current harmonic distortion [EDP15]. The zero vector placement strategy has been investigated with a sub hexagonal centre and decoupled vector based on PWM switching scheme [SOM08a], [SOM08b]. The switching on-time for the zero vectors is modified in order to minimise the common mode voltage and zero sequence current. For the suppression of the zero sequence current caused by open winding PM machines, the zero vector redistribution concept has been proposed, in which the zero vector is utilised to counteract the third-order harmonic back emf in the machines [ZHO15].

1.5.2 6/7 Variable Flux Reluctance Machine

In the integrated current control scheme, the dc offset component generates a virtual rotor flux as the field current, whilst the three-phase sinusoidal currents produce a rotating stator field. To generate the sinusoidal phase currents with a dc offset, the zero sequence current has been utilised by using the asymmetric H-bridge inverter [NAK14]. The zero vector redistribution technique has been proposed to implement the integrated current control based on the open winding configuration. [ZHU15a] However, these configurations can only be applied to the 6/4 and 6/8 VFRMs because they have the same polarity between the field and armature windings for all stator teeth. In contrast, in the 6/5 and 6/7 VFRMs, one of the three-phase winding sets has the same polarity between the field and armature windings, but the other set has a different polarity as shown in Fig. 1.19 [LIU13b]. Therefore, the integrated control method based on the H-bridge inverter or open winding inverter cannot be directly applied to the 6/5 and 6/7 VFRM drives.

In order to drive the 6/5 and 6/7 VFRMs with the integrated current control, the integrated

windings should be divided into two winding sets in Fig. 1.23, and the resultant winding configuration is similar to a six phase or dual three-phase winding having a 180° phase difference. For VFRM drives with the dual three-phase configuration, the mathematical model should be derived to apply the vector control in the synchronous *dq*-axis frame. A six-phase induction machine has been analysed [NEL74], in which an equivalent circuit has been derived with an arbitrary angle displacement between the two winding sets. Additionally, the machine model for the six-phase induction machine was developed in the synchronous *dq*-axis frame [LIP80], [SIN05]. Similar concepts can be found in the dual three-phase and double-star three-phase configurations. The digital field-oriented control for dual three-phase induction motor drives has been proposed with the machine dynamic model, based on the vector space decomposition [BOJ03]. For the control simplicity, a space vector control technique has been proposed for dual three-phase machines, in which three two-dimensional orthogonal subspaces are introduced for analytical modeling and machine control [ZHA95].

Based on the open winding configuration, the zero vector redistribution has been proposed for suppressing an alternating zero sequence current [ZHO15]. In the same manner, zero vector modification has been proposed for the 6/4 VFRM in order to generate the constant zero sequence current, whilst suppressing the alternating component [ZHU15a]. This method utilised the zero vector difference between two inverters for the generation of the common mode voltage introducing the zero sequence current. When a neutral point is linked between two winding sets in the dual three-phase configuration, the zero sequence current can flow through the machine. This quantity exhibits a standing wave in the air gap, and this component

is crucial because it generates the field current in the integrated current control. Hence, the zero vector redistribution technique is also applicable for the dual three-phase inverter through the neutral point [ZHU16b].

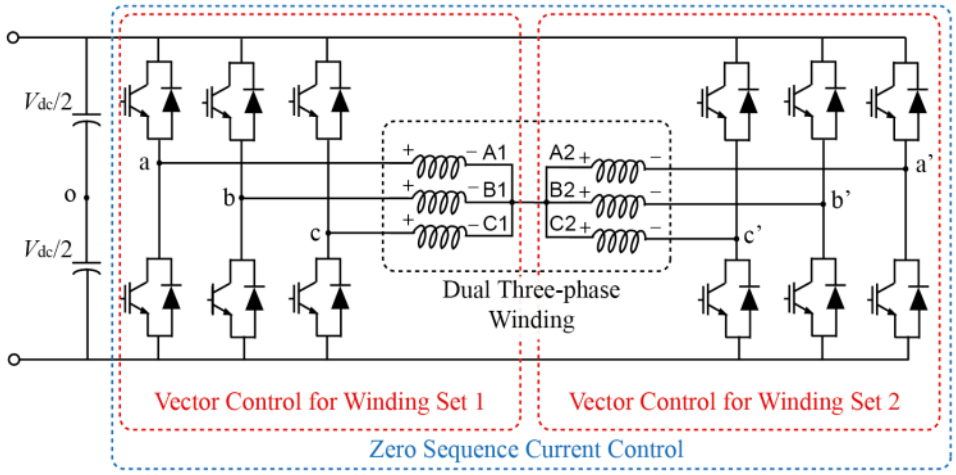

Fig. 1.23. Dual three-phase inverter configuration with a neutral point [LIP80].

1.5.3 FEA Calculation for External and Integrated Current Controls

When the electromagnetic torque of the VFRMs is calculated with the aid of FEA software, the dc and ac components of the currents can be excited to stator tooth together or separately. In this section, it will be shown that the electromagnetic torque of the VFRMs is identical when the dc and ac components of the currents are excited together or separately. Then, due to the identical torque production, the FEA results under the external current control scheme can be transferred to FEA results with the integrated current control scheme.

Fig. 1.24 shows the circuit view of the Flux FEA software in the 6/4 VFRM drives. In the external current control scheme, the field windings from DC A1 to DC C2 are connected in series with the equivalent inductances and resistances in Fig. 1.24(a). The armature windings are connected in Y-connection, and these windings are excited by three-phase currents. The

excited current waveforms are presented in Fig. 1.25(a), which shows the constant dc field current and the three-phase armature currents. On the other hand, the circuit view of the integrated current control in the Flux FEA software is presented in Fig. 1.24(b). The dc and ac windings are in parallel connection, whilst the integrated current waveforms are excited as shown in Fig. 1.25 (b)

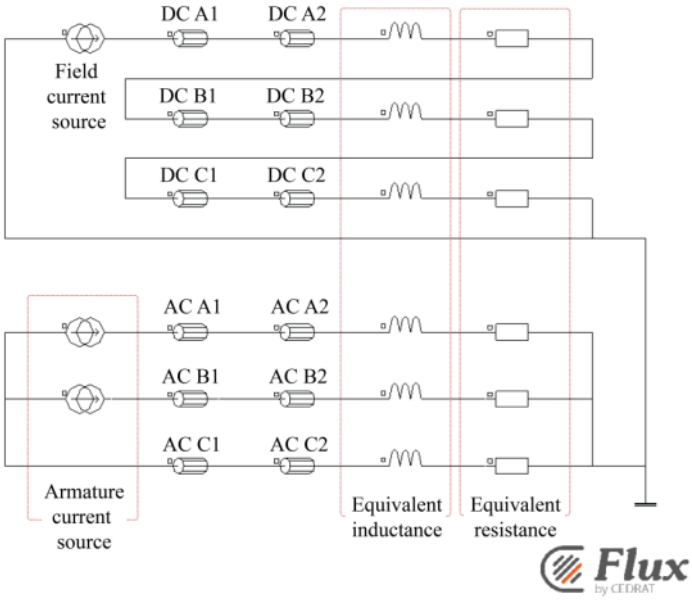

(a) External field current control scheme

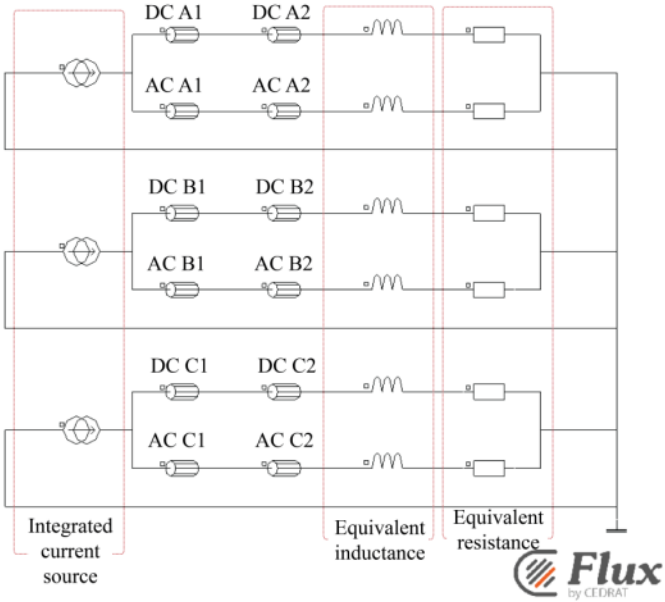

(b) Integrated current control scheme

Fig. 1.24. Circuit view of Flux FEA software in the 6/4 VFRM drives.

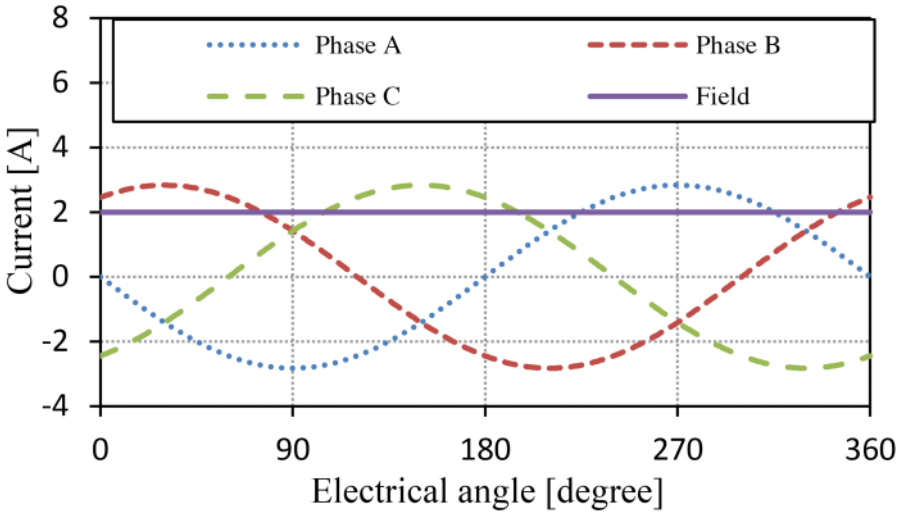

(a) External field current rontrol scheme

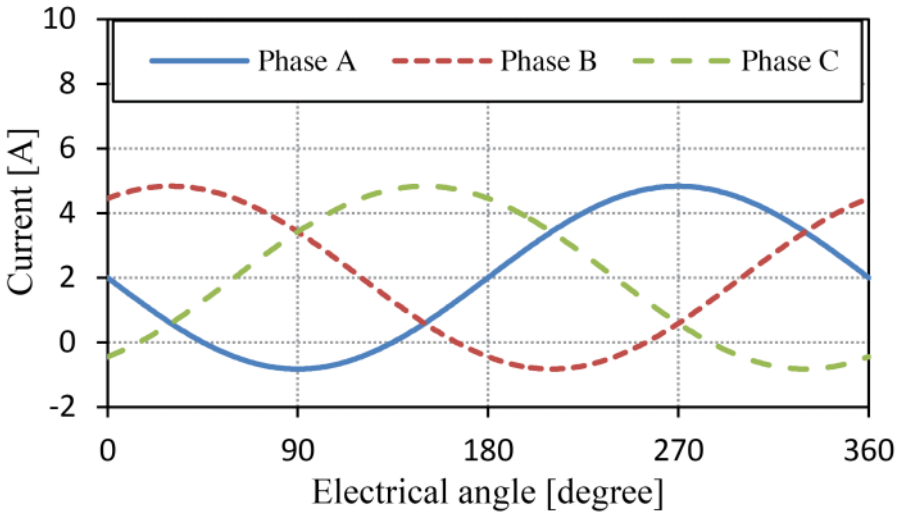

(b) Integrated current control scheme

Fig. 1.25. Current waveforms in the 6/4 VFRM drives.

Meanwhile, Fig. 1.26 shows the circuit views of the FEA software in the 6/5 VFRM drives. The field windings are connected in series having the same polarity, whilst the armature windings have the different polarity in one phase as shown in Fig. 1.26(a). As with the external field current control of the 6/4 VFRM, the field and armature current waveforms are presented in Fig. 1.27(a). In order to realise the integrated current control scheme in the 6/5 VFRM, the dc and ac windings are connected in parallel as shown in Fig. 1.26(b). The current waveforms are shown in Fig. 1.27(b) due to the different polarity.

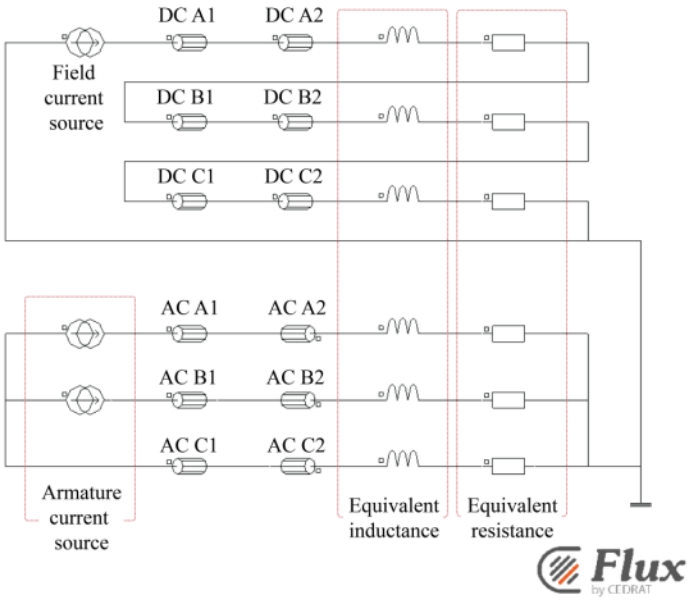

(a) External field current control scheme

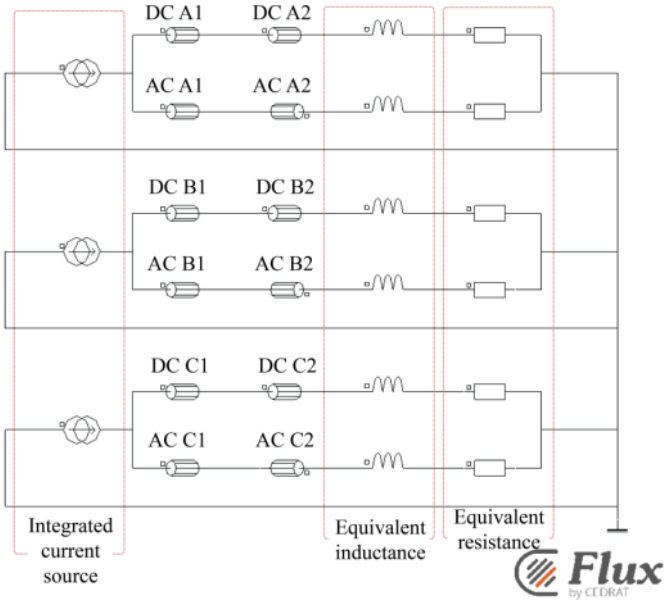

(b) Integrated current control scheme

Fig. 1.26. Circuit view of Flux FEA software in the 6/5 VFRM drives.

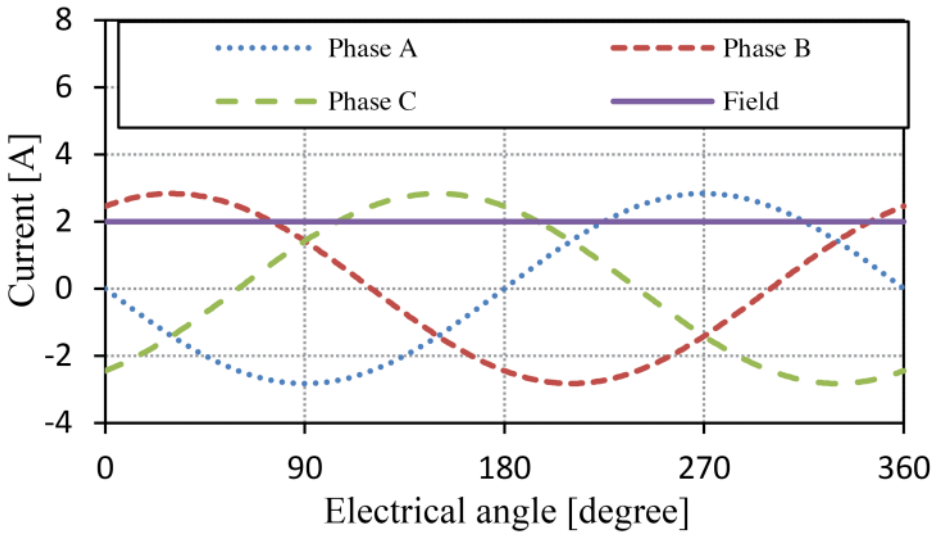

(a) External field current control scheme

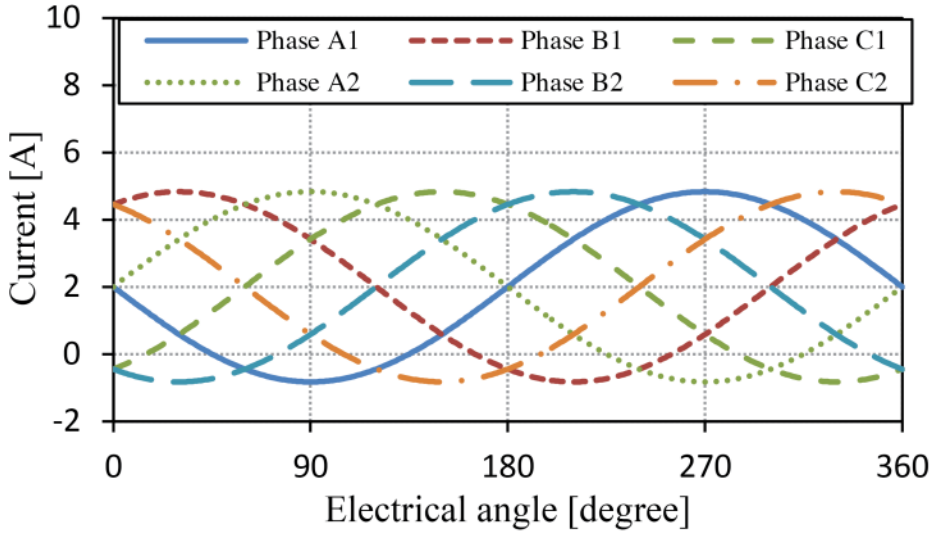

(b) Integrated current control scheme

Fig. 1.27. Current waveforms in the 6/5 VFRM drives.

With both configurations in the 6/4 and 6/5 VFRM drives, the calculated torque waveforms are presented in Fig. 1. 28. It shows that the torque waveforms are identical when dc and ac components of the currents are excited separately or together in both 6/4 and 6/5 VFRM drives. Hence, the FEA results will be converted between the external field current control scheme and the integrated current control method in this paper.

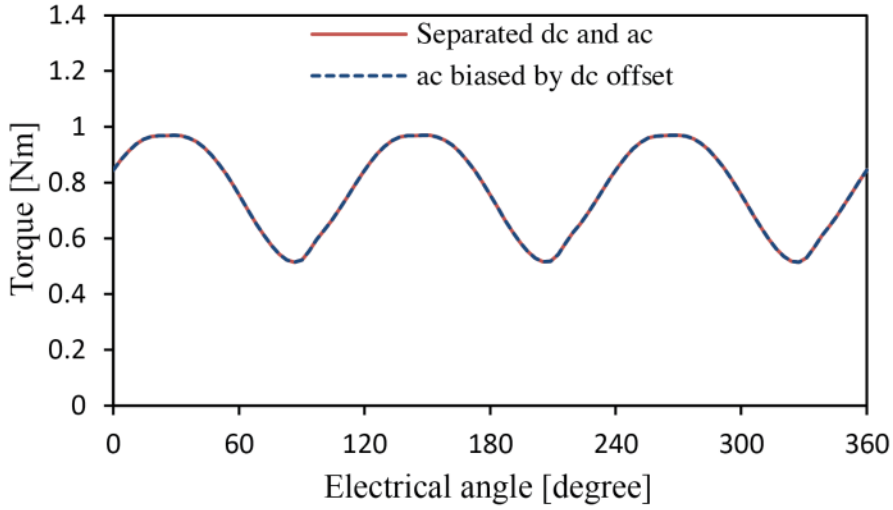

(a) 6/4 VFRM drives

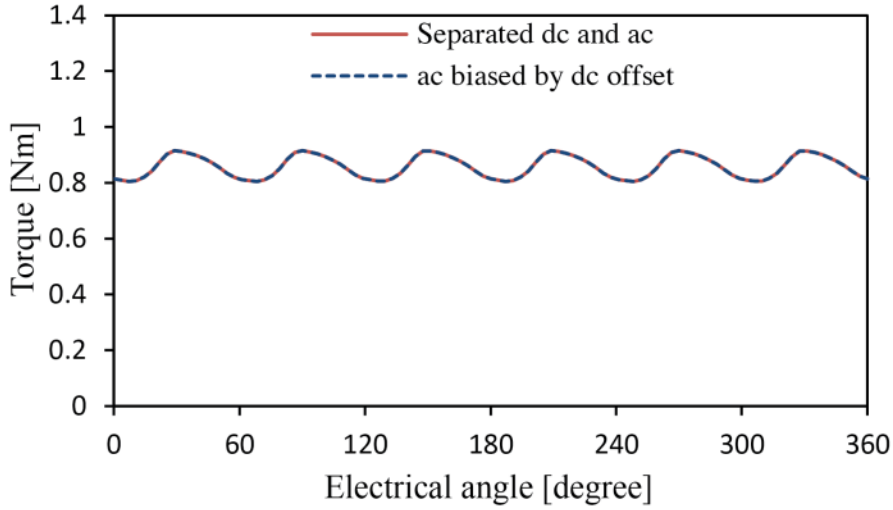

(b) 6/5 VFRM drives

Fig. 1.28. Torque waveforms calculated by Flux FEA software.

1.6 Outline and Contributions of the Thesis

VFRMs and other machines have been reviewed in this chapter, whilst the torque production principle and the possibility of the integrated current control are addressed. This thesis mainly investigates the torque production and control methods for the VFRMs as shown in Fig. 1.29. The torque production of the 6/4 VFRM is investigated in Chapter 3. Based on the analytic torque equation, the torque ripple is minimized by using the harmonic field

current injection in Chapter 4. Moreover, the integrated current control strategy is applied to the 6/4 VFRM with the open winding inverter in Chapter 5, and 6/7 VFRM with the dual three-phase inverter in Chapter 6. Further investigation of the 6/7 VFRM torque production and torque ripple reductions are presented in Chapter 7.

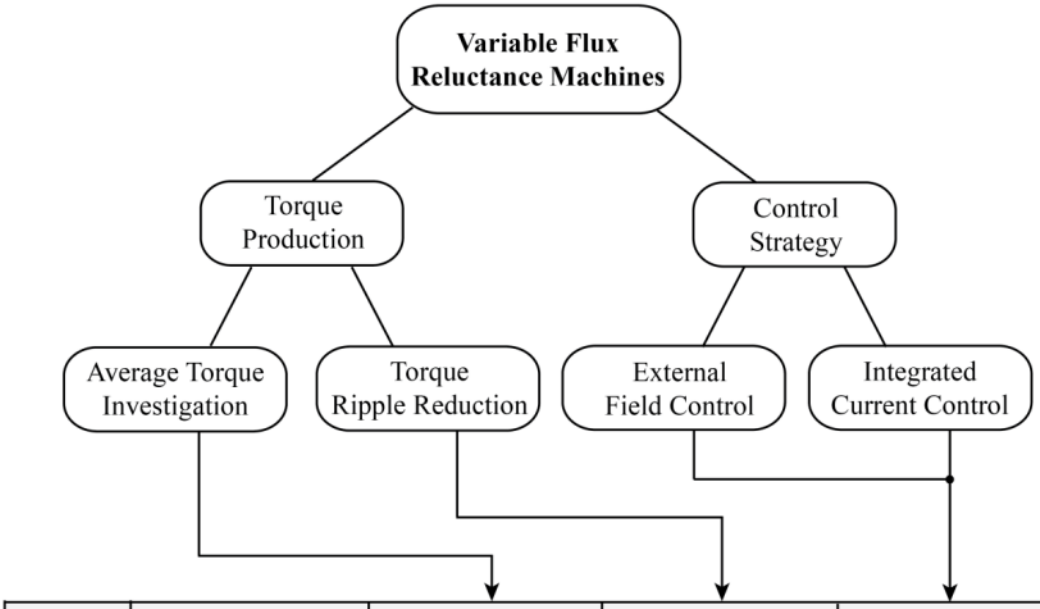

Machine	Winding configuration	Average Torque Investigation	Torque Ripple Reduction	Control Strategy
6/4 VFRM	External field current control	Chapter 3	Chapter 4	Chapter 5
	Integrated current control	Chapter 3	Chapter 7	Chapter 5
6/7 VFRM	External field current control	Chapter 7	Chapter 7	Chapter 6
	Integrated current control	Chapter 7	Chapter 7	Chapter 6

Fig. 1.29. Diagram of whole thesis structure and corresponding topic for each chapter.

The contents of the following chapters are summarised as follows:

Chapter 2: A detailed experimental setup is described including the hardware platform and software implementation is given. For the VFRM drives, a vector control strategy is provided, in which the MTPA control and flux-weakening control are presented.

Chapter 3: The torque equation of the 6/4 SRM is derived considering the harmonics in inductances and currents. Due to the fundamental component of the self-inductance variation, the harmonic current injection method is introduced for the average torque improvement.

Chapter 4: Based on the derived torque equations, the torque ripple waveforms are predicted analytically. By injecting the harmonic field current, the torque ripple minimisation method is proposed for the 6/4 VFRM.

Chapter 5: The integrated field and armature current control strategy is proposed for the 6/4 VFRM using the open winding. The proposed method can increase the machine efficiency and extend the operating speed range due to smaller winding resistance. The zero sequence current is utilised as the field current, whilst the *dq*-axis currents generate the rotating field.

Chapter 6: In order to drive the 6/5 and 6/7 VFRMs with the integrated current control, the dual three-phase configuration with the neutral point is adopted due to the its winding configuration. The conventional *dq*-axis current control scheme is applicable for the armature current control based on the vector control in the synchronous reference frame.

Chapter 7: The instantaneous torque equation of the 6/7 VFRM is derived considering all the harmonics of the inductances and currents. Based on the derived torque equations, the torque ripple waveforms are predicted analytically. By injecting a harmonic field current, the torque ripple minimisation method is proposed for the 6/7 VFRM. Additionally, the harmonic components are injected to the zero sequence current in the integrated current control configurations for the torque ripple reduction.

Chapter 8: The research works are summarised and future work discussions are given.

The major contributions of this thesis are:

- The instantaneous torque equations of the VFRMs are derived considering all the harmonics of the inductances and currents, which provide a better understanding of the torque production in the VFRMs. Contribution of the current harmonics is studied from the respects of analytical investigations and experimental test. It is found that the average torque of the 6/4 VFRM is mainly produced by the interaction between the dc, fundamental and second harmonic components of the phase currents and the fundamental component of the self-inductance.
- It is shown that the third harmonic torque ripple in the 6/4 VFRM is primarily resulted from the fundamental component of the self-inductance in the armature windings. On the other hand, the 6/5 and 6/7 VFRMs exhibit the torque ripple with a multiple of the sixth harmonic component due to the opposite polarity of the armature windings. Based on the harmonic field current injection, the torque ripples of the VFRMs are effectively minimised.
- With the zero sequence current control, the integrated field and armature current control strategy is proposed and integrated into the conventional vector control over the entire operating range. It allows the efficiency improvement and extended operating range due to the reduced winding resistance through the integrated winding of the field and armature windings. Due to its different winding configurations, the open winding inverter is utilised for the 6/4 VFRM, whilst the dual three-phase inverter having a neutral point is adopted for the 6/7 VFRM drives.

CHAPTER 2

EXPERIMENTAL SYSTEM AND VECTOR CONTROL

2.1 Introduction

The experimental system is implemented based on a dSPACE platform, which is a commercial engineering tool for developing and testing mechatronic control systems. dSPACE has different peripheral modules such as host interface, pulse width modulation (PWM) generator, encoder interface, analog-to-digital (A/D) and digital-to-analog (D/A) interfaces. The overall block diagram of the experimental system consists of three parts, i.e. control system, power stage and test rig as shown in Fig. 2.1. With respect to the user's command, the programmed dSPACE generates PWM signals to the inverter so that a machine is controlled at a certain operating point. It should be noted that the power stage and test rig were developed by former Ph.D. students in the Electrical Machines and Drives Group in University of Sheffield. For the machine drives, the vector control will be briefly given including constant torque region and flux weakening region. In order to avoid the degraded performance in the flux weakening operation due to a parameter mismatch, a feedback method is implemented, which does not require the machine parameters.

2.2 Experimental system

2.2.1 Control System

The main processor board provides a basis of the dSPACE modular system, especially in laboratory environments for different purposes. Based on AMD Opteron™ processor, the real-time calculation is performed and it gives the real-time interface to the I/O boards and the host PC. The host interface provides information exchanges and debugging functions between the host PC and the dSPACE. Hence, the command input, parameter acquisition and waveform capture can be easily accomplished with the aid of the real-time communication.

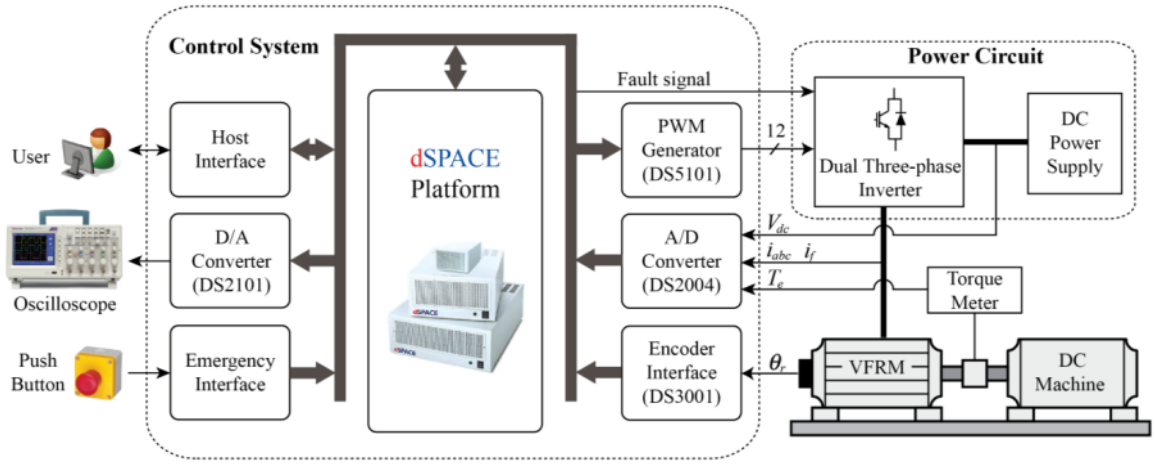

Fig. 2.1. Overall block diagram of experimental systems.

The PWM signals are generated by a DS5101 digital waveform output board. It has been developed to generate complex, high-speed digital signals with high resolution. The board supports the generation of TTL pulse patterns up to 16 channels, which includes PWM signal generation. Additionally, all output channels can be configured as input channels for trigger signals. For the mechanical rotor position measurement, an incremental encoder is mounted to

the shaft of the prototype machine. The encoder signals are linked to a DS3001 incremental encoder interface board. It has been developed to offer precise position measurement in many applications such as machine drive control and robotics. The interface board provides five independent channels and is able to process phase signals from digital incremental encoders having either differential RS422 or single-ended TTL. For the machine speed measurement from the encoder pulses, M method is widely utilised. The principle is shown in Fig. 2.2, where m_e is the number of pulses in a fixed sampling period T_s. A sampling period represents interval time to count the number of the pulse periodically. The counted pulse m_e is utilised for the rotor angular speed calculation by difference derivative. The following equations present the measured angular speed as [NAM10]

$$\omega_r = \frac{2\pi m_e}{NT_s} \tag{2.1}$$

where N is the encoder pulse number per rotation. The switching frequency of the inverter is set to 10 kHz, which is 100 μs for the sampling period T_s. The incremental rotary encoder (Hengstler RI58-D hollow shaft type) is adopted, which has the number of the encoder pulse per rotation at 5,000. In practical operation, the machine shaft should be rotated manually in initial condition for index pulse detection due to its incremental encoder property. The maximum speed of the encoder is 5,000 rpm, and experiments are performed up to 1,500 rpm in this thesis.

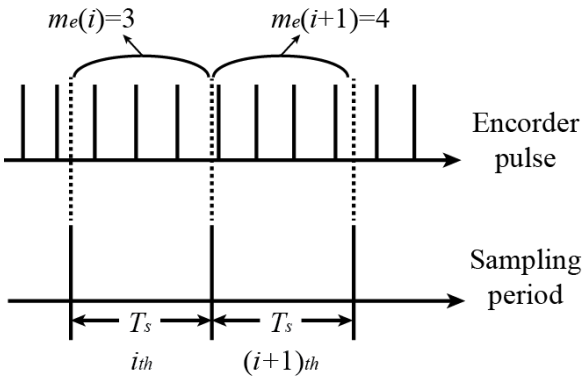

Fig. 2.2. Principle of M method for rotor angular speed measurement.

In order to measure the actual currents and dc link voltage, A/D converter is implemented by DS2004 high speed A/D board. It has been designed for digitising analog input signals at high sampling rates. The A/D conversion can be supported up to 16 independent channels equipped with a separate A/D converter. BNC connectors are utilised for the minimisation of noise influence, and selectable input mode is available at single-ended or differential mode. For the data acquisition through the oscilloscope, D/A converter is implemented with a DS2101 D/A board with five 12-bit D/A channels. The board has been designed to generate analog signals from dSPACE digital signals so that the oscilloscope can capture the waveforms. Additionally, when the push button is activated by a user, the main dc link power line is disconnected by a relay in the inverter. As a result, although dSPACE generates the PWM signals to the switching devices in the inverter, the inverter and machine can be protected from an emergency situation.

2.2.2 Power Circuit

In order to drive the VFRMs with the external current control configuration, the conventional three-phase inverter is required for the armature current control. An additional

current source or an inverter leg is necessary for the field current control. Also, two conventional three-phase inverters should be implemented for the open winding inverter and dual three-phase inverter so that the integrated current control can be implemented. Two three-phase inverters consist of four parts, i.e. two inverters, fans, sensor board, and terminals as shown in Fig. 2.3. The commercial inverter board is utilised, which is STEVAL-IHM027V1 manufactured by STMicroelectronics. The inverter board is designed for three-phase machine control demonstration featuring STGIPS10K60A 600 V, 10 A IGBT intelligent power module. This board can be utilised with single-phase ac supply up to 220 V, or dc supply up to 350 V. As a dc link voltage supplier, the microprocessor controlled laboratory power supply (EA-PSI8360-30) is utilised. It can produce the output voltage up to 360 V, and output current up to 30 A with maximum power rating at 3,000 W.

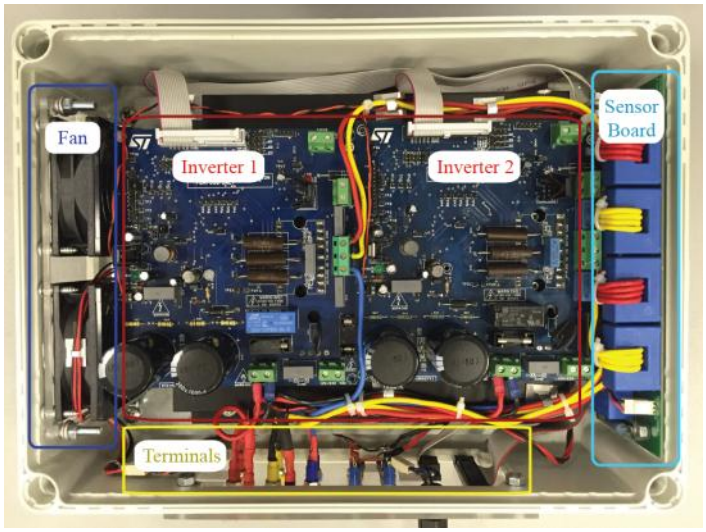

Fig. 2.3. Top view of two three-phase inverter.

The sensor board provides the measurement of the actual phase currents and dc link voltage. The phase current of the machines is measured by the current transducers. The output voltage of the current transducer is transformed to a bipolar voltage signal by using analog

conditioning circuits. Then, the measured voltage is converted to a digital signal by the dSPACE A/D converter. The scale between the actual current I and the voltage of the sensor V_o is set as

$$V_0 = \frac{4 \times I}{1000} \times 100 = 0.4I \tag{2.2}$$

On the other hand, the scale for dc link voltage measurement is presented as

$$V_0 = \frac{V_{in}}{20000} \times 2.5 \times 100 = \frac{V_{in}}{80} \tag{2.3}$$

where V_{in} is the measured dc link voltage. In practice, in order to consider the manufacture error and component tolerance, the offset adjustment is performed experimentally.

2.2.3 Test Rig

The mechanical part consists of three components, i.e. prototype VFRMs, torque transducer, and dc load machine. The prototype machines are the VFRMs having 6-stator pole with different rotor pole combinations. These machines are developed and made by former Ph.D. students in the Electrical Machines and Drives Group in University of Sheffield. The major parameters of the prototype machines will be presented in the corresponding chapters.

For the instantaneous torque measurement, the torque transducer (MAGTROL TM 308/011) is implemented between the test machine and dc machine. It provides extremely accurate torque up to 20 Nm with Sensitivity 250 mV/Nm and speed measurement over a very broad range. Additionally, a conditioning electronic module is integrated providing 0 V to ± 10 V torque output and an open collector speed output. A torque display (MAGTROL 3410) is designed for use with the torque transducer, which powers the transducer and utilises high speed digital signal processing (DSP) to display the torque, speed and mechanical power.

Real-time torque values can be obtained by connecting the torque output to the data acquisition system in the dSPACE. Although the average torque can be observed in the torque display equipment, the torque waveforms are captured by the capture function in order to obtain the data accurately. According to the user manual [MAG12], the gain of the A/D converter is set to 20, whilst the offset is adjusted experimentally. As a mechanacal load, A dc load machine is connected to the prototype machine. In order to dissipate the generated power from the dc load machine, a power resistor is utilised connecting to the armature winding of the dc machine. The field current of the dc machine is supplied by a dc power supply externally so that the load condition can be changed by adjusting the field current or the resistance of the power resistor.

Based on the operation principle of dc machine, the generated torque can be presented as

$$T_L = \frac{k i_f^2 \omega_m}{R_a + R_L} \tag{2.4}$$

where k is a constant, i_f is the field excitation current, ω_m is the mechanical machine speed, R_a is the resistance of the armature winding in the dc machine, and R_L is the resistance of the external resistor, respectively. Then, at a given load resistance and field current, the load torque generated by the dc machine is proportional to the shaft speed as

$$T_L = B_L \omega_m \tag{2.5}$$

where $B_L = k i_f^2/(R_a + R_L)$, it is constant for a given i_f and R_L. Therefore, the load torque is speed dependent by the dc generator. The description of the prototype VFRMs will be presented in each chapter.

2.3 Vector Control

The vector control has been extensively used for ac machine drives in industrial and commercial applications. In the ac machine drives, torque is expressed as the outer product of flux and current vectors. Therefore, the two vectors should be placed in orthogonal for the maximised torque generation. It can be achieved dynamically in a synchronous reference frame by transforming the phase currents to the equivalent *dq*-axis currents for a field oriented control. The transformed *dq*-axis currents are controlled to obtain the required magnitude of flux and torque over the constant torque and constant power regions.

The *dq*-axis currents are defined from the phase current I_s and current angle β as

$$i_{ds} = -I_s \sin(\beta) \tag{2.6}$$

$$i_{qs} = I_s \cos(\beta). \tag{2.7}$$

From the basic mathematical model of the PM machines [NAM10], the voltage and torque equations can be written using the defined *dq*-axis currents as

$$v_{ds} = R_s i_{ds} + L_{ds} \frac{di_{ds}}{dt} - \omega_e L_{qs} i_{qs} \tag{2.8}$$

$$v_{qs} = R_s i_{qs} + L_{qs} \frac{di_{qs}}{dt} + \omega_e L_{ds} i_{ds} + \omega_e \psi_m \tag{2.9}$$

$$T_e = \frac{3P}{4}\left\{\psi_m i_{qs} + \left(L_{ds} - L_{qs}\right) i_{ds} i_{qs}\right\} \tag{2.10}$$

where R_s is the phase winding resistance, ω_e is the electrical angular speed of the machine, and ψ_m is the open-circuit flux-linkage produced by the PMs, respectively.

In the *dq*-axis current plane, the current constrain forms a circle whose centre is located at the origin with the radius I_{max}, which is maximum phase peak current as

$$i_{ds}^2 + i_{qs}^2 \le I_{\max}^2. \tag{2.11}$$

The voltage limit locus in the *dq*-axis current plane can be obtained from the voltage constraint V_{max} as

$$v_{ds}^2 + v_{qs}^2 \le V_{\max}^2 . \tag{2.12}$$

If the winding phase resistance is neglected, the voltage constraint can be simplified to

$$\left(L_{qs} i_{qs}\right)^2 + \left(L_{ds} i_{ds} + \psi_m\right)^2 \le \left(\frac{V_{\max}}{\omega_e}\right)^2 . \tag{2.13}$$

This is the equation of the ellipse centered on the point (ψ_m/L_{ds}, 0) in the *dq*-axis current plane. An operating point can be positioned in the intersection between the current circle and the voltage ellipse unless it exceeds the inverter voltage or current limits.

The machines can have three operating regions limited by the different constraints.

- Region I : constant torque region $I_s = I_{max}$, $V_s < V_{max}$
- Region II : flux weakening region $I_s = I_{max}$, $V_s = V_{max}$
- Region III : flux weakening region $I_s < I_{max}$, $V_s < V_{max}$

2.3.1 Constant Torque Operation

The circle diagram is a graphical technique to determine optimal current vectors for vector controlled ac drive systems in Fig. 2.4 [JAH87], [MOR90], [KIM96]. It can show how these limits restrict the operation region in the *dq*-axis current plane. If the centre point of the voltage ellipse is located outside the current circle, the machine only has Region I and II. Region III only exists when ψ_m/L_{ds} is lower than the current limit, I_{max}.

Region I corresponds to the constant torque region, which is mainly limited by the phase current. Geometrically, Region I operates at the point from O to A in Fig. 2.4. In the constant

torque region, the MTPA control is widely used due to its simplicity and significant performance. For the PM machines with saliency, such as those having inset and interior PMs, the *d*-axis inductance L_d is smaller than the *q*-axis inductance L_q. In that case, the MTPA control results in a negative *d*-axis current in order to utilise the reluctance torque component.

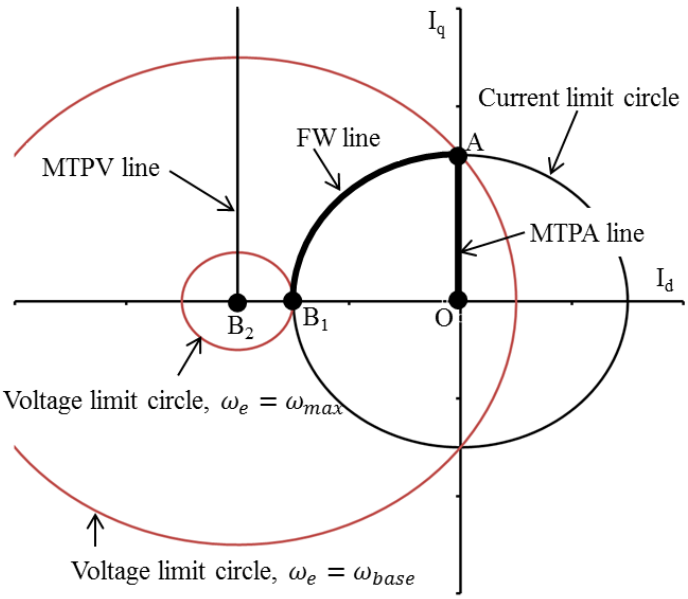

(a) $\psi_m/L_{ds} > I_{max}$

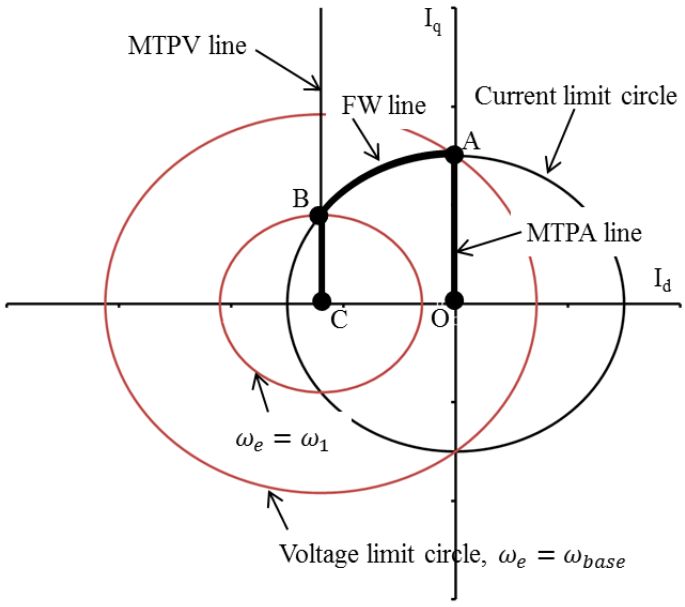

(b) $\psi_m/L_{ds} < I_{max}$

Fig. 2.4. Current and voltage trajectories in SPM machines.

If L_d is equal to L_q, which means no saliency such as the SPM machines, the zero *d*-axis current is maintained due to its no contribution to the torque. It should be noted that although the VFRMs have the doubly salient structure, the torque is mainly determined by the *q*-axis current in the synchronous reference frame rather than the *d*-axis current because the inductance saliency can be assumed as one in the VFRMs [LIU13b].

Under the vector control, the constant torque of the machine can be maintained from zero speed to the base speed of the machine ω_{base} along with the MTPA contour. The machine operates under the current limitation of the inverter, whilst the inverter is able to supply a voltage higher than the required voltage from the machine in the constant torque region. At the base speed, the required voltage of the machine will reach at the maximum voltage which the inverter can produce. Over the base speed, the machine has to be operated under the flux weakening control.

2.3.2 Flux Weakening Operation

In the PM machines, the magnetic flux cannot be controlled directly, since the flux-linkage decreases irreversibly if a demagnetisation occurs significantly. Flux weakening control utilises the stator current component to counteract the fixed amplitude magnetic air-gap flux generated by the PMs, performing a similar role with the field weakening in a separately excited dc machine. In other words, the air-gap flux can be adjusted by injecting the *d*-axis stator current. With the separated excited dc machine, it can be accomplished by reducing the field current of the machine as the speed increases.

Region II corresponds to the flux weakening region which is limited by both constraints

from voltage and current of the inverter. Typically, the machines are designed to reach the maximum inverter voltage at the rated speed and full load conditions. Above the rated speed, the current angle β should be increased due to the supply voltage and current limitations. By using more negative *d*-axis current and less *q*-axis current, the air-gap flux is weakened and the speed increases. It is clear from a geometric viewpoint that the maximum operating point is found at an intersection point of the two curves between the current and voltage. The intersection point satisfies the necessary conditions of the current and voltage constraints. According to (2.13), the voltage ellipse shrinks along with the current limit circle as the machine speed increases. When the machine does not have Region III, the operating point B_1 is the maximum speed ω_{max}, because the intersection point does not exist over the speed at point B_1.

Region III corresponds to the flux weakening region limited by the voltage constraint, in which the centre point of the voltage ellipse is positioned inside the current limit circle. Between the operating points from B to C, the machine operates in the flux weakening control along with the maximum torque per voltage (MTPV) contour. When operating point reaches the point B, the magnitude of the magnetic air-gap flux is fully counteracted by the *d*-axis current. Clearly, further increase in the *d*-axis current will reduce the machine efficiency because the *d*-axis current does not contribute to the torque generation or weakening the field of the air-gap in the SPM machines. Therefore, above the region II speed ω_1, the optimal *d*-axis current will be fixed at $i_{ds}^* = -\psi_m/L_{ds}$, and it moves along with the line from point B to C in Fig. 2.4 with speed increase. Then, the *q*-axis current will be reduced gradually as the speed

increases due to the voltage limitation. If the centre point of the voltage limit ellipse intersects with the current circle, the operating point can be maintained to infinite speed theoretically.

Many flux weakening control schemes have been proposed to realise the optimal current trajectories for different purposes since 1990s. These flux weakening control schemes can be generally classified as two categories, i.e. feed-forward method and feedback method.

Feed-forward method utilises the machine parameters, machine speed and dc link voltage in order to calculate the reference currents based on the voltage equations of the machines [JAH86], [MOR90]. Fast transient response is a main advantage of the feed-forward method since the *d*-axis current is calculated directly from the voltage equations. Additionally, these calculations can be applied for low cost applications with look up table [TUR10]. However, although the feed-forward methods have the fast transient response, they are significantly sensitive to the operating points and machine parameters such as the inductances and flux-linkage.

In contrast, feedback methods utilise the difference between the reference value and predicted value in terms of voltages, currents or machine speed in order to generate the negative *d*-axis current [KIM97]. These schemes do not require the machine parameters such as the *dq*-axis inductances and flux-linkage. Flux weakening control method maximising the voltage utilisation factor has been proposed for Region II, which is shown as *d*-axis reference current modification part in Fig. 2.5 [KWO06]. This scheme is also designed in the synchronous reference frame using the PI current controller and SVPWM with over modulation block. It utilises the *dq*-axis voltage differences between the output of the current

controller and the output of over modulation block to generate the demagnetising current preventing the saturation of current controllers. It can maximise the output torque in the flux weakening region with fast dynamics due to maximised voltage utilisation, which is close to a six-step operation. Additionally, steady-state torque per ampere ratio (T/A) has been introduced affecting influence on the transient performance and average torque. Larger flux weakening gain ρ results in better transient performance, but lower T/A.

In order to drive the machine in Region III, *q*-axis reference current modification scheme has been also proposed as shown in Fig. 2.5 [LIU12c]. Resistive voltage drop in the machine and inverter non-linearity are considered with *q*-axis voltage controller since the output of the current controller is not actual voltage. The *q*-axis current modification allows the machine to operate along with MTPV line. With these two current modification methods, the voltage utilisation can be maximised which is close to the six step operation, and the operating point of the machine can follow the real MPTV line in Region III.

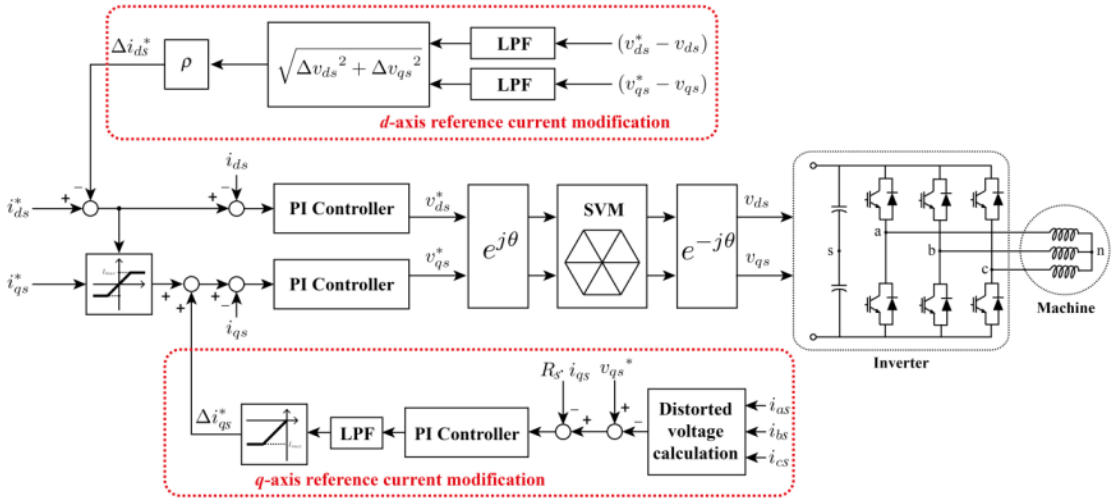

Fig. 2.5. Vector control block diagram for all the operating ranges [KWO06], [LIU12c].

2.4 Conclusion

This chapter provides a detail description of the developed drive system, especially hardware platform, software implementation, and brief vector control strategy. The experimental setup is based on dSPACE with MATLAB/*Simulink*. The commercial inverters are utilised for high accuracy phase current control, whilst the incremental encoder provides the information of the instantaneous rotor position. For both constant torque and flux weakening operations, the vector control scheme is utilised in the synchronous reference frame. In the constant torque region, MTPA control is used with zero *d*-axis current control, whilst the feedback method is implemented for the flux weakening operation. The control schemes are successfully implemented in the hardware platform.

CHAPTER 3

CONTRIBUTION OF CURRENT HARMONICS TO AVERAGE TORQUE AND TORQUE RIPPLE IN SWITCHED RELUCTANCE MACHINES

3.1 Introduction

The average torque of the VFRMs is mainly produced by the mutual coupling between the field and armature windings [LIU13a]. For more in-depth investigation of the torque production, the instantaneous torque equation is derived in this chapter, which reveals the contributions of the harmonics in the phase currents and inductances. The 6/4 VFRM has the same structure as the 6/4 SRM except for the divided field and armature windings. Conventionally, the SRM is excited by the unipolar excitation using the asymmetric bridge inverter [WAN05]. The dc component of the unipolar phase current can be replaced by the field current, and the armature currents can be exchanged for the ac components in an excitation of the SRMs. Hence, the investigation of the torque production in the SRMs can be directly applied to the 6/4 VFRM.

For specific purposes, many different current excitations have been proposed in the SRM drives, i.e. maximum average torque [NAK12], [LIU10], torque ripple reduction [NAG00], [MOR12], [MIK13], and noise and vibration [AHN99], [TAK15]. Additionally, optimised

solutions are derived based on the numerical calculations, which consider not only the minimisation of the acoustic noise and vibration but also copper loss, peak current or torque ripple [BAY15]. However, the principle of the torque production was not presented theoretically. Moreover, the influence of the excitation current harmonics on the torque production has not been investigated.

This chapter focuses on the contribution of the current harmonics to the average torque and torque ripple in the SRMs as well as the optimal current waveform for the maximum torque under a given rms current. In order to make it more general, the analyses are analytically based. In the following section, an instantaneous torque equation, which is able to predict the torque contribution of each current harmonic, is derived by using the Fourier series analysis. Then, the contribution of the current harmonics on the average torque and torque ripple is quantitatively investigated based on the developed torque equation and five designated current waveforms. Additionally, the optimal current waveform for the maximum average torque under a given rms current is further discussed. The experimental validation is provided, whilst the validation by 2D non-linear finite element analysis (FEA) is given in all sections [ZHU16d].

3.2 Instantaneous Torque Equation of 6/4 SRM

For SRMs, their torque production is very often calculated as a function of the phase inductances and phase currents as [MIL01]

$$T_e = \frac{P}{2}\left(i_a^2 \frac{dL_a}{d\theta_e} + i_b^2 \frac{dL_b}{d\theta_e} + i_c^2 \frac{dL_c}{d\theta_e} \right) \tag{3.1}$$

where P is the number of rotor poles, θ_e is the electrical rotor position, i_a, i_b and i_c are the *abc*-axis phase currents, and L_a, L_b and L_c are the *abc*-axis phase self-inductances, respectively.

Actually, this equation is derived based on two assumptions. First, the mutual inductances between different phases are neglected, which is applicable to SRMs [MIL01]. Second, the store magnetic energy in the machine is predicted as:

$$W_{analytic} = \frac{1}{2}\left(L_a i_a^2 + L_b i_b^2 + L_c i_c^2\right). \tag{3.2}$$

When SRMs are on light load and not magnetically saturated, the stored magnetic energy in the machine can be predicted by (3.2). Hence, (3.1) can predict the instantaneous torque of SRMs under light load which will be validated later in this chapter by the numerical results.

When SRMs are magnetically saturated, the stored magnetic energy can no longer be accurately predicted by (3.2). Although (3.1) is still able to predict the average torque accurately, it cannot predict the torque ripple accurately in this case. With the stored magnetic energy calculated by FEA, more general instantaneous torque equation for SRMs machines even under the magnetically saturated operations can be presented as:

$$T_e = \frac{P}{2}\left(i_a^2 \frac{dL_a}{d\theta_e} + i_b^2 \frac{dL_b}{d\theta_e} + i_c^2 \frac{dL_c}{d\theta_e}\right) + P\frac{d}{d\theta_e}\left(W_{analytic} - W_{FE}\right). \tag{3.3}$$

where W_{FE} is the stored magnetic energy by FEA.

In this chapter, the contribution of current harmonics to the average torque and torque ripples is firstly quantitatively discussed under light load condition based on (3.1) and FEA results. The influence of magnetic saturation is also discussed later based on (3.3) and FEA results.

In order to identify the contribution of current harmonics to the average torque and torque ripples, the phase current and relevant self-inductance are expressed as Fourier series of the rotor position. Due to the symmetric winding distribution of three-phase SRMs, the *abc*-axis phase currents and self-inductances have the same waveform but 120° electrical phase shift. Hence, only the *a*-phase current and self-inductance expressions are given as example.

$$i_a(\theta_e) = I_0 + \sum_{m=1}^{\infty} I_m \sin(m\theta_e + \beta_m) \tag{3.4}$$

$$L_a(\theta_e) = L_0 + \sum_{n=1}^{\infty} L_n \cos(n\theta_e + \alpha_n) \tag{3.5}$$

where m and n are the current and inductance harmonic orders. L_0 is the dc component of self-inductance. I_m and β_m are the magnitude and phase of the mth phase current harmonic,. L_n and α_n are the magnitude and phase of the nth self-inductance harmonic, respectively.

Please note that any arbitrary periodic current can be expressed by (3.4). For the self-inductance, it depends on the current waveform. In other words, the SRM and its load current determine the self-inductance waveform. In order to predict the inductance accurately under different current amplitudes and waveforms, the self-inductances are calculated by using frozen permeability method [CHU13] and shown in Appendix.

By substituting (3.4) and (3.5) into (3.1), the instantaneous torque equation can be derived under an arbitrary current excitation as

$$\begin{aligned}
T_e = & -P\sum_{n=1}^{\infty}\frac{3n}{2}L_n I_0^2 \sin\left(n\theta_e + \alpha_n\right) && n = 3k \\
& + P\sum_{n=1}^{\infty}\sum_{m=1}^{\infty} \mp\frac{3n}{2}L_n I_0 I_m \cos\left((m \pm n)\theta_e + \beta_m \pm \alpha_n\right) && (m \pm n) = 0 \text{ or } 3k \\
& + P\sum_{n=1}^{\infty}\sum_{m=1}^{\infty}\sum_{r=1}^{\infty}\left\{\begin{array}{l} \mp\frac{3n}{8}L_n I_m I_r \sin\left((m - r \pm n)\theta_e + \beta_m - \beta_r \pm \alpha_n\right) \\ \pm\frac{3n}{8}L_n I_m I_r \sin\left((m + r \pm n)\theta_e + \beta_m + \beta_r \pm \alpha_n\right) \end{array}\right. & \begin{array}{l} (m - r \pm n) = 0 \text{ or } 3k \\ (m + r \pm n) = 0 \text{ or } 3k \end{array}
\end{aligned} \tag{3.6}$$

where r is the harmonic order of the phase currents and k is an integer starting from 1.

It should be noted that for all of the torque components in (3.6), they are zero unless the relevant constraints listed on the right hand side are met. For example, the first term is zero when $n \neq 3k$. This is due to the sub-components of this term produced by three-phase cancel each other when $n \neq 3k$.

The first term of (3.6) is due to the dc current only and a pure torque ripple, which is similar to the cogging torque in the PM machines. For the second term, it is due to the interaction between the dc and the other current harmonics. When $m \pm n = 0$, it contributes to the average torque. When $m \pm n = 3k$, it only contributes to the torque ripple. For the third term, it is due to the interaction between the current harmonics except the dc one. When $(m \pm r \pm n) = 0$, it contributes to the average torque. When $(m \pm r \pm n) = 3k$, it only contributes to the torque ripple. It also should be noted that the lowest torque ripple order is three, which will confirmed later in Figs. 3.6-3.7.

3.3 Torque Production Under Different Phase Current Waveform Excitations

From the derived torque equation (3.6), it can be seen that different current waveforms result in the different average torques and torque ripples. Hence, in this section, the influence of current waveform and contribution of current harmonics are quantitatively investigated.

The widely used rectangular unipolar current waveform is selected as the bench mark. Its phase current waveform and spectra are given in Fig. 3.1. It can be seen that the rectangular

unipolar current waveform contains all of the current harmonics except the third and its multiple harmonics. In order to quantitatively investigate the contribution of the current harmonics on the average torque and torque ripples, another four current waveforms are developed by only selecting relevant low order current harmonics from the spectra of the rectangular unipolar current waveform. The amplitude and phase of the current harmonics are kept the same. These current waveforms are also shown in Fig. 3.1(a) and their harmonic contents are listed in Table 3.1. From Case I to Case IV, each case contains one more current harmonic than previous case. For example, the Cases I only contains the dc and fundamental harmonics. The Case II contains the dc, fundamental and second current harmonics. Thus, the contribution of the current harmonics can be represented by the differences between two relevant cases.

TABLE 3.1

HARMONICS OF RECTANGULAR WAVEFORM AT 2 APEAK

	I_0	I_1	I_2	I_4	I_5	…
Amplitude (A)	0.667	1.102	0.551	0.276	0.221	…
Phase (rad)	-	0	*π/2*	*π/2*	*π*	…
Rectangular	√	√	√	√	√	√
Case I	√	√				
Case II	√	√	√			
Case III	√	√	√	√		
Case IV	√	√	√	√	√	

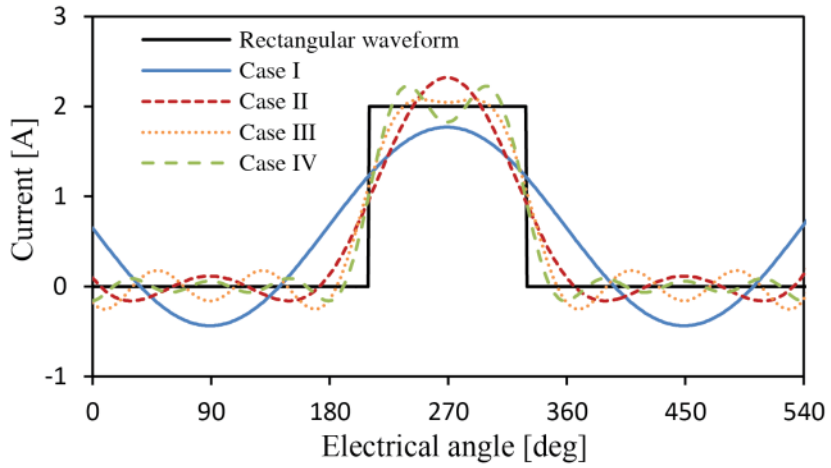

(a) Different phase current waveforms

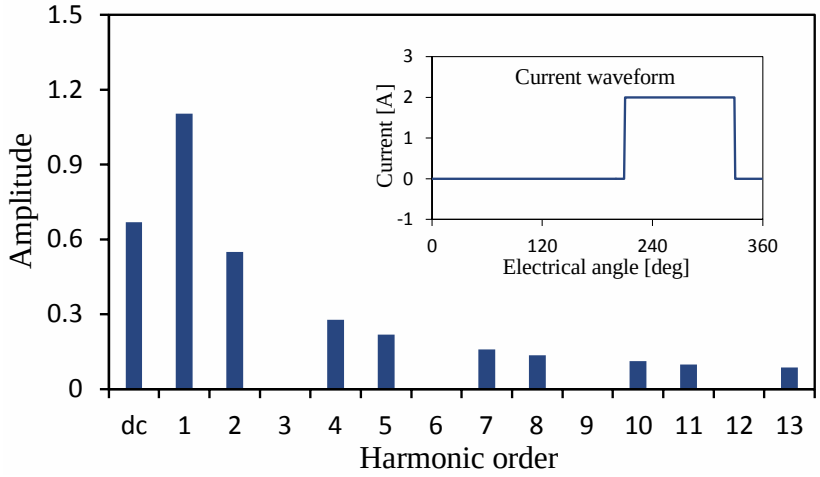

(b) Corresponding current harmonics of rectangular unipolar current waveform

Fig. 3.1. Phase current waveforms at 2 Apeak.

On the other hand, it can be seen from the inductance spectra in the Appendix that the inductance is dominated by the dc and fundamental components for all investigated cases. Since the dc inductance component does not influence the torque and torque ripple, the output torque can be approximated by only considering the fundamental inductance harmonic. Thus, the torque equation (3.6) can be greatly simplified to help reveal the influence of current harmonics.

When only the fundamental inductance component is considered, the average torque is derived from (3.6) as

$$T_{avg} = \frac{3PL_1}{2}\left\{ I_0 I_1 \cos\left(\beta_1 - \alpha_1\right) + \sum_{k=1}^{\infty} \frac{I_k I_{k+1} \sin\left(\beta_{k+1} - \beta_k - \alpha_1\right)}{2} \right\}. \tag{3.7}$$

Combined with the current harmonics listed in Table 3.1, the output torque expressions for the four cases only considering the fundamental inductance component can be obtained and listed in Table 3.2. Please note that by adding the second current harmonic, another torque term is produced due to the interaction between the fundamental and second current harmonics. However, no additional torque is produced when the fourth current harmonic is added if only the fundamental inductance component is considered. By further adding the fifth current harmonic, another torque term is produced due to the interaction between the fourth and fifth current harmonics.

TABLE 3.2

AVERAGE TORQUE COMPONENTS PRODUCED BY FUNDAMENTAL SELF-INDUCTANCE UNDER DIFFERENT CURRENT EXCITATIONS

Case (current harmonics)	Average torque
Case I	$T_{avg\_I} = \frac{3P}{2} L_1 I_0 I_1 \cos\left(\beta_1 - \alpha_1\right)$
Case II	$T_{avg\_II} = T_{avg\_I} + \frac{3P}{4} L_1 I_1 I_2 \sin\left(\beta_2 - \beta_1 - \alpha_1\right)$
Case III	$T_{avg\_III} = T_{avg\_II}$
Case IV	$T_{avg\_IV} = T_{avg\_III} + \frac{3P}{4} L_1 I_4 I_5 \sin\left(\beta_5 - \beta_4 - \alpha_1\right)$

In the similar way, the expressions for the torque ripples considering the fundamental inductance component can also be obtained. Since the third torque ripple harmonic is the lowest order harmonic and the dominating one [LIU10], the expression for the other order

torque ripples are not presented. The expressions of the third torque ripple harmonic only considering the fundamental inductance component are listed in Table 3.3. Being different from the average torque, adding current harmonics always results in additional terms of torque ripples.

TABLE 3.3

THIRD HARMONIC TORQUE RIPPLE PRODUCED BY FUNDAMENTAL SELF-INDUCTANCE UNDER DIFFERENT CURRENT EXCITATIONS

Case (current harmonics)	Third harmonic torque ripple
Case I	$T_{r\_\mathrm{I}} = \frac{3P}{8} L_1 I_1^2 \sin(3\theta_e + 2\beta_1 + \alpha_1)$
Case II	$T_{r\_\mathrm{II}} = T_{r\_\mathrm{I}} - \frac{3P}{2} L_1 I_0 I_2 \cos(3\theta_e + \beta_2 + \alpha_1) - \frac{3P}{8} L_1 I_2^2 \sin(3\theta_e + 2\beta_2 - \alpha_1)$
Case III	$T_{r\_\mathrm{III}} = T_{r\_\mathrm{II}} + \frac{3P}{2} L_1 I_0 I_4 \cos(3\theta_e + \beta_4 - \alpha_1) - \frac{3P}{4} L_1 I_2 I_4 \sin(3\theta_e - \beta_2 + \beta_4 + \alpha_1)$
Case IV	$T_{r\_\mathrm{IV}} = T_{r\_\mathrm{III}} + \frac{3P}{4} L_1 I_1 I_5 \sin(3\theta_e - \beta_1 + \beta_5 - \alpha_1)$

In order to validate the foregoing analytical analyses, the non-linear FEA predicted average torques and torque ripples are also obtained under different current waveforms. The FEA is carried out on a 6/4 SRM as an example. The cross-section, winding layout and main parameters of the 6/4 SRM are shown in Fig. 3.2 and Table 3.4. The rotor position θ_e is zero when the Phase A winding is aligned with a rotor tooth. In this case, $\alpha_1 = 0°$. The optimal β_1 for the maximum torque with rectangular unipolar phase current is 0, which is well-known [NAG00], [LIU10], and it is confirmed by FEA results. More importantly, it can also be explained by the average torque expression in Table 3.2. First, since $I_4 I_5 << I_1 I_2 < I_0 I_1$, the average torque is mainly contributed by the terms containing $I_0 I_1$ and $I_1 I_2$, which will be

confirmed by the average torque difference between five current waveforms. Second, since α_1 = 0°, $\cos(\beta_1-\alpha_1) = \cos(\beta_1)$ and $\cos(\beta_2-\beta_1-\alpha_1) = \cos(\pi/2)$. Both the two major torque terms are maximum when β_1 = 0°.

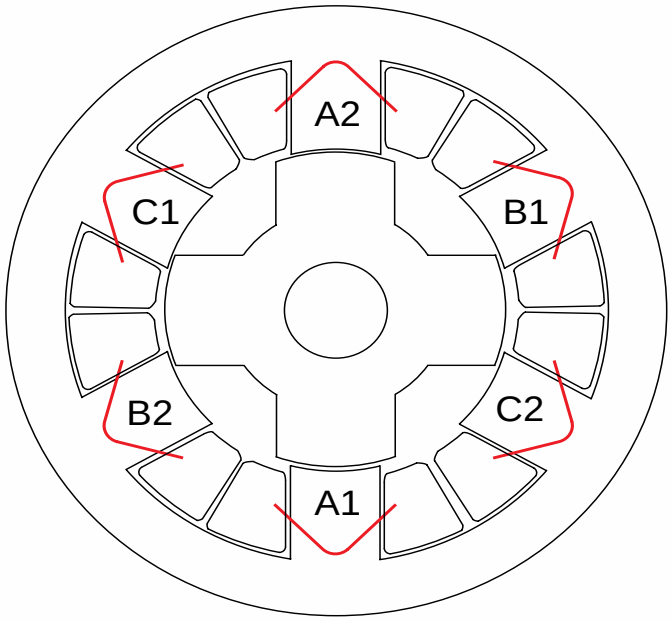

Fig. 3.2. Cross section and winding layout of 6/4 SRM. θ_e =0° when Phase A is aligned with a rotor tooth.

TABLE 3.4

MAIN MACHINE PARAMETERS

Machine parameters	Value
Number of phases	3
Number of stator poles	6
Number of rotor poles (P)	4
Winding resistance (R_s)	3 Ω
Air gap	0.5 mm
Number of turns per phase	366

In Fig. 3.3, the analytically and FEA predicted torque results are compared both on the

average torque and torque ripple. The Fig. 3.3(a) is based on that the current harmonics in Cases I-IV remain the amplitude with the rectangular unipolar waveform. Since Cases I-IV only utilise selected current harmonics, the current rms value and consequently the copper loss are relatively lower than the ones of the rectangular waveform. Thus, in Figs. 3.3(b) and (c), the comparisons are based on the same current rms value. In other words, the current amplitudes of Cases I-IV are increased accordingly, whilst their current waveforms remain the same as shown in Fig. 3.1.

Based on the average torque comparison in Figs. 3.3(a) and (b), the average torque can be predicted accurately by the analytical equations developed in this chapter even when the SRM is under magnetic saturation. It also confirms that the average torque can be approximated by the torque equations listed in Table 3.2 only considering the fundamental inductance harmonics. Based on Fig. 3.3(a), which compares the average torque under the same current harmonic amplitude, it validates the prediction on average torque contributions based on Table 3.2. The average torque due to the interaction between dc and fundamental current harmonics, which is represented by Case I, has the highest contribution. Adding the second current harmonic, the average torque can still be increased substantially. This can be seen from the average torque difference between Case I and Case II. The smallest torque difference between Case II and Case III implies the negligible average torque change by adding the fourth current harmonic. Further adding fifth current harmonic is still able to slightly increase the average torque, represented by the small torque difference between Case III and Case IV. The very little average torque difference between Case IV and the rectangular one also confirms the

contribution of higher order current harmonics are much smaller. The further comparison on the average torque between different current waveforms when the current rms value is the same is shown in Fig. 3.3(b). The average torque per copper loss become similar between all cases except Case I. This means the only utilising the low order current harmonics is able to achieve the same torque density with the one having rectangular unipolar current waveforms.

The comparison on the torque ripple is shown in Fig. 3.3(c). The torque ripple is defined as the difference between the maximum and minimum torques. The torque ripple can be predicted accurately by (3.1) when the SRM is under light load. However, explained earlier, due to the error on stored magnetic energy calculation under magnetic saturation, (3.1) becomes less accurate on the torque ripple prediction when machine is under magnetic saturation. More specifically, the predicted values are less than FEA calculated values since the inductances and flux-linkages are reduced due to magnetic saturation. However, on the other hand, the variation of the torque ripples with the current harmonics can still be explained by the torque ripple equations listed in Table 3.3. When adding another current harmonic, additional torque ripple terms are produced as shown in Table 3.3 and consequently the torque ripple changes significantly as shown in Fig. 3.3(c).

Comparing the current harmonic influence on the average torque and torque ripple, it can conclude that the second current harmonic have high contribution both on the average torque and torque ripple. The fourth and fifth current harmonics play an important role in term of torque ripple but have much lower influence on the average torque.

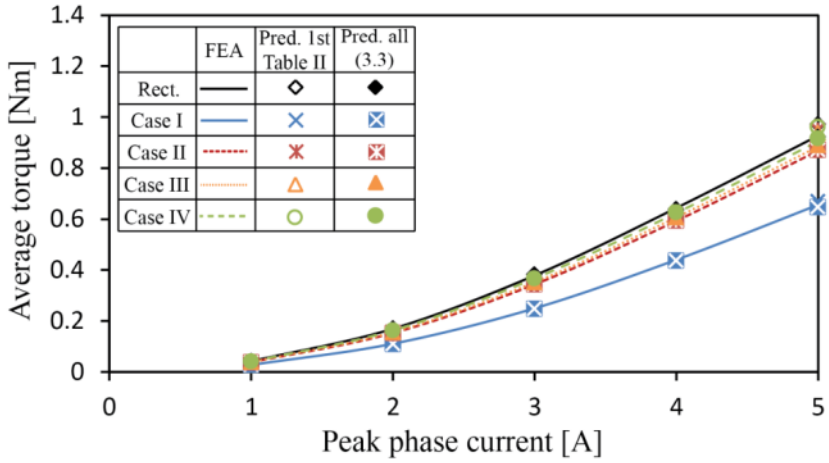

(a) Average torque against the peak current

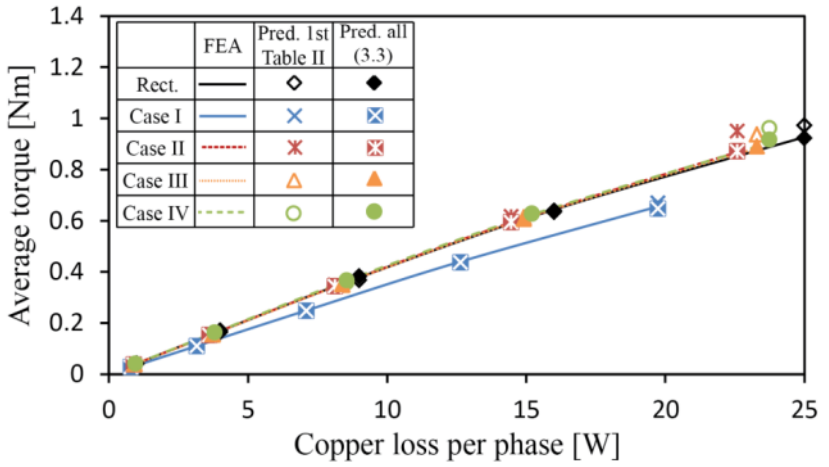

(b) Average torque against copper loss

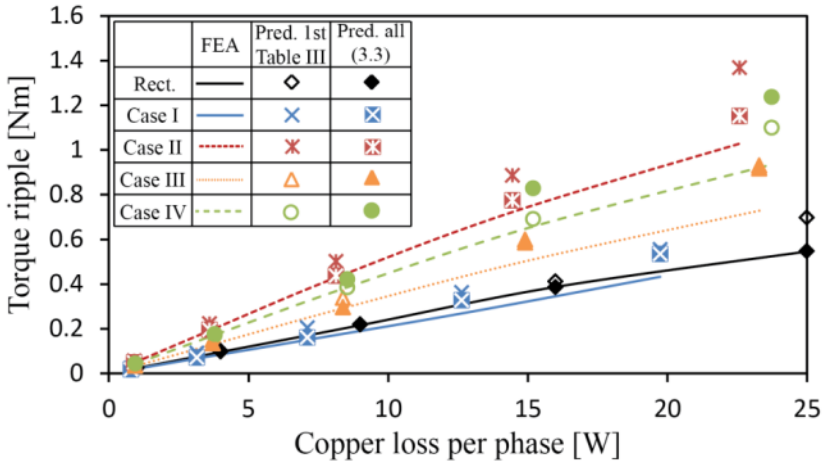

(c) Torque ripple against copper loss

Fig. 3.3. Comparison of the calculated results by FEA under different current excitations.

3.4 Optimisation of Current Harmonics

In the previous section, both the amplitude and phase of the current harmonics are kept the same to the ones when the current is rectangular. However, it is mathematically possible to optimise both amplitudes and phases of each current harmonic to maximise the average torque under a given rms current.

Since $\alpha_1 = 0°$, the average torque equation (3.7) can be rewritten as follows to ease the mathematic operation.

$$T_{avg} = \frac{3PL_1}{2}\left\{ I_0 I_{1q} + \sum_{k=1}^{\infty} \frac{I_{kq} I_{(k+1)d} - I_{kd} I_{(k+1)q}}{2} \right\}. \tag{3.8}$$

where $I_{kd} = I_k \sin(\beta_k)$ and $I_{kq} = I_k \cos(\beta_k)$.

Please note I_k is the amplitude of the kth current harmonic. The rms value of the input current is calculated as

$$I_{rms} = \sqrt{I_0^2 + \frac{1}{2}\sum_{k=1}^{\infty} I_k^2} = \sqrt{I_0^2 + \frac{1}{2}\sum_{k=1}^{\infty}\left(I_{kd}^2 + I_{kq}^2\right)}. \tag{3.9}$$

For Case I only containing dc and fundamental current harmonics, the optimal distribution between current harmonics and the maximum average torque can be obtained as:

$$\sqrt{2} I_0 = I_{1q} = I_{rms}, \tag{3.10}$$

$$T_{\max\_case\mathrm{I}} = \frac{3}{2} PL_1 I_0 I_{1q} = \frac{3}{2\sqrt{2}} PL_1 I_{rms}^2. \tag{3.11}$$

The average torque in this case is maximum when the dc and fundamental current harmonics have the same rms value.

For Case II, the optimal current harmonics and the maximum average torque under given rms phase current can also be obtained by using Lagrange multiplier method as:

$$\sqrt{3} I_0 = I_{1q} = \sqrt{3} I_{2d} = I_{rms}, \quad I_{1d} = I_{2q} = 0, \tag{3.12}$$

$$T_{\max\_caseII} = \frac{3\sqrt{3}}{4} P L_1 I_{rms}^2. \tag{3.13}$$

It can be seen that the optimal phase for the current harmonics are $\beta_1 = 0°$ and $\beta_2 = \pi/2$. Please note these values are the same to the current harmonic phases of the rectangular phase current.

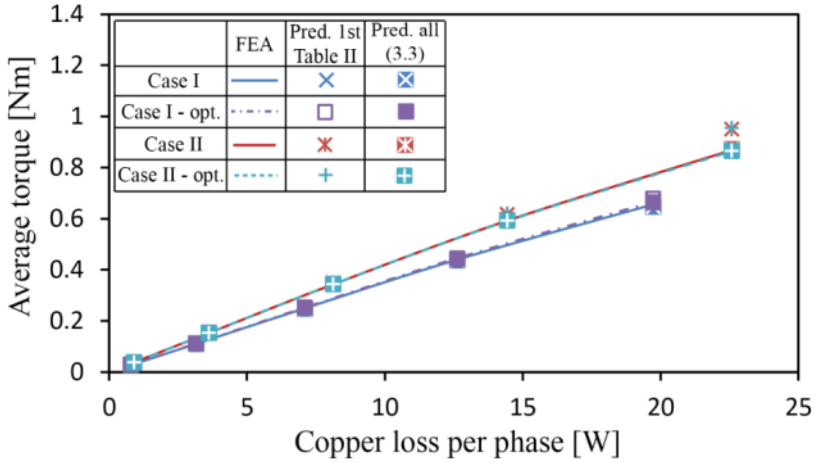

(a) Average torque against copper loss

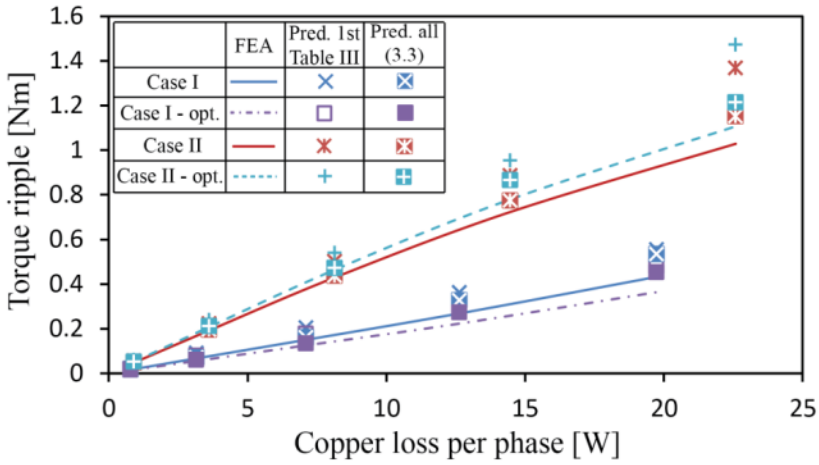

(b) Torque ripple against copper loss

Fig. 3.4. Comparison of the average torque and torque ripple with/without the optimised current magnitude and phase angle.

Based on the same principle, the optimal current harmonics and the maximum average torque for Cases III and IV can also be obtained. It is found the maximum average torque under a given rms current for Cases III and IV is the same as the maximum torque of Case II. This conclusion is identical to the phenomenon in Fig. 3.3(b). It also confirms that the average

torque is majorly contributed by the dc, fundamental and second current harmonics.

In Fig. 3.4, the torque variations are compared for Cases I and II when the current harmonics are optimal or remain the same as listed in Table 3.1. In terms of the average torque, the difference between two cases is negligible. This is due to that the current harmonic phases are already at the optimal value. The current harmonic amplitudes are also not far away from the optima. In terms of the torque ripple, it is slightly reduced in Case I after optimisation. However, it is slightly increased in Case II after optimisation.

3.5 Experimental Validations

In order to experimentally validate the foregoing investigations, the average torque and torque ripple under different current waveforms are measured based on the 6/4 SRM shown in Fig. 3.2 and Table 3.4. The torque waveforms are measured by a torque transducer as shown in Fig. 3.5. Due to the limited bandwidth of the torque transducer, the machine speed is 15 rpm. In order to generate the designate current waveforms having negative part, an H-bridge inverter is employed rather than the conventional asymmetric bridge inverter. The control part is implemented on dSPACE platform.

The analytically predicted, FEA calculated and measured torque waveforms under different current waveforms at 3 A peak and 5 A peak are compared in Figs. 3.6 and 3.7, respectively. 3 A peak and 5 A peak represent the light and heavy loads, respectively. It shows that the analytically predicted torque waveforms match well with the FEA calculated and measured torque waveforms for all investigated current waveforms and loads. Since the predicted results

by (3.1) are not matched well in Fig. 3.7 due to the inaccurately predicted stored energy, the stored energy must be calculated by FEA to compensate the predicted stored energy as shown in (3.3) for the 5 A peak case. The average torque can be predicted based on the derived torque equation in both light and heavy loads by using the frozen permeability. The overall feature of the torque waveforms under different current waveforms remains similar when the SRM is under light or heavy load.

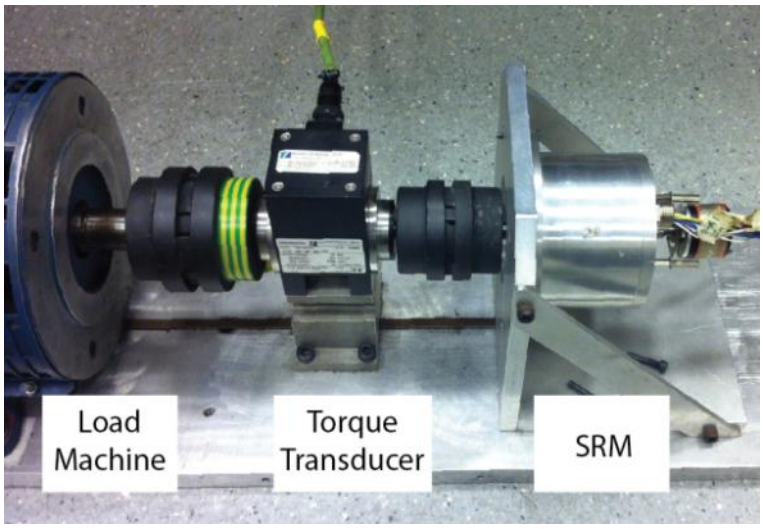

Fig. 3.5. Experimental test rig.

Based on the measured torque waveforms under different current waveforms and amplitudes, the variation of measured average torque and torque ripple with the load can be obtained and shown in Fig. 3.8. Comparing Fig. 3.8 with Fig. 3.3, the results match well with each other. It also confirms that the average torque of Case I is the lowest. There is a big average torque increase by adding second current harmonic. However, the average torque increases very mildly when the fourth and fifth current harmonics are added. If under the same rms current, all cases have similar average torque except the Case I. In terms of the torque ripple, it confirms that the Case II has the largest torque ripple, whilst the Case I has the lowest.

The torque ripple is reduced by adding fourth and fifth current harmonics. Hence, the fourth and fifth current harmonics have higher influence on the torque ripple but much lower effect on the average torque.

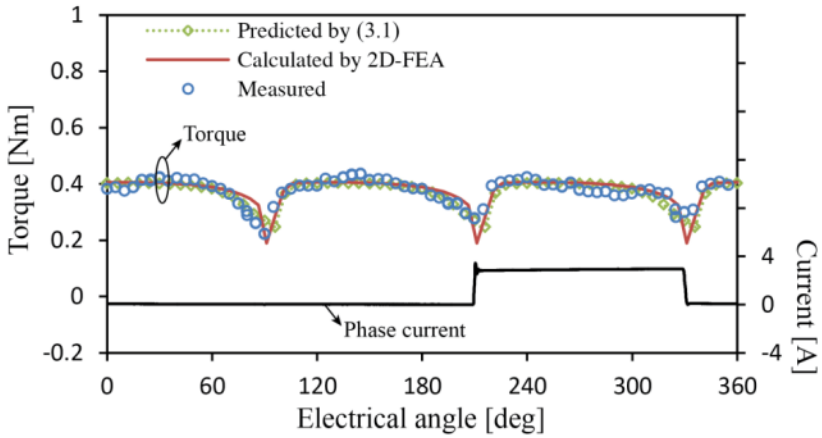

(a) Rectangular current

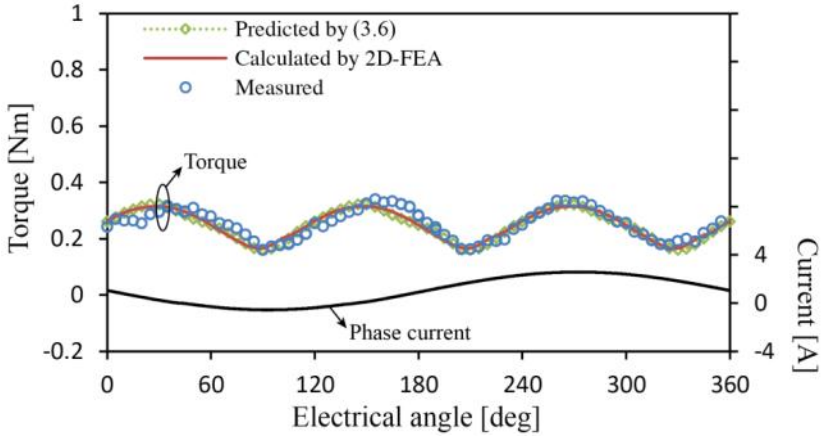

(b) Case I

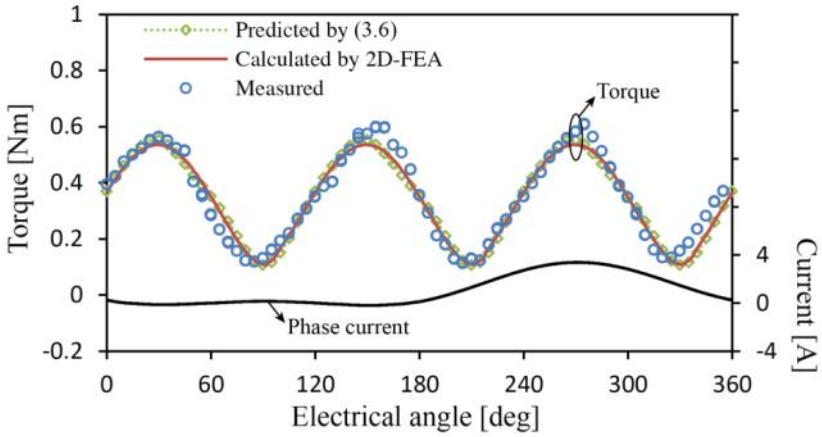

(c) Case II

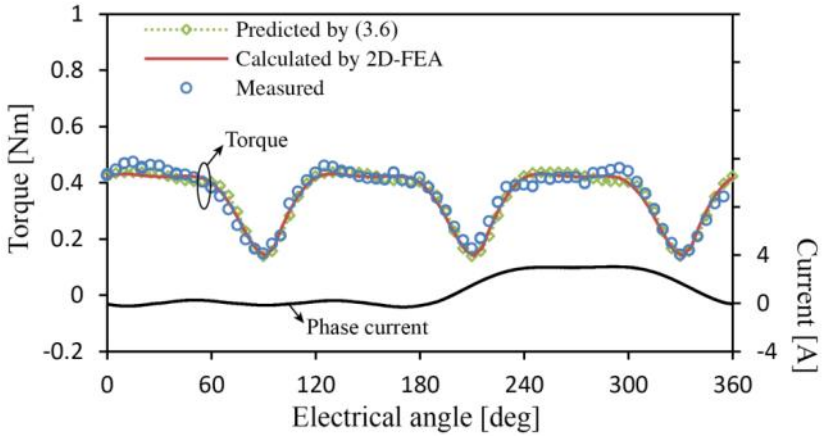

(d) Case III

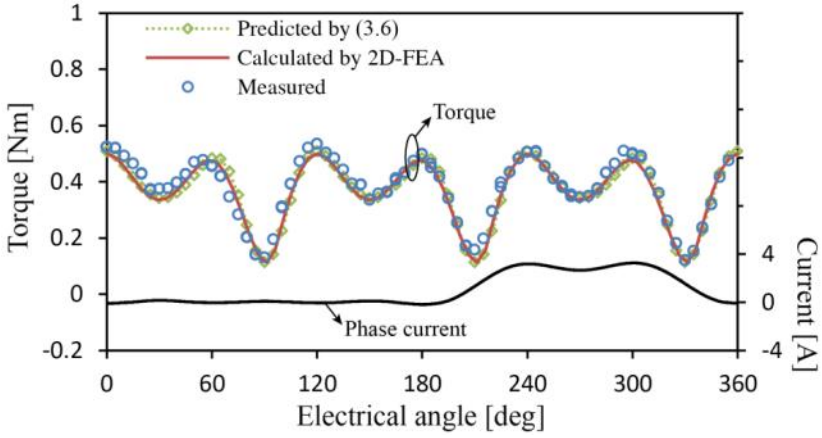

(e) Case IV

Fig. 3.6. Comparison of the torque waveforms between FEA calculated, analytically predicted, and measured results under the different current excitations at 3 Apeak.

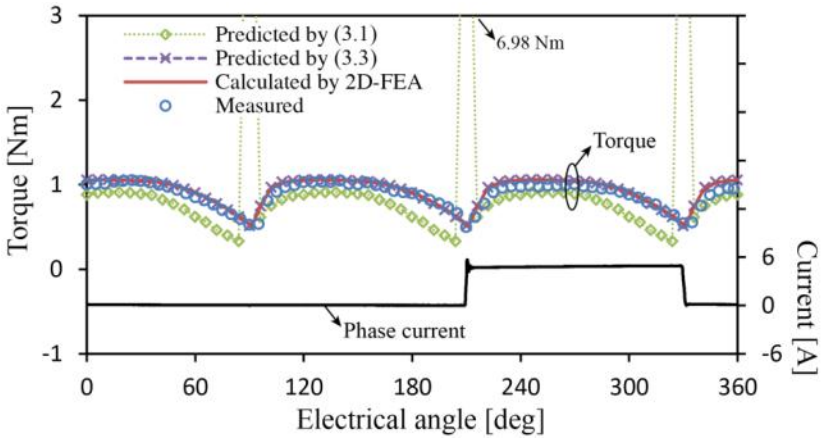

(a) Rectangular current

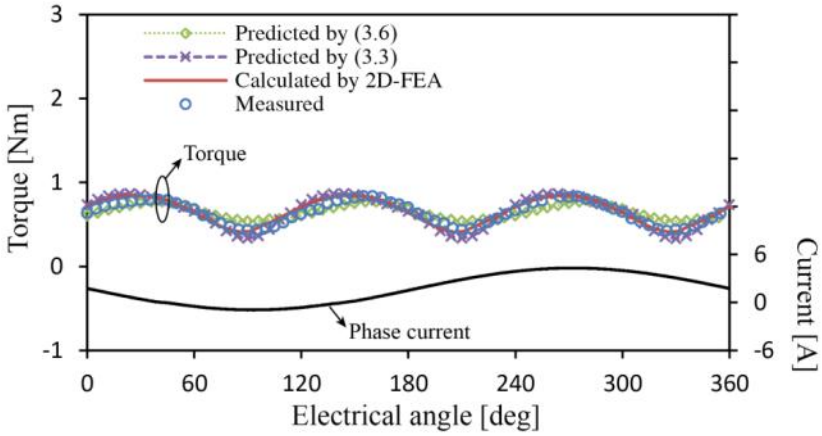

(b) Case I

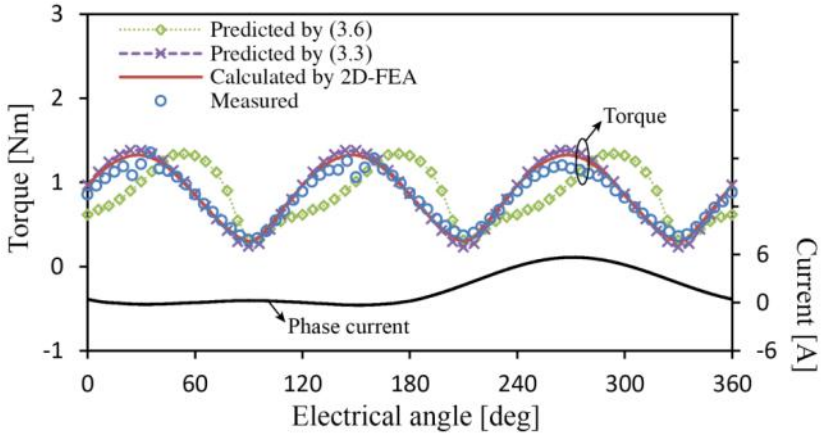

(c) Case II

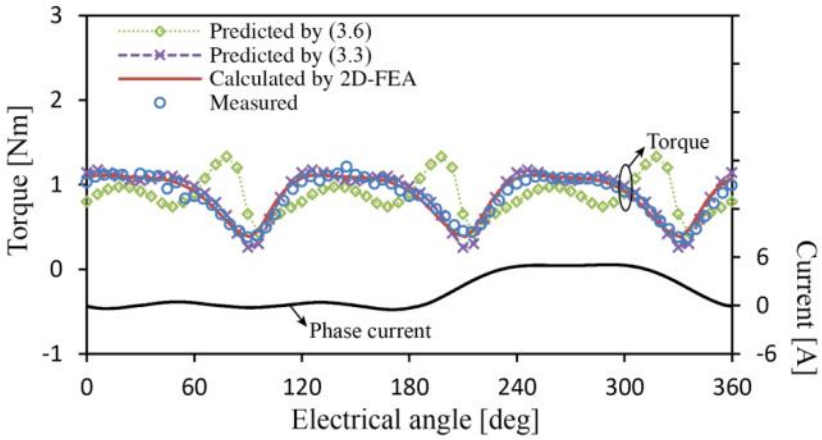

(d) Case III

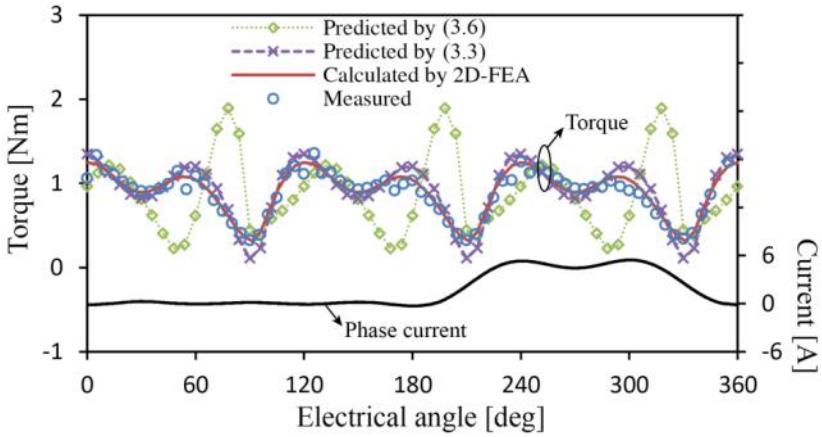

(e) Case IV

Fig. 3.7. Comparison of the torque waveforms between FEA calculated, analytically predicted, and measured results under the different current excitations at 5 Apeak.

The comparison of the average torque and torque ripple with/without optimising current harmonics are also shown Fig. 3.8. It shows that the difference of the average torque is negligible for both cases. This matches with the analytical prediction in section IV. It is due to the current harmonics obtained from the rectangular waveform are already very close to the optima. For the torque ripple, it is slightly reduced with optimal current for Case I but increased for Case II. This also matches the prediction in Fig. 3.4.

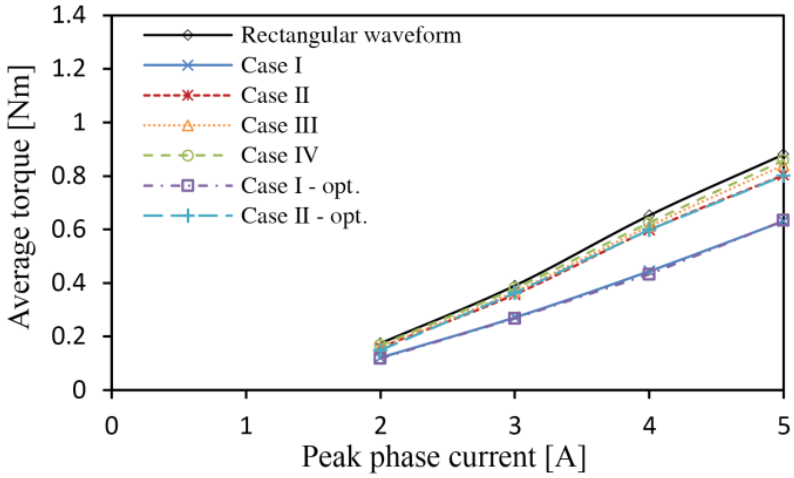

(a) Average torque against the peak current

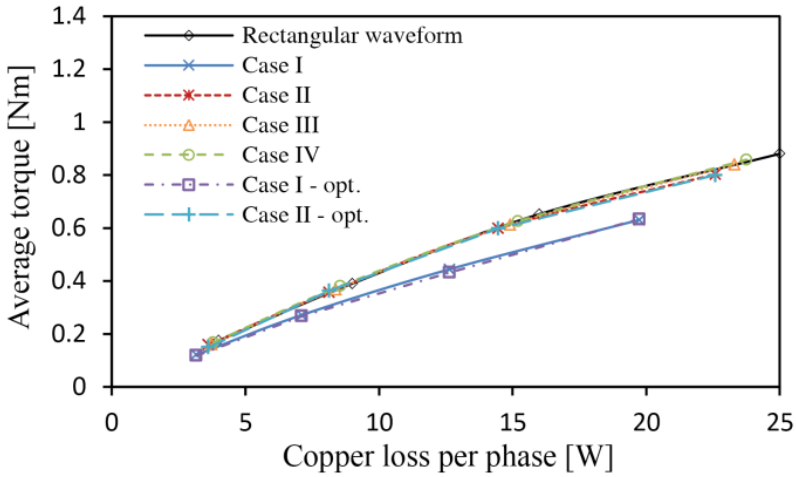

(b) Average torque against copper loss

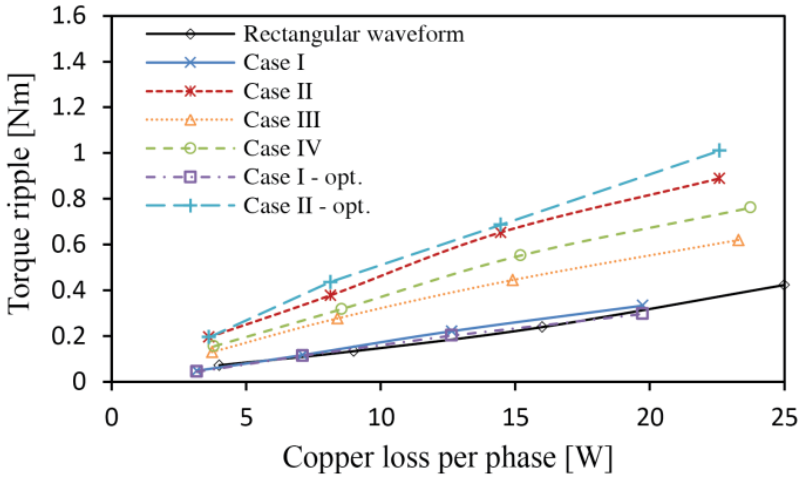

(c) Torque ripple against copper loss

Fig. 3.8. Experimental results under different current excitations.

3.6 Conclusion

This chapter investigates the contribution of current harmonics to the average torque and torque ripple in the SRMs based on the developed the instantaneous torque equation and designate five different current waveforms. The further current waveform optimisation is also discussed. The investigations are validated by FEA and measured results. The average torque is majorly contributed by the dc, fundamental, and second harmonic currents. The fourth and fifth current harmonics mainly affect the torque ripple but not the average torque. The current harmonics in the rectangular waveform are already very close to the optima. As mentioned in the introduction, the SRM can be transferred into a VFRM having both field and armature windings on the stator [LIU13b]. The investigation based on the different current waveform excitations can be also applied to the 6/4 VFRM.

CHAPTER 4

TORQUE RIPPLE REDUCTION FOR 6/4 VARIABLE FLUX RELUCTANCE MACHINE BY USING HARMONIC FIELD CURRENT INJECTION

4.1 Introduction

In machine drives, torque ripple is a critical concern, especially for high performance applications, such as traction drives and servo applications, which require low acoustic noise and low speed variation. The torque pulsations have periodical characteristics with rotor position. The presence of the torque ripple deteriorates the control performance of the machine speed degrading the machine performance. Compared with the 6/5 or 6/7 VFRM, the 6/4 VFRM has a significant torque ripple due to its self-inductance variation of the armature windings. In order to overcome this problem, many torque ripple reduction methods have been investigated.

The harmonic components of the *q*-axis current is utilised to counteract the fundamental and specific torque ripple including both torque ripple and cogging torque for the PM machines [LEE08], for the SFPM machines [JIA10], for flux-controllable PM machines [ZHU09]. For the implementation of the additional harmonic components, it has been proposed based on an iterative learning control [QIA04] and a repetitive current control in the

PM machine drives [MAT05]. Additionally, duty cycles of each inverter leg has been used for a smooth torque control, which considers the non-ideal back emf waveforms and the finite dc bus supply voltages [LU08].

Current waveform shaping techniques for the individual phase current have been proposed based on injecting specific harmonic components for the desired torque ripple cancellation [LEH86], [JAH96]. The optimally shaped reference phase current waveforms are applied to the PM machines considering three-phase unbalanced conditions [PAR00]. With the combinations of harmonic components in the phase currents, a numerical solution has been proposed in order to reduce the acoustic noise and torque ripple [BAY15]. By using voltage vectors with variable amplitude and angle, a modified DTC has been also proposed for the PM machines [ZHA11], [ZHU12]. It was extended to the DSPM machines with a model based predictive torque control [YAN12].

As discussed in the previous chapter, the 6/4 VFRM has the torque ripple with specific harmonic components, which are multiples of the third harmonics. Therefore, in this chapter the torque ripple reduction method is proposed for the 6/4 VFRM by injecting the harmonic field current. It is shown that the third harmonic torque ripple is dominantly produced by the fundamental component of the self-inductance in the armature windings. The inductance harmonics also produce the additional torque ripples having the harmonic components at multiples of three. The reference field current harmonics are calculated by the analytical prediction of the instantaneous torque waveform, which considers all the harmonics in the self- and mutual inductances. The comparison results are analysed between analytical

prediction and FEA calculation. The experimental results on a prototype 6/4 VFRM are provided for the validity and the practical availability of the proposed method [LEE16a].

4.2 Instantaneous Torque Equation of 6/4 VFRM

Fig. 4.1 shows the cross section and the field and armature windings of the 6/4 VFRM. The stator consists of 6-stator poles with the concentrated windings. Each armature winding is composed of two coils in series with the same polarity, e.g. coils A1 and A2 for phase A. Additionally, all of the field windings are connected in series with the same polarity.

The instantaneous torque of the VFRMs can be analysed based on the transient performance which reveals the principle of torque generation and its relationship of the machine parameters. Since the saturation influences on electromagnetic performances are related to the machine geometry, the magnetic property and excitation currents, it is complicated to obtain the analytical expression including nonlinear characteristics between the inductances and currents. Hence, the analysis of torque production is utilised with some assumptions in this chapter. Firstly, it is assumed that the iron of the stator and rotor has infinite permeability and the magnetic saturation does not occur. Hence, the inductance is not affected by the phase current. Secondly, the three-phase windings are in a balanced condition. The *abc*-axis inductances and currents have the same amplitude, but 120° elec. phase shift. Lastly, the mutual inductance between the armature windings is neglected since the flux-linkage of the armature coil passes through the other armature coil of the same phase in the 6/4 VFRM [LIU13b].

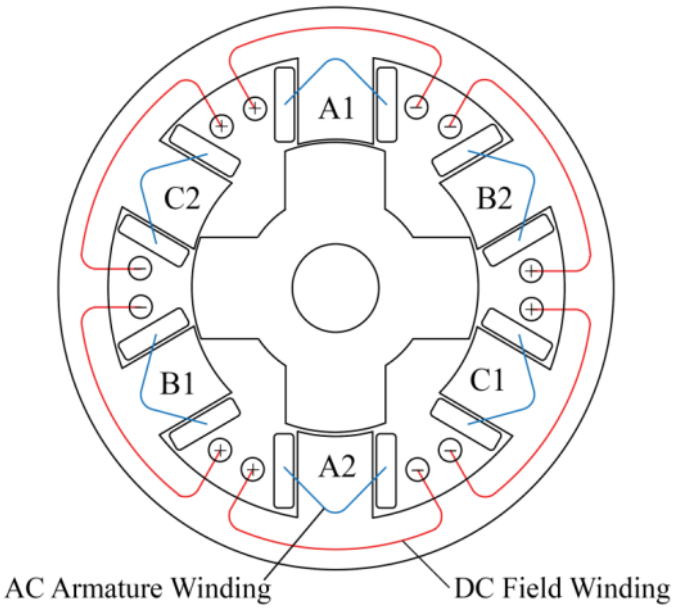

Fig. 4.1. Cross section and winding configurations of 6/4 VFRM (The rotor pole is aligned with phase A, i.e. $\theta_e = 0$) [LIU13b].

Due to the periodic nature of the waveforms, the self-inductance of the armature winding L_a and the mutual inductance between the field and armature windings M_a can be expressed by Fourier series as a function of rotor position:

$$L_a(\theta_e) = L_0 + \sum_{n=1}^{\infty} L_n \cos(n\theta_e + \alpha_n) \tag{4.1}$$

$$M_a(\theta_e) = M_0 + \sum_{n=1}^{\infty} M_n \cos(n\theta_e + \gamma_n) \tag{4.2}$$

where n is the harmonic order, L_0 and M_0 are the dc components of the self- and mutual inductances, L_n and M_n are the amplitudes at the nth harmonic, and α_n is the phase shifts of self-inductance and γ_n is the phase shifts of the mutual inductance at the nth harmonic, respectively. θ_e is the electrical rotor angle of the VFRM. In this chapter, leakage flux is neglected since the field and armature windings are identically wound on the stator tooth. Hence, the self- and mutual inductances are assumed to be the same, i.e. $L_n = M_n$ and $\alpha_n = \gamma_n$ for all n.

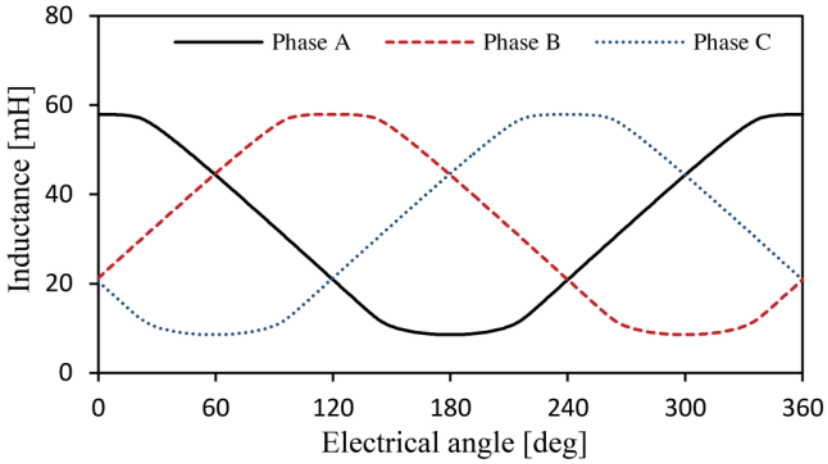

(a) *abc*-axis self-inductance waveforms

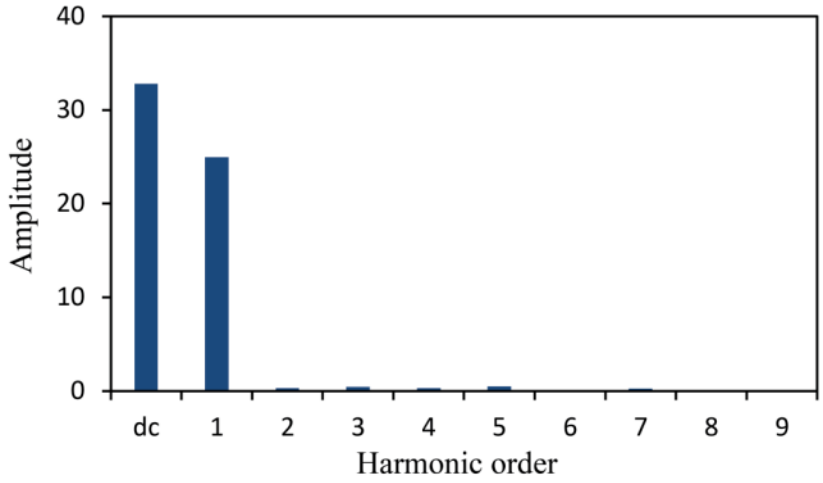

(b) Corresponding harmonics

Fig. 4.2. Self-inductance waveforms of the armature windings and harmonics in 6/4 VFRM [LIU13b].

Fig. 4.2 shows the self-inductance waveforms of the armature windings and the corresponding harmonics. The self-inductance of the armature windings exhibits symmetrical waveforms biased by dc offset component. From the corresponding harmonic analysis, it can be seen that the dc and fundamental components are dominant, whilst the third, fifth and seventh harmonic components are slightly larger than the second and fourth harmonics. It should be noted that the phase shifts of the fifth and seventh harmonics are in anti-phase, whilst other harmonics are in phase compared with the fundamental component.

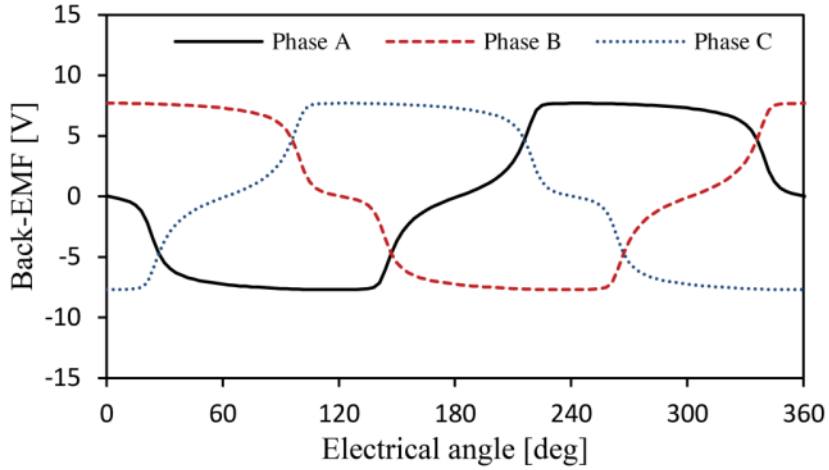

(a) *abc*- axis back-emf waveforms

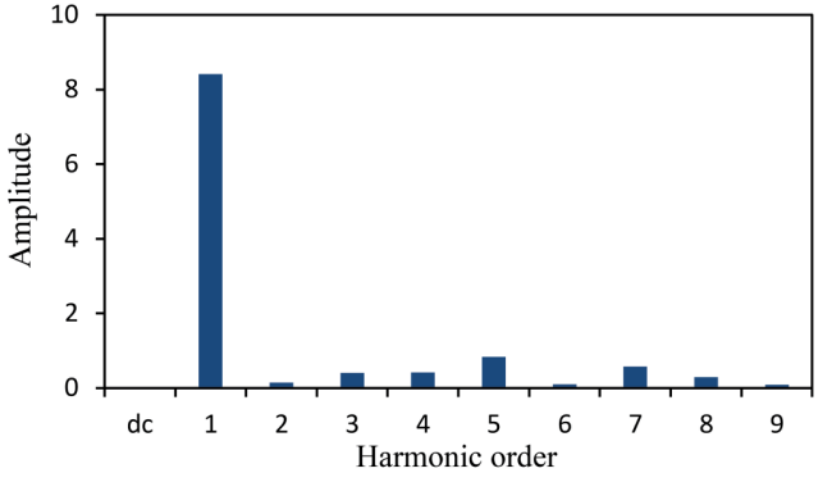

(b) Corresponding harmonics

Fig. 4.3. Back emf calculated by FEA when 2 A field current is applied at 400 rpm [LIU13b].

Since the flux-linkage of Phase A is formed by the field current i_f and the mutual inductance between the field and armature windings M_a, the back emf of Phase A e_a is written as

$$e_a(t) = \frac{d}{dt}\left\{M_a(\theta_e) i_f(\theta_e)\right\} = \omega_e \frac{d}{d\theta_e}\left\{M_a(\theta_e) i_f(\theta_e)\right\} \tag{4.3}$$

where ω_e is the electrical rotor speed of the VFRMs. The three-phase back emf waveforms calculated by FEA are shown in Fig. 4.3 when 1 A field current is applied at 400 rpm. It can be seen that although the back emfs are non-sinusoidal, they have identical and symmetrical waveforms. Each harmonic component is amplified by its harmonic order due to the derivative

of the mutual inductance.

In the conventional VFRM drives, the armature current of the Phase A can be represented as

$$i_{as}(\theta_e) = -I_1 \sin(\theta_e + \beta_1) \tag{4.4}$$

where I_1 is the amplitude of the fundamental component of the armature current, and β_1 is the advanced current angle of the fundamental component, respectively. The field current is controlled at a constant value I_f.

Based on the torque production, the instantaneous torque of the 6/4 VFRM can be written by the field and armature currents and the self- and mutual inductances as

$$\begin{aligned} T_e = {} & \frac{P}{2}\left(i_{as}^2 \frac{dL_a}{d\theta_e} + i_{bs}^2 \frac{dL_b}{d\theta_e} + i_{cs}^2 \frac{dL_c}{d\theta_e} \right) + \frac{P}{2}\left(i_f^2 \frac{dL_a}{d\theta_e} + i_f^2 \frac{dL_b}{d\theta_e} + i_f^2 \frac{dL_c}{d\theta_e} \right) \\ & + P\left(i_{as} i_f \frac{dM_a}{d\theta_e} + i_{bs} i_f \frac{dM_b}{d\theta_e} + i_{cs} i_f \frac{dM_c}{d\theta_e} \right) \end{aligned} \tag{4.5}$$

where P is the number of poles in the VFRMs. The rotor pole number of the VFRMs is corresponding to the pole pair numbers of the conventional PM machine. i_{as}, i_{bs} and i_{cs} are the *abc*-axis phase currents and i_f is the field current. L_a, L_b and L_c are the *abc*-axis self-inductances of the armature windings. M_a, M_b and M_c are the *abc*-axis mutual inductances between the field and armature windings.

Under the constant field and sinusoidal current excitation, the instantaneous torque equation is rewritten as

$$
\begin{aligned}
T_{e1} &= -\frac{3P}{2}\sum_{n=1}^{\infty} nL_n I_f^2 \sin\left(n\theta_e + \alpha_n\right) \\
&+ \frac{3P}{2}\sum_{n=1}^{\infty} \mp nM_n I_f I_1 \cos\left((1 \pm n)\theta_e + \beta_1 \pm \gamma_n\right) \\
&+ \frac{3P}{2}\sum_{n=1}^{\infty}\left\{-\frac{n}{2}L_n I_1^2 \sin\left(n\theta_e + \alpha_n\right) \pm \frac{n}{4}L_n I_1^2 \sin\left((2 \pm n)\theta_e + 2\beta_1 \pm \alpha_n\right)\right\}.
\end{aligned}
\tag{4.6}
$$

The first component is caused by the self-inductance of the field windings when n is a multiple of three. This torque ripple can be regarded as a cogging torque. The second component is resulted from the mutual inductance harmonics when $(1 \pm n)$ is zero or a multiple of three. These torque components are produced by the back emf components. The last components are caused by the self-inductance of the armature windings when $\pm n$ is a multiple of three or $(2 \pm n)$ is zero or a multiple of three. Depending on the harmonic inductances, each component can produce the average torque or torque ripple. In terms of torque ripple multiples of the third harmonic components exist only since the other harmonic components are cancelled by the three-phase windings.

For verification, the torque waveforms predicted by the derived equation are compared with the results calculated by FEA at I_1 = 2 A and I_f = 1 A and 2 A. The inductance information is obtained from FEA calculation as listed in Table 4.1. It should be noted that the magnetic saturation is considered in FEA calculation. Hence, the inductance parameters are obtained under a small current excitation at 0.1 A. Fig. 4.4 shows the instantaneous torque waveforms and the corresponding harmonics. The calculated and predicted results are well matched at both operating conditions. From the harmonic analysis, the torque ripple dominantly contains the third harmonic component.

From the instantaneous torque equation, the average torque can be rearranged as

$$T_{avg} = \frac{3P}{2}\left\{ M_1 I_f I_1 \cos\left(\beta_1 - \gamma_1\right) - \frac{1}{2} L_2 I_1^2 \sin\left(2\beta_1 - \alpha_2\right)\right\}. \tag{4.7}$$

When the machine is driven by the sinusoidal phase currents and constant field current, the average torque is mainly produced by the fundamental component of the mutual inductance between field and armature windings. The principle of the average torque generation with the mutual inductance is similar to that of the PM machines, whose torque is generated by the interaction between flux-linkage and armature current. In the VFRMs, the interaction between field current and mutual inductance generates flux-linkage, and the resultant flux-linkage contributes to the torque production with the armature currents. Additionally, the square of the fundamental current produces relatively small average torque generated from the second harmonic inductance. In order to maximise the average torque, the current angle β_1 can be advanced rather than zero so that the second harmonic component of the self-inductance contributes to the average torque production. However, since L_2 value is relatively small and can be neglected, the current advanced angle β_1 is selected to zero, which utilises the *q*-axis current control with zero *d*-axis current in the synchronous *dq*-axis frame.

In contrast, the winding inductance harmonics produce multiples of the third harmonic torque ripples. Based on (4.6), torque ripple components are rewritten as

$$\begin{aligned} T_{r\_(3k)th} = \frac{3P}{2}\Bigg\{ & -3kL_{3k} I_f^2 \sin\left(3k\theta_e + \alpha_{3k}\right) - \frac{3k}{2} L_{3k} I_1^2 \sin\left(3k\theta_e + \alpha_{3k}\right) \\ & -(3k-1) M_{(3k-1)} I_f I_1 \cos\left(3k\theta_e + \beta_1 + \gamma_{(3k-1)}\right) + (3k+1) M_{(3k+1)} I_f I_1 \cos\left(3k\theta_e - \beta_1 + \gamma_{(3k+1)}\right) \\ & + \frac{(3k-2)}{4} L_{(3k-2)} I_1^2 \sin\left(3k\theta_e + 2\beta_1 + \alpha_{(3k-2)}\right) + \frac{(3k+2)}{4} L_{(3k+2)} I_1^2 \sin\left(3k\theta_e - 2\beta_1 + \alpha_{(3k+2)}\right)\Bigg\} \end{aligned} \tag{4.8}$$

where *k* is the integer starting from 1. The fundamental component of the self-inductance is a main source of the third harmonic torque ripple interacting with the fundamental phase

currents due to the relatively large inductance compared with the other harmonics. Additionally, the derived torque ripple equation shows that the third harmonic torque ripple is caused by the inductance harmonics from the fundamental to the fifth harmonic components. In case of higher harmonic torque ripple, the inductance harmonics from the fourth to eighth orders contribute to the sixth harmonic torque ripple and ninth harmonic torque ripple from the seventh to eleventh orders.

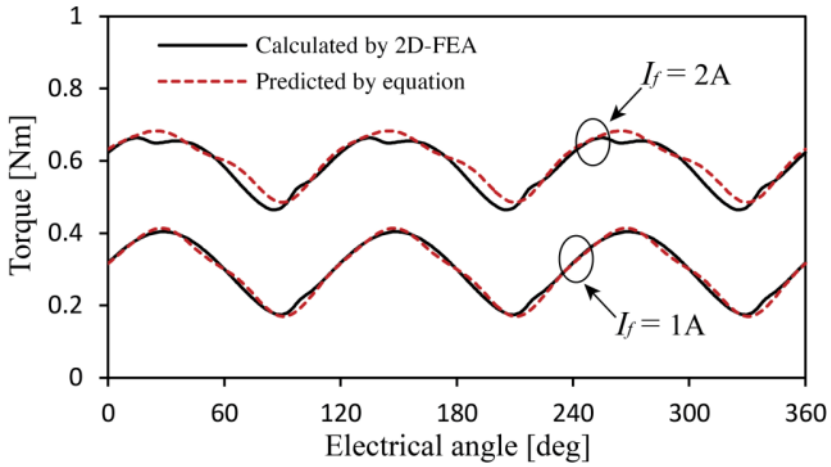

(a) Torque waveforms

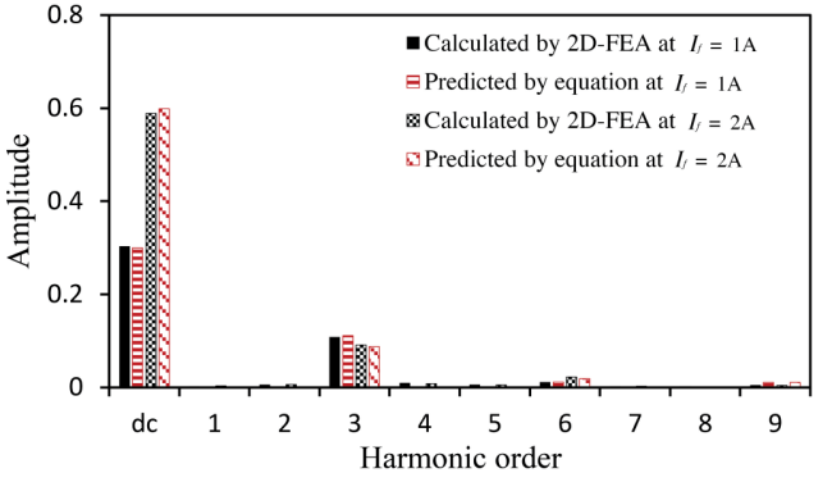

(b) Spectra

Fig. 4.4. Comparison of torque waveforms in 6/4 VFRM at I_1 = 2 A and I_f = 1 A and 2 A.

4.3 Harmonic Field Current Injection

4.3.1 Harmonic Current Calculation from FEA

Due to the degree of freedom, the harmonic current can be injected into field or armature current, or both currents to suppress the torque ripple. However, if the armature current, mainly *q*-axis current, is modified to inject the harmonic component, it will also cause additional harmonic torque ripple significantly since the third harmonic torque ripple is mostly proportional to the square of the armature current magnitude. Hence, by injecting the harmonic current into the field windings, the mutual inductance torque is utilised to counteract the torque ripple.

The harmonic field current can be directly obtained from the torque waveform calculated by FEA and added to the reference field current as

$$i_{fm}^{*} = I_{f}^{*} + \Delta i_{f}^{*}(\theta_e), \quad \Delta i_{f}^{*}(\theta_e) = -\frac{2}{3P}\frac{1}{M_1 I_1}\left(T_{e\_FEA}(\theta_e) - T_{avg\_FEA}\right) \tag{4.9}$$

where I_{f}^{*} is the reference value for a constant field current, and Δi_{f}^{*} is the additional term for the torque ripple reduction, respectively. $T_{e\_FEA}(\theta_e)$ is the instantaneous torque with respect to the electrical rotor angle, and T_{avg_FEA} is the average torque obtained from FEA. Fig. 4.5(a) shows the harmonic field current waveforms calculated by FEA. When the instantaneous torque is larger than the average torque, the negative harmonic field current is added to reduce the torque ripple, whilst the positive harmonic field current is provided when the torque is smaller than the average torque. Fig. 4.5(b) shows the torque waveforms with/without the harmonic current injection. When the harmonic field current injection is applied, the torque ripples are significantly reduced under both current conditions.

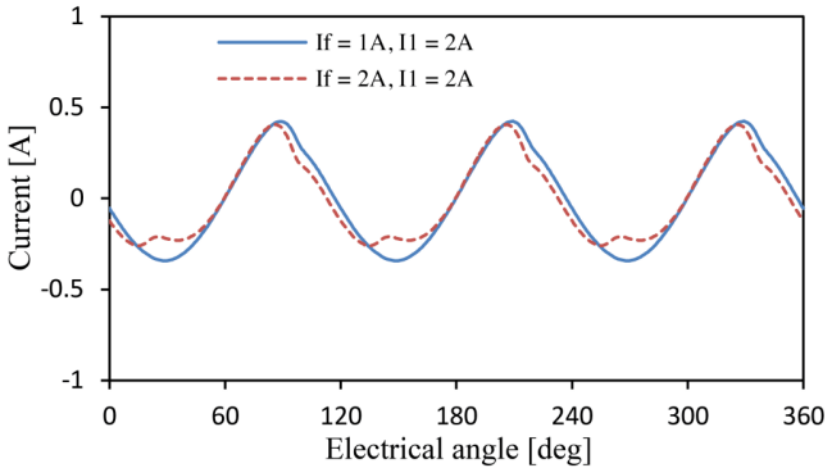

(a) Harmonic field current calculated by FEA

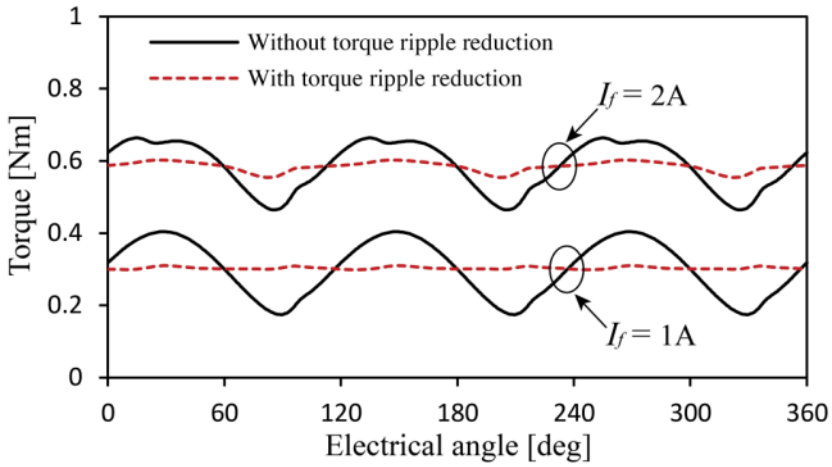

(b) Torque waveforms

Fig. 4.5. Comparison with/without torque ripple reduction at I_1 = 2 A and I_f = 1 A and 2 A.

However, since these harmonic field currents are entirely relied on the FEA calculation, it requires many prerequisite calculations against different current magnitude and angle conditions. Hence, the harmonic field current based on the derived torque equation is proposed, which is easily applicable to different current conditions.

4.3.2 Harmonic Current Calculation from Torque Equation

Due to the dominant magnitude, the fundamental component of the self-inductance can be only utilised for the harmonic current calculation, namely Method I. The reference field

current added with the third harmonic component can be simply expressed from (4.9)

$$\Delta i_f^* = -\frac{1}{4} I_1 \cos(\beta_1) \sin\left(3\theta_e + 2\beta_1\right). \tag{4.10}$$

Since L_1 is cancelled out by M_1, Method I does not require any inductance information.

In order to take the self-inductance harmonics into account, Method II is proposed. By using the torque ripple equation (4.8), the modified reference field current can be expressed as

$$\Delta i_f^*(\theta_e) = -\frac{2}{3P} \frac{1}{M_1 I_1} T_{r\_(3k)th}(\theta_e). \tag{4.11}$$

These harmonic field current amplitudes can be updated based on the operation conditions. With the aid of the FEA calculation, the harmonic inductance information is obtained. Additionally, the proposed method can be utilised in both the rated torque and the flux weakening operation since the advanced current angle β_1 is considered. In this chapter, the third, sixth, and ninth harmonic field currents are injected for the torque ripple reduction since higher harmonic components contribute less to the torque ripple, and the generation of the high order harmonic currents may be limited due to the control system.

Fig. 4.6 shows the comparison of the calculated torque waveforms by FEA and the corresponding harmonics with/without employing Method II. Similar with the previous results of the harmonic field current calculated by FEA, the average torque is maintained at the same level, whilst the torque ripple is significantly reduced.

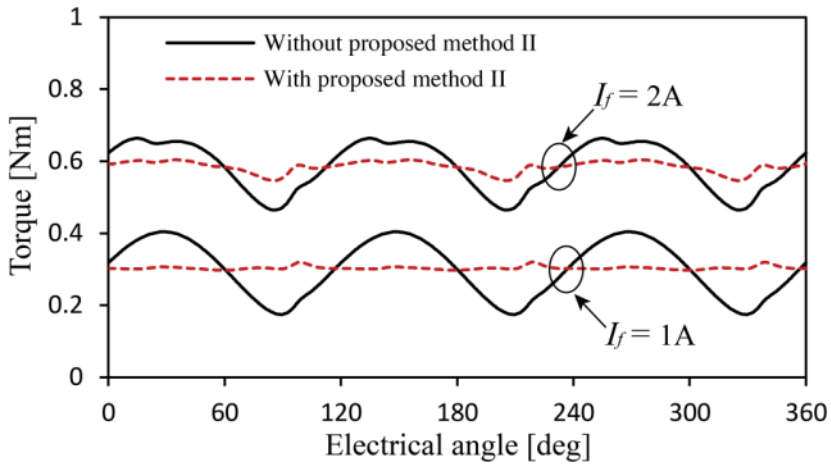

(a) Torque waveforms

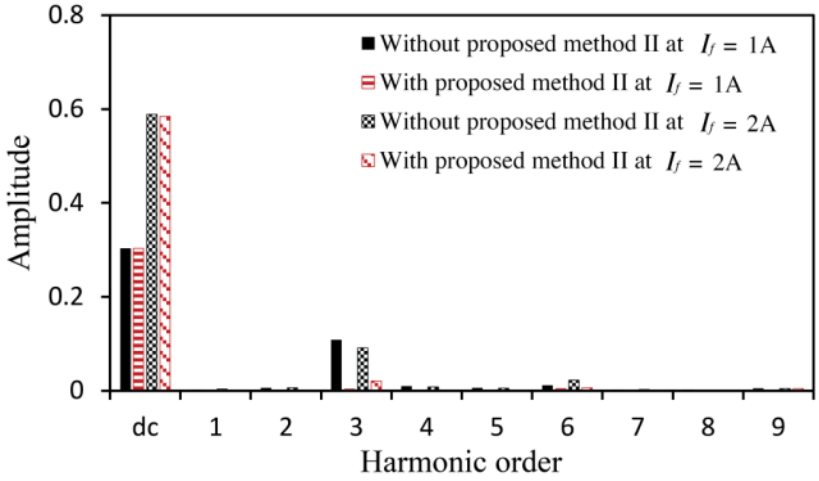

(b) Spectra

Fig. 4.6. Comparison of torque waveforms calculated by FEA with/without proposed Method II in 6/4 VFRM at I_1 = 2 A and I_f = 1 A and 2 A.

4.4 Influence of Harmonic Field Current Injection

Although the injected harmonic current helps the torque ripple reduction, it also contributes to the additional torque generation. Since the third harmonic field current is dominant in the proposed methods compared with the sixth and ninth harmonic field currents, the additional torque equation is derived considering only the third harmonic field current as an example. When β_1 is zero, the field current with the third harmonic component can be expressed as

$$i_f(\theta_e) = I_f - I_{3S}\sin(3\theta_e) - I_{3C}\cos(3\theta_e) \tag{4.12}$$

where I_{3S} and I_{3C} are the amplitudes of the injected third harmonic currents for sine and cosine waveforms in (4.11), respectively. The third harmonic field current can be represented in terms of sine waveform as

$$i_f(\theta_e) = I_f - I_3\sin(3\theta_e + \beta_3),\ \ I_3 = \sqrt{I_{3S} + I_{3C}},\ \ \beta_3 = \tan^{-1}\left(\frac{I_{3C}}{I_{3S}}\right). \tag{4.13}$$

Then, by using (4.5), the additional torque components T_{e3} caused by the third harmonic field current injection can be presented as

$$\begin{aligned} T_{e3} &= P\sum_{n=1}^{\infty} \mp\frac{3n}{2} M_n I_f I_3 \cos\left((3\pm n)\theta_e + \beta_3 \pm \gamma_n\right) \\ &+ P\sum_{n=1}^{\infty}\left\{\begin{array}{l} \mp\frac{3n}{4} L_n I_1 I_3 \sin\left((-2\pm n)\theta_e + \beta_1 - \beta_3 \pm \alpha_n\right) \\ \pm\frac{3n}{4} L_n I_1 I_3 \sin\left((4\pm n)\theta_e + \beta_1 + \beta_3 \pm \alpha_n\right) \end{array}\right\} \\ &+ P\sum_{n=1}^{\infty}\left\{\begin{array}{l} \mp\frac{3n}{8} L_n I_3^2 \sin\left((\pm n)\theta_e \pm \alpha_n\right) \\ \pm\frac{3n}{8} L_n I_3^2 \sin\left((6\pm n)\theta_e + 2\beta_3 \pm \alpha_n\right) \end{array}\right\}. \end{aligned} \tag{4.14}$$

where each component only exists when the frequency term is a multiple of the third harmonic.

The fundamental self-inductance component is mainly utilised for the torque ripple reduction and it can be written as

$$T_{r\_3rd} = -\frac{3P}{2} L_1 I_1 I_3 \sin\left(3\theta_e + \beta_3\right). \tag{4.15}$$

The other terms in (4.14) are the torque components additionally produced by the injected third harmonic field current as shown in Fig. 4.7. The torque ripple component produced by the fundamental component of the self-inductance is excluded. Although the third harmonic current injection generates the additional third multiple harmonic torque ripple, the influence

of the third harmonic current injection is not significant on the torque ripple. Additionally, the average torque can be also slightly increased due to the third harmonic current injection, but the contribution to the average torque is negligible.

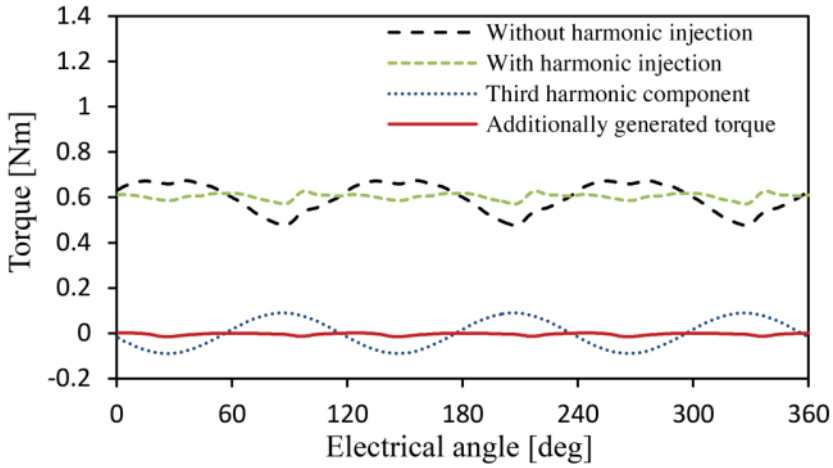

Fig. 4.7. Predicted torque waveforms additionally produced by the third harmonic field current injection at 2 A for both I_1 and I_f .

4.5 Experimental Results

For the experimental validation, the proposed methods are applied to the prototype 6/4 VFRM in dSPACE platform. Fig. 4.8(a) shows the VFRM control block diagram with external field current control configuration. The armature currents are controlled by the conventional three-phase inverter, and the field current is controlled by an external field current converter. For the three-phase armature current controls, the PI controllers are used in the synchronous *dq*-axis frame. At the parameter design process of the PI controllers, the proportional gain K_P is set to $2\pi f_c L_1$ and the integral gain K_I is set to $2\pi f_c R_s$, in which f_c is the current control loop bandwidth. The switching frequency is set to 10 kHz for both the inverter and the converter. The PI controller bandwidth f_c is selected to 500 Hz. The initial conditions in all of the

controller blocks are set to zero. In order to drive the VFRMs, the PWM switching based inverter system is implemented. But the inverter system does not contribute to the torque ripple much due to mainly high switching frequency and large winding inductance.

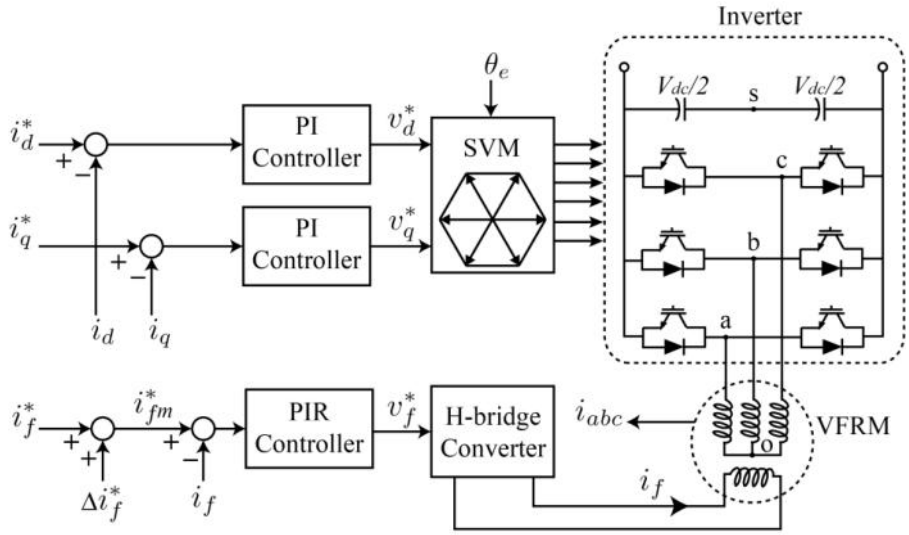

(a) External field current control system

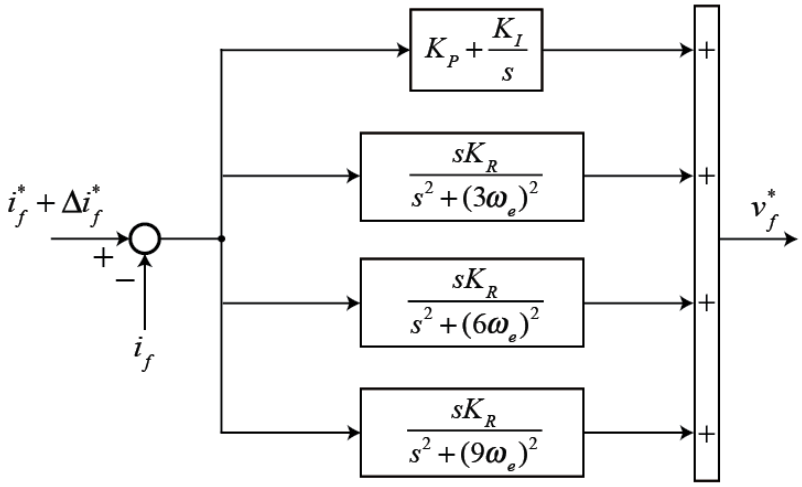

(b) Conceptual PIR controller for the harmonic field current control

Fig. 4.8. Overall block diagram for VFRM drives.

In case of the field current control, the modified field current contains the constant component and additional multiples of the third harmonic, which cannot be effectively controlled by the PI controller. Hence, in order to track the reference field current having

alternating components, the PIR controller is applied as shown in Fig. 4.8(b) [XIA15]. Each resonant controller operates in parallel configuration so that the dc, third, sixth, and ninth harmonic components are regulated, respectively. In every resonant controller, the resonant coefficients K_R are all set to 50, which affect the dynamic performance. The resonant frequencies of the PIR controller are adjusted as the machine speed changes.

Fig. 4.9 shows the experimental rig, in which the prototype 6/4 VFRM is connected to the dc load machine through the torque transducer. The instantaneous torque is measured by the torque transducer, and the machine speed is set to 15 rpm due to the limited bandwidth of the torque transducer. The prototype machine parameters are listed in Table 4.1.

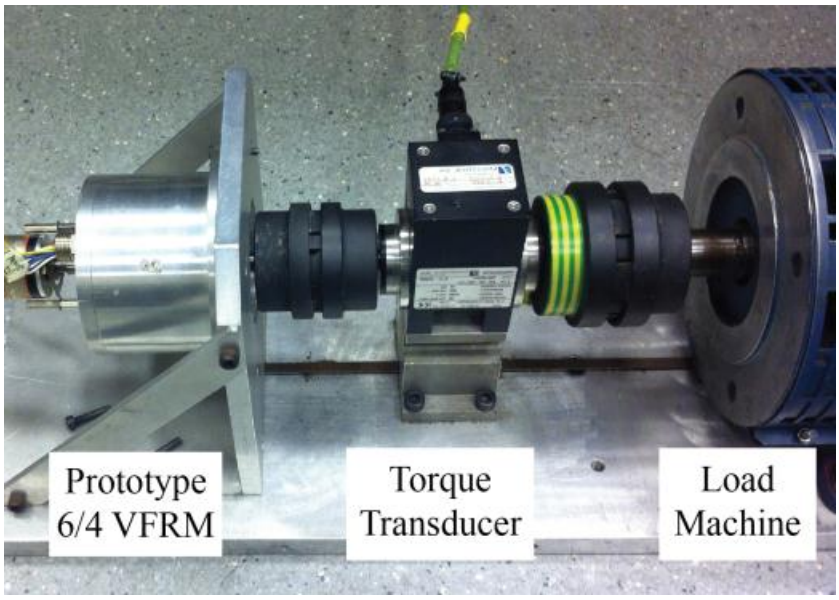

Fig. 4.9. Experimental setup with prototype machine and torque transducer.

TABLE 4.1

MACHINE PARAMETERS

Machine parameters	Value
Number of phases	3
Number of stator poles	6
Number of rotor poles (P)	4
Number of turns per phase for armature winding	366
Number of turns for field winding	6 × 366
Air gap	0.5 mm
Winding resistance (R_s)	6 Ω
dc component of self-inductance (L_0)	30 mH
Fundamental component of self-inductance (L_1)	24 mH
dc component of mutual inductance (M_0)	30 mH
Fundamental component of mutual inductance (M_1)	24 mH

Inductance magnitude (mH)		Inductance phase (rad)	
L_0	33	α_0	-
L_1	25	α_1	0
L_2	0.29	α_2	0
L_3	0.45	α_3	0
L_4	0.31	α_4	0
L_5	0.49	α_5	π
L_6	0.00	α_6	0
L_7	0.25	α_7	π

4.5.1 Comparison of Torque Waveforms

Fig. 4.10 compares the measured torque and current waveforms with/without the torque ripple reduction at I_f = 1 A, I_1 = 2 A. The torque ripple is significantly reduced by using the harmonic current injection, whilst the average torque is maintained. Fig. 4.10(b) shows the torque waveform when the harmonic field currents calculated by FEA torque waveforms are injected, whilst the result with proposed Method II is shown in Fig. 4.10(c). It can be seen that both methods can reduce the torque ripple effectively. The Method II has similar torque ripple reduction performance compared with the harmonic field current directly calculated by FEA

torque waveform.

When the machine is operated at I_f = 2 A, I_1 = 2 A, the comparison results are shown in Fig. 4.11. Although the torque ripple reduction performance is degraded due to the magnetic saturation of the machine, the proposed methods can suppress the torque ripple component under different current conditions. In the proposed methods, the field current contains the harmonic components, whilst the *q*-axis current is maintained at a constant value. Additionally, the machine speed cannot be maintained at a constant speed without the proposed methods due to the torque ripple, and the oscillation of the rotor angle can be seen in the electrical angle waveforms.

Fig. 4.12 shows the measured torque ripple and average torque under different load conditions. The fundamental component of the armature current is set to $1.414I_f$ for the minimum copper loss operation [CHE10]. If the magnetic saturation is neglected, the average torque is directly proportional to the square of the field current as shown in the predicted result by the derived torque equation. It is because that the average torque is proportional to both the field and the armature currents. However, as the current magnitude increases the difference between the measured and predicted average torques becomes larger due to magnetic saturation. By comparing the torque ripples with/without the Method II, although the torque ripple becomes larger as the field current increases, the proposed method can reduce the torque ripple in saturation region.

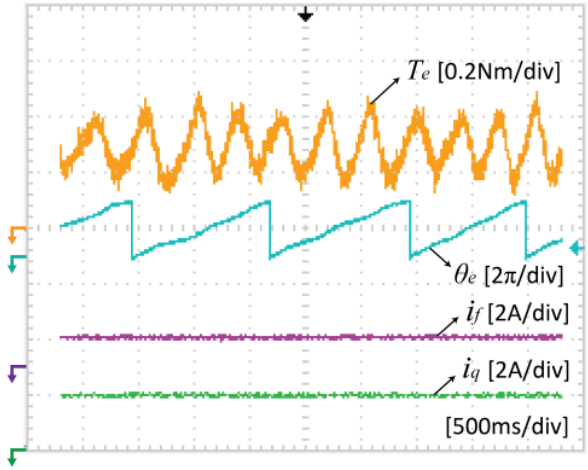

(a) Without torque ripple reduction

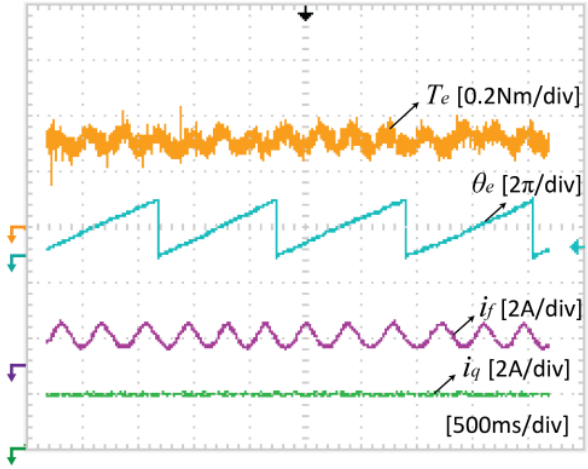

(b) With harmonic current injection calculated by FEA

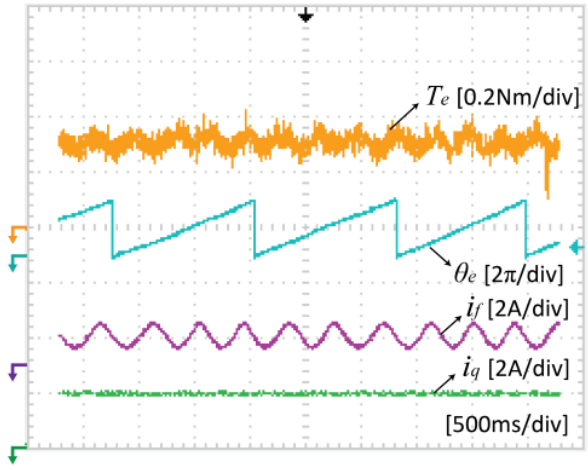

(c) With proposed Method II

Fig. 4.10. Comparison of the measured torque waveforms at I_f = 1 A, I_1 = 2 A.

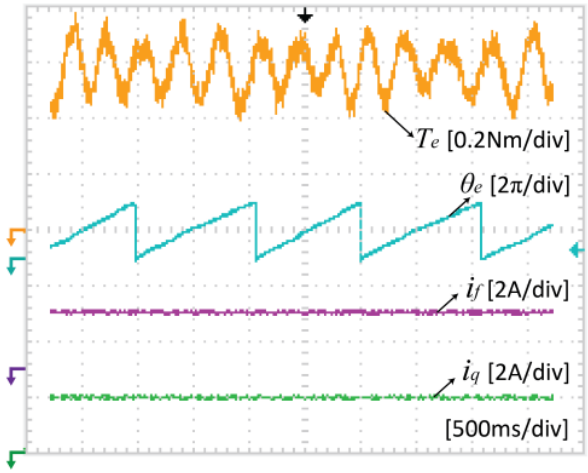

(a) Without torque ripple reduction

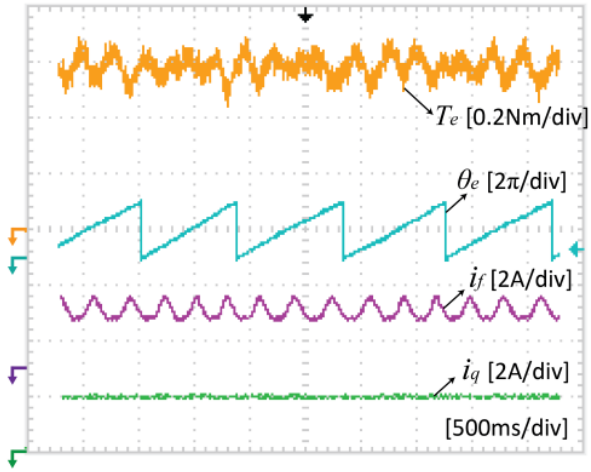

(b) With harmonic current injection calculated by FEA

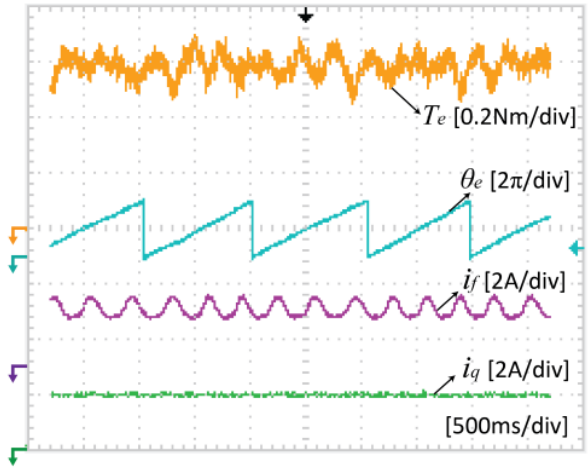

(c) With proposed Method II

Fig. 4.11. Comparison of the measured torque waveforms at I_f = 2 A, I_1 = 2 A.

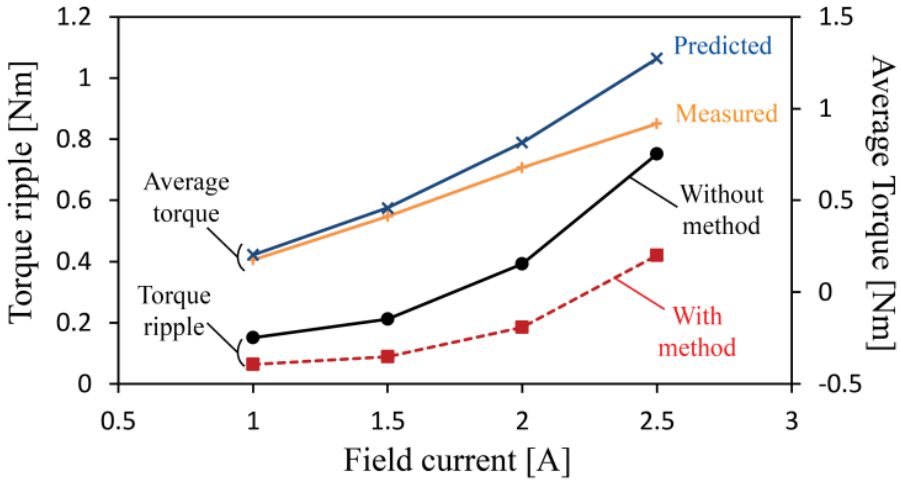

Fig. 4.12. Measured torque ripples with/without the proposed Method II and average torque under different load conditions ($\beta = 0$).

4.5.2 Influence of Parameter Mismatch

Since the proposed Method II utilises the machine inductance parameters, the influence of the parameter variation is analysed on the torque ripple reduction performance. From (4.11), the third harmonic magnitude is calculated from each harmonic component divided by the fundamental inductance component. The parameter variation of the fundamental component will be reflected in the harmonic component variation. Hence, the nominal value of the fundamental component inductance changes from 20 % to 200 %. The torque ripple is defined as the difference between the maximum and minimum values of the calculated torque waveform.

The torque ripple comparisons are conducted by FEA calculations and experiments by injecting the harmonic current considering the parameter variation. Fig. 4.13(a) shows the torque ripple comparison under the parameter variation at I_f = 1 A and I_1 = 1.414. It should be noted that the fundamental component of the armature current is set to $1.414I_f$ for the

minimum copper loss operation. When the nominal inductance is larger than the actual inductance at 100 %, it does not significantly affect the torque ripple reduction performance. As the nominal value becomes larger than the actual inductance, the magnitude of the third harmonic field current converges to the $1/4I_1$, which is the same as the Method I. When the underestimated nominal inductance is utilised, torque ripple reduction performance is degraded and it can be even higher than that without the proposed method.

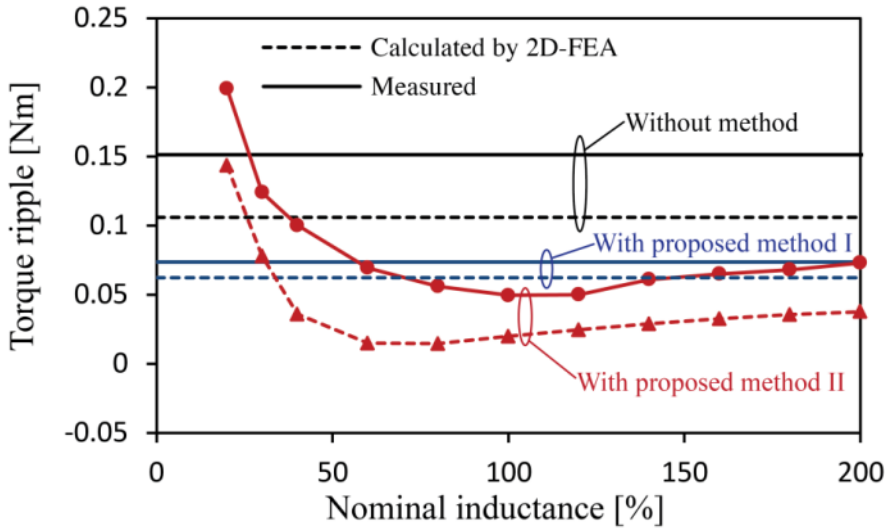

(a) At I_f = 1 A, I_1 = 1.414 A

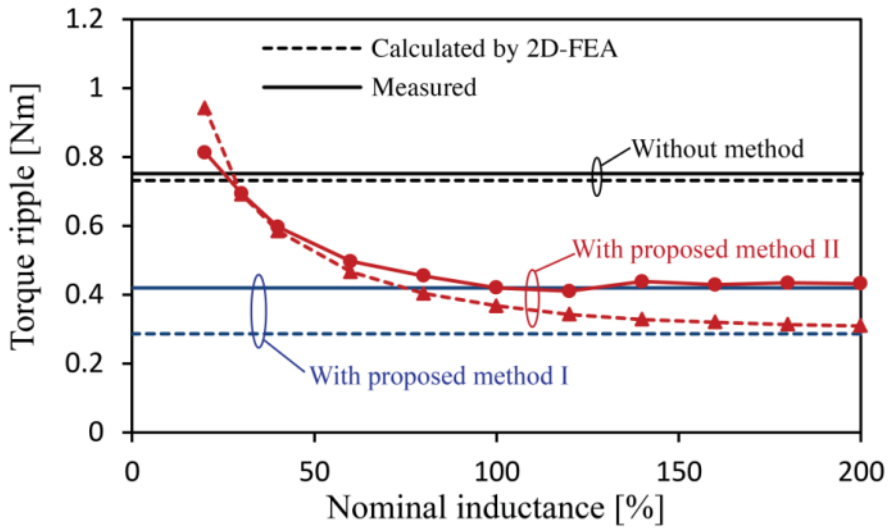

(b) At I_f = 2.5 A, I_1 = 3.535 A

Fig. 4.13. Comparison of torque ripple under the parameter mismatch of nominal inductance.

When the machine operates in the saturation region at I_f = 2.5 A, the calculated third harmonic field current may be insufficient to reduce the third harmonic current due to the reduced inductance under the saturation condition. Hence, more third harmonic current is required to reduce the torque ripple. From Fig. 4.13(b), the torque ripple is slightly reduced as the nominal value increases, which uses more third harmonic field current. The similar results are obtained in the measured torque ripples under both current conditions except for the different values.

4.6 Conclusion

In this chapter, a torque ripple reduction method is proposed based on the harmonic current injection for the 6/4 VFRM. Since the machine has multiples of the third harmonic torque ripple, the harmonic currents are injected into the field current for the torque ripple reduction. The magnitudes of the harmonic field currents are calculated by the derived torque equation considering all of the harmonics in the inductances. In order to control the reference field current containing the harmonic components, a PIR controller is implemented. Despite the utilisation of the machine parameters, the torque ripple reduction performance is not affected much unless the fundamental component of the nominal inductance is underestimated. Although the reference field current can be obtained by FEA calculation, the proposed method can reduce the computation time, whilst the torque ripple reduction performance is maintained at a similar level. The torque waveforms are measured by a torque transducer, and the results with/without applying the proposed methods are compared. The effectiveness of the proposed

torque ripple reduction method is validated by the experimental results in both linear and saturation regions.

CHAPTER 5

INTEGRATED FIELD AND ARMATURE CURRENT CONTROL STRATEGY FOR 6/4 VARIABLE FLUX RELUCTANCE MACHINE USING OPEN WINDING

5.1 Introduction

In the conventional VFRM drives, the external field excitation current control has been utilised with the separated converter [LIU12a], [FUK12]. In this excitation scheme, the three-phase inverter is employed for the armature current control, which has been commonly used in other machine drives. The field excitation current is controlled by a separated current source or an additional inverter bridge. In the meantime, the field and armature currents can be employed together as a sinusoidal current biased by dc offset [LIU12b] [NAK14]. In the VFRMs, both field and armature windings are wound on the same stator tooth with concentrated winding configuration. As a result, the terminals of both windings can be connected in parallel to the integrated phase windings. Thus, the sinusoidal current biased by dc offset can be applied into the integrated phase winding. From the synchronous machine point of view, the dc bias of the phase current generates the virtual rotor flux, whilst the three-phase sinusoidal phase current produces the rotating stator field.

The control method of the sinusoidal current with dc offset has been introduced based on a

zero sequence current control with an asymmetric H-bridge inverter [NAK14]. However, since the asymmetric H-bridge inverter cannot generate a negative current, an open winding inverter can be a good candidate for the dc component generation. In the open winding inverter, two three-phase inverters are connected to the terminals of the open winding machine, in which the dc component can be controlled by the zero sequence current control. Since the open winding inverter using two isolated dc link voltage sources cannot produce the zero sequence current, [STE93], [LEV12], [SRI12], a single voltage source will be considered in this chapter [BAI04]. As a drawback of the open winding inverter with a single voltage source, it also produces alternating zero sequence currents depending on inverter switching patterns [CHE06], [SOM13]. For the suppression of the alternating zero sequence current, a common mode voltage elimination has been proposed [BAI04]. The modified reference voltage vectors of two inverters has been proposed in the synchronous reference frame, in which two voltage vectors have 120° phase difference.

The three-phase armature currents can be controlled with SVM in the synchronous reference frame. Due to no saliency between the *dq*-axis inductances, zero *d*-axis current control can be applied to the 6/4 VFRM for the MTPA control in the rated torque region. For the flux weakening operation of the conventional three-phase machine, the anti-windup method of the current controller has been proposed in [KWO06]. As an extended study to the open winding configuration, the modified flux weakening scheme has been proposed in order to extend the operating speed range and to prevent the inverter saturation [SAN13]. Also, the magnitudes and phase angles of the voltage harmonic components have been utilised to

achieve a better utilisation of the dc link voltage [SAN14]. Additionally, different flux weakening methods have been compared and implemented.

In this chapter, the integrated field and armature current control strategy is proposed for VFRMs using open winding topology. By connecting the field and armature windings in parallel, only one set of three-phase winding is required. Thus, the resistance of the phase winding is halved, whilst the number of turns remains the same. It generates the same torque compared with the conventional field excitation current control. Hence, the proposed method can increase the machine efficiency due to smaller winding resistance. Moreover, the reduced resistance leads to less resistive voltage drop in the phase windings, which results in the extended machine operating range. In order to generate dc component in the zero sequence as a field current, the open winding inverter with a single voltage source is adapted. Zero vector modification technique is implemented, in which the switching on-time of the zero vectors is controlled for each inverter. For the flux weakening operation, anti-windup of the current controller is applied in the synchronous reference frame. In order to verify the proposed method, the dynamic simulation is performed with the aid of mathematical modeling in the VFRMs. The experimental results are presented to validate the effectiveness of the proposed control strategy in terms of copper loss reduction and extended operating range [ZHU16a].

5.2 Modeling of VFRM

Generally, the voltage equation of the three-phase VFRM can be written as

$$v_{abc} = R_s i_{abc} + \frac{d}{dt}\psi_{abc} \tag{5.1}$$

where R_s is the resistance of the stator windings, i_{abc} and ψ_{abc} are the phase currents and the flux-linkages of the armature windings, respectively. In order to consider the operating principle in the synchronous *dq*-axis frame, some assumptions have been made. Firstly, the magnetic saturation is neglected. Secondly, only dc and fundamental components are considered in the self-inductance and mutual inductance. Although the VFRM may operate under the saturation condition, the calculation of the voltage and torque equations can provide a better understanding of the operating principle.

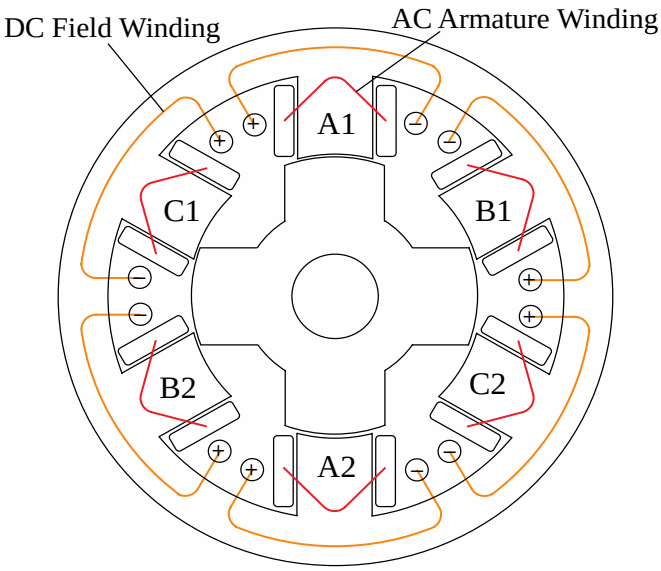

Fig. 5.1. Cross section and winding configuration of 6/4 VFRM with separated AC and DC windings (The rotor pole is aligned with phase A, i.e. θ_e = 0°) [LIU13b].

The initial position (θ_e = 0°) is defined when a rotor pole is aligned with one tooth of phase A wound by A1 in Fig. 1. By exciting a constant current in the A1 winding, the rotor will be rotating to align with the stator tooth where the A1 winding is wound. Then, the flux-linkages in VFRM can be expressed in terms of the inductance and current as

$$\begin{cases} \psi_{as} = \left(L_0 + L_1\cos(\theta_e)\right)i_{as} + \left(M_0 + M_1\cos(\theta_e)\right)i_f \\ \psi_{bs} = \left(L_0 + L_1\cos(\theta_e - 2/3\pi)\right)i_{bs} + \left(M_0 + M_1\cos(\theta_e - 2/3\pi)\right)i_f \\ \psi_{cs} = \left(L_0 + L_1\cos(\theta_e + 2/3\pi)\right)i_{cs} + \left(M_0 + M_1\cos(\theta_e + 2/3\pi)\right)i_f \end{cases} \tag{5.2}$$

where L_0 and L_1 are the static and fundamental components of the self-inductance of the armature winding, and M_0 and M_1 are the static and fundamental components of the mutual inductance between the field and armature windings, respectively. θ_e denotes the electrical rotor position of the VFRM, and i_f is the field excitation current. It should be noted that different from the PM and induction machines, the self-inductance changes with respect to the angular rotor position at fundamental frequency. Additionally, the mutual inductance between the armature windings is negligible in the 6/4 VFRM [LIU13b].

In the synchronous *dq*-axis frame, the *dq*-axis currents can be transformed from the *abc*-axis phase currents as

$$\begin{bmatrix} i_{ds} \\ i_{qs} \\ i_0 \end{bmatrix} = \frac{2}{3}\begin{bmatrix} \cos(\theta_e) & \cos(\theta_e - 2\pi/3) & \cos(\theta_e + 2\pi/3) \\ -\sin(\theta_e) & -\sin(\theta_e - 2\pi/3) & -\sin(\theta_e + 2\pi/3) \\ 1/2 & 1/2 & 1/2 \end{bmatrix}\begin{bmatrix} i_{as} \\ i_{bs} \\ i_{cs} \end{bmatrix}. \tag{5.3}$$

The voltage equations in the synchronous *dq*-axis frame can be transformed from (1) by using (3) as

$$\begin{bmatrix} v_{ds} \\ v_{qs} \\ v_f \end{bmatrix} = R_s\begin{bmatrix} i_{ds} \\ i_{qs} \\ i_f \end{bmatrix} + \begin{bmatrix} L_0 + \frac{L_1}{2}\cos 3\theta_e & -\frac{L_1}{2}\sin 3\theta_e & M_1 \\ -\frac{L_1}{2}\sin 3\theta_e & L_0 - \frac{L_1}{2}\cos 3\theta_e & 0 \\ \frac{M_1}{2} & 0 & M_0 \end{bmatrix}\begin{bmatrix} \frac{di_{ds}}{dt} \\ \frac{di_{qs}}{dt} \\ \frac{di_f}{dt} \end{bmatrix} \tag{5.4}$$
$$+\omega_e\begin{bmatrix} -L_1\sin 3\theta_e & -L_0 - L_1\cos 3\theta_e & 0 \\ L_0 - L_1\cos 3\theta_e & L_1\sin 3\theta_e & M_1 \\ 0 & 0 & 0 \end{bmatrix}\begin{bmatrix} i_{ds} \\ i_{qs} \\ i_f \end{bmatrix}$$

where ω_e is the electrical angular speed. The coordinated operation of the mutual inductance

variation, M_1, and field current, i_f, operates as the flux-linkage produced by the PMs in the PM machines. However, different from the conventional PM machines, the third harmonic inductance components in the *dq*-axis voltage equations are observed with respect to the rotor position due to the variation of self-inductance. Additionally, the cross-coupling components in the *dq*-axis voltage equations have third harmonic components, in which the amplitude is proportional to the machine speed. Although zero sequence voltage does not have the varying components, all of the voltages will be affected by the third harmonic components since zero sequence voltage is linked with *d*-axis current through mutual inductance, M_1. Those third harmonics may deteriorate the control performance.

The voltage equations can be rearranged in the ordinary differential equation form for numerical computations as

$$\frac{di_{dq0}}{dt} = -R_s L^{-1} i_{dq0} - \omega L^{-1} C i_{dq0} + L^{-1} v_{dq0} \tag{5.5}$$

where C and L^{-1} are derived in (5.6) and (5.7), respectively. Inductances of the VFRMs, L_0 and L_1, are assumed as the same M_0 and M_1 [LIU13b].

$$C = \begin{bmatrix} -L_1 \sin 3\theta_e & -L_0 - L_1 \cos 3\theta_e & 0 \\ L_0 - L_1 \cos 3\theta_e & L_1 \sin 3\theta_e & L_1 \\ 0 & 0 & 0 \end{bmatrix} \tag{5.6}$$

$$L^{-1} = \frac{1}{\Delta} \begin{bmatrix} {L_0}^2 - L_0 \frac{L_1}{2} \cos 3\theta_e & L_0 \frac{L_1}{2} \sin 3\theta_e & -L_0 L_1 + \frac{{L_1}^2}{2} \cos 3\theta_e \\ L_0 \frac{L_1}{2} \sin 3\theta_e & {L_0}^2 - \frac{{L_1}^2}{2} + L_0 \frac{L_1}{2} \cos 3\theta_e & -\frac{{L_1}^2}{2} \sin 3\theta_e \\ -L_0 \frac{L_1}{2} + \frac{{L_1}^2}{4} \cos 3\theta_e & -\frac{{L_1}^2}{4} \sin 3\theta_e & {L_0}^2 - \frac{{L_1}^2}{4} \end{bmatrix} \tag{5.7}$$

where $\Delta = {L_0}^3 - \frac{3}{4} L_0 {L_1}^2 + \frac{{L_1}^3}{4} \cos(3\theta_e)$.

It should be noted that to satisfy the non-singularity of the inductance inverse matrix, L^{-1},

L_0 should be larger than L_1 so that Δ is not zero. This ordinary differential equation will be used in dynamic simulation in order to show the validity of the proposed method by using MATLAB/*Simulink*.

The torque equation can be derived from the energy conversion consideration in terms of an equivalent circuit containing emf, resistance, and inductance components in magnetically linear machines [HEN10]. In the VFRMs, the formula for instantaneous electromagnetic torque can be represented as

$$T_e = \frac{P}{\omega_e}\left[\{e_a i_{as} + e_b i_{bs} + e_c i_{cs}\} + \frac{1}{2}\left\{ {i_{as}}^2 \frac{dL_a}{d\theta_e} + {i_{bs}}^2 \frac{dL_b}{d\theta_e} + {i_{cs}}^2 \frac{dL_c}{d\theta_e} \right\}\right] \tag{5.8}$$

where P is the number of rotor poles, in which the rotor pole number is equivalent to the pole pair numbers of a conventional synchronous machine. e_a, e_b, e_c are the emfs entirely due to the mutual inductance between field and armature windings in the *abc*-axis frame, and L_a, L_b, L_c are the self-inductance of the armature windings, respectively. It should be noted that the instantaneous torque produced by the mutual inductance between the armature windings is neglected due to small quantity.

From (5.8), the instantaneous torque is derived in the synchronous *dq* frame as

$$T_e = \frac{3P}{2}\left\{ M_1 i_f i_{qs} + \frac{1}{4} L_1 \left({i_{ds}}^2 + {i_{qs}}^2 \right) \sin\left(3\theta_e + 2\beta_1\right) \right\} \tag{5.9}$$

where β_1 is the advanced current angle of the fundamental component. It is important to distinguish the average torque and instantaneous torque. From (5.9), the instantaneous torque of the VFRM is produced by two components; the self-inductance variation, and the mutual inductance variation between the armature and field windings. Both torque components are proportional to the rate of change of inductance with rotor position. The principle of average

torque generation in the VFRM is similar to that of the PM machines, in which the average torque is generated by the interaction between the flux-linkage and armature current. In the VFRM, the interaction between field current and mutual inductance variation produces flux-linkage, which contributes to the average torque production with armature current. Therefore, it can be expected that the higher field current is injected, the higher torque will be obtained when magnetic saturation is not considered.

The principle of torque production generated by the self-inductance variation is the same as that of the SRMs. The torque component caused by the self-inductance variation is proportional to the square of the phase current magnitude, but not related to the polarity of armature current. There is no contribution of the self-inductance to the average torque in VFRMs. For the torque ripple minimisation, the field or *q*-axis current can be utilised, in which the third harmonic reference current counteracts the torque ripple component.

5.3 Control Strategies of VFRM

5.3.1 Conventional Field Excitation Current Control

The conventional field excitation current control strategy for the VFRMs is illustrated in Fig. 5.2 [LIU12a]. The conventional PI current controllers are utilised for armature and field excitation current control. All of the field windings are connected in series connection, and field excitation current is provided by the H-bridge converter. The armature windings are connected to the three-phase inverter in Y-connection, and the conventional three-phase inverter circuit is utilised for the armature currents, which is similar to that in the PM

machines and induction machines. Owing to the vector control, SVM strategy can be also utilised for the VFRM drives.

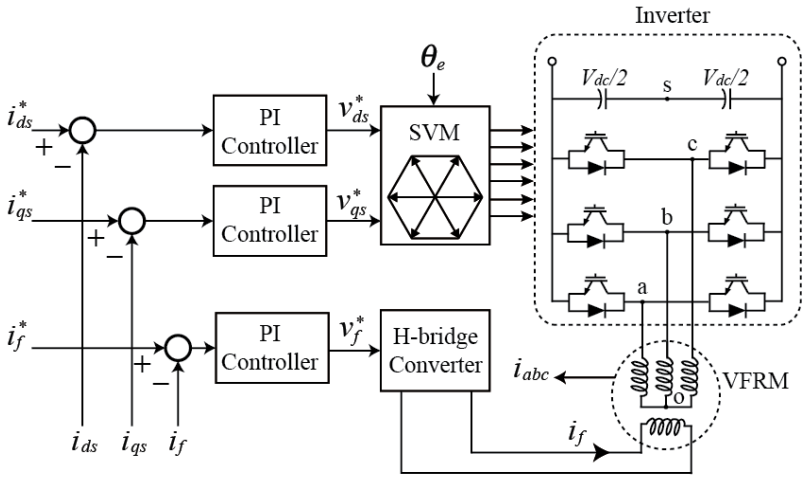

Fig. 5.2. VFRM control with external field excitation current.

5.3.2 Proposed Integrated Current Control

As represented in Fig. 5.1, VFRM has the field and armature windings on the same stator tooth. From the winding configuration, the field and armature currents can be injected together, which helps the field and armature windings be connected in parallel as shown in Fig. 5.3.

The overall torque production is mainly contributed by the dc, fundamental, and second harmonic current components [LIU12b]. The other high order harmonics have less contribution to the average torque. Additionally, the utilisation of high order harmonic components will cause additional loss. Hence, the dc and fundamental current components are only utilised in the integrated current control method. Compared with the conventional method, the armature current will be a sinusoidal waveform, whilst the field current has a dc component. Then, the integrated field and armature current can be represented by a sinusoidal current with a dc offset component as

$$\begin{cases} i_{as} = i_f + i_s \cos(\omega_e t + \beta_1) \\ i_{bs} = i_f + i_s \cos(\omega_e t - 2/3\pi + \beta_1) \\ i_{cs} = i_f + i_s \cos(\omega_e t + 2/3\pi + \beta_1) \end{cases} \tag{5.10}$$

where i_s is the magnitude of the armature current.

Generally, the phase winding resistance has a relationship as

$$R_s \propto \frac{l}{A} \tag{5.11}$$

where l is the winding length and A is the cross section area of the winding, respectively Since the integrated current control allows using field and armature windings in parallel connection, the cross section area becomes double compared with that of the field excitation control, and it leads to the half of the winding resistance. As a result, the copper loss can be decreased by half.

The number of turns per phase is the same between the external field excitation current and integrated current control. Thus, the static and varying components of the phase inductance in both current control methods are the same because the inductance is proportional to the square of the number of turns. According to (5.9), the output torque is only related to the winding inductance components rather than the winding resistance. As a result, the torque can be maintained in both control method if the current condition is the same. It should be noted that the derived voltage and torque equations are still applicable when the integrated current control is adopted.

The key of the proposed method is the utilisation of the constant zero sequence current as a field current. However, the conventional three-phase inverter with Y-connection cannot produce the constant zero sequence current. Hence, the open winding inverter with a single

voltage source is adopted, in which this configuration allows common mode current flowing through a zero sequence current loop.

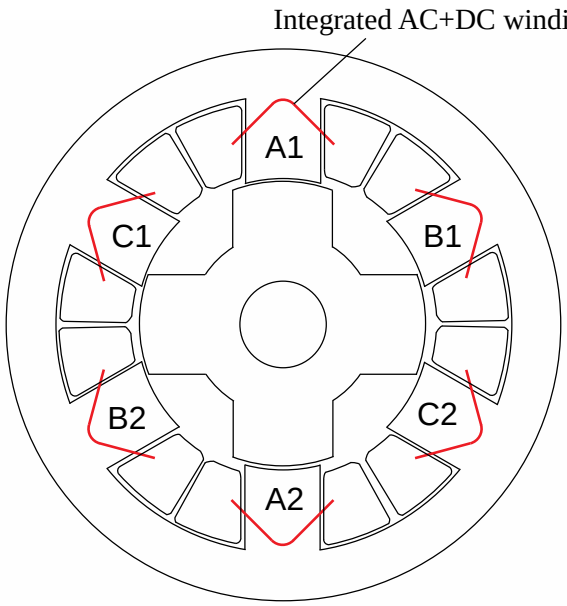

Fig. 5.3. Cross section and winding configuration of 6/4 pole VFRM with integrated AC+DC windings (The rotor pole is aligned with phase A, i.e., θ_e = 0°).

5.4 Zero Sequence Current Based on Open Winding Inverter

5.4.1 Open Winding Inverter with a Single Voltage Source

Fig. 5.4 shows the open winding inverter configuration with a single voltage source, in which the output terminals of the two inverters are connected to both ends of the stator windings. The voltage vectors synthesised by the two inverters can be represented as a hexagon shape in Fig. 5.5, in which the maximum envelope of the voltage vectors is marked with dash line, GIKMPR. However, the open winding inverter topology with a single voltage source can cause a significant third harmonic current in zero sequence depending on the switching patterns.

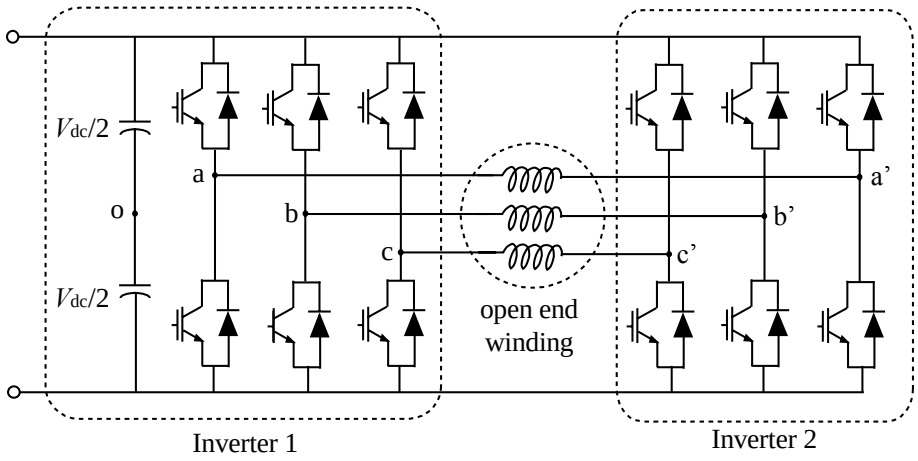

Fig. 5.4. Open winding inverter with a single voltage source [BAI04].

In order to suppress the alternating zero sequence voltage, the voltage vector of the Inverter 1 should be either leading or lagging that of the Inverter 2 by 120° electrical angle [BAI04]. With 120° phase difference between the individual inverters, the third harmonic of the zero sequence voltage will be phase shifted by 120°, and consequently, becomes 360°, which does not generate any third harmonic component in the zero sequence voltage. Due to the phase shift between two inverters, the synthesised vectors can be classified into 7 vectors, in which the voltage vectors are located at the points of H, J, L, N, Q, S and O. As a result, the maximum magnitude of the voltage vector is reduced from $1.33V_{dc}$ to $1.15V_{dc}$.

Each of the conventional inverters can produce eight voltage space vectors independently, and the maximum magnitude of active vector is $0.66V_{dc}$ as shown in Fig. 5.6(b). If the reference voltage vector is V^*_{dq} in Fig. 5.6(a), the reference phase voltages for two individual inverters can be calculated as

$$V^*_{\alpha\beta\_1} = \frac{1}{\sqrt{3}} e^{j(\theta_e - 30^\circ)} V^*_{dq} \tag{5.12}$$

$$V^*_{\alpha\beta\_2} = \frac{1}{\sqrt{3}} e^{j(\theta_e - 150^\circ)} V^*_{dq} \tag{5.13}$$

where $V^*_{\alpha\beta\_1}$ and $V^*_{\alpha\beta\_2}$ denote the reference voltages of Inverter 1 and Inverter 2 in stationary

$\alpha\beta$-axis frame, respectively. φ is the reference voltage angle from a-axis in stationary reference frame. V^*_{dq} is the reference voltage of the open winding inverter in the synchronous dq-axis frame. An arbitrary space voltage vector of the individual inverters can be represented as a combination of the decomposed vectors. Then, the decomposed vectors are synthesised by turning on each switching devices in inverters during switching period. The switching on time T_1, T_2 and T_0 are determined from the stationary reference voltages [NAM10].

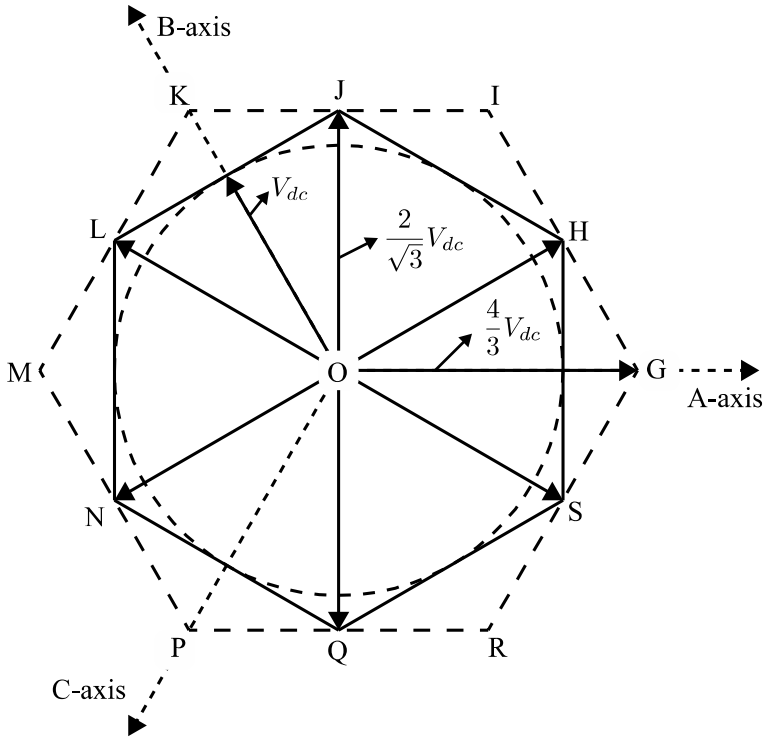

Fig. 5.5. Synthesised voltage vectors in open winding configuration with a single voltage source.

5.4.2 Modulation of Zero Sequence Voltage

Based on SVM technique, the switching on-time of the effective vector can be calculated according to the required voltage. In the conventional three-phase inverter with Y-connection, the switching duties for the zero voltage vector are equally divided into V_0 and V_7 based on the SVM technique, since the zero voltage vectors can be employed by shorting either upper

or lower switches. In the open winding inverter, the zero vectors can be modulated to produce the zero sequence current. For example, in case of V_7 in Inverter 1 and V_0' in Inverter 2, the zero sequence voltage is V_{dc}, whilst -V_{dc} in case of V_0 in Inverter 1 and V_7' in inverter 2. Therefore, in order to produce the constant zero sequence current, the zero vectors of two inverters will be modulated.

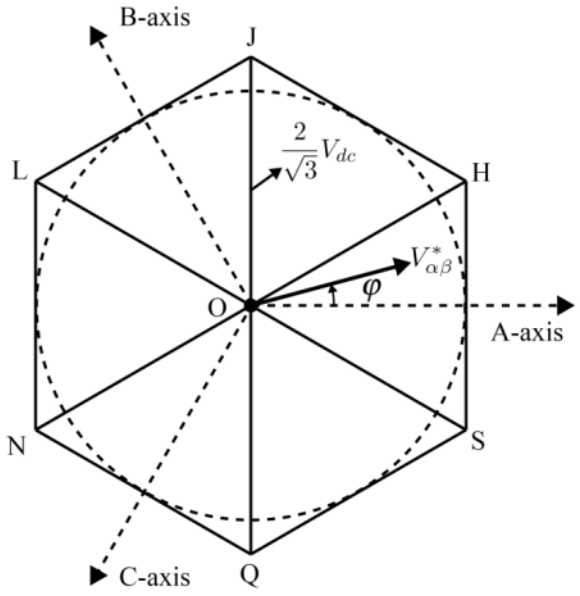

(a) Synthesised voltage vectors from the individual vectors

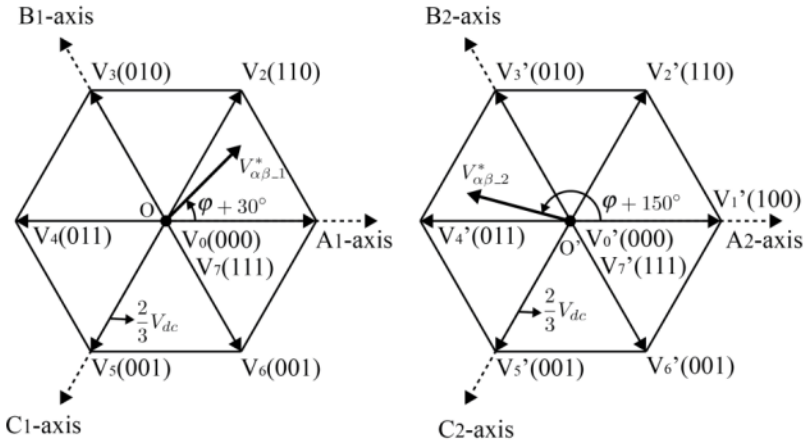

(b) Individual voltage vectors for each inverter

Fig. 5.6. Reference voltage vectors for open winding configuration with a single voltage source [BAI04].

The required zero vector duty can be determined by PI controller as

$$T_z = \frac{1}{2V_{dc}}(PI)\left(i_0^* - i_0\right) \tag{5.14}$$

where i^*_0 and i_0 are the reference and measured zero sequence currents. Based on the voltage-second equivalent principle, the switching duty for the zero vectors can be added to each inverter. For example, when $0^\circ \le \varphi \le 60^\circ$, the switching duty can be calculated as [ZHO15]

$$T_{c1} = \frac{T_0}{2} + \frac{T_z}{2}, \quad T_{b1} = T_{c1} + \frac{T_2}{2}, \quad T_{a1} = T_{b1} + \frac{T_1}{2} \tag{5.15}$$

$$T_{a2} = \frac{T_0}{2} - \frac{T_z}{2}, \quad T_{c2} = T_{a2} + \frac{T_2}{2}, \quad T_{b2} = T_{c2} + \frac{T_1}{2} \tag{5.16}$$

where T_{a1}, T_{b1}, T_{c1} are the on-time of each leg in Inverter 1, and T_{a2}, T_{b2}, T_{c2} are the on-time of each leg in Inverter 2, respectively. By using the modification of switching on-time, the zero sequence voltages, $V^*_{0\_1}$ and $V^*_{0\_2}$ can be generated by Inverter 1 and Inverter 2, respectively.

Fig. 5.7 shows the switching on-time and the symmetrical PWM patterns when the reference voltage vector of the open winding inverter is located at $0^\circ \le \varphi \le 60^\circ$ in Fig. 5.6(a). The corresponding voltage vectors for inverters are also presented, in which the duties for the effective voltage vectors, T_1, T_2, are maintained at the same. The difference of the zero vectors between two inverters is shown on the right side. The zero voltage vectors do not contribute to effective voltage vector, since zero voltage vectors are always located at the origin in space vector diagram in $\alpha\beta$-axes.

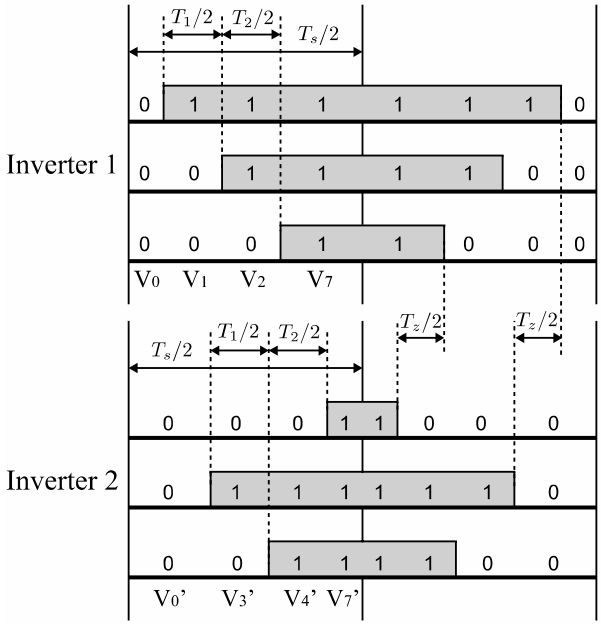

Fig. 5.7. Switching on-time for individual inverters and corresponding voltage vectors.

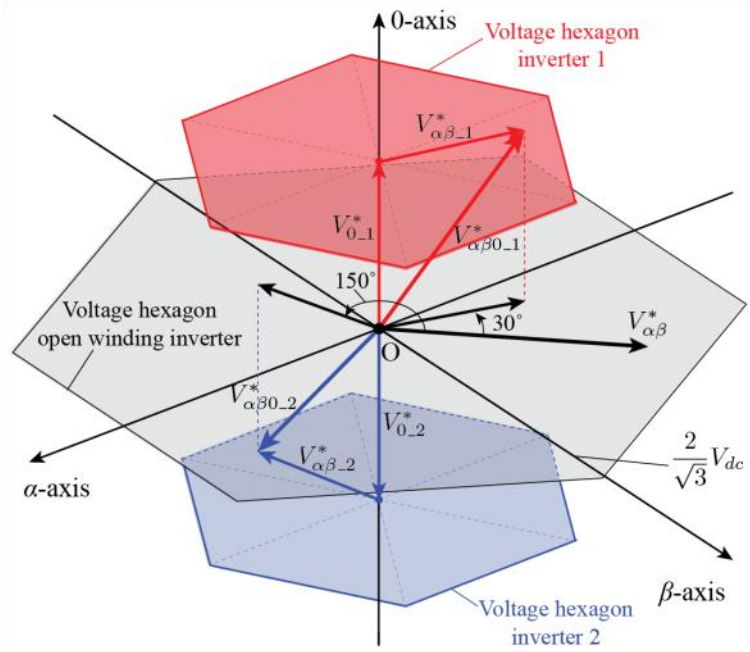

Fig. 5.8. Reference voltage vectors and voltage hexagon in $\alpha\beta$0-axis frame.

Fig. 5.8 shows the reference voltage vectors in $\alpha\beta$0-axis frame in order to clarify each voltage vector component. For the generation of the reference voltage vector V^*_{dq}, each voltage vector $V^*_{dq\_1}$ from Inverter 1 and $V^*_{dq\_2}$ from Inverter 2 can be utilised. And, $V^*_{0\_1}$ and

$V^*_{0\_2}$ will be added to voltage vectors for the zero sequence voltage vector generation. As a result, the voltage hexagon of Inverter 1 in $\alpha\beta$ plane will be located at $V^*_{0\_1}$ in 0-axis. The projection on the $\alpha\beta$ plane in 0-axis is the same as the hexagon shape in the vector diagram. The reference voltage vector for Inverter 1 can be shown as $V^*_{dq0\_1}$, which consists of $V^*_{dq\_1}$ and $V^*_{0\_1}$. On the other hand, in case of inverter 2, the voltage hexagon will be located at $V^*_{0\_2}$ in 0-axis.

5.5 Integrated Current Control

5.5.1 Rated Torque Operation

The overall block diagram of the proposed control method for the three-phase open winding VFRM is shown in Fig. 5.9. Based on the Park's transformation, the ac components of the phase currents are transformed into the *dq*-axis currents, whilst the dc component of the phase currents is transformed to the zero sequence current. The *dq*0-axis current can be regulated to the reference values by using the PI controller. The determination of *dq*-axis reference currents is the same as that in the conventional PM machines. The *q*-axis reference current is determined by a speed controller, and the *d*-axis reference current is set to zero in the constant torque region due to no contribution to the average torque. In order to minimise the copper loss in the VFRM, the field and armature windings have the same number of turns [CHE10]. In this condition, the minimisation of the copper loss can be achieved, when the reference field current is set to $1/\sqrt{2}$ times of *q*-axis current ($i_f = i_q / \sqrt{2}$, i.e., the same rms current).

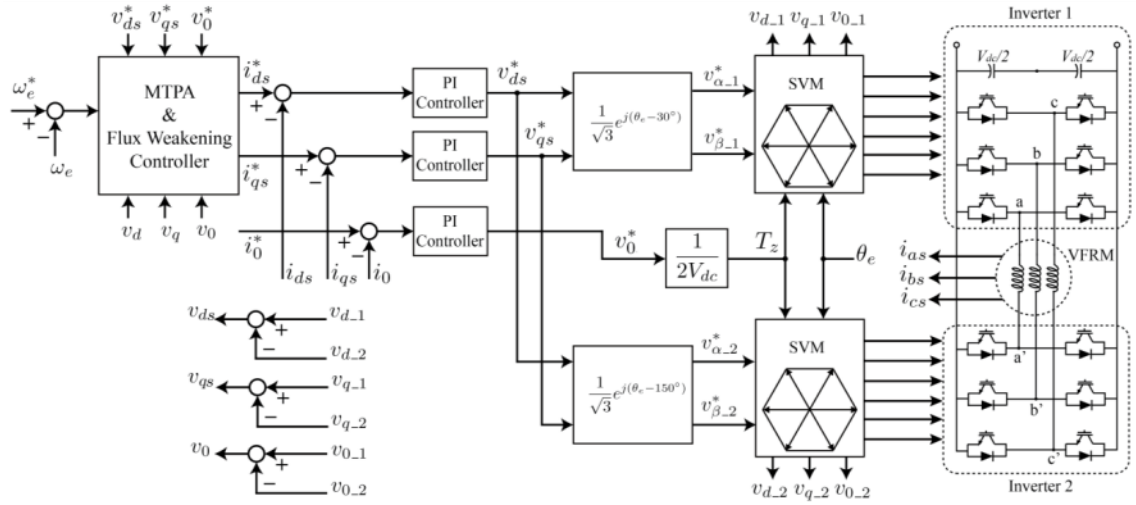

Fig. 5.9. Overall control block diagram of the proposed integrated current control.

Fig. 5.10 shows the voltage vector diagrams of the integrated and external current control schemes in the steady state condition, in which third harmonic components in the voltage equations are neglected for simplicity. In the external current control, the voltage vector is two-dimension, whilst the voltage vector in the integrated current control consists of three-dimension due to the zero sequence component. Under the rated torque region, *d*-axis current is controlled to zero since it does not contribute to the average torque generation. Then, *d*-axis voltage has only coupling component, $\omega_e L_s i_{qs}$. The *q*-axis voltage consists of two components, i.e. back emf, $\omega_e M_\delta i_0$, and resistive voltage drop, $R_s i_{qs}$. Since the inductances are the same in both control methods, the coupling and back emf terms are the same. In external field control method the resistive voltage drop is $R_s i_{qs}$, whilst $1/2R_s i_{qs}$ + $1/2R_s i_0$ in the integrated current control method. If the field current is controlled at $i_f = i_{qs}/\sqrt{2}$, the magnitude of total resistive voltage vector in the external field scheme will be reduced in the integrated current control. Therefore, the base speed can be increased in the proposed method due to the reduced resistive voltage drops, although the zero voltage vector generation reduces

the voltage utilisation of the *dq*-axis voltages.

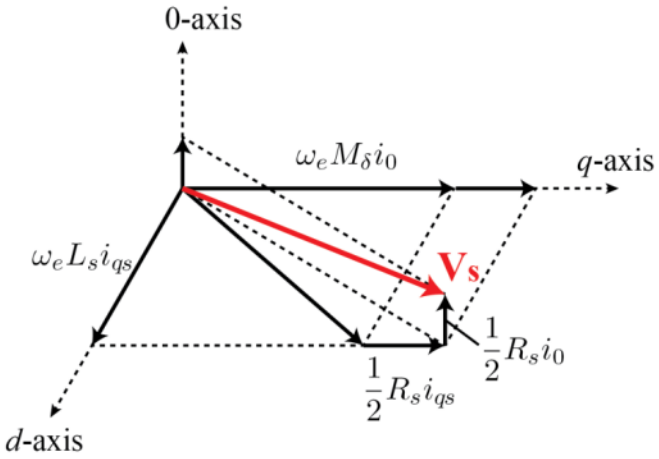

(a) Integrated current control scheme

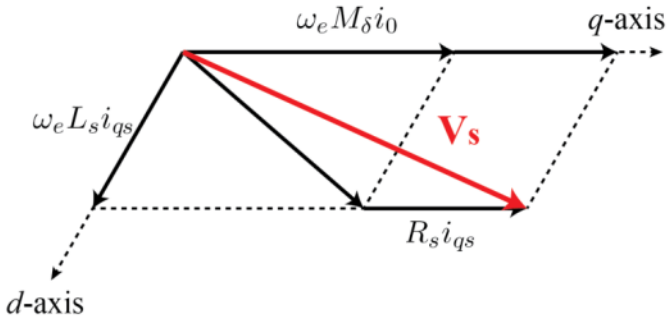

(b) External field current control scheme

Fig. 5.10. Voltage vector diagram showing the different resistive voltage drops.

5.5.2 Flux Weakening Operation

In order to prevent the saturation of the current controllers, flux weakening controller is implemented based on the anti-windup method in the synchronous *dq*-axis frame [KWO06]. The difference between the reference value and output of the SVM block is utilised to modify the negative *d*-axis current as

$$i_{ds}^{*} = -\rho \cdot LPF\left(\sqrt{\left(v_{ds}^{*} - v_{ds}\right)^2 + \left(v_{qs}^{*} - v_{qs}\right)^2 + \left(v_0^{*} - v_0\right)^2}\right) \tag{5.17}$$

where ρ is a positive gain, and *LPF* is the first-order low pass filter. To satisfy the maximum

current condition, the *q*-axis reference current should be changed as

$$i_{qs}^{*} = \sqrt{\mathrm{I}_{max}^{2} - i_{ds}^{*\,2}}. \tag{5.18}$$

The field reference current is selected at $0.707I_{max}$ so that the rms value is the same between the field and armature currents in the constant torque and flux weakening regions.

When the machine speed increases, the third harmonic components will be also increased due to the cross coupling in the voltage equations. Then, the peak of the voltage magnitude can reach to the maximum inverter voltage, although the average value of the voltage magnitude is lower than maximum voltage. In order to avoid saturation of the current controller, the anti-windup will be activated which generates the negative *d*-axis current. Consequently, the voltage utilisation factor will be decreased due to the presence of the third harmonic components as a drawback of the 6/4 VFRM.

The integrated control method results in a higher peak current than external control method, since the field and armature currents are generated together as a sinusoidal current biased by dc offset. A larger peak current requires a higher current rating for the switching devices. It should be noted that the maximum current limit is determined by the electric loading of the machine rather than from the inverter constraint.

5.6 Simulation and Experimental Validations

For the validation of the proposed integrated current control method, the simulation is performed in MATLAB/*Simulink*. In order to develop the dynamic VFRM model, the voltage equation (5.5) and torque equation (5.9) are utilised. It is worth mentioning that the dynamic

simulation considers the inverter and PWM models. The dc link voltage is set to 80 V, and SVM is applied with 10 kHz switching frequency for both control methods. For the experimental validation, the prototype VFRM is tested, in which the machine parameters are listed in Table 5.1. The experimental rig is shown in Fig. 5.11, whilst the control system is implemented on a dSPACE platform. A dc machine is connected to the shaft as load, and the generated torque is measured by torque meter.

TABLE 5.1

MACHINE PARAMETERS

Machine parameters	**Value**
Number of phases	3
Number of rotor poles (P)	4
Number of turns per phase for armature winding	366
Number of turns for field winding	6 × 366
Air gap	0.5 mm
Winding resistance (R_s)	6 Ω
dc component of self-inductance of armature winding (L_0)	30 mH
Fundamental component of self-inductance of armature winding (L_1)	24 mH
dc component of mutual inductance between field and armature windings (M_0)	30 mH
Fundamental component of mutual inductance between field and armature windings (M_1)	24 mH

Fig. 5.12 shows comparison of the phase current, field current, measured torque waveforms and machine speed for both conventional and proposed methods. The machine speed is controlled at 400 rpm and load torque is set to 0.4 Nm. For the maximum efficiency operation, the field current is controlled at $\sqrt{2}$ A, and q-axis current is set to 2 A. Unlike the conventional method injecting the field and armature currents separately into the machine, the

proposed method utilises the sinusoidal current biased by dc offset. As can be seen from the results, the operating condition is the same between both methods, whilst the resistance of the phase winding is reduced from 6 Ω to 3 Ω. Hence the total copper loss is reduced by half due to half of the winding resistance in the proposed method. It should be noted that the total copper loss is estimated based on the measured currents and resistance.

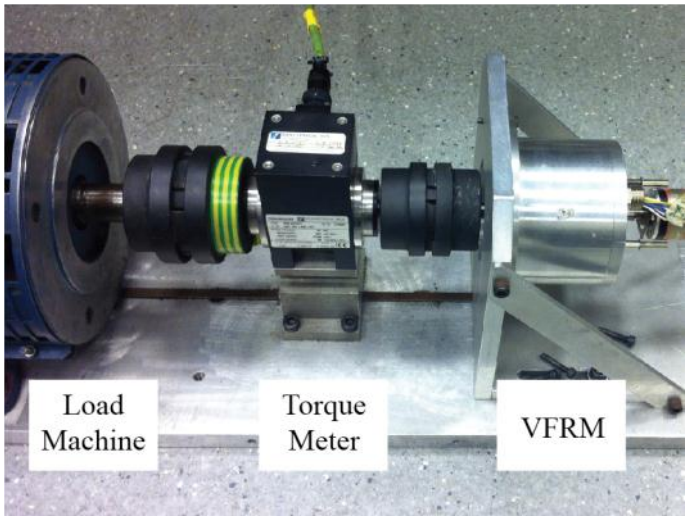

Fig. 5.11. Picture of the experimental rig.

In the constant torque region and flux weakening region, both simulation and experiments are performed with three different configurations. Fig. 5.13 and Fig. 5.14 show the dynamic simulation and experimental results of torque-speed, efficiency-speed and voltage-speed characteristic curves. As a conventional method, the three-phase inverter with the H-bridge inverter for the external current source is utilised, whilst the two three-phase inverters are used for the open winding scheme in the proposed method. Additionally, the external field current control with the open winding inverter is also tested in order to compare the performance at the same voltage utilisation. The *dq*-axis peak current limitation is 2 A and the field excitation current is set to $\sqrt{2}$ A. It should be noted that the total rms current in both control methods

are the same at 2.83 A for the entire region. In the constant torque region, the maximum torque is the same approximately at 0.42 Nm for different configurations, whilst the base speed is significantly extended in the open winding configurations. The main reason of the extended operating range is due to the open winding topology, in which the voltage utilisation factor can be increased to 1.73 times compared with that of the conventional three-phase inverter. In the proposed method, although the zero sequence voltage generation leads to the reduced dc link voltage utilisation, the reduced winding resistance provides the machine with increased voltage utilisation. Hence, the base speed in the proposed method can be higher than that of the external field control method with the open winding configurations. The extended operating range can be also seen in the experimental results in Fig. 5.14(a), in which the base speed is extended from around 550 rpm in the conventional method to around 1,200 rpm in control method with open winding.

Fig. 5.13(b) shows the voltage profiles with respect to the machine speed, in which these voltages are the output voltages of the SVM block. When the machine operates under the base speed, the *q*-axis voltage difference is mainly from the resistive voltage drops since the back emf component is the same for both methods. On the other hand, it is shown that the *d*-axis voltage curves are the same for different configurations due to the zero *d*-axis current in the constant torque region. The experimental results also show the similar voltage profiles in Fig. 5.14(b). Additionally, the zero sequence voltage with proposed method is presented in the voltage characteristic curve.

As a result of the reduced winding resistance, the machine efficiency in the proposed

method is increased as shown in Fig. 5.13(c) and Fig. 5.14(c). In order to calculate the efficiency, the loss caused by the field current is also considered in both simulation and experiments. However, the efficiency difference can be seen between simulation and experimental results. It can be explained that the practical losses are not considered in simulation such as iron loss, inverter loss and mechanical losses.

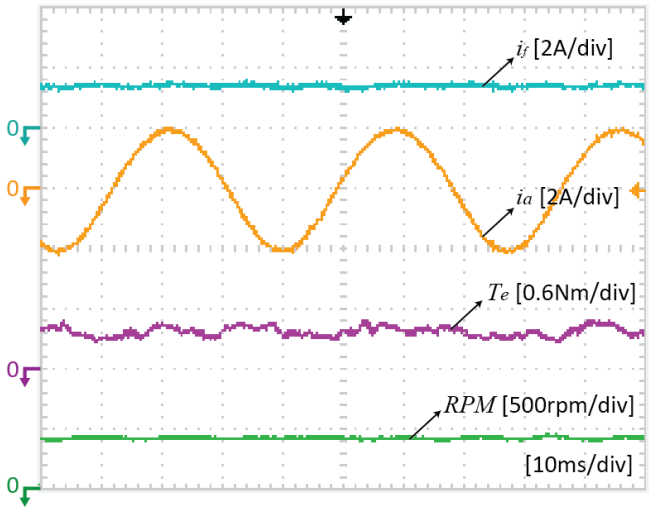

(a) External field excitation current control (copper loss ≈ 101.8 W)

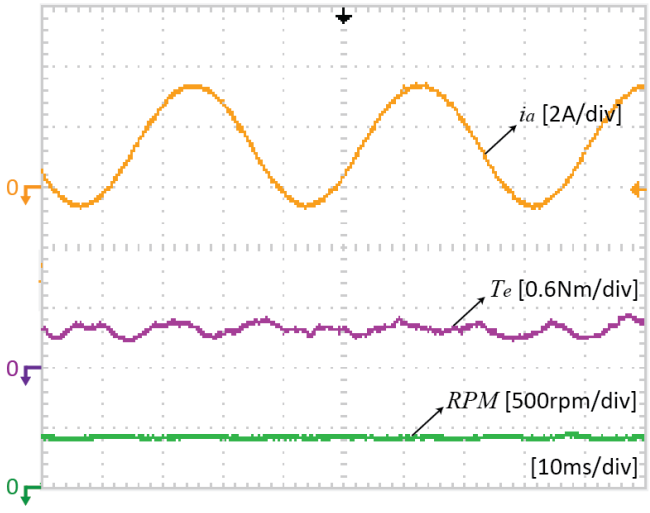

(b) Proposed integrated current control (copper loss ≈ 50.9 W)

Fig. 5.12. Experimental results of phase current, field current, torque waveform and machine speed at 400rpm, $i_f = \sqrt{2}$ A, i_{qs} = 2 A.

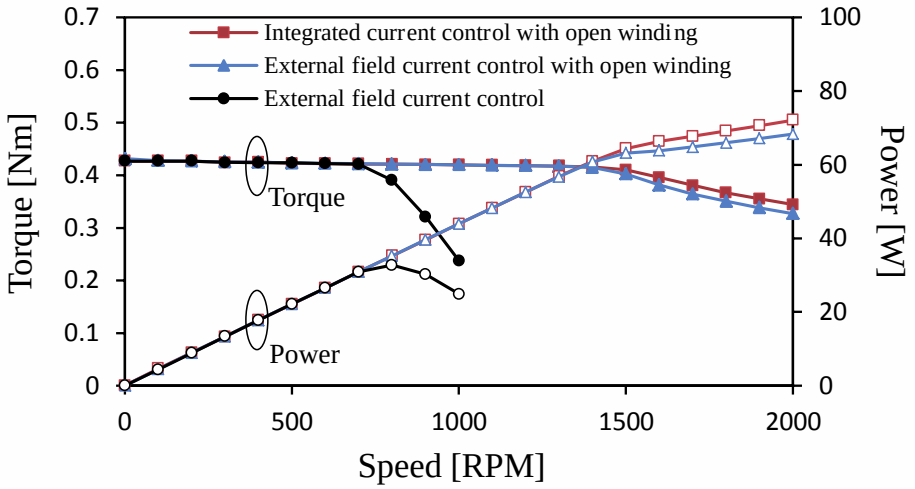

(a) Torque-speed characteristic curve

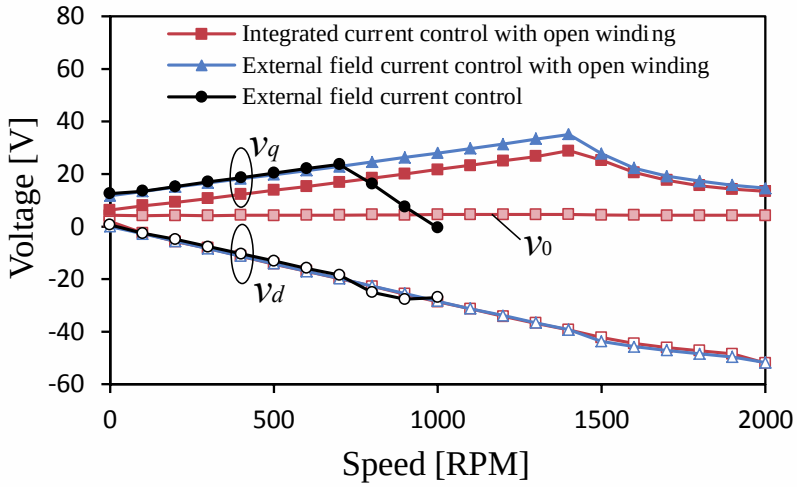

(b) Voltage-speed characteristic curve

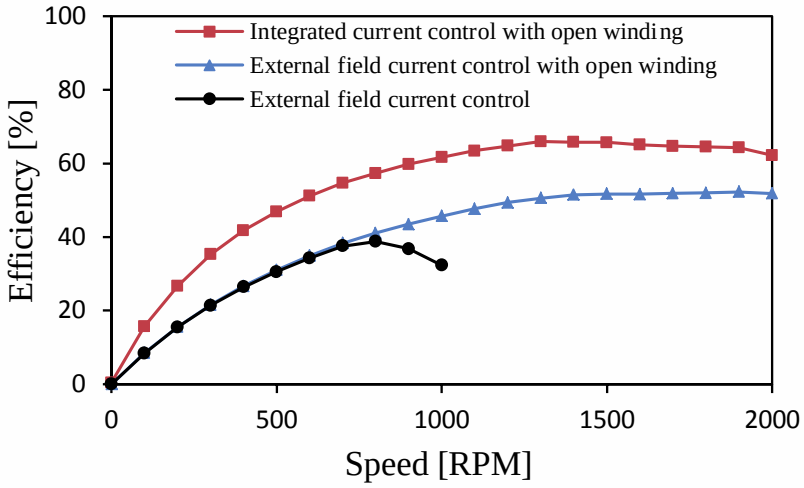

(c) Efficiency-speed characteristic curve

Fig. 5.13. Dynamic simulation results at V_{dc} = 80 V, i_f = $\sqrt{2}$ A, I_{max} = 2 A.

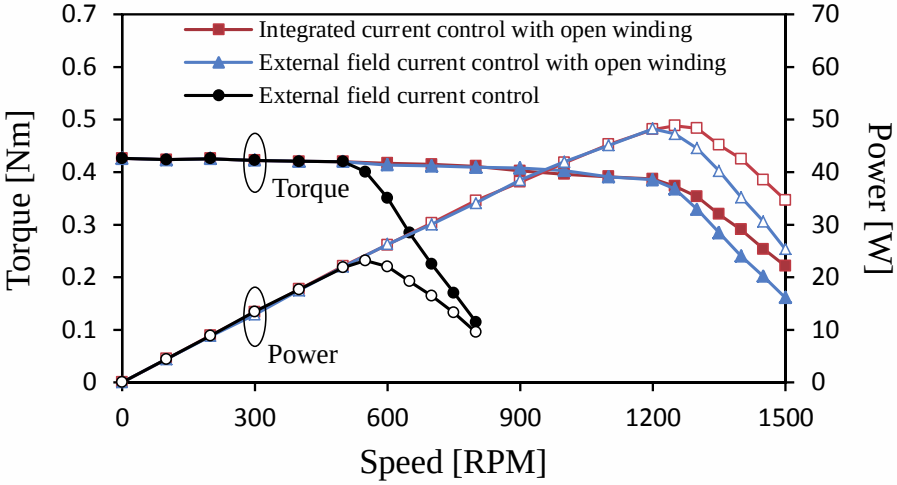

(a) Torque-speed characteristic curve

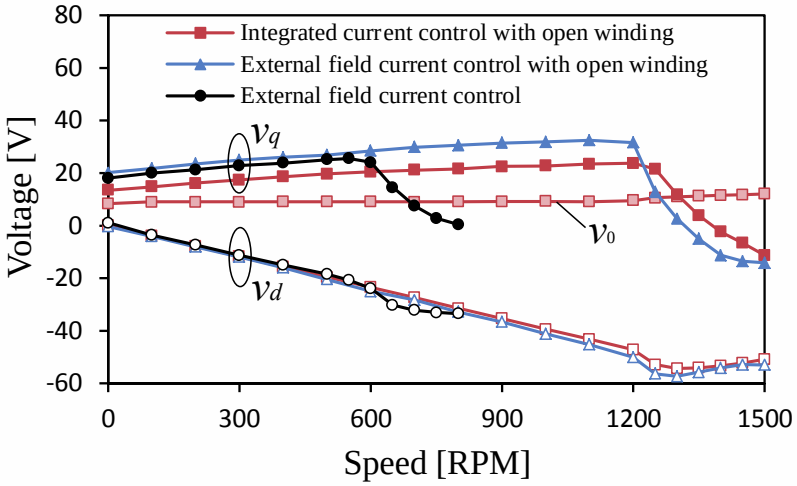

(b) Voltage-speed characteristic curve

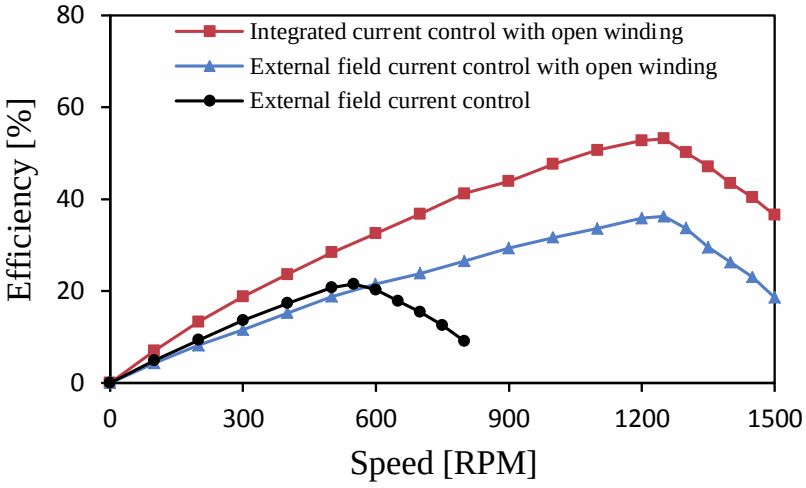

(c) Efficiency-speed characteristic curve

Fig. 5.14. Experimental results at V_{dc} = 80 V, i_f = $\sqrt{2}$ A, I_{max} = 2 A.

Fig. 5.15 shows experimental results of the voltage magnitude curves in different configurations, which are calculated from Fig. 5.14(b). It should be noted that the voltage magnitude consists of only *dq*-axis voltages in the external field control, whilst the integrated control has *dq*-axis voltage and zero sequence voltage together. Although zero voltage is utilised in the integrated control, the required voltage from the VFRM is decreased due to the reduced resistance under the constant torque region. The *q*-axis voltage difference between the external field control with conventional inverter and the open winding is resulted from the additional voltage drops in the open winding inverter. As a drawback of the VFRM, the dc link voltage is not fully utilised due to the third harmonics in the voltage equations. At 80 V of the dc link voltage, the maximum voltage magnitude is around 51 V in the three-phase inverter and 88.5 V in the open winding configuration. However, the maximum voltage magnitude in experiments is decreased to around 36 V in the three-phase inverter, and 60 V in the open winding configurations.

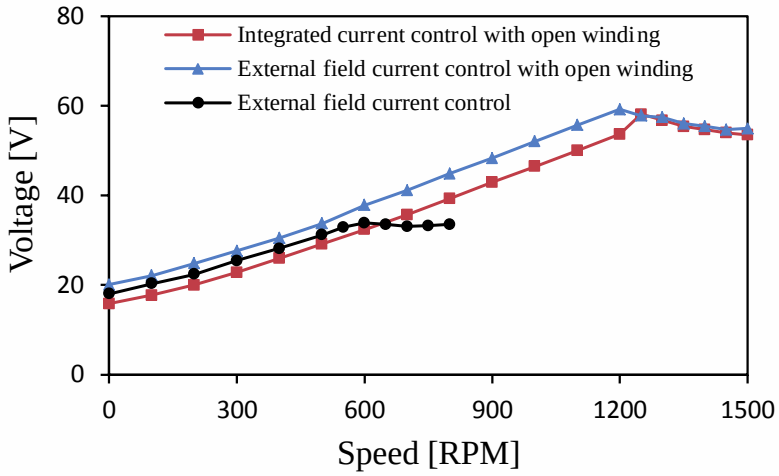

Fig. 5.9. Voltage magnitude in different control strategies at V_{dc} = 80 V, i_f = $\sqrt{2}$ A, I_{max} = 2 A.

5.7 Conclusion

In this chapter, an integrated field and armature current control strategy is proposed for the VFRM. In order to utilise the zero sequence current as a field current, the zero vector modification technique is proposed for the zero sequence component generation with the open winding configuration. As a feature of this method, the winding resistance can be halved by connecting the field and armature windings in parallel. Hence, the proposed method can increase the machine efficiency over the entire operating region. For the comparison of the performances in terms of efficiency and base speed at the same voltage utilisation factor, the characteristic curves are presented and compared, in which both conventional and proposed method use the open winding configuration. It is shown that the proposed method can provide higher base speed than the external field current control with the open winding configuration. Although the zero voltage vector generation reduces the voltage utilisation of the *dq*-axis voltages, the *dq*-axis resistive voltage drops will be decreased due to the reduced winding resistance. The effectiveness of the proposed method is validated by the dynamic simulation and experiments on the prototype 6/4 VFRM. For the dynamic simulation model, the *dq*-axis voltage and torque equations are derived. For a better flux weakening performance in terms of operating speed range and torque generation, the third harmonic component will be considered as a future work. Additionally, this proposed method is also applicable to the 6/8 and 12/8 VFRMs.

CHAPTER 6

INTEGRATED FIELD AND ARMATURE CURRENT CONTROL FOR DUAL THREE-PHASE VARIABLE FLUX RELUCTANCE MACHINE DRIVES

6.1 Introduction

An integrated field and armature current control strategy can provide the efficiency improvement and an extended operating range in the VFRM drives. In this chapter, the integrated field and armature current control method is applied to the 6/5 or 6/7 VFRM by taking 6/7 VFRM as example. Different from the 6/4 VFRM, the 6/7 VFRM has the different polarity between the field and armature windings in one of the three-phase winding sets, but the same polarity for the other set [LIU13b]. For the integrated current control, the integrated windings of the 6/7 VFRM should be divided into two winding sets. As a result, the asymmetric inverter [NAK14] or open winding inverter [ZHU15] cannot be directly applied to the 6/7 VFRM drives. The resultant winding configuration is similar to a six phase [LIP80], [LIP96] or dual three-phase winding having 180° phase difference [NEL74], [SIN05]. Hence, a dual three-phase configuration with a neutral point is adopted to produce a zero sequence current and the phase current having opposite polarity between the two winding sets. In the integrated current control, the zero sequence current is utilised as the field current, whilst the

dq-axis currents generate a rotating field. For the zero sequence current generation, the zero vector redistribution technique is employed, which utilises the voltage difference between the two inverters. In order to utilise the vector control, the voltage equation of the 6/7 VFRM is derived in the synchronous *dq*-axis frame. Simulation and test results show the effectiveness of the proposed scheme [ZHU16b].

6.2 Conventional Field Current Control

Fig. 6.1 shows the cross section and stator windings of the VFRM, whose number of stator teeth is 6 and rotor poles is 7, i.e. 6/7 VFRM. The initial position (θe = 0°) is defined to be where the centre of the rotor pole is aligned with one tooth of Phase A wound with coil A1. Hence, if a constant current is excited in the A1 winding, the rotor will be aligned with the stator tooth wound by the A1 winding.

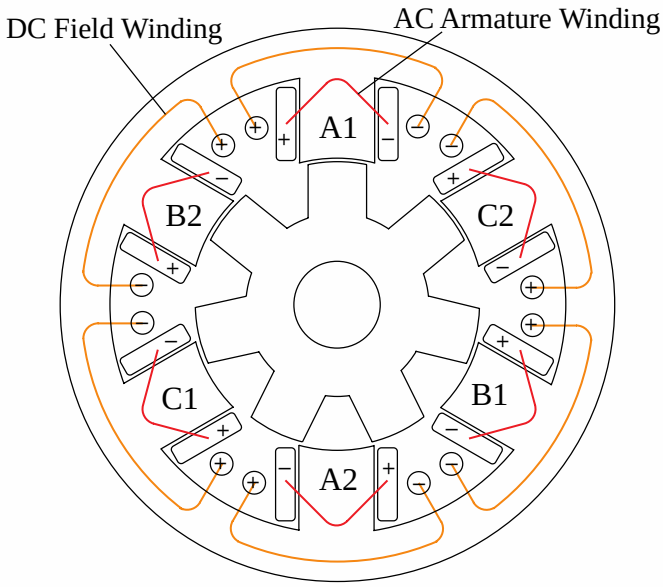

Fig. 6.1. Cross section and winding configurations of 6/7 VFRM with separated AC and DC windings (The rotor pole is aligned with phase A, i.e. $\theta_e = 0^o$).

For the VFRM drives, the separated field current control method can be applied [ZHU14]. Fig. 6.2 shows the conventional field excitation current control block diagram with the external field current source and three-phase inverter. All of the field windings are connected in series, and the field current is supplied by the H-bridge converter. The armature windings have a Y-connection, and a conventional three-phase inverter is utilised, which is the same as a synchronous PM machine drive. Then, in the 6/5 and 6/7 VFRMs the even and third order harmonics in the flux-linkage and back emf can be cancelled out so that more sinusoidal waveforms can be obtained due to the opposite direction of the armature windings in each phase [LIU13b]. Hence, the torque ripple caused by the even and third order harmonics can be much lower compared with the 6/4 and 6/8 VFRMs. In order to control the field and *dq*-axis currents, conventional PI current controllers are implemented based on a space vector control strategy.

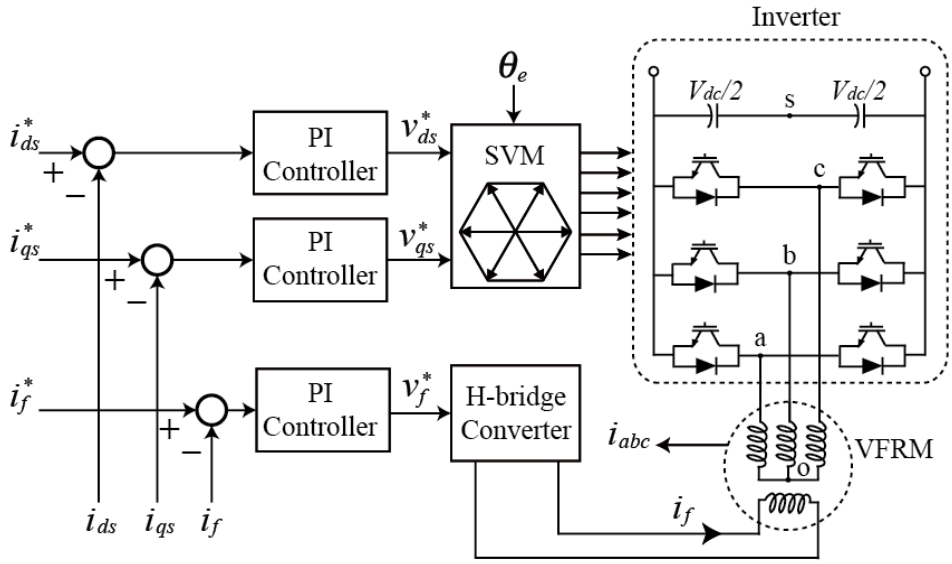

Fig. 6.2. VFRM control with external field excitation current scheme.

The field and armature windings can be connected to form a single coil in parallel as an

integrated winding in Fig. 6.3 since the field and armature windings are identically wound on each stator tooth. The polarities of the field and armature windings are indicated in Fig. 6.1, in which the polarities between field and armature windings are the same in A1, B1, and C1. However, due to the coil back emf, A2, B2, and C2 have a different polarity between the field and armature windings [LIU13b]. Therefore, in order to utilise the integrated windings, they should be divided into two winding sets due to the opposite polarity between the armature winding sets, whilst the polarities of the dc component are the same. Fig. 6.4 shows the external field winding and integrated winding configurations. The field windings are connected in series for the external field current control scheme, and the armature windings are connected in Y-connection. For the integrated windings, the divided two winding sets have 180° shift due to the opposite back emf as shown in Fig. 6.4(b).

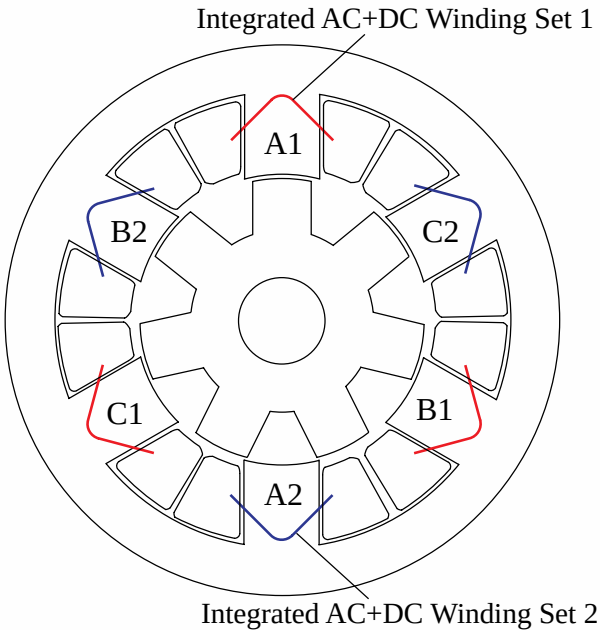

Fig. 6.3. Cross section and winding configurations of 6/7 VFRM with integrated AC+DC windings (The rotor pole is aligned with phase A, i.e., $\theta_e = 0°$).

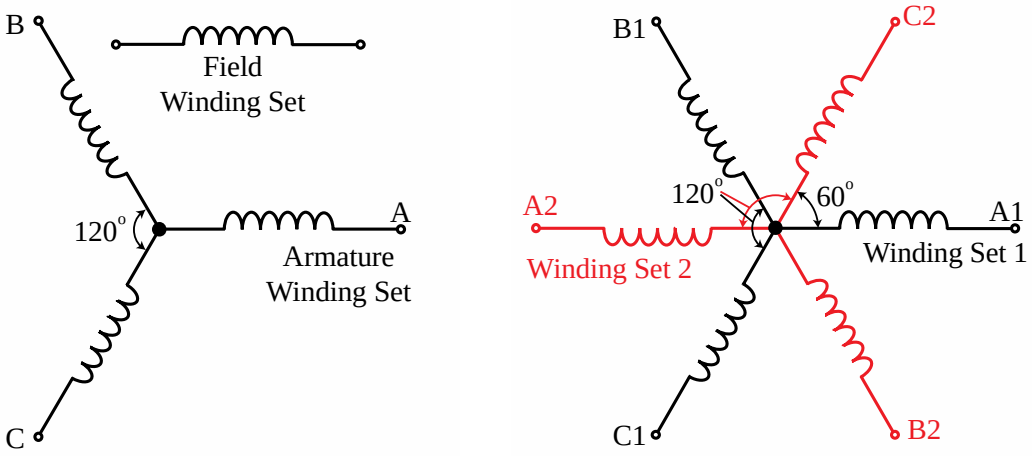

(a) External field winding (b) Dual three-phase winding

Fig. 6.4. VFRM winding configurations.

6.3 Modeling of VFRM

To derive the voltage and torque equations in the synchronous *dq*-axis frame, some assumptions have been made. For simplicity, the dc and fundamental components in inductances are only considered. The magnetic saturation effect is neglected in this chapter, but the derived equations can provide a better understanding of the operating principle of VFRMs.

6.3.1 Voltage and Torque Equations with External Current Configuration

In the VFRMs with external field excitation, the voltage equations in the synchronous *dq*-axis frame can be represented as

$$\begin{bmatrix} v_{ds} \\ v_{qs} \\ v_f \end{bmatrix} = R \begin{bmatrix} i_{ds} \\ i_{qs} \\ i_f \end{bmatrix} + L \begin{bmatrix} di_{ds}/dt \\ di_{qs}/dt \\ di_f/dt \end{bmatrix} + \omega_e \begin{bmatrix} 0 & -L & 0 \\ L & 0 & M_{fa} \\ 0 & 0 & 0 \end{bmatrix} \begin{bmatrix} i_{ds} \\ i_{qs} \\ i_f \end{bmatrix} \tag{6.1}$$

where v_d, v_q are the *dq*-axis voltages; i_d, i_q are the *dq*-axis currents in the synchronous *dq*-axis frame; v_f and i_f are the field voltage and current respectively. R is the stator winding resistance,

L is the winding self-inductance; ω_e is the angular machine speed; M_{fa} is the fundamental component of mutual inductance between the field and armature windings. The voltage equation is exactly the same as that of the SPM machines, except for the presence of the field components and flux-linkage. In the PM machines, the flux-linkage is generated by PMs and is not controllable. In the case of the VFRMs, the interaction between the field current and the mutual inductance M_{fa} produces the flux-linkage, and it can be changed by the field current adjustment.

The electromagnetic torque equation can be derived from the voltage equations as

$$T_e = \frac{3}{2} P M_{fa} i_f i_{qs} \tag{6.2}$$

where P is the number of rotor poles. In terms of the torque generation, the average torque is directly proportional to the mutual inductance variation, the field and q-axis currents under no saturation.

6.3.2 Voltage Equations with Dual Three-phase VFRM

The voltage equation of the 6/7 VFRM in the dual three-phase configuration is written as

$$\mathbf{v}_s = R_s \mathbf{i}_s + \frac{d}{dt}\left(\mathbf{L}_s \mathbf{i}_s\right) \tag{6.3}$$

where $\mathbf{v}_s = [v_{a1}\ v_{b1}\ v_{c1}\ v_{a2}\ v_{b2}\ v_{c2}]^T$, $\mathbf{i}_s = [i_{a1}\ i_{b1}\ i_{c1}\ i_{a2}\ i_{b2}\ i_{c2}]^T$ are the stator voltages and stator currents, respectively. R_s is the stator resistance and $\mathbf{L}_s$ is the inductance matrix in the dual three-phase configuration. The inductance matrix can be represented as

$$\mathbf{L}_s = \mathbf{L}_{s0} + \mathbf{L}_{s1}(\theta_e) \tag{6.4}$$

where $\mathbf{L}_{s0}$ is the constant component of the inductance matrix in the stator windings, and $\mathbf{L}_{s1}$ is the fundamental component of the inductance matrix with respect to the electrical angle, θ_e.

The constant component $\mathbf{L}_{s0}$ can be presented as

$$\mathbf{L}_{s0}=\left[\begin{array}{c:c}\mathbf{L}_{0(3\times3)} & \mathbf{M}_{0(3\times3)}\\ \hdashline \mathbf{M}_{0(3\times3)} & \mathbf{L}_{0(3\times3)}\end{array}\right],\quad \mathbf{L}_0=\begin{bmatrix}L_s & -M_1 & -M_1\\ -M_1 & L_s & -M_1\\ -M_1 & -M_1 & L_s\end{bmatrix},\quad \mathbf{M}_0=\begin{bmatrix}M_2 & M_3 & M_3\\ M_3 & M_2 & M_3\\ M_3 & M_3 & M_2\end{bmatrix} \tag{6.5}$$

where L_s is the self-inductance of the stator winding. M_1 is the mutual inductance between the two different phases of the same winding set, i.e. $M_1 = \{M_{ij} \mid i, j = a, b, c,$ or $i, j = a', b', c'$ and $i \neq j\}$. It is worth mentioning that M_1 has a positive value, since the windings are shifted in space by 120°. M_2 is the mutual inductance between the same phases of the different winding sets, i.e. $M_2 = \{M_{ii'} \mid i = a, b, c\}$ or $\{M_{i'i} \mid i = a, b, c\}$. M_3 is the mutual inductance between the two difference phases of the different winding sets, i.e. $M_3 = \{M_{ij'} \mid i, j = a, b, c$ and $i \neq j\}$ or $\{M_{i'i} \mid i = a, b, c$ and $i \neq j\}$.

The fundamental component $\mathbf{L}_{s1}(\theta_e)$ can be presented as

$$\mathbf{L}_{s1}(\theta_e)=\left[\begin{array}{c:c}\mathbf{L}_{1(3\times3)}(\theta_e) & \mathbf{M}_{1(3\times3)}(\theta_e)\\ \hdashline -\mathbf{M}_{1(3\times3)}(\theta_e) & -\mathbf{L}_{1(3\times3)}(\theta_e)\end{array}\right],$$

$$\mathbf{L}_1(\theta_e)=\begin{bmatrix}L_\delta\cos(\theta_e) & -M_{1\delta}\cos(\theta_e+\gamma) & -M_{1\delta}\cos(\theta_e-\gamma)\\ -M_{1\delta}\cos(\theta_e+\gamma) & L_\delta\cos(\theta_e-\gamma) & -M_{1\delta}\cos(\theta_e)\\ -M_{1\delta}\cos(\theta_e-\gamma) & -M_{1\delta}\cos(\theta_e) & L_\delta\cos(\theta_e+\gamma)\end{bmatrix}, \tag{6.6}$$

$$\mathbf{M}_1(\theta_e)=\begin{bmatrix}M_{2\delta}\cos(\theta_e) & -M_{3\delta}\cos(\theta_e-\gamma) & -M_{3\delta}\cos(\theta_e+\gamma)\\ -M_{3\delta}\cos(\theta_e) & M_{2\delta}\cos(\theta_e-\gamma) & -M_{3\delta}\cos(\theta_e+\gamma)\\ -M_{3\delta}\cos(\theta_e) & -M_{3\delta}\cos(\theta_e-\gamma) & M_{2\delta}\cos(\theta_e+\gamma)\end{bmatrix}$$

where L_δ is the fundamental component of self-inductance. $M_{1\delta}$ is the fundamental component of the mutual inductance between the two different phases of the same winding set. $M_{2\delta}$ is the fundamental component of the mutual inductance in the same phase of the different winding sets. $M_{3\delta}$ is the fundamental component of the mutual inductance between the different phases in the different winding sets. γ is the electrical angle difference between phases, i.e. $2/3\pi$.

In order to obtain the *dq*-axis inductance matrix, the transformation matrix is used as

$$\mathbf{T}(\theta_e)=\begin{bmatrix}\mathbf{T}_\theta(\theta_e) & \mathbf{0}_{(3\times3)}\\ \mathbf{0}_{(3\times3)} & \mathbf{T}_\theta(\theta_e)\end{bmatrix},\quad \mathbf{T}_\theta(\theta_e)=\begin{bmatrix}\cos(\theta_e) & \cos(\theta_e-\gamma) & \cos(\theta_e+\gamma)\\ -\sin(\theta_e) & -\sin(\theta_e-\gamma) & -\sin(\theta_e+\gamma)\\ 1/2 & 1/2 & 1/2\end{bmatrix} \tag{6.7}$$

where $\mathbf{0}_{(3x3)}$ is the zero matrix with 3x3 dimension. Then, *dq*0-axis voltage equation can be rewritten as

$$\mathbf{v}_{dq0}=R_s\mathbf{i}_{dq0}+\mathbf{L}_{dq0}\frac{d}{dt}\left(\mathbf{i}_{dq0}\right)+\omega_e\mathbf{L}_{dq0}\mathbf{i}_{dq0} \tag{6.8}$$

where $\mathbf{v}_{dq0}$ = [v_{d1} v_{q1} v_{01} v_{d2} v_{q2} v_{02}]$^{\mathrm{T}}$, $\mathbf{i}_{dq0}$ = [i_{d1} i_{q1} i_{01} i_{d2} i_{q2} i_{02}]$^{\mathrm{T}}$. The dc component of the inductance matrix can be transformed to the *dq*0-axis inductance as

$$\mathbf{L}_{dq0}=\mathbf{L}_{dq0\_m}+\mathbf{L}_{dq0\_\delta}(\theta_e). \tag{6.9}$$

The constant component $\mathbf{L}_{dq0\_m}$ can be presented as

$$\mathbf{L}_{dq0\_m}=\begin{bmatrix}\mathbf{L}_{dq0(3\times3)} & \mathbf{M}_{dq0(3\times3)}\\ \mathbf{M}_{dq0(3\times3)} & \mathbf{L}_{dq0(3\times3)}\end{bmatrix},\quad \mathbf{L}_{dq0(3\times3)}=\begin{bmatrix}L_m & 0 & 0\\ 0 & L_m & 0\\ 0 & 0 & L_m\end{bmatrix},\quad \mathbf{M}_{dq0(3\times3)}=\begin{bmatrix}M_m & 0 & 0\\ 0 & M_m & 0\\ 0 & 0 & M_m\end{bmatrix} \tag{6.10}$$

where $L_m = L_s+M_1$ and $M_m = M_2-M_3$. It can be seen that the inductance matrix has only diagonal components due to a symmetrical matrix in the sub-matrix. Also, the *dq*0-axis inductance matrix considering the dc and fundamental components can be transformed as

$$\mathbf{L}_{dq0\_\delta}=\begin{bmatrix}\mathbf{L}_{dq0\_\delta(3\times3)} & \mathbf{M}_{dq0\_\delta(3\times3)}\\ -\mathbf{M}_{dq0\_\delta(3\times3)} & -\mathbf{L}_{dq0\_\delta(3\times3)}\end{bmatrix},$$

$$\mathbf{L}_{dq0\_\delta(3\times3)}=\begin{bmatrix}(\frac{1}{2}L_\delta+M_{1\delta})\cos(3\theta_e) & -(\frac{1}{2}L_\delta+M_{1\delta})\sin(3\theta_e) & L_\delta-M_{1\delta}\\ -(\frac{1}{2}L_\delta+M_{1\delta})\sin(3\theta_e) & -(\frac{1}{2}L_\delta+M_{1\delta})\cos(3\theta_e) & 0\\ \frac{1}{2}L_\delta-\frac{1}{2}M_{1\delta} & 0 & L_m\end{bmatrix}, \tag{6.11}$$

$$\mathbf{M}_{dq0\_\delta(3\times3)}=\begin{bmatrix}\frac{1}{2}(M_{2\delta}+M_{3\delta})\cos(3\theta_e) & -\frac{1}{2}(M_{2\delta}+M_{3\delta})\sin(3\theta_e) & M_{2\delta}+M_{3\delta}\\ -\frac{1}{2}(M_{2\delta}+M_{3\delta})\sin(3\theta_e) & -\frac{1}{2}(M_{2\delta}+M_{3\delta})\cos(3\theta_e) & 0\\ \frac{1}{2}M_{2\delta}-M_{3\delta} & 0 & M_m\end{bmatrix}.$$

The coupling component can be also derived as

$$\mathbf{L}_{dq0'} = \mathbf{L}_{dq0'\_m} + \mathbf{L}_{dq0'\_\delta}(\theta_e). \tag{6.12}$$

The constant component $\mathbf{L}_{dq0'\_m}$ can be presented as

$$\begin{gathered}\mathbf{L}_{dq0'\_m} = \begin{bmatrix} \mathbf{L}_{dq0'(3\times3)} & \mathbf{M}_{dq0'(3\times3)} \\ \mathbf{M}_{dq0'(3\times3)} & \mathbf{L}_{dq0'(3\times3)} \end{bmatrix}, \quad \mathbf{L}_{dq0'(3\times3)} = \begin{bmatrix} 0 & -L_m & 0 \\ L_m & 0 & 0 \\ 0 & 0 & 0 \end{bmatrix}, \\ \mathbf{M}_{dq0'(3\times3)} = \begin{bmatrix} 0 & -M_m & 0 \\ M_m & 0 & 0 \\ 0 & 0 & 0 \end{bmatrix}.\end{gathered} \tag{6.13}$$

The *dq*0-axis inductance matrix considering the dc and fundamental components can be transformed as

$$\begin{gathered}\mathbf{L}_{dq0'\_\delta} = \begin{bmatrix} \mathbf{L}_{dq0'\_\delta(3\times3)} & \mathbf{M}_{dq0'\_\delta(3\times3)} \\ -\mathbf{M}_{dq0'\_\delta(3\times3)} & -\mathbf{L}_{dq0'\_\delta(3\times3)} \end{bmatrix}, \\ \mathbf{L}_{dq0'\_\delta(3\times3)} = \begin{bmatrix} -(L_\delta + 2M_{1\delta})\sin(3\theta_e) & -(L_\delta + 2M_{1\delta})\cos(3\theta_e) & 0 \\ -(L_\delta + 2M_{1\delta})\cos(3\theta_e) & (L_\delta + 2M_{1\delta})\sin(3\theta_e) & L_\delta - M_{1\delta} \\ 0 & 0 & 0 \end{bmatrix}, \\ \mathbf{M}_{dq0'\_\delta(3\times3)} = \begin{bmatrix} -(M_{2\delta} + M_{3\delta})\sin(3\theta_e) & -(M_{2\delta} + M_{3\delta})\cos(3\theta_e) & 0 \\ -(M_{2\delta} + M_{3\delta})\cos(3\theta_e) & (M_{2\delta} + M_{3\delta})\sin(3\theta_e) & M_{2\delta} + M_{3\delta} \\ 0 & 0 & 0 \end{bmatrix}.\end{gathered} \tag{6.14}$$

Unlike the 6/4 VFRM, the coupling component is not only generated by the self-inductance, but also the mutual inductance components between different phases. It can be seen that each sub-matrix has a similar structure to the *dq*0-axis inductance matrix in the 6/4 VFRM [ZHU16a]. The third harmonic inductance components result in the oscillation of the voltage equations in the synchronous *dq*-axis frame. The winding sets should be divided into two for the integrated current control and those harmonics cannot be eliminated from each winding set. Hence, the advantage of 6/7 VFRMs with the external field current control is no longer available for the integrated current control.

6.3.3 Torque Equation with Dual Three-phase Windings

The torque equation can be derived from an energy conversion consideration in terms of an equivalent circuit containing emf, resistance, and inductance components in magnetically linear machines. In general, the instantaneous electromagnetic torque can be represented as [MIL01]

$$T_e = \frac{P}{2}\sum\left(i_x i_y \frac{dL_{xy}}{d\theta_e} \right), \text{ where } x, y = \{a, b, c, a', b', c'\}. \tag{6.15}$$

Then, the electromagnetic torque in the 6/7 VFRM can be derived in the synchronous *dq*0-axis frame as

$$\begin{aligned} T_e = {} & \frac{3}{2}P\left\{ \left(L_\delta - M_{1\delta}\right)\left(i_{01}i_{q1} - i_{02}i_{q2}\right) + \frac{3}{2}M_{3\delta}\left(i_{02}i_{q1} - i_{01}i_{q2}\right) \right\} \\ & + \frac{3}{8}P\left\{ \left(L_\delta - M_{1\delta}\right)\left(i_{d1}{}^2 + i_{q1}{}^2 - i_{d2}{}^2 - i_{q2}{}^2\right)\sin(3\theta_e + 2\beta) \right\}. \end{aligned} \tag{6.16}$$

The average torque is produced by the interaction between the fundamental component of the inductance variation, *q*-axis current and zero sequence current. For each winding set, the self-inductance L_δ and the mutual inductance $M_{1\delta}$ generate the torque in conjunction with the currents. Additionally, the mutual inductance between different phase windings in different winding sets contributes to the average torque, since the flux-linkage of the 6/7 VFRM passes through the adjacent stator pole. In the 6/7 VFRM with the dual three-phase configuration a third harmonic torque ripple is also produced due to the self-inductance and mutual inductance variations. This phenomenon is the same as that with the 6/4 VFRM, and the instantaneous torque ripple is proportional to the square of the current magnitude.

If the magnitudes of the phase currents are the same between two winding sets, the third harmonic torque ripple can be cancelled out due to the opposite polarity of the armature

winding sets. As a result, the torque equation can be simplified as

$$T_e = \frac{3}{2} P\left(2L_\delta - 2M_{1\delta} + 3M_{3\delta}\right) i_0 i_{qs}. \tag{6.17}$$

It should be noted that the summation of the inductance component is the same as the fundamental component of mutual inductance M_{fa} between the field and armature windings in the external field current control method.

6.4 Proposed Control Strategy for 6/7 VFRM

6.4.1 Dual Three-phase Inverter with a Single Voltage Source

The separated field and armature currents in the conventional method can be replaced by the sinusoidal current biased by a dc offset in the integrated current control scheme. The integrated currents can be split into two groups as

$$\begin{cases} i_{a1} = i_f + I_s \cos(\omega_e t + \beta) \\ i_{b1} = i_f + I_s \cos(\omega_e t - \gamma + \beta) \\ i_{c1} = i_f + I_s \cos(\omega_e t + \gamma + \beta) \end{cases} \tag{6.18a}$$

$$\begin{cases} i_{a2} = i_f - I_s \cos(\omega_e t + \beta) \\ i_{b2} = i_f - I_s \cos(\omega_e t - \gamma + \beta) \\ i_{c2} = i_f - I_s \cos(\omega_e t + \gamma + \beta) \end{cases} \tag{6.18b}$$

where I_s is the magnitude of the armature current. Due to the opposite polarities of the emf phasors in the two winding sets, the sinusoidal currents should be injected into the two winding sets with different polarities.

Fig. 6.5 shows the dual three-phase inverter configuration with a single voltage source. One side of each stator winding is connected to each output terminal of the inverter, and the other side of the winding is connected to a neutral point. The key of the proposed method is the

utilisation of the constant zero sequence current as the field current, whilst two three-phase currents are controlled by two inverters. Through the neutral point of the machine, this configuration allows the zero sequence current to flow across the machine windings. Additionally, the neutral point in the dual three-phase configuration can be regarded as that of three-phase current control from the control point of view.

In order to control the *dq*-axis currents of the dual three-phase VFRM, PI current controllers can be utilised as shown in Fig. 6.6. If the third order harmonic components are neglected in the voltage equations, two winding sets are identical. Then, the instantaneous reference phase voltages for individual inverters can be determined from the overall voltage vector as

$$v_{d1}^{*} = v_{d2}^{*} = \frac{1}{2} v_{ds}^{*}, \quad v_{q1}^{*} = v_{q2}^{*} = \frac{1}{2} v_{qs}^{*} \tag{6.19}$$

where v_{d1}^{*}, v_{q1}^{*}, v_{d2}^{*} and v_{q2}^{*} denote the *dq*-axis reference voltages of Inverter 1 and Inverter 2, respectively. v_{ds}^{*} and v_{qs}^{*} are the *dq*-axis reference voltages of the dual three-phase inverter.

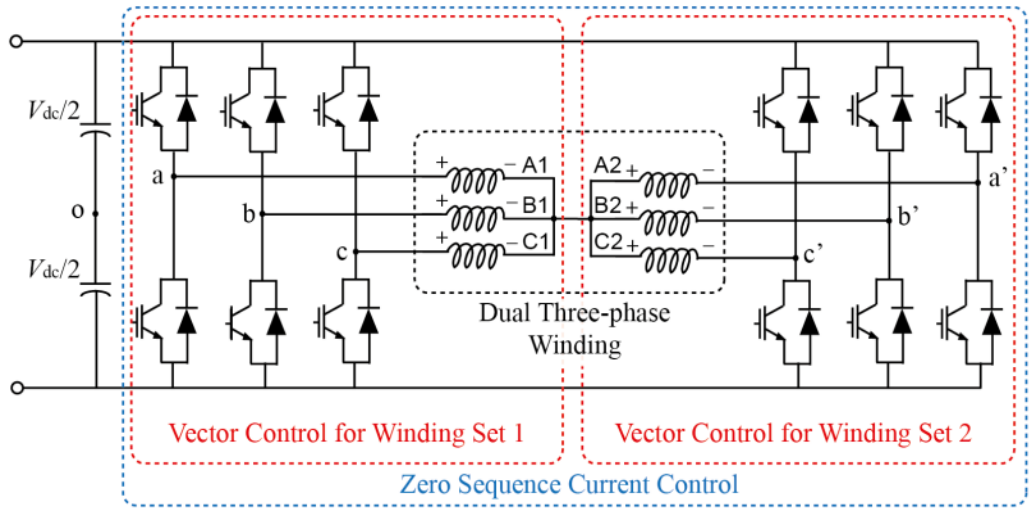

Fig. 6.5. Dual three-phase inverter configuration with a single voltage source.

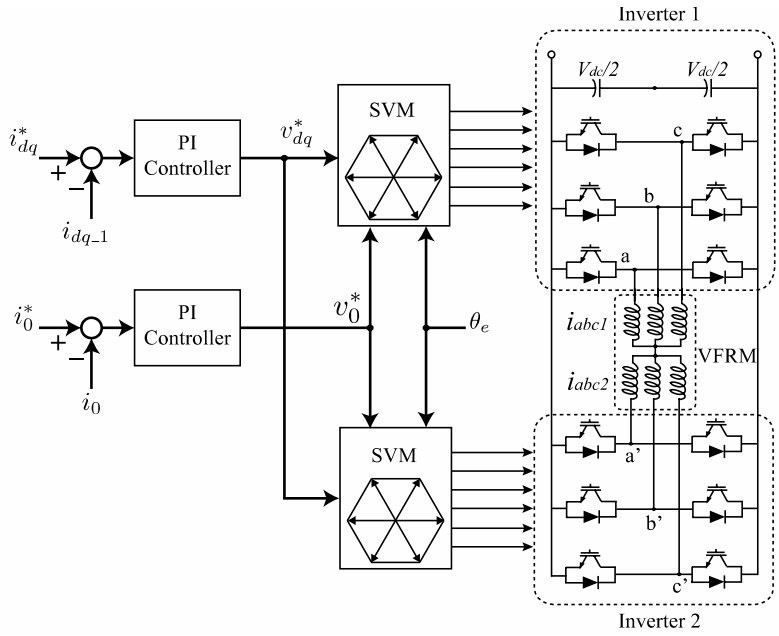

Fig. 6.6. PI current controller for dual three-phase VFRM.

The arbitrary demanded voltages of the dual three-phase inverter can be established by a composition of the decomposed voltages as shown in Fig. 6.7. Each inverter can generate the eight voltage vectors, i.e. six effective vectors in *dq*-axis and two zero vectors in Fig. 6.7(a). By utilising the dual three-phase inverter configuration, the maximum synthesised voltage vectors can be represented as a hexagon shape in Fig. 6.7(b), which has twice the magnitude of voltage compared with the individual inverter. The demanded voltages of each inverter can be synthesised based on the voltage-second method.

In the open winding configuration with a single voltage source, the voltage hexagon needs to be reduced to the inner hexagon (HJLNQS) due to the third harmonic suppression. In the dual three-phase configuration with a single voltage source, the difference of zero sequence voltage between the two inverters can also generate undesirable alternating an zero sequence voltage. However, the alternating components in the zero sequence voltage can be eliminated since each inverter produces the same voltage vector across the neutral point. Hence, the

voltage hexagon can be fully utilised without the third harmonic suppression. The maximum synthesised vectors are classified into 6 vectors, where the voltage vectors are located at the points of G, I, K, M, P, and R, Fig. 6.7(b).

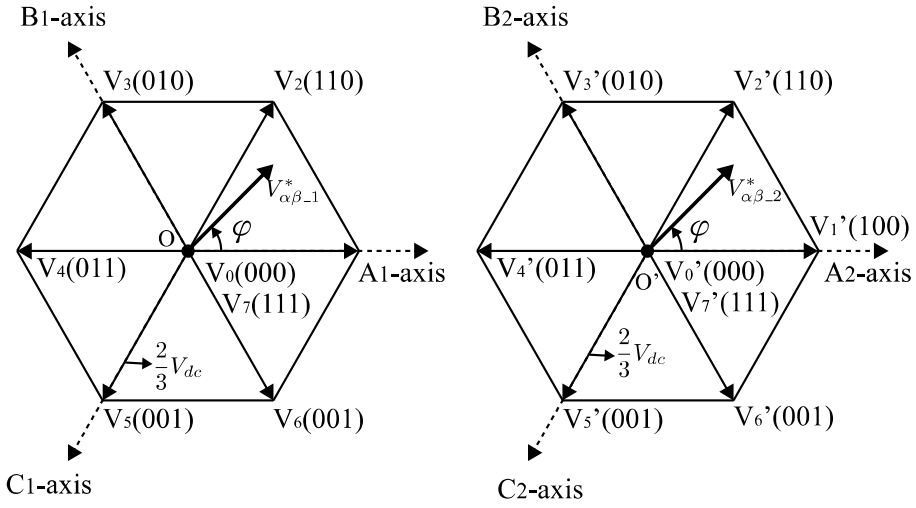

(a) Individual voltage vectors

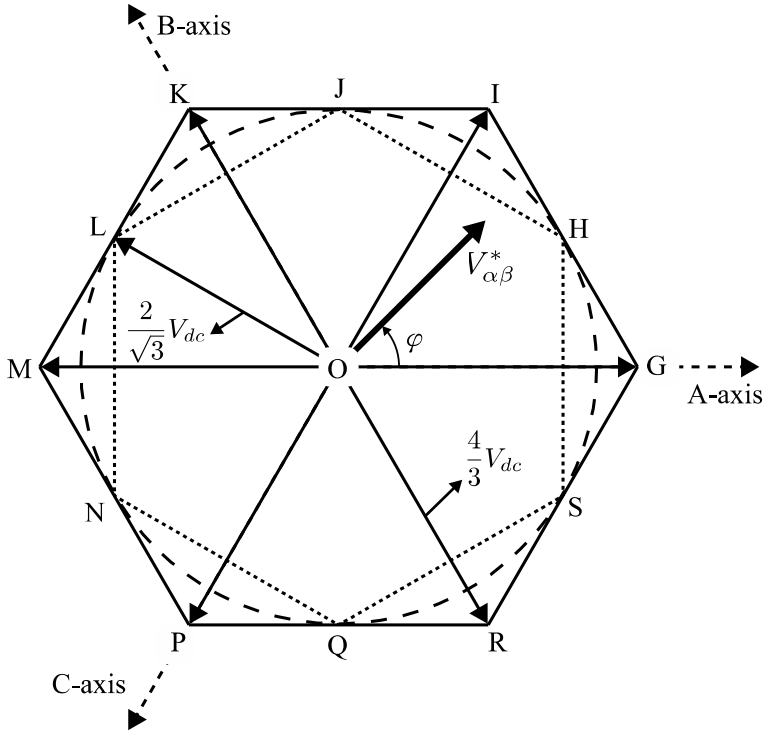

(b) Synthesised voltage vectors

Fig. 6.7. Voltage vectors with dual three-phase inverter configuration.

6.4.2 Zero Sequence Voltage Generation

When the conventional three-phase inverter is utilised with a Y-connected machine, the zero voltage vectors can be achieved by using V_0 or V_7 vectors, which shorts either the upper or lower switches. Hence, the switching on time for the zero voltage vector is evenly divided into V_0 and V_7 based on the SVM scheme. Unlike conventional inverter, the zero vectors are utilised to generate zero sequence current in the dual three-phase inverter. The reference voltage of the zero sequence component can be determined by the PI controller, which minimises the error between the reference and actual zero sequence currents.

In order to generate the zero sequence voltage, the switching on-time can be modified based on the voltage-second equivalent principle. As an example, when the voltage vector is located at $0^{\circ} \le \varphi \le 60^{\circ}$, the on-time of each inverter leg can be calculated as,

$$T_{c1} = \frac{T_0}{2} + \frac{T_z}{2}, \quad T_{b1} = T_{c1} + \frac{T_2}{2}, \quad T_{a1} = T_{b1} + \frac{T_1}{2} \tag{6.20a}$$

$$T_{c2} = \frac{T_0}{2} - \frac{T_z}{2}, \quad T_{b2} = T_{c2} + \frac{T_2}{2}, \quad T_{a2} = T_{b2} + \frac{T_1}{2} \tag{6.20b}$$

where T_{a1}, T_{b1}, T_{c1} are the on-time of each leg in Inverter 1, and T_{a2}, T_{b2}, T_{c2} in Inverter 2, respectively. T_z is the reference voltage of the zero sequence vector controlled by the PI controller. Based on the zero vector modification method, the zero sequence reference voltages, $V^*_{0\_1}$ and $V^*_{0\_2}$ can be produced from Inverter 1 and Inverter 2.

When the reference voltage vector of the dual three-phase inverter is placed at $0^{\circ} \le \varphi \le 60^{\circ}$ in Fig. 6.7(b), the voltage vectors and the corresponding switching on-time are shown in Fig. 6.8 based on the symmetrical SVM technique. In the switching on-time diagram, it can be seen that the duties for the *dq*-axis voltage generation, T_1 and T_2, are maintained at the same

duration. On the right side of the figure, the different duties of zero vector between two inverters are presented. Therefore, the zero vector generation does not affect the effective voltage vectors unless the current controllers are saturated since zero voltage vectors are always placed on the origin in the *dq*-axis space vector diagram.

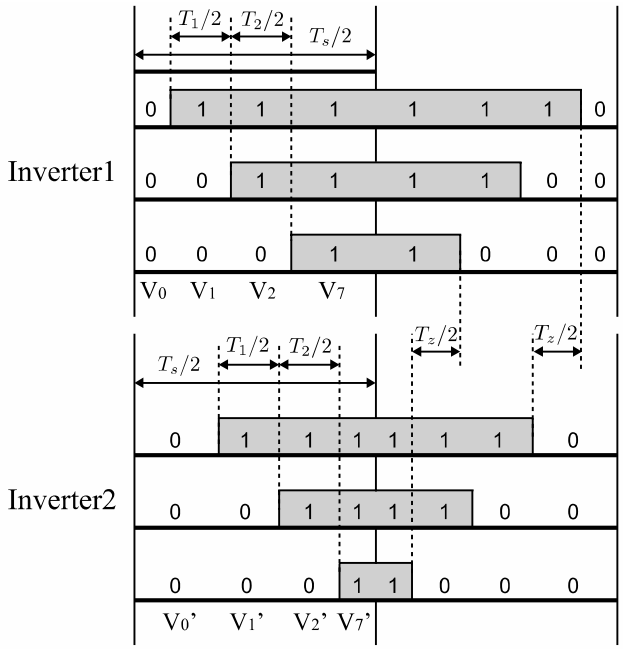

Fig. 6.8. Switching on-time of inverters and corresponding voltage vectors.

6.5 Proposed Integrated Current Control Strategy

Ideally, when the third harmonic components in the voltage equations are ignored, the PI current controller presented in Fig. 6.6 can be implemented for the dual three-phase VFRM. However, it is not able to compensate for the inherent asymmetries such as the third harmonic components and practical mismatch between the two winding sets. As a result, the two winding sets of three-phase currents can have different amplitudes with respect to the operating conditions due to the asymmetries in the stator winding sets and applied voltages [BOJ03]. To regulate the *dq0*-axis currents in the presence of the asymmetry in the VFRM, a

dual current controller scheme is implemented for dual three-phase VFRM drives. The overall control system of the proposed method is shown in Fig. 6.9 with the dual three-phase inverter. The ac components of each winding set current are transformed into *dq*-axis currents based on the Park's transformation, whilst the dc component of the phase currents are transformed to zero sequence current. The separate current controllers facilitate the vector control scheme for the VFRM which can control the electromagnetic torque and the flux-linkage independently.

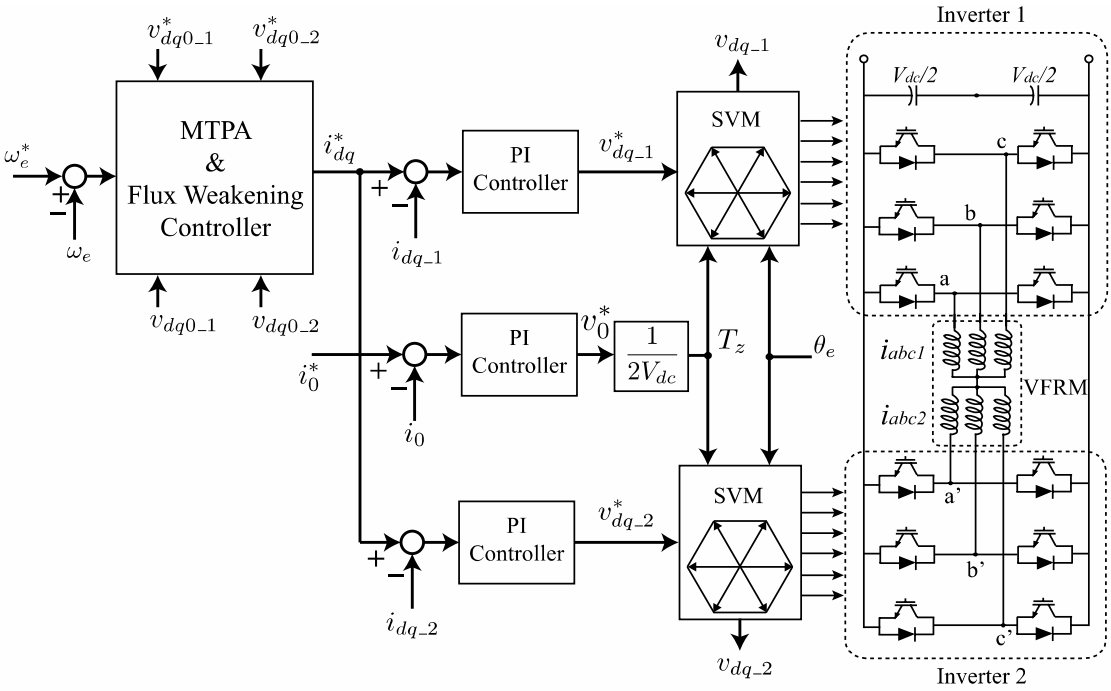

Fig. 6.9. Proposed control method block diagram using dual current controller for dual three-phase VFRM.

6.5.1 Constant Torque Operation

In general, the phase winding resistance is proportional to the winding length, and it is inversely proportional to the cross section area of the winding. Since the integrated current control strategy allows the integrated winding, which connects the field and armature windings in parallel, the cross section area of the winding can be doubled compared with that

of the conventional external field current control method. As a result of the increased cross section area, the copper loss is reduced and resistive voltage drop in phase windings is also reduced.

Meanwhile, the torque generation is only related to the winding inductance component rather than the winding resistance. The number of turns per phase is maintained as the same value between the external field current and the integrated current control methods. Hence, if the same current is applied to VFRMs, the torque generation is the same between the two methods, although the winding sets are divided into dual three-phase VFRMs. In other words, the mutual inductance between the field and armature windings in the external field current control is the same as the summation of inductance components in the integrated current control method, i.e. $M_{fa} = 2L_{\delta} - 2M_{1\delta} + 3M_{3\delta}$.

According to the derived torque equation for VFRM in (6.2) and (6.17), the *d*-axis current does not contribute to the torque generation, which is the same as SPM machines. Hence, the *d*-axis reference current is set to zero, whilst the *q*-axis reference current is determined by a PI speed controller in the constant torque region. For the copper loss minimisation, the field reference current is set to 0.707 times of *dq*-axis current magnitude, which has the same rms current.

Since the inductance components are maintained between the two methods, the coupling components are also kept at the same operating point except for the resistive voltage drop [ZHU15a]. The *d*-axis voltage will be the same since it only contains the coupling component due to the zero *d*-axis current under base speed operation. The reduced *q*-axis resistive voltage

drop in the proposed method will lead to less *q*-axis voltage demand compared with that of the conventional method. Although the proposed method requires the zero voltage vector generation, which reduces the voltage utilisation ratio of the *dq*-axis voltages, the proposed method requires less voltage due to the reduced resistance [ZHU16a].

6.5.2 Flux Weakening Operation

For the flux weakening operation, an anti-windup method is implemented in synchronous *dq*-axis frame [KWO06]. This method produces negative *d*-axis current in order to avoid saturation of the current controllers. The negative *d*-axis current is generated by the difference between the reference and output of the SVM block as

$$i_{ds}^{*} = -\rho \cdot LPF\left(\sqrt{\left(v_{ds}^{*} - v_{ds}\right)^{2} + \left(v_{qs}^{*} - v_{qs}\right)^{2} + \left(v_{0}^{*} - v_{0}\right)^{2}} \right) \tag{6.21}$$

where ρ is a positive gain for adjusting the torque ripple and transient response, and *LPF* is the first-order low pass filter. Additionally, the *q*-axis current should be changed depending on the *d*-axis current so that the phase current is generated under current limitation. When the maximum phase current is larger than the field current, VFRMs can operate in flux weakening region III, which is known as a constant power speed region (CPSR) [KWO07]. In order to maximise the output power, the *q*-axis voltage v_q should be controlled to zero so that the *dq*-axis current can be placed along the MTPV line [LIU12].

6.6 Simulation and Experimental Validations

For the validation of the proposed scheme, dynamic simulation of the prototype 6/7 VFRM is performed in MATLAB/*Simulink*. The dynamic model is developed based upon the derived

voltage and torque equations in the VFRM model. The dc link voltage is set to 48 V in both control methods, and a 10 kHz switching frequency is applied with SVM technique. The prototype machine parameters are listed in Table 6.1 for both the external current control and dual three-phase configurations. In experiments, the control schemes are implemented on a dSPACE platform. In addition, the output torque is measured by a torque transducer, which is installed between the prototype machine and a dc load machine. The dq-axis current limitation is 2.83 A, and the field current is set to 2 A so that the rms current is the same. The experiments are performed up to 1,500 rpm due to a speed limitation of the dc machine.

TABLE 6.1
MACHINE PARAMETERS

Machine parameters		**Value**	
Number of phases		3	
Number of rotor poles (P)		7	
Number of turns per phase for armature winding		288	
Number of turns for field winding		288	
Air gap		0.5 mm	
Parameters with the external field current control			
Winding resistance (R)		2.7 Ω	
Self-inductance (L)		14.6 mH	
Mutual inductance (M_{fa})		8.69 mH	
Parameters with the dual three-phase configuration			
Winding resistance (R_s)		0.69 Ω	
L_s	5.64 mH	L_δ	3.16 mH
M_1	0.91 mH	$M_{1\delta}$	0.66 mH
M_2	0.79 mH	$M_{2\delta}$	0 mH
M_3	1.19 mH	$M_{3\delta}$	1.23 mH

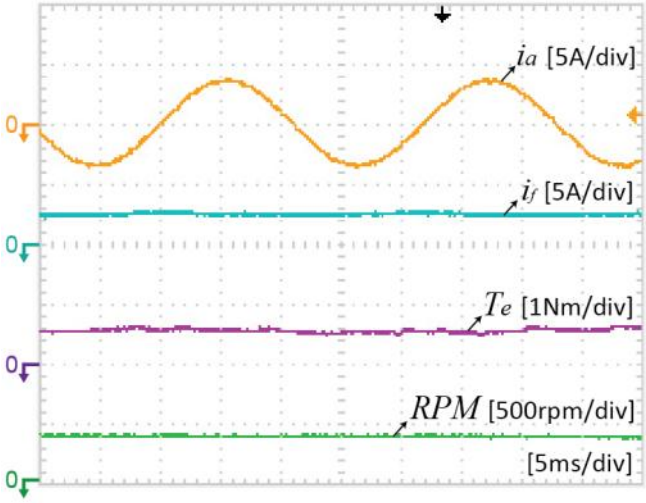

(a) External field current control (copper loss ≈ 64.8 W)

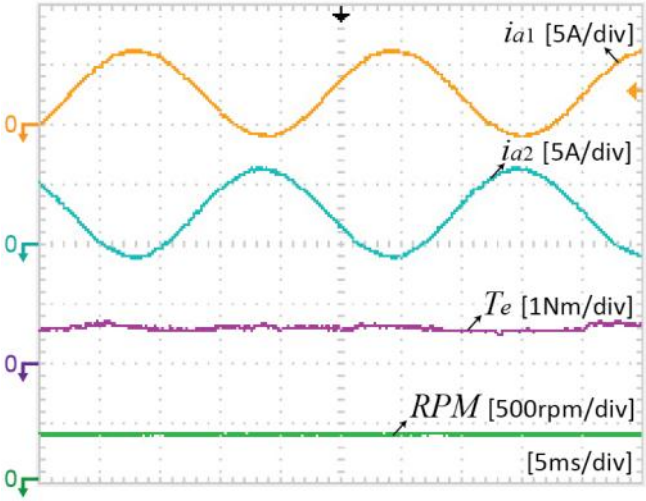

(b) Proposed integrated control (copper loss ≈ 32.4 W)

Fig. 6.10. Experimental results of phase current, field current, torque and machine speed at 400 rpm, i_f = 2 A, i_q = 2.83 A.

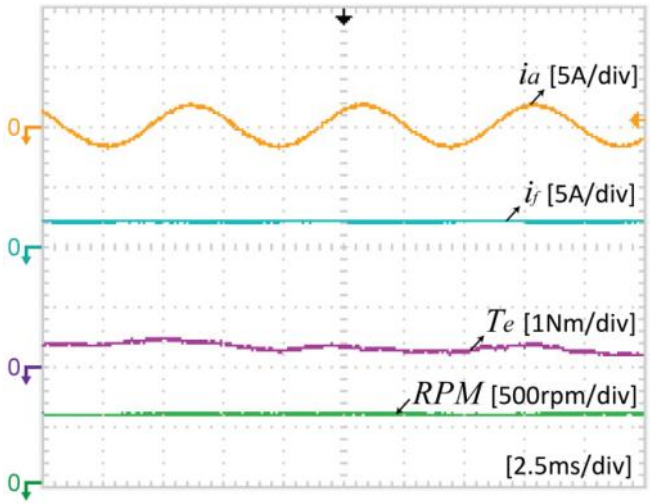

(a) External field current control at i_f = 2 A, i_d = -0.66 A, i_q = 1.64 A

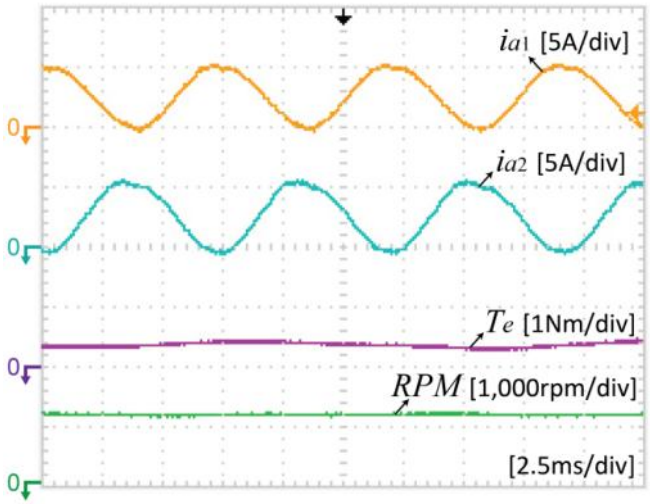

(b) Proposed integrated control at i_f = 2 A, i_d = -0.59 A, i_q = 2.56 A

Fig. 6.11. Experimental results of phase current, field current, torque and machine speed in the flux weakening region II at 1,200 rpm.

Fig. 6.10 and Fig. 6.11 show the experimental results of the phase current, field current, measured torque and machine speed in both conventional and proposed methods. In the constant torque region, Fig. 6.10, the machine speed is maintained at 400 rpm, and the load torque is set to around 0.5 Nm. The *q*-axis current is set to 2.83 A, whilst the field current is 2 A for the maximum efficiency operation. In the conventional method, the field and phase

currents are injected separately into the machine. The proposed method produces the sinusoidal current biased by a dc offset. At the same operating condition, the proposed method can reduce the copper loss by half compared to the conventional method. The waveforms in the flux weakening operation are shown in Fig. 6.11. The machine speed is set to 1,200 rpm. Since the proposed method can operate over an extended speed range, it can produce larger torque compared with the conventional method. Additionally, when the machine operates at 1,200 rpm, it is in the flux weakening region II. Hence, the current magnitude is reduced in both control methods for the MTPV operation.

In order to demonstrate the dynamic performance, Fig. 6.12 shows the machine speed and *dq*-axis currents in both control methods. The reference speed 1,200 rpm is applied at 0.5 s as a step input, whilst the load resistor is maintained as a constant. It should be noted that the target speed of the conventional method is set to 800 rpm since it takes more than 10 s to reach 1,200 rpm. The figures show a good dynamic performance from the constant torque to the flux weakening operations including region I and II. Additionally, more ripple in the *dq*-axis currents can be observed due to the third harmonic components in the dual three-phase VFRM.

The experiment is carried out to investigate the transient performance in the constant torque region when the load torque is changed from 0.2 Nm to 0.5 Nm. Fig. 6.13 shows the transient responses of the output torque, *q*-axis current, speed response and phase current. When the load torque is applied, the speed controller generates more *q*-axis current for the speed regulation. The machine speed drop is around 7 rpm, and the speed is recovered within

2 seconds due to the large inertia of the dc load machine. In both cases, a similar transient response can be observed. In addition, the difference between the two methods is also shown in the phase current waveforms with/without the offset current.

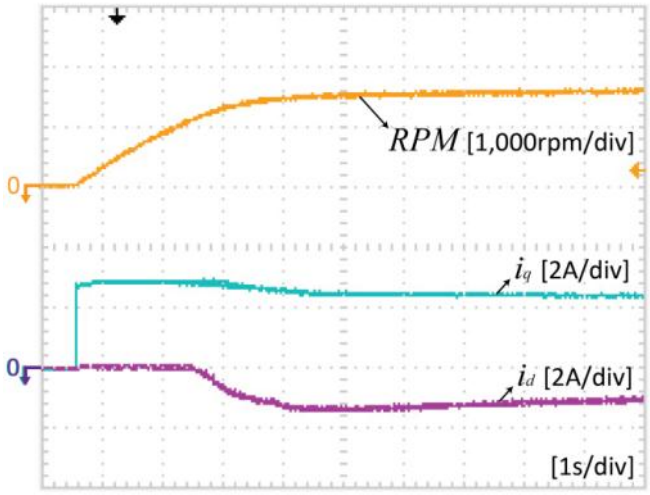

(a) Conventional method

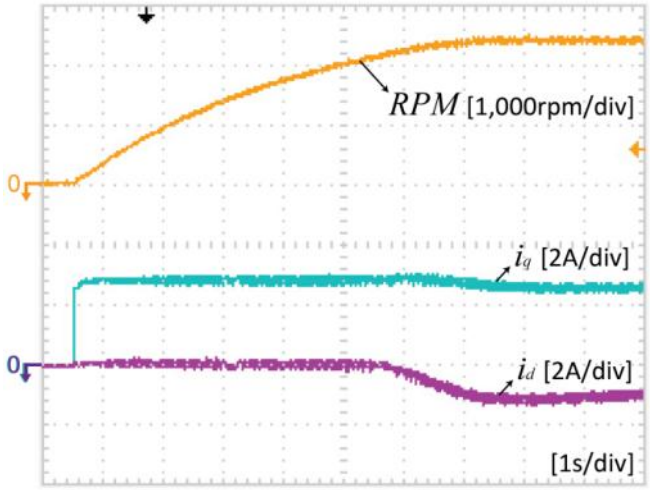

(b) Proposed method

Fig. 6.12. Experimental results of dynamic performance from standstill at V_{dc} = 48 V, i_f = 2 A, I_{max} = 2.83 A.

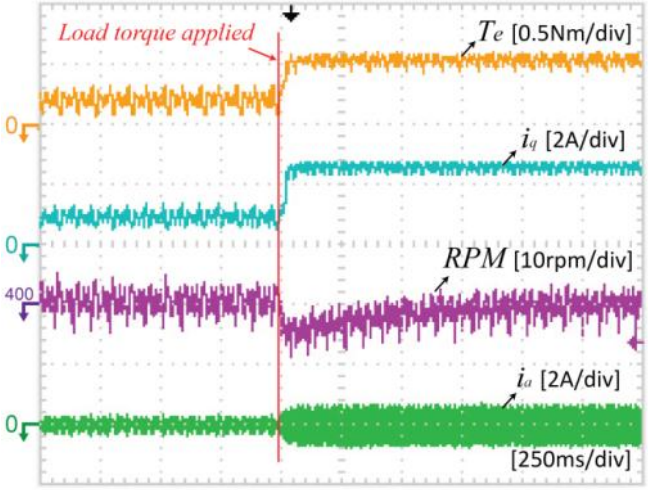

(a) Conventional method

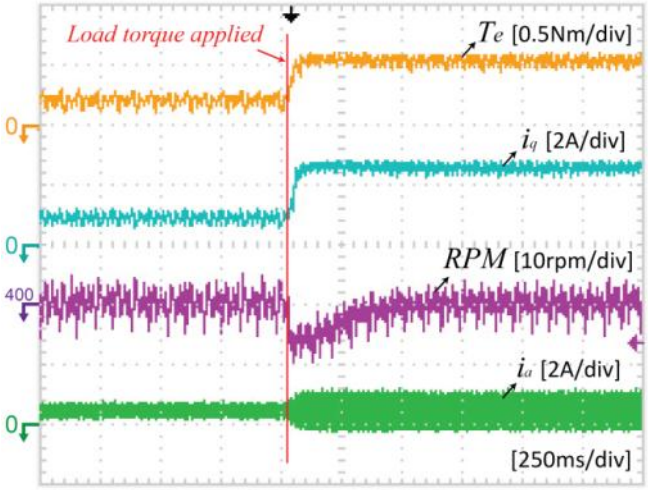

(b) Proposed method

Fig. 6.13. Experimental results of transient torque response at 400rpm.

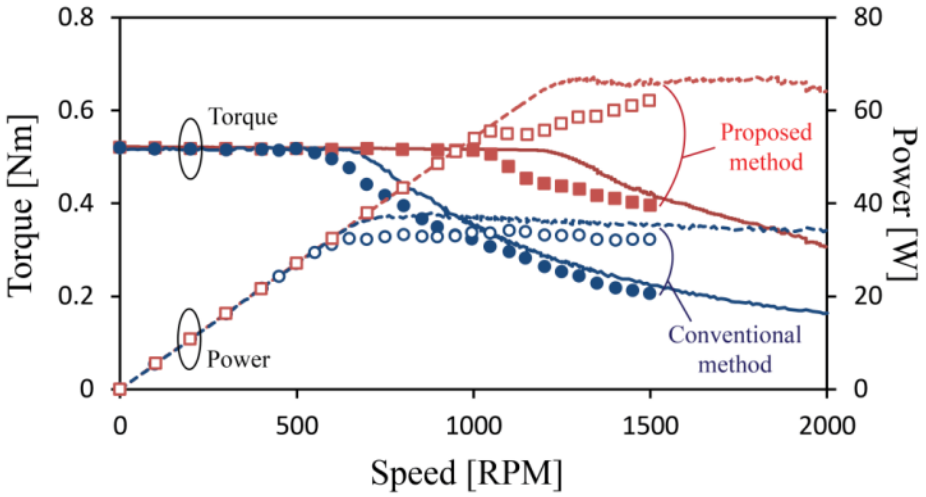

(a) Torque-speed curve

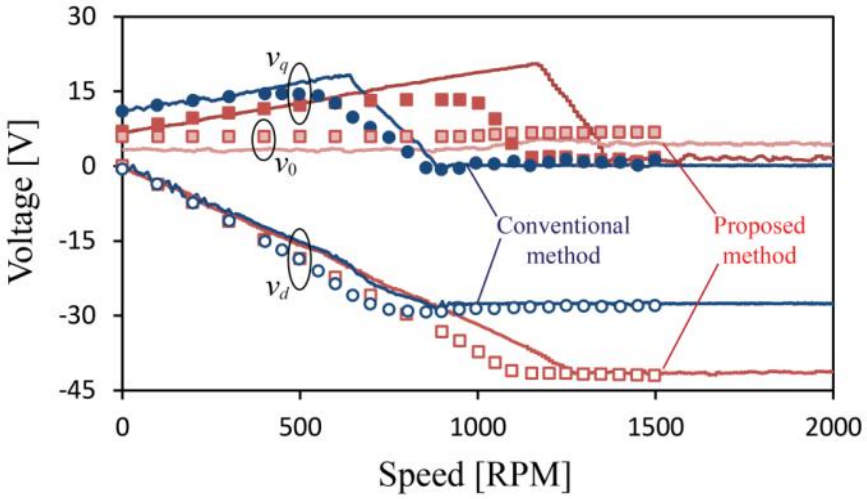

(b) Voltage-speed curve

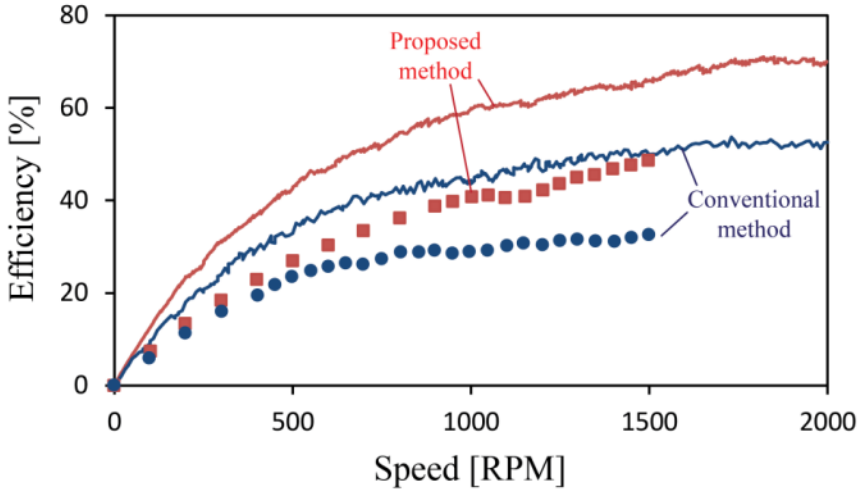

(c) Efficiency-speed curve

Fig. 6.14. Characteristic curves with/without the proposed method at V_{dc} = 48 V, i_f = 2 A, I_{max} = 2.83 A.

The simulation and experimental results are shown with/without the proposed method in the constant torque and flux weakening regions in Fig. 6.14. The experiments are performed at every 100 rpm in the constant torque region, and at 50 rpm in the flux weakening region.

In the constant torque region, the maximum torque is the same, whilst the base speed is extended from 500 rpm to 1,000 rpm in the proposed method as shown in Fig. 6.14(a). The extended speed mainly results from the dual inverter configuration. It should be noted that although the zero sequence voltage generation reduces dc link voltage utilisation, the reduced resistance delivers the increased voltage utilisation to the inverter. In the dynamic simulations, the onset speeds of the flux weakening operation are 640 rpm in the conventional method and 1,210 rpm in the proposed method. The differences between the simulation and experimental results are mainly caused by the mechanical loss of the test rig and the iron loss of the machine, which are not considered in the simulation.

The VFRM exhibits the third harmonic components in the voltage equations when the proposed method is applied in the dual three-phase configuration. It results in the condition that the peak voltage of the voltage magnitude can reach the hexagon voltage. Then, the flux weakening controller will be activated to prevent the saturation of the current controllers. The influence of the third harmonic components will be reflected to the onset speed of the flux weakening operation. From the derived voltage equations, it can be assumed that the third harmonic components are neglected, whilst the constant components are only considered in the synchronous reference frame. When the third harmonic components are neglected in the voltage equations, the constant torque region in the dynamic simulation is extended to 1,355

rpm. In other words, the third harmonic components lead to a base speed reduction of 145 rpm.

Fig. 6.14(b) shows the *dq*0-axis voltage characteristic curves. The voltages are obtained from the output of the SVM block. Under the constant torque region, the *q*-axis voltage difference can be observed due to the different resistive voltage drop between the two methods in both simulation and experiments. Due to i_d = 0 A control, the *d*-axis voltage does not contain the resistive voltage drop. Thus, the *d*-axis voltage curves are similar in the constant torque region. It is worth mentioning that v_q is controlled at zero, whilst v_d exhibits the maximum voltage in the flux weakening operation. This is for the achievement of the flux weakening region II under the given current condition.

Due to the integrated winding configuration, the proposed method can reduce the winding resistance. Consequently, the copper loss is also reduced, which leads to an efficiency improvement in the proposed method as shown in Fig. 6.14(c). The efficiency difference between the simulation and experiments can be explained by the mechanical loss and iron loss, which are not considered in the simulation.

6.7 Conclusion

This chapter proposes an integrated field and armature current control strategy for a dual three-phase VFRM. The integrated current control method allows the integrated winding, which reduces the winding resistance by half. Hence, the copper loss can be halved at the same operating condition compared with that of the conventional external field current control.

To generate the sinusoidal current biased by a dc offset, the zero vector modification technique is proposed by using a dual three-phase inverter configuration. For the vector control of the VFRM, the voltage and torque equations are derived in synchronous *dq*-axis frame, and a mathematical model is utilised for dynamic modeling with the aid of MATLAB/*Simulink*. The effectiveness of the proposed integrated current control is validated by experimental results on the prototype machine.

CHAPTER 7

FURTHER INVESTIGATIONS OF TORQUE RIPPLE REDUCTION FOR VARIABLE FLUX RELUCTANCE MACHINES

7.1 Introduction

The torque ripple reduction scheme based on the harmonic current injection has been introduced in Chapter 4. As an extended study of the smooth torque control for the 6/4 VFRM, it will be extended and applied to the 6/7 VFRM for the same purpose in this chapter. For further investigation of the torque production, the instantaneous torque equation is firstly derived for the 6/7 VFRM. By using Fourier series, all of the harmonic components in the inductances and currents are considered in the derived torque equation. Due to the opposite polarity of the armature windings, the even order harmonic components are cancelled out. It results in the elimination of the third harmonic torque ripple, whilst a multiple of the sixth harmonic torque ripple exists. The torque waveforms predicted by the derived torque equation are compared with the calculated results by FEA. Additionally, the derived torque equation is verified with the torque waveforms measured by a torque transducer.

The integrated current control strategy is introduced and implemented for the VFRMs in Chapter 5 and Chapter 6. The torque ripple reduction scheme is accomplished by the harmonic

field current injection in the external field current control. In the same manner, the torque ripple reduction scheme can be applied to the integrated current control scheme. The field current in the external field excitation control is replaced by the zero sequence current in the integrated current control scheme. As the torque ripple reduction method is applied to the external field current control scheme, it can be also implemented in the integrated current control with zero sequence current harmonic injection. When the VFRMs are driven in the integrated current control scheme, the torque production is the same as that with the external current control method as discussed in Chapter 5 and Chapter 6. The experimental results are given by measuring the torque waveforms with/without the harmonic injection methods [LEE16b].

7.2 Torque Ripple Reduction for 6/7 VFRM in External Field Current Control

7.2.1 6/7 Variable Flux Reluctance Machine

Fig. 7.1 shows 6/7 VFRM cross section and winding configurations of the field and armature, in which the rotor pole number of the VFRMs is equivalent to the rotor pole pair number of a conventional synchronous machine. VFRMs have doubly fed doubly salient configuration so that the rotor structure is simple and robust. Since the field and armature windings are identically wound on the stator, the symmetrical flux-linkage and back emf can be obtained. Each armature winding is composed of two windings in series connection, e.g. coils A1 and A2 for Phase A. The half of the armature windings are connected in different

polarity, whilst all of the field windings are connected in the same polarity. In the 6/5 and 6/7 VFRMs the armature windings in each phase are connected in opposite polarity different from the 6/4 VFRM having the same polarity in the armature windings. The opposite connection of the armature windings leads to bipolar phase flux-linkage waveforms because the dc component is cancelled out between two armature windings in each phase [LIU13a]. This feature affects the self- and mutual inductances, and also torque production, as will be discussed in the following section.

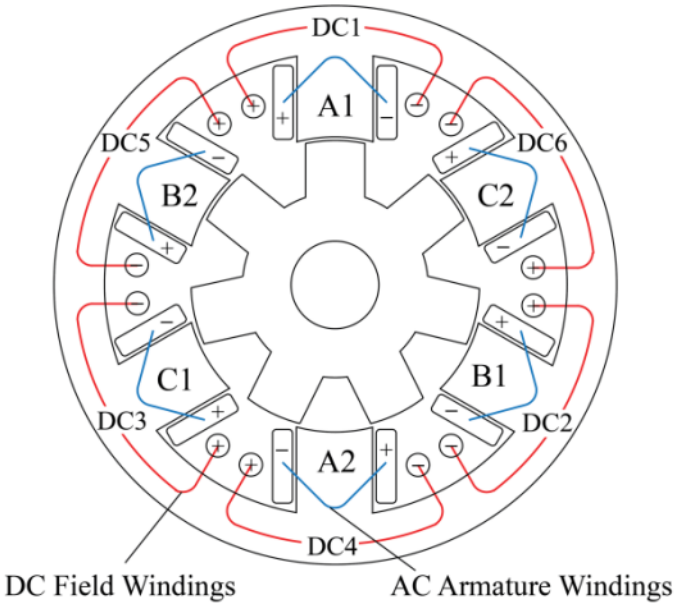

Fig. 7.1. Cross section and winding configurations of 6/7 VFRM (The rotor pole is aligned with phase A, i.e., $\theta_e = 0$).

The abc-axis self-inductance of the armature windings are shown in Fig. 7.2(a) with respect to the electrical rotor angle. Due to the opposite polarity of armature windings in each phase, the fundamental component of self-inductance is cancelled out. In the 6/4 VFRM, the fundamental component of the self-inductance in the armature windings is a main source of the third harmonic torque ripple. Hence, compared with the 6/4 VFRM, it can be expected that the significant third harmonic torque ripple can be eliminated due to the absence of the

fundamental self-inductance in the 6/5 and 6/7 VFRMs. Additionally, from the corresponding harmonic analysis, the odd order harmonics in the armature windings are also cancelled out as shown in Fig. 7.2(b).

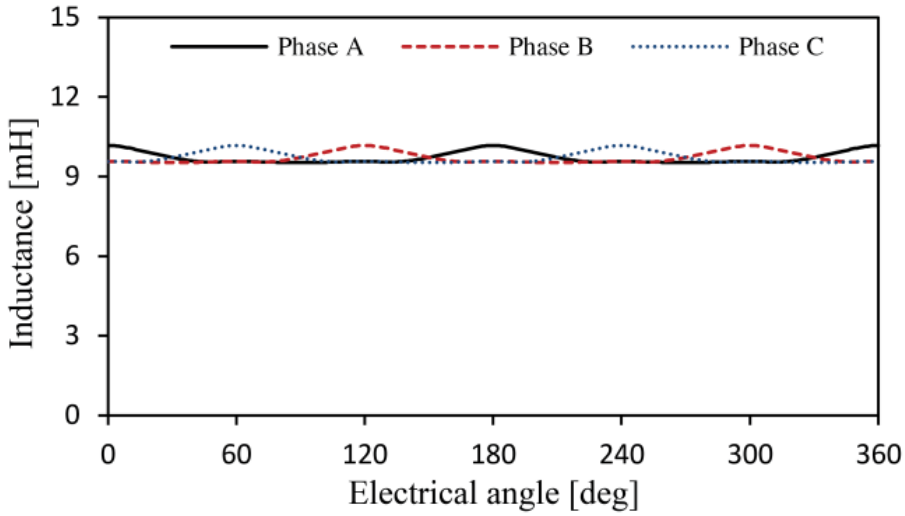

(a) *abc*-axis self-inductance waveforms

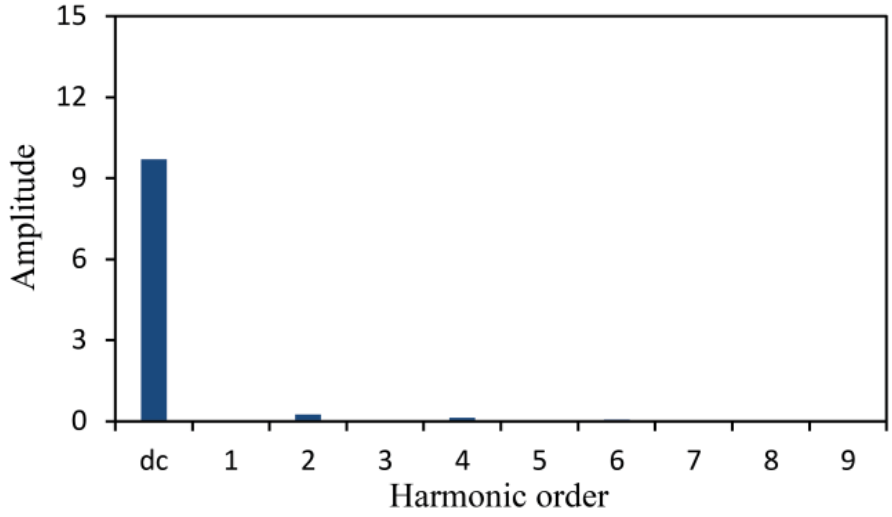

(b) Corresponding harmonics

Fig. 7.2. Self-inductance of the armature windings in 6/7 VFRM.

Different from the 6/4 VFRM, the mutual inductances between the armature windings exist and cannot be neglected since the flux passes through the adjacent stator poles in the 6/5 and 6/7 VFRMs. The dc component of the mutual inductance between the armature windings is given by the half of self-inductance except for the leakage inductance. It is because each phase

winding is separated spatially by $2/3\pi$ and $\cos(2/3\pi) = -1/2$, which is the same as the PM machines. The mutual inductance waveforms and corresponding harmonic analysis are presented in Fig. 7.3. Similar with the self-inductance of the phase windings, the odd order harmonic components are cancelled due to the opposite connection of the armature windings.

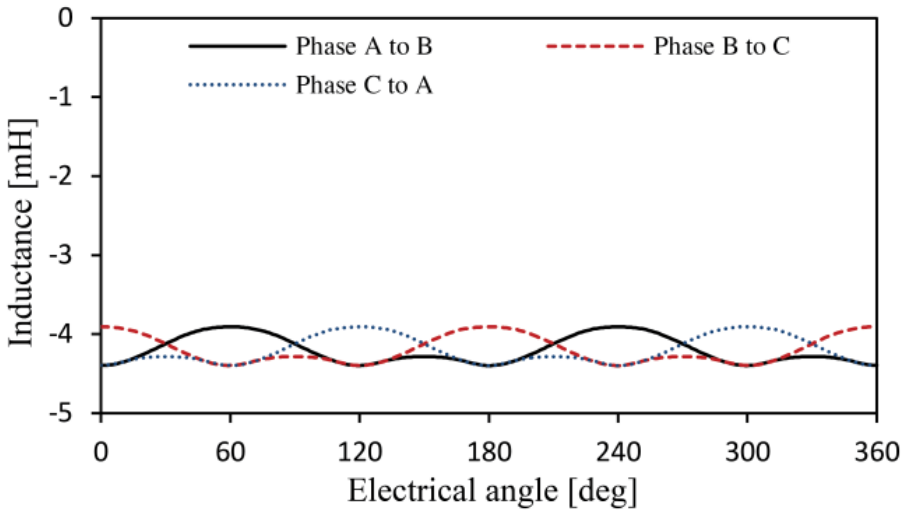

(a) *abc*-axis mutual inductance waveforms

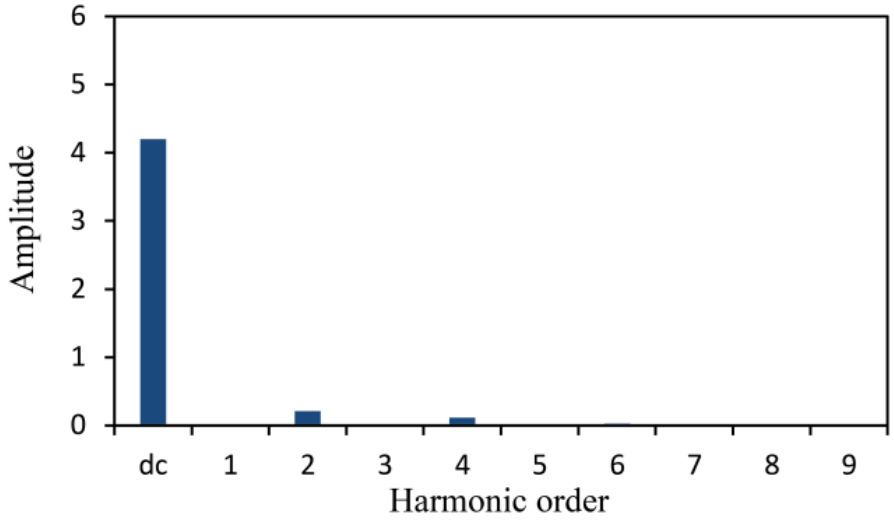

(b) Corresponding harmonics

Fig. 7.3. Mutual inductance between the armature windings in 6/7 VFRM

In the VFRMs, all the field windings are connected with the same polarity. As discussed in the self-inductance of the armature windings, if each winding in the same phase is connected with the same polarity, the fundamental component of the self-inductance is doubled rather

than cancelled out each other. For example, the connection of DC1 and DC4 produces significant fundamental component of the self-inductance. However, since the field windings from DC1 to DC6 are connected in series, the harmonics including the fundamental component are cancelled out except for a multiple of the sixth harmonics shown in Fig. 7.4.

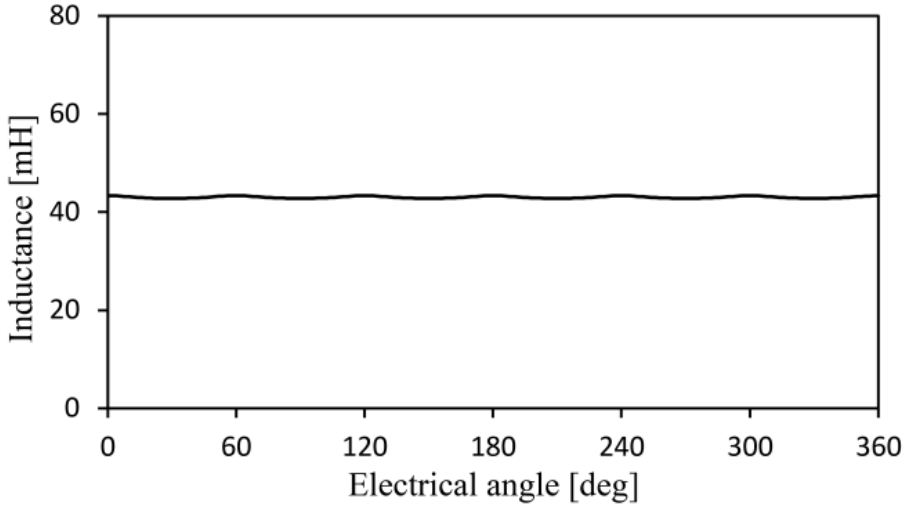

(a) *abc*-axis self-inductance waveforms

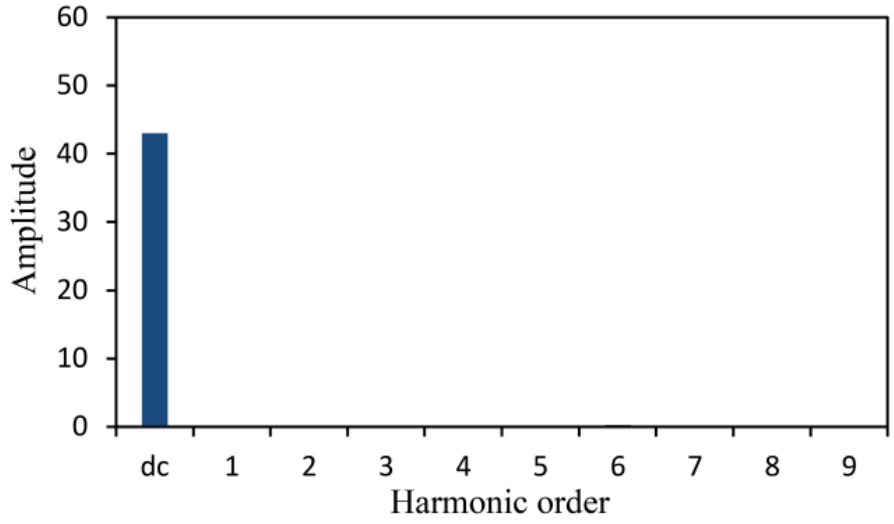

(b) Corresponding harmonics

Fig. 7.4. Self-inductance of the field windings in 6/7 VFRM.

Due to the same polarity in the field windings and the opposite polarity in the armature windings, the mutual inductance between the field and armature windings has significant fundamental component, whilst the even order harmonic components are cancelled. These

mutual inductance components will be reflected to the back emf when the field current is excited. Compared with the 6/4 VFRM, the mutual inductance waveform is more sinusoidal and symmetrical due to the cancellation of the even order harmonic components as shown in Fig. 7.5. Therefore, it can be also expected that the torque ripple will be further reduced resulted from the back emf harmonics.

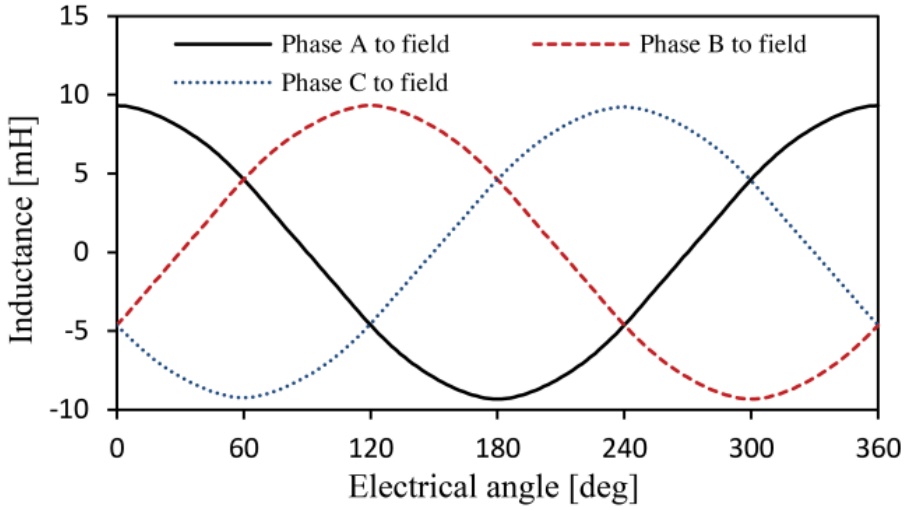

(a) *abc*-axis mutual inductance waveforms

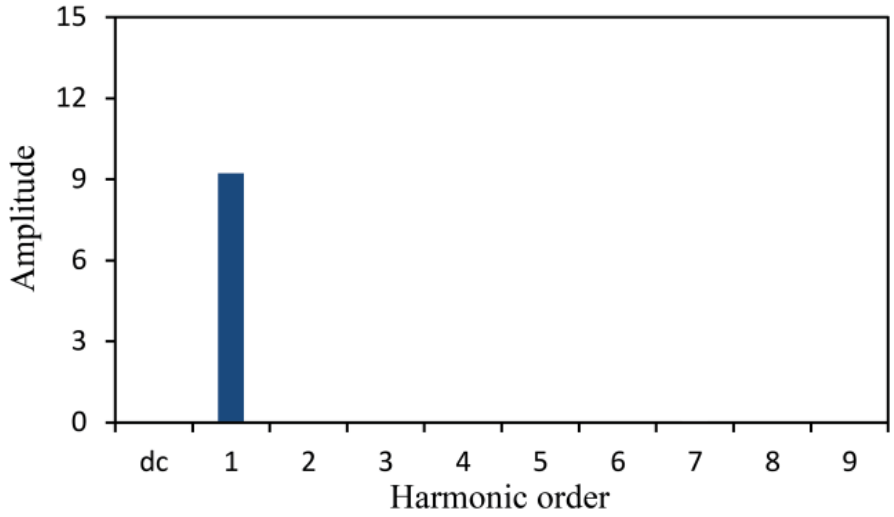

(b) Corresponding harmonics

Fig. 7.5. Mutual inductance between the field and armature windings in 6/7 VFRM.

7.2.2 Instantaneous Torque Equation of 6/7 VFRM

7.2.2.1 Under an Arbitrary Armature Current Excitation

From the principle of the torque production, the instantaneous torque equation of the VFRMs can be derived. In order to obtain the contribution of the inductances to the torque generation, some assumptions are given in this chapter. Firstly, the linear analysis of torque production is considered, in which magnetic saturation does not occur and the stator and rotor has infinite permeability on the iron. Although the saturation region of the VFRMs is utilised in a practical operation, the contribution of the inductances to the torque generation can give a better understanding. Secondly, three-phase windings are in a balanced condition, in which each inductance has the same magnitude and 120° phase shift.

Based on Fourier series, the self-inductance of the field and armature windings can be presented as a function of rotor position [LIU12b]

$$L_f(\theta_e) = L_0^f + \sum_{n=1}^{\infty}\left(L_n^f \cos(n\theta_e + \alpha_n^f)\right) \tag{7.1}$$

$$L_a(\theta_e) = L_0^a + \sum_{n=1}^{\infty}\left(L_n^a \cos(n\theta_e + \alpha_n^a)\right) \tag{7.2}$$

where n is the harmonic order, L_0^f, L_0^a are the dc components of the self-inductance, L_n^f, L_n^a and α_n^f, α_n^a are the amplitudes and the phase shifts at the nth harmonic of self-inductances in the field and armature windings, respectively. θ_e is the electrical rotor angle of the VFRM.

The mutual inductance of the field and armature windings is represented as

$$M_{fa}(\theta_e) = M_0^f + \sum_{n=1}^{\infty}\left(M_n^f \cos(n\theta_e + \gamma_n^f)\right) \tag{7.3}$$

where M_0^f is the dc component, M_n^f and γ_n^f is the amplitude and the phase shift of the mutual inductance between the armature windings at the nth harmonic, respectively.

Additionally, different from the 6/4 VFRM, the 6/7 VFRM has the mutual inductance of the armature windings as

$$M_{ab}(\theta_e) = M_0^a + \sum_{n=1}^{\infty}\left(M_n^a \cos(n\theta_e + \gamma_n^a)\right) \tag{7.4}$$

where M_0^a is the dc component, M_n^a and γ_n^a is the amplitude and the phase shift of the mutual inductance between the armature windings at the *n*th harmonic, respectively. In the same manner, the Phase A current is presented as Fourier series

$$i_{as}(\theta_e) = -\sum_{m=1}^{\infty}\left(I_m \sin(m\theta_e + \beta_m)\right) \tag{7.5}$$

where m is the harmonic order, I_m is the magnitude and β_m is the advanced phase angle of the *m*th harmonic, respectively.

Based on the general torque production, the instantaneous torque of the 6/7 VFRM can be represented by the field and phase currents and the self- and mutual inductances as

$$\begin{aligned} T_e = {} & \frac{P}{2}\left(i_{as}^2\frac{dL_a}{d\theta_e} + i_{bs}^2\frac{dL_b}{d\theta_e} + i_{cs}^2\frac{dL_c}{d\theta_e}\right) + P\left(i_{as}i_{bs}\frac{dM_{ab}}{d\theta_e} + i_{bs}i_{cs}\frac{dM_{bc}}{d\theta_e} + i_{cs}i_{as}\frac{dM_{ca}}{d\theta_e}\right) \\ & + \frac{P}{2}\left(i_f^2\frac{dL_f}{d\theta_e}\right) + P\left(i_{as}i_f\frac{dM_{fa}}{d\theta_e} + i_{bs}i_f\frac{dM_{fb}}{d\theta_e} + i_{cs}i_f\frac{dM_{fc}}{d\theta_e}\right) \end{aligned} \tag{7.6}$$

where P is the number of poles in the VFRMs. i_{as}, i_{bs} and i_{cs} are the *abc*-axis phase currents and i_f is the field current. L_f, L_a, L_b and L_c are the self-inductances of the field and *abc*-axis armature windings, M_{ab}, M_{bc} and M_{ca} are the *abc*-axis mutual inductances between the armature windings, M_{fa}, M_{fb} and M_{fc} are the *abc*-axis mutual inductances between the field and armature windings, respectively.

The torque component caused by the self-inductance in the armature windings can be rearranged as

$$T_{self\_a} = P\sum_{n=1}^{\infty}\sum_{m=1}^{\infty}\sum_{r=1}^{\infty}\begin{Bmatrix} \mp\frac{3n}{8}L_n^a I_m I_r \sin\left((m-r\pm n)\theta_e + \beta_m - \beta_r \pm \alpha_n^a\right) \\ \pm\frac{3n}{8}L_n^a I_m I_r \sin\left((m+r\pm n)\theta_e + \beta_m + \beta_r \pm \alpha_n^a\right) \end{Bmatrix} \tag{7.7}$$

where r is the harmonic order of the armature currents. It should be noted that this torque component is only valid when ($m - r \pm n$) or ($m + r \pm n$) is zero or a multiple of three. The self-inductance of the field windings affects the torque ripple

$$T_{self\_f} = P\sum_{n=1}^{\infty}\left\{-\frac{3n}{2}L_n^f I_f^2 \sin\left(n\theta_e + \alpha_n^f\right)\right\} \tag{7.8}$$

when n is a multiple of three. The contribution of the mutual inductance between the field and armature windings on the instantaneous torque is rearranged as

$$T_{mut\_f} = P\sum_{n=1}^{\infty}\sum_{m=1}^{\infty}\left\{\mp\frac{3n}{2}M_n^f I_f I_m \cos\left((m\pm n)\theta_e + \beta_m \pm \gamma_n^f\right)\right\} \tag{7.9}$$

when ($m \pm n$) is zero or a multiple of three. However, the torque component caused by the mutual inductance between the armature windings cannot be simplified due to the phase difference between the armature currents when an arbitrary armature current is applied to the 6/7 VFRM.

7.2.2.2 Under a Sinusoidal Armature Current Excitation

In the conventional VFRM drives, the field current is controlled at a constant value, and the armature current of Phase A can be represented as

$$i_{as}(\theta_e) = -I_1 \sin(\theta_e + \beta_1) \tag{7.10}$$

where I_1 is the amplitude, and β_1 is the advanced angle of the fundamental component of the armature current, respectively. The field current is controlled at a constant value I_f. Under the sinusoidal armature current excitation with the constant field current, the instantaneous torque is rewritten as

$$
\begin{aligned}
T_e &= P\sum_{n=1}^{\infty}\frac{n}{2}L_n^f I_f^2\left\{-\sin\left(n\theta_e+\alpha_n^f\right)\right\}\\
&+P\sum_{n=1}^{\infty}\frac{3n}{2}M_n^f I_f I_1\left\{\mp\cos\left((1\pm n)\theta_e+\beta_1\pm\gamma_n^f\right)\right\}\\
&+P\sum_{n=1}^{\infty}\frac{3n}{8}L_n^a I_1^2\left\{-2\sin\left(n\theta_e+\alpha_n^a\right)\pm\sin\left((2\pm n)\theta_e+2\beta_1\pm\alpha_n^a\right)\right\}\\
&+P\sum_{n=1}^{\infty}\frac{3n}{4}M_n^a I_1^2\left\{\sin\left(n\theta_e+\gamma_n^f\right)\pm\sin\left((2\pm n)\theta_e+2\beta_1\pm\gamma_n^f-\frac{2\pi}{3}\right)\right\}.
\end{aligned}
\tag{7.11}
$$

where the first component is caused by the self-inductance of the field windings when *n* is a multiple of three. The second torque component is generated from the mutual inductance between the field and armature windings when (1 ± *n*) is zero or a multiple of three. The third component is produced by the self-inductance of the armature windings when *n* is a multiple of three or (2 ± *n*) is zero or a multiple of three. The last two components are caused by the mutual inductances between the armature windings when *n* is a multiple of three for fourth component and (2 ± *n*) is zero or a multiple of three. The torque component caused by the mutual inductance between the field and armature windings exhibits the cosine waveform, whilst the other components are based on the sine waveform. Additionally, the last component in the torque equation has the phase shift -2/3π since it is generated by the different phase armature currents.

Under the sinusoidal armature current excitation, the average torque and torque ripple are determined by the harmonic orders of the inductances. The average torque can be rewritten based on the derived instantaneous torque equation as

$$
T_{avg}=P\left\{\frac{3}{2}M_1^f I_f I_1\cos\left(\beta_1-\gamma_1^f\right)-\frac{6}{8}L_2^a I_1^2\sin\left(2\beta_1-\alpha_2^a\right)-\frac{6}{4}M_2^a I_1^2\sin\left(2\beta_1-\gamma_2^f-\frac{2\pi}{3}\right)\right\}. \tag{7.12}
$$

As a feature of the VFRMs, the average torque is mainly generated from the fundamental component of the mutual inductance between the field and armature windings. Similar to the

torque production of the PM machines, VFRMs utilise the interaction between the armature currents and the flux-linkage, which resulted from the field current and mutual inductance between the field and armature windings. In the PM machines, the average torque is produced by the armature currents and the flux-linkage from the PMs. Meanwhile, the second harmonic self-inductance and mutual inductance between the armature windings also contributes to the average torque production. Hence, the advanced current angle β_1 can be adjusted so that the second harmonic inductances can contribute to the average torque production in order to maximise the average torque. However, due to relatively small second harmonic inductance values, the current angle β_1 is set to zero, which only utilises the mutual inductance between the field and armature windings.

Based on the torque equation, the third multiple harmonic torque ripple can be presented as

$$\begin{aligned}
T_{(3k)th} = \frac{3P}{2}\Big\{ & -kL^f_{3k}I_f^2\sin\left(3k\theta_e+\alpha^f_{3k}\right)-\frac{3k}{2}L^a_{3k}I_1^2\sin\left(3k\theta_e+\alpha^a_{3k}\right)+\frac{3k}{2}M^a_{3k}I_1^2\sin\left(3k\theta_e+\gamma^a_{3k}\right) \\
& -(3k-1)M^f_{(3k-1)}I_fI_1\cos\left(3k\theta_e+\beta_1+\gamma^f_{(3k-1)}\right)+(3k+1)M^f_{(3k+1)}I_fI_1\cos\left(3k\theta_e-\beta_1+\gamma^f_{(3k+1)}\right) \\
& +\frac{(3k-2)}{4}L^a_{(3k-2)}I_1^2\sin\left(3k\theta_e+2\beta_1+\alpha^a_{(3k-2)}\right)+\frac{(3k+2)}{4}L^a_{(3k+2)}I_1^2\sin\left(3k\theta_e-2\beta_1+\alpha^a_{(3k+2)}\right) \\
& +\frac{(3k-2)}{2}M^a_{(3k-2)}I_1^2\sin\left(3k\theta_e+2\beta_1+\gamma^a_{(3k-2)}-\frac{2\pi}{3}\right) \\
& +\frac{(3k+2)}{2}M^a_{(3k+2)}I_1^2\sin\left(3k\theta_e-2\beta_1+\gamma^a_{(3k+2)}+\frac{2\pi}{3}\right)\Big\}
\end{aligned} \tag{7.13}$$

where k is the integer starting from 1. The inductances from the fundamental to the fifth harmonic lead to the third harmonic torque ripple, whilst the sixth harmonic torque ripple is caused by the inductances from the fourth to the eight harmonics. It should be noted that since the 6/5 and 6/7 VFRMs have the opposite winding connection of the armature windings, the inductance components causing the third harmonic torque ripple are cancelled out. Hence, in the 6/5 and 6/7 VFRMs, the dominant torque ripple is produced at sixth harmonic, whilst the

6/4 VFRM have a significant third harmonic torque ripple.

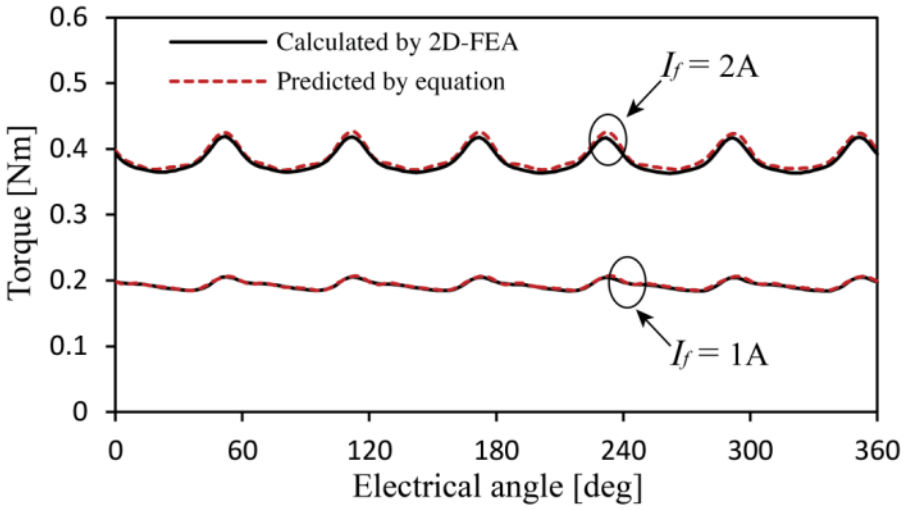

(a) Torque waveforms

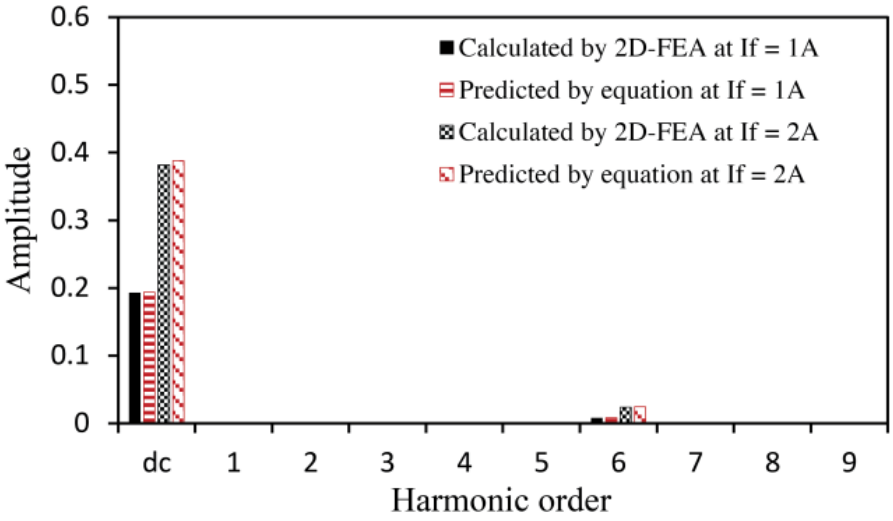

(b) Spectra

Fig. 7.6. Comparison of torque waveforms in 6/7 VFRM at I_1 = 2 A and I_f = 1 A and 2 A.

For verification, the torque waveforms predicted by the derived instantaneous torque equation are compared with the calculated results with the aid of FEA calculation at I_1 = 2 A and I_f = 1 A and 2 A. For the torque waveform predictions, the machine parameters calculated by FEA are utilised, which is listed in Table 7.1. It is worth mentioning that the harmonic orders are considered up to the thirtieth harmonic components for the prediction of torque

waveforms. The torque waveforms and the corresponding harmonic analysis results are shown in Fig. 7.6. The predicted torque waveforms are well matched with the calculated results in both current conditions. Additionally, the sixth harmonic torque ripple is dominant rather than the third harmonic torque ripple based on the harmonic analysis.

7.2.3 Torque Ripple Reduction Method for 6/7 VFRM

7.2.3.1 Harmonic Current Injection Based on FEA results

The reference field current can be calculated from the FEA torque waveforms so that the torque component produced by the mutual inductance between the field and armature windings counteracts the torque ripple component. From the torque waveforms calculated by FEA, the additional field current Δi^*_f for torque ripple reduction can be represented as

$$i^*_{fm} = I^*_f + \Delta i^*_f(\theta_e), \quad \Delta i^*_f(\theta_e) = -\frac{2}{3PM^f_1 I_1}\left(T_{e\_FEA}(\theta_e) - T_{avg\_FEA}\right) \tag{7.14}$$

where I^*_f is the reference constant field current, $T_{e\_FEA}(\theta_e)$ is the torque waveform with respect to the electrical rotor angle, and T_{avg_FEA} is the average torque calculated by FEA, respectively.

The reference field current waveforms calculated by the FEA torque waveforms are shown in Fig. 7.7(a). At a lower torque than the average torque, the additional reference field current is added to the constant reference value, whilst it is subtracted from the constant value at a higher torque. At 2 A of the armature current, the torque waveforms are compared with/without the torque ripple reduction method in Fig. 7.7(b). From the harmonic analysis, it can be seen in Fig. 7.7(c) that the torque ripple components can be significantly reduced.

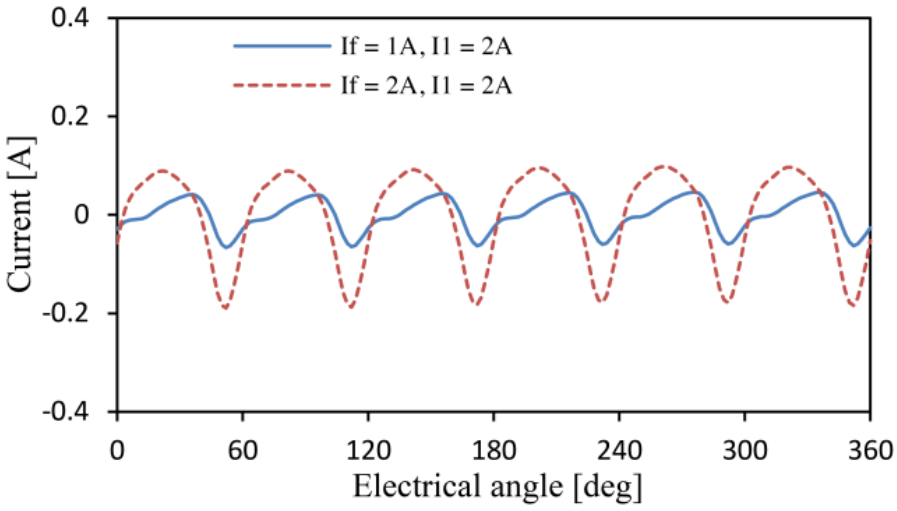

(a) Reference field current waveforms

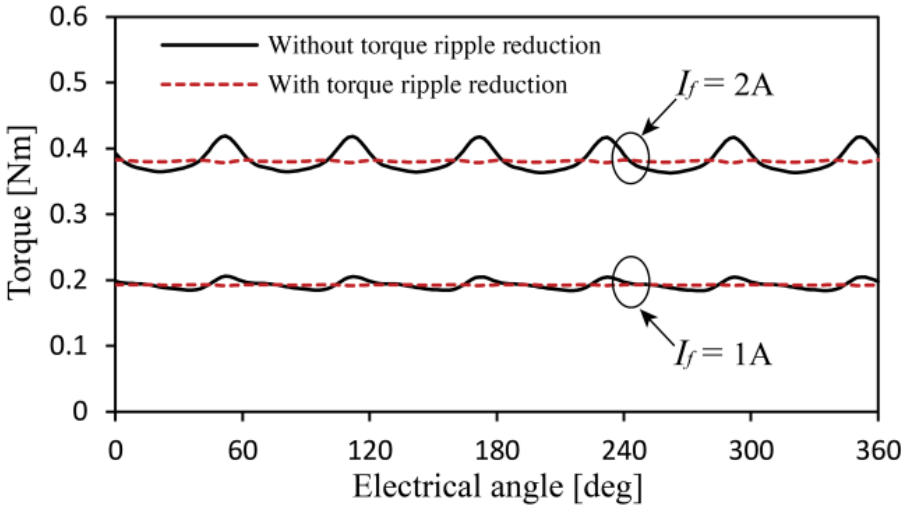

(b) Torque waveforms

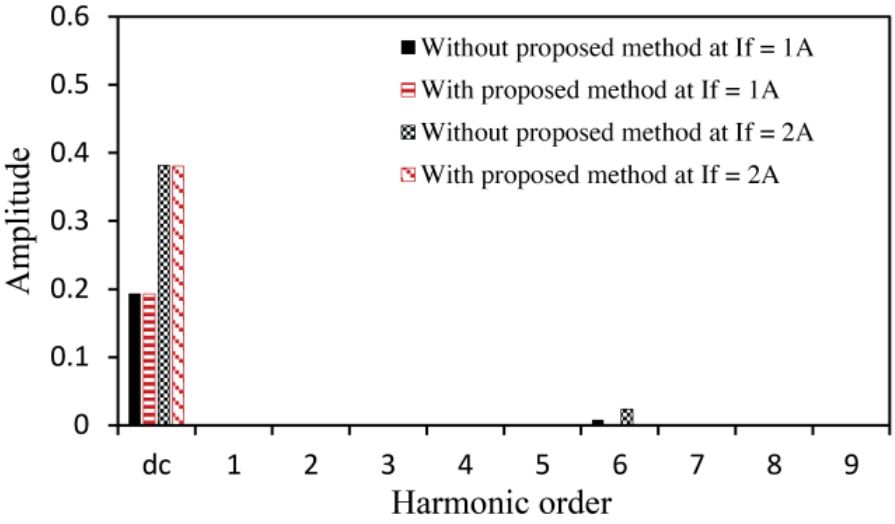

(c) Spectra of torque waveforms

Fig. 7.7. Comparison of torque waveforms in 6/7 VFRM at I_1 = 2 A and I_f = 1 A and 2 A.

In order to obtain the required harmonic field current, the FEA calculation should be done in the operating points. Since it may require a significant calculation time and large memory capacity, the calculation of the harmonic field current is utilised based on the derived torque equation.

7.2.3.2 Harmonic Current Injection Based on Torque Equation

Based on the derived torque equation, the third harmonic torque ripple equation can be utilised in order to generate the harmonic field current as

$$\Delta i_f^*(\theta_e) = -\frac{2}{3PM_1^f I_1} T_{(3k)th}(\theta_e). \tag{7.15}$$

By considering the harmonic inductances more precise torque ripple reduction can be achieved. Although this torque ripple reduction scheme requires the machine parameters, the reference field current can be updated under different current condition with the aid of precedent calculation of FEA. Additionally, since the torque ripple equation is derived taking into account for the current angle β_1, the torque ripple reduction method can be utilised in both rated torque and flux weakening operations.

The torque ripple harmonics up to the eighteenth order is considered in this chapter, since higher torque ripple components can be neglected. Also, it may be ineffective in practical test due to the control system bandwidth, although the reference harmonic field current is calculated for high order harmonic torque ripples. Fig. 7.8 shows the torque waveforms and corresponding harmonics when the harmonic current calculated by the derived equation is injected into the field windings. The harmonic field current based on the derived torque equation can be applied for the torque ripple reduction scheme when the VFRM operates in

the linear region. More importantly, the harmonic field current calculated by the derived equation is almost the same as that calculated by FEA. Hence, the field harmonic field current injection based on the derived torque equation can be utilised except for other high order harmonic components, which have less contribution.

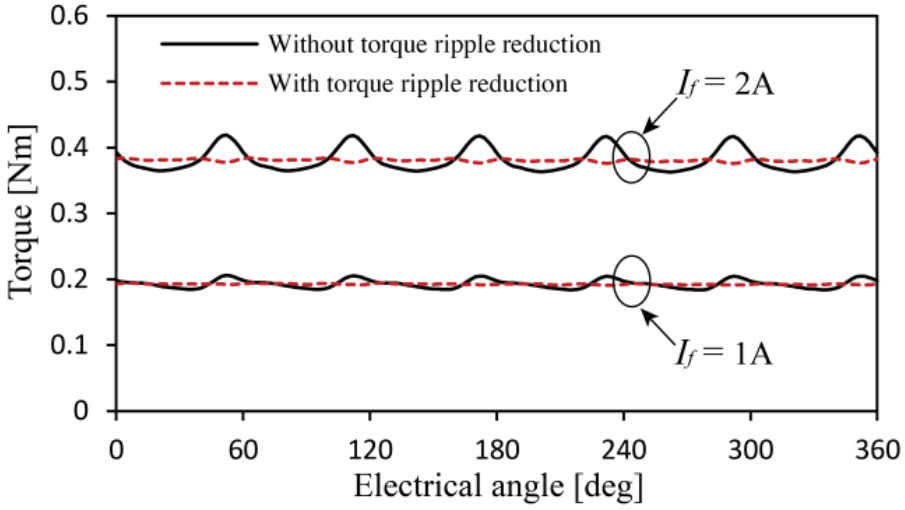

(a) Torque waveforms

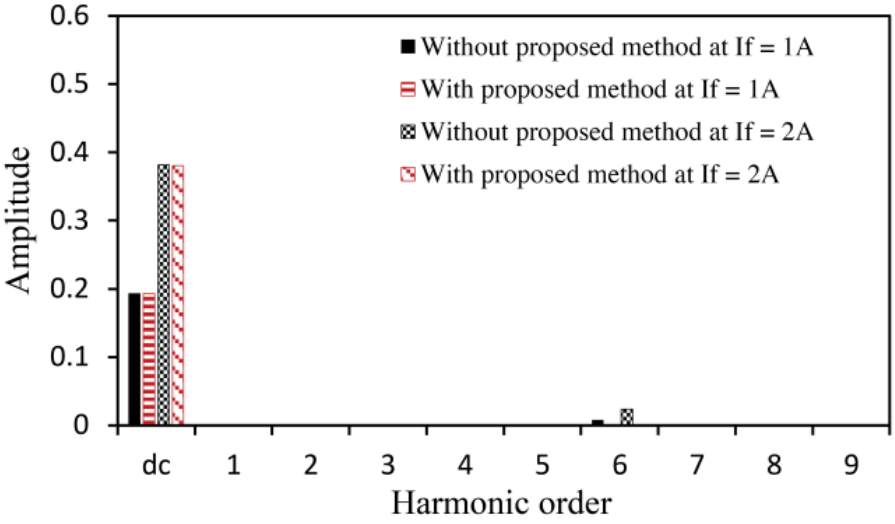

(b) Spectra

Fig. 7.8. Comparison of torque waveforms in 6/7 VFRM at I_1 = 2 A and I_f = 1 A and 2 A.

7.2.4 Experimental Results

Fig. 7.9 shows the control block diagram for the 6/7 VFRM with the external field current

control. For the armature current control, the conventional three-phase inverter is utilised, whilst the field current is controlled by the H-bridge converter. Based on a vector control, the armature currents are transformed to the *dq*-axis currents, and gate switching signals are generated into the inverter based on PI controllers and SVM technique. Apart from the armature currents, since the harmonic field current is added to the constant value, PIR controller is adopted. PIR controller consists of PI block and other resonant blocks, which can control resonant reference at some selected frequencies. In this chapter, three resonant blocks are utilised for the sixth, twelfth, and eighteenth harmonic component regulation, respectively.

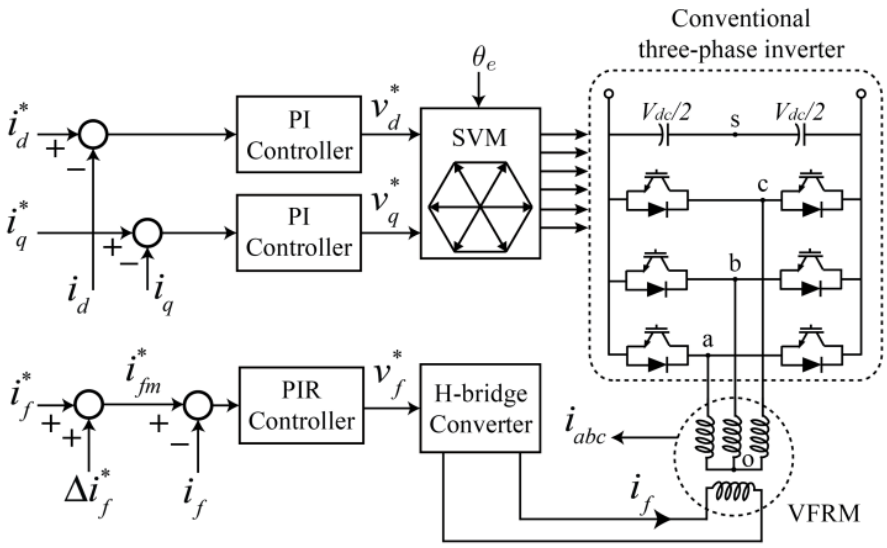

Fig. 7.9. VFRM control strategy with an external field current control.

For the experimental verification of the derived torque equation and torque ripple reduction scheme, the prototype 6/7 VFRM is utilised as shown in Fig. 7.10. In order to measure the torque waveforms, a torque transducer is equipped between the prototype machine and the load machine through the shaft. Since the test rig has a mechanical friction or unaligned shaft influence, the torque waveform is measured statically. Since the required currents are relied on the rotor position, the field and armature currents are appropriately applied to the prototype

machine. At every five electrical degree, the torque is measured by a torque transducer, whilst the rotor is locked by hands. At each position, the torque measurement is performed for one second, and the measured values are averaged for the accurate torque measurement. The machine parameters are listed in Table 7.1, in which the parameters not listed in the table are negligible. The VFRM control method is applied to the prototype 6/7 VFRM on dSPACE platform, whilst the prototype 6/7 VFRM is controlled under the *dq*-axis current control.

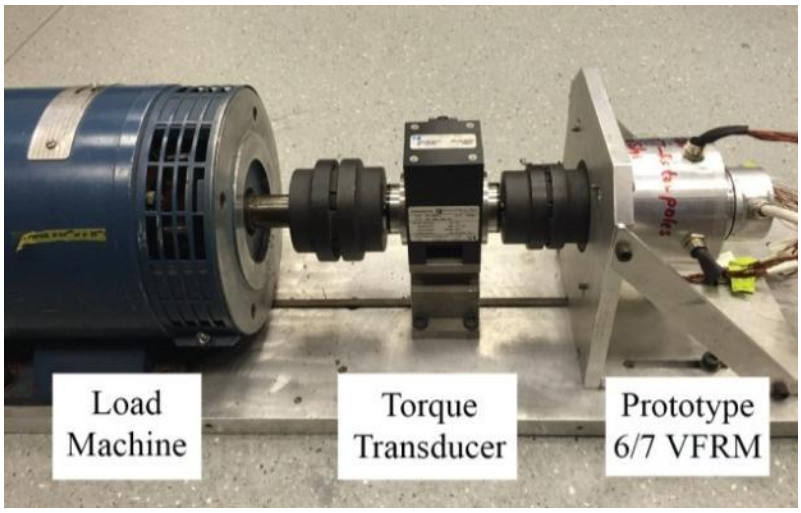

Fig.10. Experimental setup with prototype machine and torque transducer.

In order to verify the torque ripple reduction method, the torque waveforms are measured and compared with the predicted and calculated torque waveform when both field and armature currents are set to 2 A with $\beta_1 = 0^{\circ}$ in Fig. 7.11(a). The average torque is measured at around 0.4 Nm at all the waveforms, which are well matched with the predicted result in Fig. 7.8. Meanwhile, the torque ripple contains mainly sixth harmonic component and its magnitude is around 0.08 Nm. Fig. 7.11(b) shows the measured torque waveforms with the torque ripple reduction method. The injected harmonic field current is calculated based on (7.15). The multiple of the sixth harmonic torque ripple is reduced with the harmonic current

injection. As a result, the torque ripple components caused by the harmonics of the inductances can be reduced by the mutual inductance torque.

TABLE 7.1
MACHINE PARAMETERS

Machine parameters				**Value**			
Number of phases				3			
Number of stator poles				6			
Number of rotor poles (P)				7			
Winding resistance (R_s)				1.6 Ω			
Air gap				0.5 mm			
Number of turns per phase for armature windings				288			
Total number of turns for field windings				6 × 288			
Self-inductance of the armature windings				**Mutual inductance between the armature windings**			
Magnitude (mH)		Phase Shift (rad)		Magnitude (mH)		Phase Shift (rad)	
L_0^a	9.705	α_0^a	-	M_0^a	4.199	γ_0^a	-
L_2^a	0.257	α_2^a	0	M_2^a	0.213	γ_2^a	-2/3π
L_4^a	0.138	α_4^a	0	M_4^a	0.111	γ_4^a	2/3π
L_6^a	0.057	α_6^a	0	M_6^a	0.029	γ_6^a	π
L_8^a	0.001	α_8^a	π	M_8^a	0.002	γ_8^a	1/3π
L_{10}^a	0.003	α_{10}^a	0	M_{10}^a	0.002	γ_{10}^a	2/3π
L_{12}^a	0.009	α_{12}^a	0	M_{12}^a	0.005	γ_{12}^a	π
L_{14}^a	0.002	α_{14}^a	0	M_{14}^a	0.001	γ_{14}^a	-2/3π
L_{16}^a	0.000	α_{16}^a	-π	M_{16}^a	0.001	γ_{16}^a	1/6π
L_{18}^a	0.001	α_{18}^a	0	M_{18}^a	0.001	γ_{18}^a	π
L_{20}^a	0.001	α_{20}^a	0	M_{20}^a	0.001	γ_{20}^a	-2/3π
Mutual inductance between the field and armature windings				**Self-inductance of the field windings**			
Magnitude (mH)		Phase Shift (rad)		Magnitude (mH)		Phase Shift (rad)	
M_1^f	9.229	γ_1^f	0	L_0^f	43.014	α_0^f	-
M_3^f	0.023	γ_3^f	0	L_6^f	0.272	α_6^f	0
M_5^f	0.002	γ_5^f	0	L_{12}^f	0.040	α_{12}^f	0
M_7^f	0.053	γ_7^f	0	L_{18}^f	0.006	α_{18}^f	0
M_9^f	0.002	γ_9^f	0				
M_{11}^f	0.004	γ_{11}^f	0				

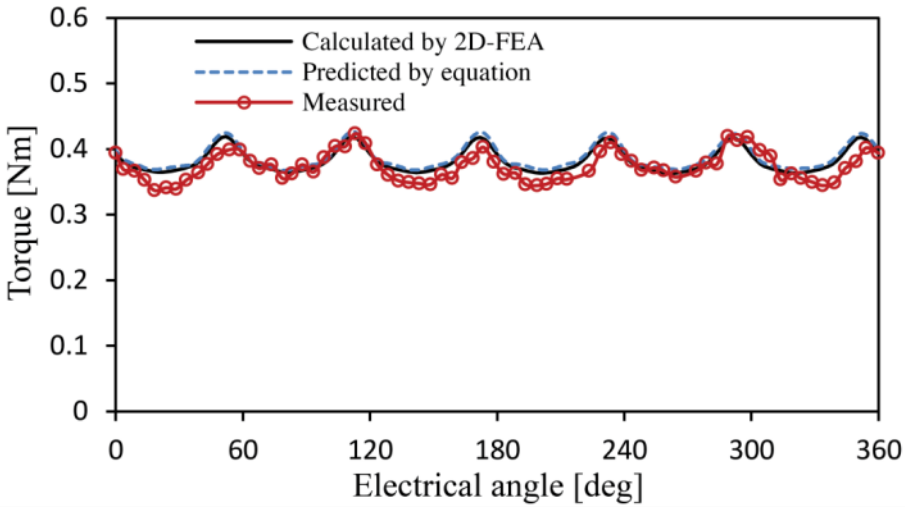

(a) Without torque ripple reduction method

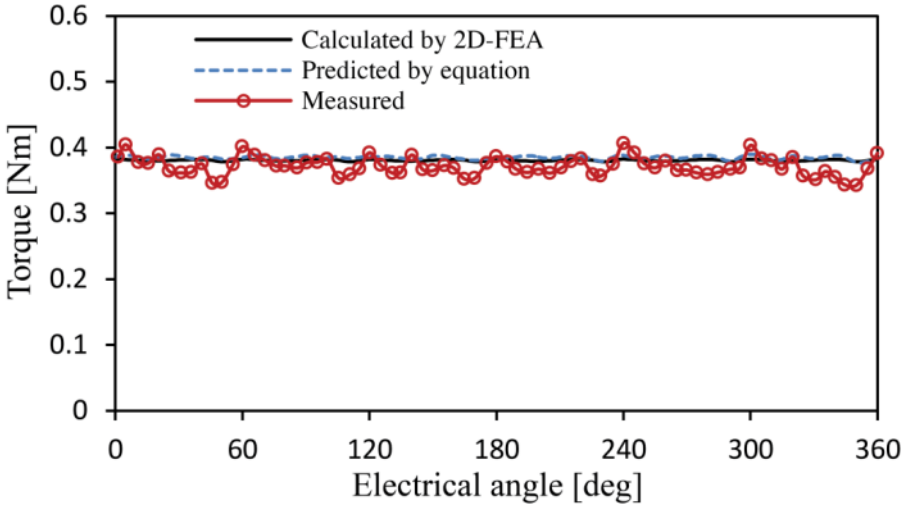

(b) With torque ripple reduction method

Fig. 7.11. Comparison of the torque waveforms with/without the torque ripple reduction at I_1 = 2 A and I_f = 2 A.

In order to compare the torque ripple reduction performance, the harmonic field current is injected in different current condition. In order to reduce the experiment points, the armature current magnitude is determined to be 1.414 I_f so that the rms current between the field and armature windings are the same for the maximum efficiency operation. Fig. 7.12 shows the torque ripple comparison against the field current. It can be observed that although the machine operates in different operating point, the torque ripple reduction method can reduce

the torque ripple, but the performance is degraded as the machine operates at high current.

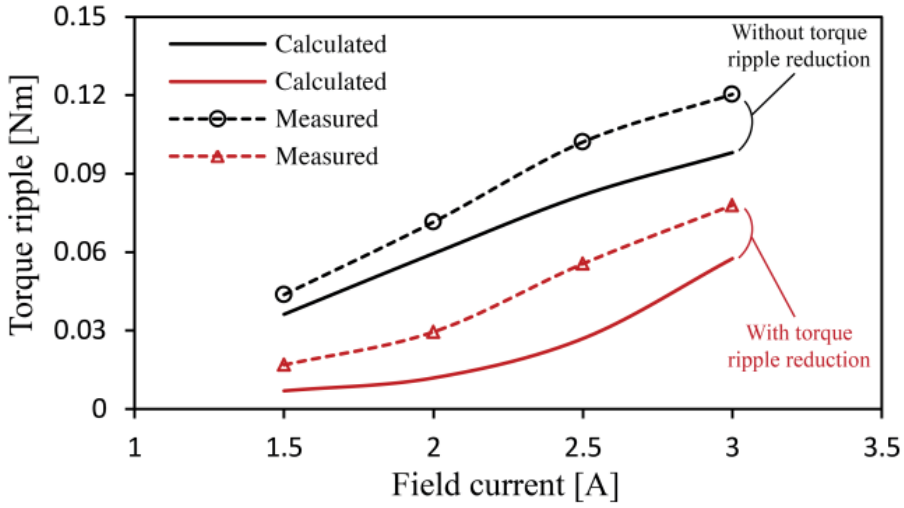

Fig. 7.12. Comparison results of the measured torque ripple under different current conditions with/without the torque ripple reduction method.

7.3 Torque Ripple Reduction for 6/4 VFRM with Integrated Current Control

7.3.1 Torque Production of 6/4 VFRM with Integrated Current Control

For the torque ripple reduction, the harmonic component is injected into the zero sequence current in the integrated current control scheme. As mentioned in Chapter 5, the inductance components are maintained in the integrated winding configuration. Since the phase current is a sinusoidal current biased by dc offset, the phase A current can be expressed as

$$i_{as}(\theta_e) = I_0 - I_1 \sin(\theta_e + \beta_1). \tag{7.16}$$

Based on the torque equation in the external field excitation current control (4.6), the torque equation with the integrated current control scheme can be rewritten as

$$
\begin{aligned}
T_{e1} &= -\frac{3P}{2}\sum_{n=1}^{\infty} nL_n I_0^2 \sin\left(n\theta_e + \alpha_n\right) \\
&+ \frac{3P}{2}\sum_{n=1}^{\infty} \mp nM_n I_0 I_1 \cos\left((1\pm n)\theta_e + \beta_1 \pm \gamma_n\right) \\
&+ \frac{3P}{2}\sum_{n=1}^{\infty}\left\{-\frac{n}{2}L_n I_1^2 \sin\left(n\theta_e + \alpha_n\right) \pm \frac{n}{4}L_n I_1^2 \sin\left((2\pm n)\theta_e + 2\beta_1 \pm \alpha_n\right)\right\}.
\end{aligned}
\tag{7.17}
$$

The field current I_f is replaced by the zero sequence current I_0. Then, the analytic torque ripple prediction can be also shown as

$$
\begin{aligned}
T_{r\_(3k)th} &= \frac{3P}{2}\left\{-3kL_{3k} I_0^2 \sin\left(3k\theta_e + \alpha_{3k}\right) - \frac{3k}{2}L_{3k} I_1^2 \sin\left(3k\theta_e + \alpha_{3k}\right)\right. \\
&-(3k-1)M_{(3k-1)} I_f I_1 \cos\left(3k\theta_e + \beta_1 + \gamma_{(3k-1)}\right) + (3k+1)M_{(3k+1)} I_f I_1 \cos\left(3k\theta_e - \beta_1 + \gamma_{(3k+1)}\right) \\
&\left.+\frac{(3k-2)}{4}L_{(3k-2)} I_1^2 \sin\left(3k\theta_e + 2\beta_1 + \alpha_{(3k-2)}\right) + \frac{(3k+2)}{4}L_{(3k+2)} I_1^2 \sin\left(3k\theta_e - 2\beta_1 + \alpha_{(3k+2)}\right)\right\}.
\end{aligned}
\tag{7.18}
$$

By using the derived analytical prediction of the torque ripple, the zero sequence current can be modified as

$$
i_{0m}^* = I_0^* + \Delta i_0^*(\theta_e), \quad \Delta i_0^*(\theta_e) = -\frac{2}{3P}\frac{1}{M_1 I_1} T_{r\_(3k)th}(\theta_e). \tag{7.19}
$$

As with the external field excitation current control, the harmonic field current amplitudes can be modified with respect to the operation current conditions. Since the generation of higher harmonic components may be limited by the control system bandwidth, the third, sixth, and ninth harmonic components are considered for the zero sequence current modification.

Fig. 7.13 shows the block diagram of the torque ripple reduction in the integrated current control scheme. The phase currents are controlled by the open winding inverter, whilst the zero sequence current is controlled by the zero vectors between the two inverters. The PI controllers are implemented in the synchronous *dq*-axis frame for the three-phase current control. Due to the harmonic component injection into the reference zero sequence current, the PIR controller is adopted for the zero sequence current control.

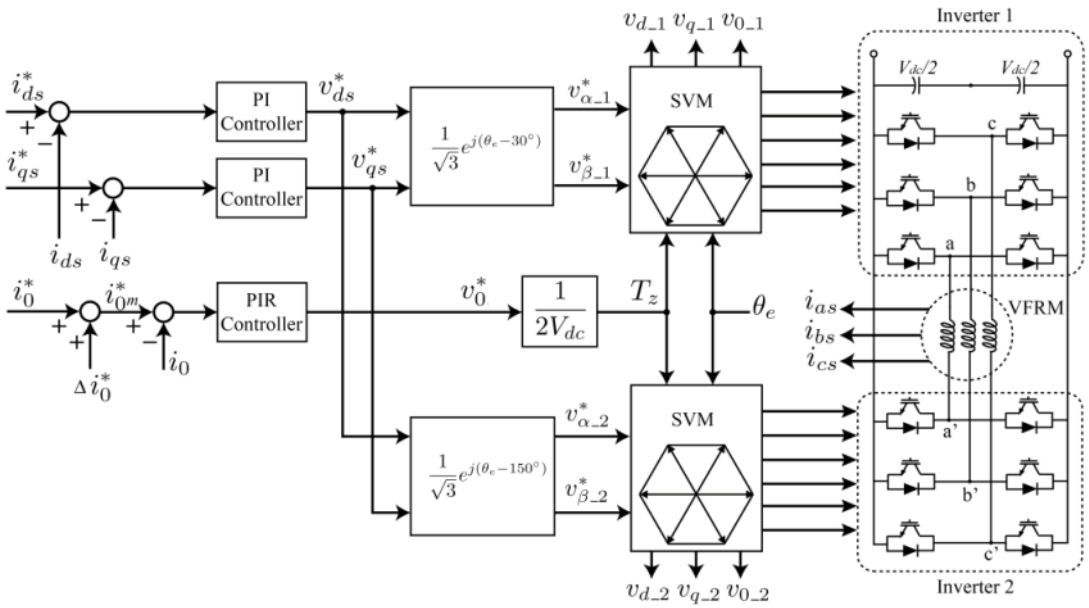

Fig. 7.13. Control block diagram of the torque ripple reduction in the integrated current control scheme.

7.3.2 Experimental Results

The measured torque and current waveforms are compared with/without the torque ripple reduction method at I_0 = 1 A and I_1 = 2 A in Fig. 7.14. With the harmonic current injection method, the torque ripple is significantly reduced. Although the phase current i_{as} is measured as a distorted sinusoidal waveform in time domain due to large torque ripple, the phase current is controlled as a sinusoidal current with respect to the rotor angle. In addition, the machine speed cannot be maintained at a constant speed due to the torque ripple without employing the proposed methods. Hence, the oscillation of the rotor angle can be seen in angle waveforms. However, this oscillation of the angle can be suppressed with the torque ripple reduction method. In the torque ripple reduction method, the phase current i_{as} contains dc, fundamental, and added harmonics, mainly the third harmonic component. It should be noted that dc and other harmonic components are controlled by the PIR controller in zero sequence current loop,

whilst the *q*-axis current is maintained at a constant value. The comparison results are shown in Fig. 7.15, at which the machine is operated at I_0 = 2 A, I_1 = 2 A. Although the torque ripple reduction performance is degraded compared with Fig. 7.14, the added harmonic zero sequence current can reduce the torque ripple under different current conditions.

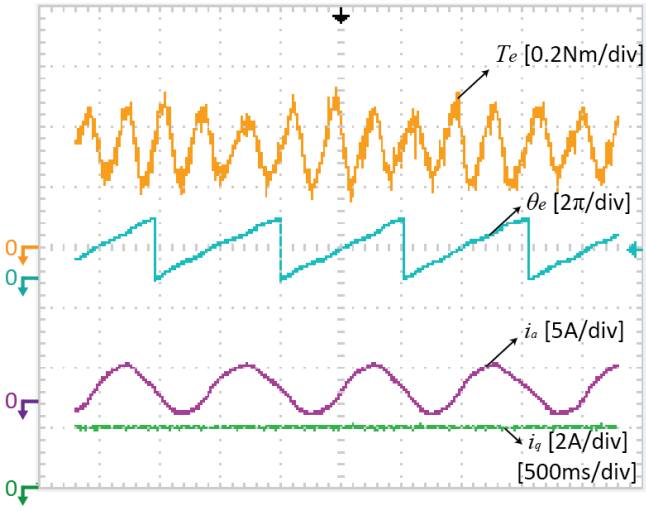

(a) Without torque ripple reduction

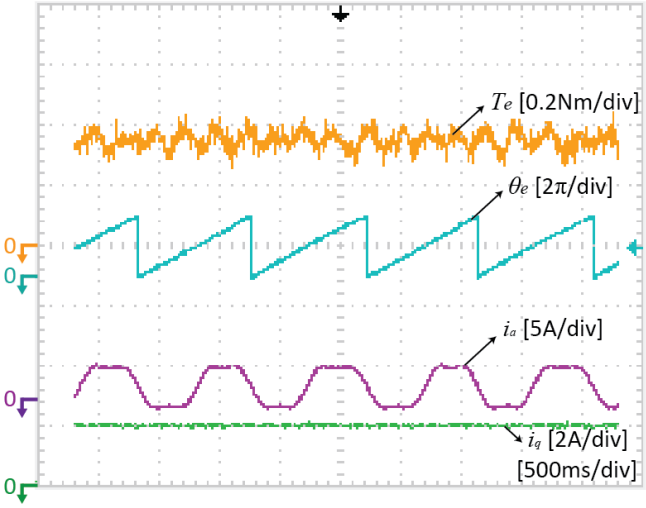

(b) With torque ripple reduction method

Fig. 7.14. Comparison of the measured torque waveforms at I_0 = 1 A, I_1 = 2 A.

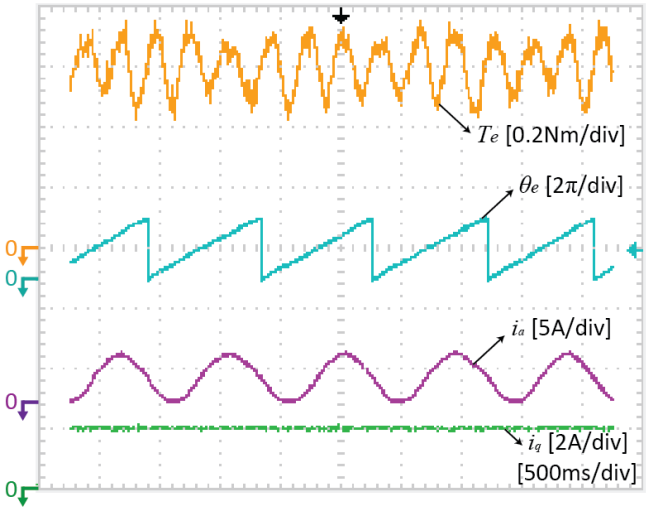

(a) Without torque ripple reduction

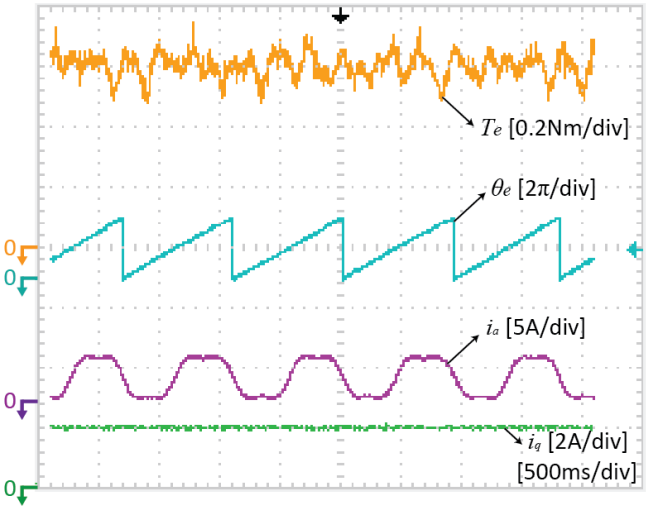

(b) With torque ripple reduction method

Fig. 7.15. Comparison of the measured torque waveforms at I_0 = 2 A, I_1 = 2 A.

7.4 Torque Ripple Reduction for 6/7 VFRM with Integrated Current Control

7.4.1 Torque Production of 6/7 VFRM with Integrated Current Control

The harmonic zero sequence current is applied to the 6/4 VFRM with integrated current

control method for the torque ripple reduction in the previous section. In the same manner, the torque ripple can be also reduced in the 6/7 VFRM with integrated current control configuration. From the previous analysis in Chapter 6, the ripple equation under the external current control can be also applied to that in the integrated current control as

$$\begin{aligned}T_{(3k)th} = \frac{3P}{2}\Big\{&-kL_{3k}^{f}I_0^2\sin\left(3k\theta_e+\alpha_{3k}^{f}\right)-\frac{3k}{2}L_{3k}^{a}I_1^2\sin\left(3k\theta_e+\alpha_{3k}^{a}\right)+\frac{3k}{2}M_{3k}^{a}I_1^2\sin\left(3k\theta_e+\gamma_{3k}^{a}\right)\\&-(3k-1)M_{(3k-1)}^{f}I_0I_1\cos\left(3k\theta_e+\beta_1+\gamma_{(3k-1)}^{f}\right)+(3k+1)M_{(3k+1)}^{f}I_0I_1\cos\left(3k\theta_e-\beta_1+\gamma_{(3k+1)}^{f}\right)\\&+\frac{(3k-2)}{4}L_{(3k-2)}^{a}I_1^2\sin\left(3k\theta_e+2\beta_1+\alpha_{(3k-2)}^{a}\right)\\&+\frac{(3k-2)}{2}M_{(3k-2)}^{a}I_1^2\sin\left(3k\theta_e+2\beta_1+\gamma_{(3k-2)}^{a}-\frac{2\pi}{3}\right)+\frac{(3k+2)}{4}L_{(3k+2)}^{a}I_1^2\sin\left(3k\theta_e-2\beta_1+\alpha_{(3k+2)}^{a}\right)\\&+\frac{(3k+2)}{2}M_{(3k+2)}^{a}I_1^2\sin\left(3k\theta_e-2\beta_1+\gamma_{(3k+2)}^{a}+\frac{2\pi}{3}\right)\Big\}\end{aligned} \tag{7.20}$$

where k is the integer starting from 1. Based on the torque ripple equation, VFRMs have a multiple of third harmonic components because the other harmonic components are cancelled out by three-phase windings. As already mentioned, the 6/5 and 6/7 VFRMs have the opposite connections of the armature windings, which leads to the cancellation of the third harmonic torque ripple. As a result, the 6/5 and 6/7 VFRMs have the torque ripple at a multiple of the sixth harmonic components.

The harmonic component of the zero sequence current for the torque ripple reduction can be calculated by the torque ripple equation as

$$\Delta i_0^*(\theta_e) = -\frac{2}{3PM_1^{f}I_1}T_{(3k)th}(\theta_e). \tag{7.21}$$

With the aid of a precedent FEA calculation, the inductance components can be obtained. The zero sequence reference current is updated under different current condition. It should be noted that the calculated zero sequence currents up to the eighteenth order are utilised for the torque ripple reduction because high order harmonic components contributes less to the torque

ripple.

Fig. 7.16 shows the block diagram of the torque ripple reduction scheme under integrated current control method. Each armature winding set is controlled by each inverter with the PI controllers in the synchronous reference frame, whilst the zero sequence current is produced by the zero voltage vectors between two inverters. The additional harmonic component for torque ripple reduction is added into the zero sequence reference current. Due to the alternating component, the PIR controlled is also adopted for zero sequence current control.

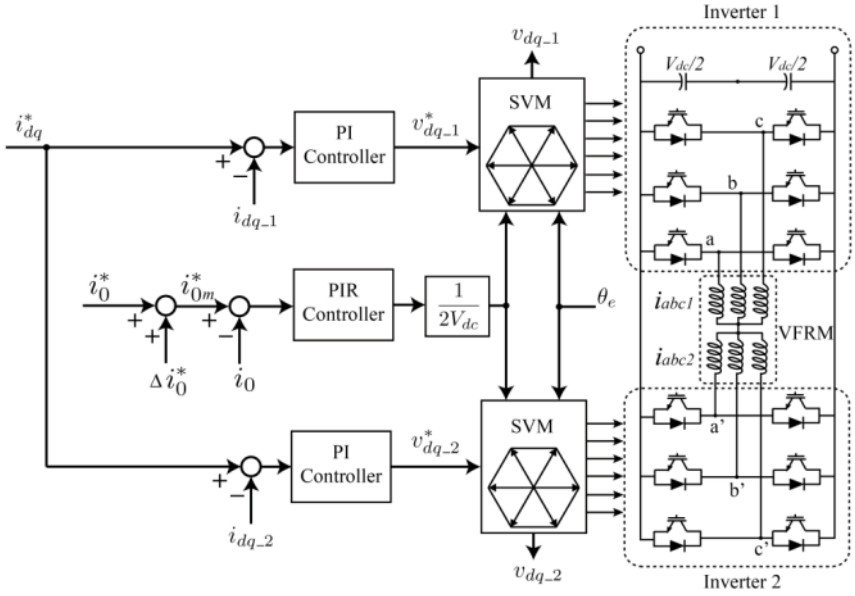

Fig. 7.16. Control block diagram of the torque ripple reduction in the integrated current control scheme.

7.4.2 Experimental Results

Fig. 7.17 shows the comparison of the torque waveforms with/without torque ripple reduction. Due to a mechanical friction or unaligned shaft influence of the test rig, the torque waveform is measured statically, whilst the field and armature currents are applied to the prototype machine. For every five electrical degree, the torque is measured with locked rotor

for one second, and the measured values are averaged. It can be observed that the measured torque waveform is matched well with the FEA calculated results. Without the torque ripple reduction method, the torque ripple contains mainly six harmonic component. With the harmonic zero sequence current, the torque ripple is reduced in both FEA calculation and experiment. Hence, the harmonic zero sequence current injection can effectively suppress the torque ripple in the integrated current control configuration.

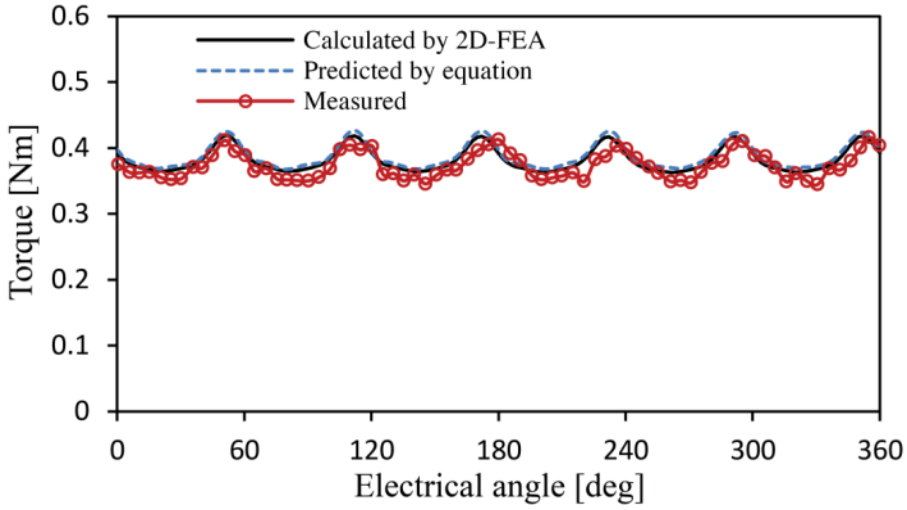

(a) Without torque ripple reduction method

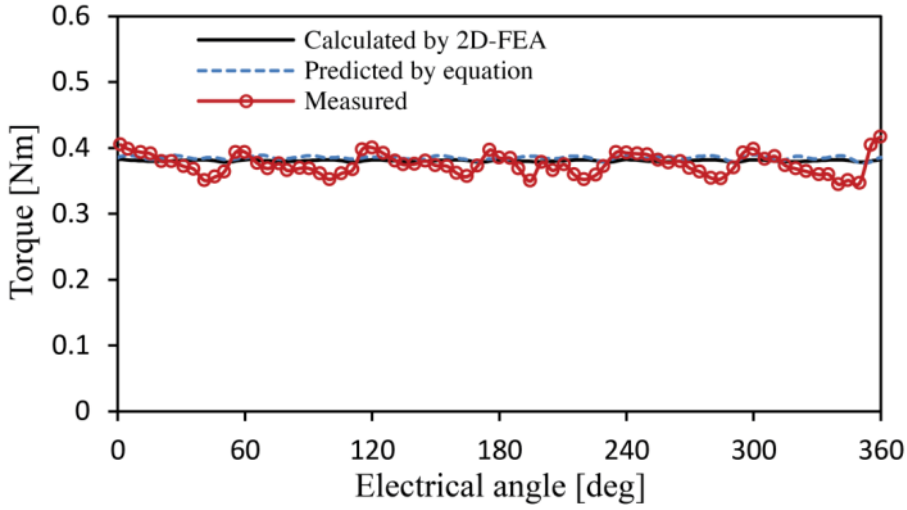

(b) With torque ripple reduction method

Fig. 7.17. Comparison of the torque waveforms with/without the torque ripple reduction under the integrated current control scheme at I_1 = 2 A and I_f = 2 A.

7.5 Conclusion

In this chapter, the torque production of the 6/7 VFRM is investigated considering all of the harmonics of the inductances and currents by using Fourier series. Based on the derived torque equation, the average torque is mainly produced by the mutual inductance between the field and armature windings. In terms of the torque ripple, the multiple of the third harmonic torque ripple is eliminated since the armature windings in each phase are connected in the opposite direction. Although the multiple of the sixth harmonic torque ripple exist, the overall torque ripple is much less than the 6/4 VFRM. The torque waveforms predicted by the derived torque equation are compared with the calculated results by FEA. Additionally, the derived torque equation is verified with the torque waveforms measured by using a torque transducer. The torque ripple reduction method is validated by the FEA calculation and the experimental results. This investigation can be identically applied to the 6/5 VFRM.

The torque ripple reduction scheme is also accomplished by the harmonic zero sequence current injection in the integrated current control for the 6/4 and 6/7 VFRMs. The field current in the external field excitation control is replaced by the zero sequence current in integrated current control scheme. When the VFRMs are driven in the integrated current control scheme, the torque production is the same as that with the external current control method as discussed in Chapter 5 and Chapter 6. Based on the derived torque equation, the harmonic component is calculated for the torque ripple reduction, and it is added to the zero sequence current. It shows that the torque ripple reduction scheme can be effectively applied to the integrated current control configuration for both 6/4 and 6/7 VFRMs.

CHAPTER 8

GENERAL CONCLUSIONS AND DISCUSSIONS

8.1 Introduction

Variable flux reluctance machines can be used for many applications, for which both constant torque and constant power operations are required as a good candidate for replacing PM machines. In this thesis, investigations into the torque production and control strategies have been described. The main subjects are summarised in Fig. 1. 19 and listed in Table 8.1. The instantaneous torque productions of the 6/4 VFRM are discussed in Chapter 3 by using Fourier series, which considers all of the harmonic components of the phase currents and winding inductances. Then, the torque ripple reduction scheme is introduced in Chapter 4 based on the harmonic field current injection. For the efficiency improvement and the extended operating range, the integrated current control methods are applied by using the open winding inverter for the 6/4 VFRM in Chapter 5 and the dual three-phase inverter for the 6/7 VFRM in Chapter 6. Additionally, further investigations of the 6/7 VFRM torque production are discussed in Chapter 7 including the torque ripple reduction with the integrated current control. The performance of the proposed methods has been investigated through the simulations and experiments.

TABLE 8.1
OVERALL STRUCTURE OF THIS THESIS

Machine	Winding configuration	Torque investigation	Torque ripple reduction	Control strategy
6/4 VFRM	External field current control	Chapter 3	Chapter 4	Chapter 5
	Integrated current control	Chapter 3	Chapter 7	Chapter 5
6/7 VFRM	External field current control	Chapter 7	Chapter 7	Chapter 6
	Integrated current control	Chapter 7	Chapter 7	Chapter 6

8.2 Torque Production

The VFRMs are stator electrically field excited synchronous machines having a similar structure with the SRMs. Especially, the 6/4 VFRM has exactly the same structure as the 6/4 SRM except for the divided field and armature windings. Hence, the contributions of the current harmonics on the torque production in the 6/4 SRM are investigated in Chapter 3. For both average torque and torque ripple predictions, the instantaneous torque equation of the 6/4 SRM is derived. Based on the harmonic analysis and on-load inductances estimated by the frozen permeability method, this torque equation is able to evaluate the torque productions of all the current harmonics in the unipolar rectangular excitation. By using the Lagrange equations, the magnitudes and phases of the current harmonics are optimised in terms of the maximum average torque under a given rms current.

From the investigation, it has been found

- The average torque of the 6/4 VFRM is mainly produced by the interaction between the dc, fundamental and second harmonic components of the phase currents.

- The fourth and fifth harmonic currents contribute to the torque ripple rather than the average torque production in the 6/4 VFRM.
- The current harmonics from the rectangular waveform are already almost optimised for the maximum average torque.
- The key of the torque production is the utilisation of the fundamental self-inductance in the phase windings due to its dominant contribution.
- The 6/5 and 6/7 VFRMs exhibit the similar characteristics with the SPM machines in terms of the inductances due to the opposite winding of the armature windings.

For verification, four excitation waveforms with different current harmonic combinations, as well as the unipolar rectangular excitation, are selected. Good agreements are found between the analytical, FEA and experimental results of the average torque. However, in the saturation region, the torque waveforms, consequently torque ripples, are different from the FEA calculated results. Hence, the stored energy calculated by FEA is utilised in order to predict the torque waveforms in the saturation region. Unlike the 6/4 VFRM, the 6/5 and 6/7 VFRMs has a different winding configuration. Since the armature windings have opposite polarities in each phase, the significant harmonics of the inductances are cancelled out each other. As a result, the 6/5 and 6/7 VFRMs exhibit the similar characteristics with the SPM machines, which has a unity saliency in the *dq*-axis inductance as discussed in Chapter 7.

8.3 Torque Ripple Reduction

According to the derived torque equations, the undesirable torque ripples having multiples

of the harmonic components exist due to the inductance harmonics in the VFRM. The proposed harmonic field current injection method has been applied for the torque ripple reduction in Chapter 4 and Chapter 7.

From the investigation, it has been found

- The 6/4 VFRM exhibits the significant third harmonic torque ripple, whilst the 6/7 VFRM has the dominant sixth harmonic torque ripple with less magnitude.
- Based on the harmonic field current injection, the torque ripple is minimized in both 6/4 and 6/7 VFRMs.
- Torque ripple reduction method is also applied to the integrated current control by injecting the harmonic components to the zero sequence current.
- The torque ripple reduction performance is not affected much unless the fundamental component of the nominal inductance is underestimated.

The proposed method serves for the investigation into effectiveness of the torque ripple reduction. Additionally, since the proposed method utilises the machine parameters, the influence of the parameter mismatch is investigated. The torque waveforms predicted by the derived torque equation are compared with the calculated results by FEA. The derived torque equation is verified with the torque waveforms measured by using a torque transducer.

8.4 Integrated Current Control

The integrated field and armature current control strategy has been discussed in Chapter 5

and Chapter 6.

From the investigation, it has been found

- In the integrated current control scheme, the field and armature currents are injected into a single coil as a sinusoidal current biased by a dc offset, rather than the separated field and armature windings.
- The three-phase sinusoidal currents produce a rotating stator field, whilst the zero sequence current generates a virtual rotor flux as the field current.
- This scheme can reduce the copper loss by half and extend the operating speed range owing to the reduction of winding resistance.
- In the 6/4 VFRM drives, the open winding configuration is adopted. The dual three-phase inverter is employed in the 6/7 VFRM, whilst one side of each stator winding is connected to the neutral point.

In the 6/4 VFRM, the open winding inverter is adopted for the integrated current control. In order to utilise the zero sequence current as the field current, the zero vector modification technique is adopted, in which the switching on-time of the zero vectors is modified to utilise the constant zero sequence voltage between the two inverters. The proposed scheme is implemented in the synchronous *dq*0-axis frame with SVM. The voltage and torque equations are derived with respect to the winding configurations in the synchronous *dq*-axis frame. Meanwhile, since the integrated current control with the open winding configuration cannot be applied to the 6/7 VFRM due to the winding configuration, the dual three-phase configuration is employed for the 6/7 VFRM. For the validation of the proposed method, the machine

models of the 6/4 and 6/7 VFRMs are developed and implemented in MATLAB/*Simulink*. The experimental results validate that the proposed strategy can effectively increase the efficiency and extend the operating speed range.

8.5 Future Work

- In this thesis, the current harmonics are optimised in order to achieve the maximum average torque under a given rms current. The torque ripple reduction scheme is also introduced. The selection of the current harmonics or control strategies can be investigated in order to achieve the maximum average torque and minimum torque ripple simultaneously. Further investigation can be extended to a vibration and acoustic noise of the VFRMs with different control strategies.
- In the 6-stator pole, the 6/5 and 6/7 VFRMs can exhibit more sinusoidal flux-linkage and back emf waveforms. Additionally, it can produce a high torque density but less torque ripple compared with the 6/4 VFRM. However, an unbalanced magnetic force (UMF) is unavoidable due to its odd rotor pole number. This can be overcome by doubling the stator and rotor poles together, i.e. a 12-tator pole VFRM with either 10- or 14-rotor poles. Additionally, a 12-stator pole VFRM provides more stator/rotor pole combinations compared with the 6-stator pole VFRMs. The investigation of the torque production and integrated current control strategy discussed in this thesis can be applied to the 12-stator pole VFRMs. Moreover, a VFRM having high power rating may be developed and tested for the

electric vehicles or hybrid vehicle applications.

- Due to the fundamental component of the self-inductance, the 6/4 VFRM exhibits the third harmonic component in the voltage equations in the synchronous reference frame. In the integrated current control strategy, the winding sets of the 6/7 VFRM should be divided into two for the integrated current control, and the third harmonic components cannot be cancelled out from each winding set. The third harmonic inductance components result in the oscillation of the voltage equations in the synchronous *dq*-axis frame. Especially, when the feedback type of the flux weakening control methods is employed, the onset speed of the flux weakening operation will be affected by the harmonic components. The quantitative analysis of the voltage utilization factor can be provided as a future work.

REFERENCES

[AFI15] I. A. A. Afinowi, Z. Q. Zhu, Y. Guan, J. C. Mipo, and P. Farah, “Hybrid-excited doubly salient synchronous machine with permanent magnets between adjacent salient stator poles,” *IEEE Trans. Magn.*, vol. 51, no. 10, Oct. 2015.

[AHN99] J. W. Ahn, S. G. Oh, J. W. Moon, and Y. M. Hwang, “A three-phase switched reluctance motor with two-phase excitation,” *IEEE Trans. Ind. Appl.*, vol. 35, no. 5, pp. 1067–1075, 1999.

[AKE00] A. D. Akemakou and S. K. Phounsombat, “Electrical machine with double excitation, especially a motor vehicle alternator,” U.S. Patent 6 147 429, Nov. 14, 2000.

[AMA09] Y. Amara, L. Vido, M. Gabsi, E. Hoang, A. H. B. Ahmed, and M. Lecrivain, “Hybrid excitation synchronous machines: Energy-efficiency solution for vehicles propulsion,” *IEEE Trans. Veh. Technol.*, vol. 58, no. 8, pp. 2137–2149, Aug. 2009.

[BAI04] M. R. Baiju, K. K. Mohapatra, R. S. Kanchan, and K. Gopakumar, “A dual two-level inverter scheme with common mode voltage elimination for an induction motor drive,” *IEEE Trans. Power Elec.*, vol. 19, no. 3, pp. 794–805, May 2004.

[BAR98] P. G. Barrass, and B. C. Mecrow, "Flux and torque control of switched reluctance machines," *lEE Proceedings Electric Power Applications*, pp. 519-527, 1998.

[BAY16] J. Bayless, N. Kurihara, H. Sugimoto, and A. Chiba, “Acoustic noise reduction of switched reluctance motor with reduced RMS current and enhanced efficiency,” *IEEE Trans. Energy Conv.*, vol. 31, no. 2, pp. 627–636, Jun. 2016.

[BEN00] M. E. H. Benbouzid, “A review of induction motors signature analysis as a medium for faults detection,” *IEEE Trans. Ind. Electron.*, vol. 47, no. 5, pp. 984–993, Oct. 2000.

[BIA01] N. Bianchi, S. Bolognani, and M. Zigliotto, “High-performance PM synchronous motor drive for an electrical scooter,” *IEEE Trans. Ind. Appl.*, vol. 37, no. 5, pp. 1348–1355, Sep./Oct. 2001.

[BOJ03] R. Bojoi, M. Lazzari, F. Profumo, and A. Tenconi, “Digital field-oriented control for dual three-phase induction motor drives,” *IEEE Trans. Ind. Appl.*, vol. 39, no. 3, pp. 752–760, 2003.

[BOS97] B. K. B. And and N. R. Patel, “A programmable cascaded low-pass filter-based flux synthesis for a stator flux-oriented vector-controlled induction motor drive,” *IEEE Trans. Ind. Electron.*, vol. 44, pp. 140–143, Feb. 1997.

[CAS00] D. Casadei, G. Serra, and A. Tani, “Implementation of a direct torque control algorithm for induction motors based on discrete space vector modulation,” *IEEE Trans. Power Electron.*, vol. 15, pp. 769–777, Jul. 2000.

[CHA02] K. T. Chau, M. Cheng, and C. C. Chan, “Nonlinear magnetic circuit analysis for a novel stator doubly fed doubly salient machine,” *IEEE Trans. Magn.*, vol. 38, no. 5, pp. 2382–2384, Sep. 2002.

[CHA03] K. T. Chau, J. Z. Jiang, and Y. Wang, “A novel stator doubly fed doubly salient permanent magnet brushless machine,” *IEEE Trans. Magn.*, vol. 39, no. 5, pp. 3001–3003, Sep. 2003.

[CHA08] K. T. Chau, C. C. Chan, and L. Chunhna, “Overview of permanent bruchless drive for electric and hybrid electric vehicle,” *IEEE Trans. Ind. Electron.*, vol. 55, no. 6, pp. 2246–2257, Jun. 2008.

[CHE01] M. Cheng, K. T. Chau, and C. C. Chan, “Design and analysis of a new doubly salient permanent magnet motors,” *IEEE Trans. Magn.*, vol. 37, no. 4, pp. 3012–3020, Jul./Aug. 2001.

[CHE02] A. D. Cheok and Y. Fukuda, "A new torque and flux control method for switched reluctance motor drives," *IEEE Trans. Power Electron.*, vol. 17, pp. 543-557, 2002.

[CHE06] T. P. Chen, “Circulating zero-sequence current control of parallel three-phase inverters,” *IEE Proc. Electr. Power Appl.*, vol. 153, no. 2, pp. 282–288, Mar. 2006.

[CHE10] J. T. Chen, Z. Q. Zhu, S. Iwasaki, and R. Deodhar, “Low cost flux-switching brushless AC machines,” *IEEE Vehicle Power and Propulsion Conference (VPPC2010)*, pp. 1–6, Sep. 2010.

[CHE11] M. Cheng, W. Hua, J. Zhang, and W. Zhao, “Overview of stator-permanent magnet brushless machines,” *IEEE Trans. Ind. Electron.*, vol. 58, no. 11, pp. 5087–5101, Nov. 2011.

[CHU13] W. Q. Chu and Z. Q. Zhu, “Average torque separation in permanent magnet synchronous machines using frozen permeability,” *IEEE Trans. Magn.*, vol. 49, no. 3, pp. 1202–1210, Mar. 2013.

[CHU15] W. Q. Chu, Z. Q. Zhu, J. Zhang, X. Liu, D. A. Stone, and M. P. Foster, “Investigation on operational envelops and efficiency electrical vehicle applications,” *IEEE Trans. Magn.*, vol. 51, no. 4, pp. 8103510–8103510, 2015.

[DES10] P. C. Desai, M. Krishnamurthy, N. Schofield, and A. Emadi, “Novel switched reluctance machine configuration with higher number of rotor poles than stator poles: Concept to implementation,” *IEEE Trans. Ind. Electron.*, vol. 57, no. 2, pp. 649–657, Feb. 2010.

[DOR11] D. G. Dorrell, M. F. Hsieh, M. Popescu, L. Evans, D. A. Staton, and V. Grout, “A review of the design issues and techniques for radial-flux brushless surface and internal rare-earth permanent magnet motors,” *IEEE Trans. Ind. Electron.*, vol. 58, no. 9, pp. 3741–3757, Sep. 2011.

[EDP15] A. Edpuganti and A. K. Rathore, “New optimal pulsewidth modulation for single dc-link dual-inverter fed open-end stator winding Induction Motor Drive,” *IEEE Trans. Power Elec.*, vol. 30, no. 8, pp. 4386–4393, Aug. 2015.

[EDR05] C. S. Edrington, M. Krishnamurthy, and B. Fahimi, “Bipolar switched reluctance machines: a novel solution for automotive applications,” *IEEE Trans. Veh. Technol.*, vol. 54, no. 3, pp. 795–808, 2005.

[ELR08] A. M. El-refaie, Z. Q. Zhu, T. M. Jahns, and D. Howe, “Winding inductances of fractional slot surface-mounted permanent magnet brushless machines,” *COMPEL - The International Journal for Computation and Mathematics in Electrical and Electronic Engineering*, pp. 1–8, 2008.

[FAN08] Y. Fanand, K. T. Chau, “Design, modeling, and analysis of a brushless doubly fed doubly salient machine for electric vehicles,” *IEEE Trans. Ind. Applicat.*, vol. 44, no. 3, pp. 727–734, May/June 2008.

[FAV93] E. Favre, L. Cardoletti, and M. Jufer, “Permanent-magnet synchronous motors: a comprehensive approach to cogging torque suppression,” *IEEE Trans. Ind. Appl.*, vol. 29, no. 6, pp. 1141–1149, 1993.

[FRE96] C. French and P. Acarnley, “Direct torque control of permanent magnet drives,” *IEEE Trans. Ind. Appl.*, vol. IA–32, pp. 1080–1088, Sep./Oct. 1996.

[FUE05] N. H. Fuengwarodsakul, M. Menne, R. B. Inderka, and R. W. De Doncker, "High-dynamic four-quadrant switched reluctance drive based on DITC," *IEEE Trans. Ind. Appl.*, vol. 41, pp. 1232-1242, 2005.

[FUK12a] T. Fukami, Y. Matsuura, K. Shima, M. Momiyama, and M. Kawamura, “A multipole synchronous machine with nonoverlapping concentrated armature and field windings on the stator,” *IEEE Trans. Ind. Electron.*, vol. 59, no. 6, pp. 2583–2591, Jun. 2012.

[FUK12b] T. Fukami, H. Aoki, K. Shima, M. Momiyama, and M. Kawamura, “Assessment of core losses in a flux-modulating synchronous machine,” *IEEE Trans. Ind. Appl.*, vol. 48, no. 2, pp. 603–611, Mar. 2012.

[FUK12c] T. Fukami, K. Shima, T. Tsuda, and M. Kawamura, “Prediction of field currents in flux-modulating synchronous machines under loaded conditions,” *XXth Int. Conf. on Elect. Mach. (ICEM 2012)*, pp. 441–446, Sep. 2012.

[HAL92] B. Hall, “Minimization of Torque Ripple in Permanent Magnet Motors: A Closed Form Solution,” *in Proc. 18th IEEE Ind. Elect. Conf.*, pp. 459–463, 1992.

[HAN94] D. D. C. Hanselman and S. Member, “Minimum torque ripple, maximum efficiency excitation of brushless permanent magnet motors,” *IEEE Trans. Ind. Electron.*, vol. 41, no. 3, pp. 292–300, 1994.

[HAQ01] M. E. Haque and M. F. Rahman, “Influence of stator resistance variation on direct torque controlled interior permanent magnet synchronous motor drive performance and its compensation,” in *Proc. IEEE-IAS Annu. Meeting*, pp. 2563–2569, 2001.

[HEN10] J. R. Hendershot and T. J. E. Miller, *Design of Brushless Permanent-Magnet Machines*. Florida: Motor Design Books LLC, 2010

[HOL96] J. Holtz and L. Springob, “Identification and compensation of torque ripple in high-precision permanent magnet motor drives,” *IEEE Trans. Ind. Electron.*, vol. 43, no. 2, pp. 309–320, 1996.

[HUS96] 1. Husain and M. Ehsani, "Torque ripple minimization in switched reluctance motor drives by PWM current control," *IEEE Trans. Power Electron.*, vol. 11, pp. 83-88, 1996.

[HUS05] I. Husain and S. A. Hossain, “Modeling, simulation, and control of switched reluctance motor drives,” *IEEE Trans. Ind. Electron.*, vol. 52, no. 6, pp. 1625–1634, 2005.

[JAH86] T. M. Jahns, G. B. Kliman, and T. W. Neumann, “Interior permanent-magnet synchronous motors for adjustable-speed drives,” *IEEE Trans. Ind. Applicat.*, no. 4, pp. 738–747, 1986.

[JAH87] T. M. Jahns, "Flux-weakening regime operation of an interior permanent-magnet synchronous motor drive," *IEEE Trans. Ind. Appl.*, Vols. IA-23, no. 4, pp. 681-689, 1987.

[JAH96] T. M. Jahns and W. L. Soong, “Pulsating torque minimization techniques for permanent magnet AC motor drives-a review,” *IEEE Trans. Ind. Electron.*, vol. 43, no. 2, pp. 321–330, Apr. 1996.

[JEO15] I. Jeong, B. G. Gu, J. Kim, K. Nam and Y. Kim, “Inductance estimation of electrically excited synchronous motor via polynomial approximations by least square method,” *IEEE Trans. Ind. Appl.*, vol. 51, pp.1526-1537, Mar./Apr. 2015.

[JIA10] H. Jia, M. Cheng, W. Hua, W. Zhao, and W. Li, “Torque ripple suppression in flux-switching PM motor by harmonic current injection based on voltage space-vector modulation,” *IEEE Trans. Magn.*, vol. 46, no. 6, pp. 1527–1530, Jun. 2010.

[KIM96] J.-M. Kim, K.-T. Park, S.-J. Kang, S.-K. Sul, J.-L. Kwon, "Improved dynamic performance of interior permanent magnet synchronous motor drive in flux-weakening operation," *Proc. of EPSC 96*, pp. 1562-1567, 1996.

[KIM97] J.-M. Kim and S.-K. Sul, “Speed control of interior permanent magnet synchronous motor drive for the flux weakening operation,” *IEEE Trans. Ind. Applicat.*, vol. 33, no. 1, pp. 43–48, 1997.

[KIM01] Y. Kim, H. Lyoo, S. Kim, and J. Lee, "Advanced torque control of switched reluctance motor," *IEEE International Symposium on Industrial Electronics*, vol.3, pp. 1798-1803, 2001.

[KIM04] J. Kim, J. Jung, and K. Nam, “Dual-inverter control strategy for high-speed operation of EV induction motors,” *IEEE Trans. Ind. Electron.*, vol. 51, no. 2, pp. 312–320, Apr. 2004.

[KOH03] C. S. Koh and J. S. Seol, “New cogging-torque reduction method for brushless permanent-magnet motors,” *IEEE Trans. Magn.*, vol. 39, no. 6, pp. 3503–3506, 2003.

[KWO06] T. S. Kwon and S. K. Sul, “Novel antiwindup of a current regulator of a surface-mounted permanent-magnet motor for flux-weakening control,” *IEEE Trans. Ind. Appl.*, vol. 42, no. 5, pp. 1293–1300, Sep./Oct. 2006.

[LAS00] C. Lascu, I. Boldea, and F. Blaabjerg, “A modified direct torque control for induction motor sensorless drive,” *IEEE Trans. Ind. Appl.*, vol. 36, pp. 122–130, Jan./Feb. 2000.

[LEE08] G. Lee, S. Kim, J. Hong, and J. Bahn, “Torque ripple reduction of interior permanent magnet synchronous motor using harmonic injected current,” *IEEE Trans. Magn.*, vol. 44, no. 6, pp. 1582–1585, Jun. 2008.

[LEH86] H. Le-Huy, R. Perret, and R. Feuillet, “Minimization of torque ripple in brushless DC motor drives,” *IEEE Trans. Ind. Appl.*, vol. I, no. 4, pp. 748–755, 1986.

[LEV12] E. Levi, I. N. W. Satiawan, N. Bodo, and M. Jones, “A space-vector modulation scheme for multilevel open-end winding five-phase drives,” *IEEE Trans. Energy Conv.*, vol. 27, no. 1, pp. 1–10, Mar. 2012.

[LIA94] F. Liang, Y. Liao, and T. A. Lipo, “A new variable reluctance motor utilizing an auxiliary commutation winding,” *IEEE Trans. Ind. Appl.*, vol. 30, no. 2, pp. 423–432, Mar./Apr. 1994.

[LIA95] Y. Liao, F. Liang, and T. A. Lipo, “A novel permanent magnet motor with doubly salient structure,” *IEEE Trans. Ind. Appl.*, vol. 31, no. 5, pp. 1069–1078, Sep./Oct. 1995.

[LIN06] Z. Lin, D. S. Reay, B. W. Williams, and X. He, "Torque ripple reduction in switched reluctance motor drives using B-spline neural networks," *IEEE Trans. Ind. Appl.*, vol. 42, pp. 1445-1453, 2006.

[LIP80] T. A. Lipo, “A d-q model for six phase induction machines,” *Int. Conf. on Electrical Machines (ICEM)*. pp. 860–867, 1980.

[LIP96] T. A. Lipo, Vector control and dynamics of AC drives. Oxford University Press, USA, 1996.

[LIU10] X. Liu, Z. P. Pan, and Z. Q. Zhu, “Analysis of average torque in switched reluctance motor with unipolar and bipolar excitations based on an improved Fourier series model,” *2010 IEEE VPPC*, pp. 1–6, Sep. 2010.

[LIU12a] X. Liu, Z. Q. Zhu, and M. Hasegawa, “Vibration and noise in novel variable flux reluctance machine with DC-field coil in stator,” *in Proc. 7th Int. Power Elect. Motion Contl. Conf. (IPEMC2012)*, pp. 1100–1107, Jun. 2012.

[LIU12b] X. Liu, Z. Q. Zhu, and Z. P. Pan, “Analysis of electromagnetic torque in sinusoidal excited switched reluctance machines having DC bias in excitation,” *XXth Int. Conf. on Elect. Mach. (ICEM2012)*, pp. 2882–2888, Sep. 2012.

[LIU12c] H. Liu, Z. Q. Zhu, E. Mohamed, Y. Fu, and X. Qi, “Flux-weakening control of non-salient pole PMSM having large winding inductance accounting for resistive voltage drop and inverter nonlinearities,” *IEEE Trans. Power Electron.*, vol. 27, no. 2, pp. 942–952, 2012.

[LIU13a] X. Liu and Z. Q. Zhu, “Comparative study of novel variable flux reluctance machines with doubly fed doubly salient machines,” *IEEE Trans. Magn.*, vol. 49, no. 7, pp. 3838–3841, Jul. 2013.

[LIU13b] X. Liu and Z. Q. Zhu, “Electromagnetic performance of novel variable flux reluctance machines with dc-field coil in stator,” *IEEE Trans. Magn.*, vol. 49, no. 6, pp. 3020–3028, Jun. 2013.

[LIU14a] X. Liu and Z. Q. Zhu, “Stator/rotor pole combinations and winding configurations of variable flux reluctance machines,” *IEEE Trans. Ind. Appl.*, vol. 50, no. 6, pp. 3675–3684, Nov./Dec. 2014.

[LIU14b] X. Liu, Z. Q. Zhu, and D. Wu, “Evaluation of efficiency optimized variable flux reluctance machine for EVs/HEVs by comparing with interior PM machine,” *17th Int. Conf. on Elect. Mach. and Syst. (ICEMS2014)*, pp. 2648–2654, Oct. 2014.

[LU08] H. Lu, L. Zhang, and W. Qu, “A new torque control method for torque ripple minimization of BLDC motors with un-ideal back EMF,” *IEEE Trans. Power Elec.*, vol. 23, no. 2, pp. 950–958, 2008.

[LUK04] P. C. K. Luk and K. P. Jinupun, "Direct work control technique for switched reluctance motors," *in Proc. Power Electronics and Motion Control Conference*, pp. 1044-1048, 2004.

[LUO00] X. Luo and T. A. Lipo, “A synchronous/permanent magnet hybrid AC machine,” *IEEE Trans. Energy Convers.*, vol. 15, no. 2, pp. 203–210, Jun. 2000.

[MAG12] *Model 3410 Torque Display User’s Manual*, rev. I, MAGTROL Inc., NY, 2012.

[MAT05] P. Mattavelli, L. Tubiana, and M. Zigliotto, “Torque-ripple reduction in PM synchronous motor drives using repetitive current control,” *IEEE Trans. Power Elec.*, vol. 20, no. 6, pp. 1423–1431, Nov. 2005.

[MBA12] R. Mbayed, G. Salloum, L. Vido, E. Monmasson, and M. Gabsi, “Hybrid excitation synchronous machine control in electric vehicle application with copper losses minimization,” *IET International Conference on Power Electronics, Machines and Drives*, 2012.

[MIK13] R. Mikail, I. Husain, Y. Sozer, M. S. Islam, and T. Sebastian, “Torque-ripple minimization of switched reluctance machines through current profiling,” *IEEE Trans. Ind. Appl.*, vol. 49, no. 3, pp. 1258–1267, 2013.

[MIL01] T. J. E. Miller, *Electronic Control of Switched Reluctance Machines*. Oxford, 2001.

[MIR99] S. Mir, M. E. Elbuluk, and 1. Husain, "Torque-ripple minimization in switched reluctance motors using adaptive fuzzy control," *IEEE Trans. Ind. Appl.*, vol. 35, pp. 461-468, 1999.

[MOR90] S. Morimoto, Y. Takeda, T. Hirasa, and K. Taniguchi, "Expansion of operating limits for permanent magnet motor by current vector control considering inverter capacity," *IEEE Trans. Ind. Appl.*, vol. 26, no. 5, pp. 866-871, 1990.

[MOR12] C. Moron, A. Garcia, E. Tremps, and J. A. Somolinos, “Torque control of switched reluctance motors,” *IEEE Trans. Magn.*, vol. 48, no. 4, pp. 1661–1664, 2012.

[MUN00] A. R. Munoz and T. A. Lipo, “Dual stator winding induction machine drive,” *IEEE Trans. Ind. Appl.*, vol. 36, no. 5, pp. 1369–1379, Sep./Oct. 2000.

[NAG00] N. Nagel and R. Lorenz, “Rotating vector methods for smooth torque control of a switched reluctance motor drive,” *IEEE Trans. Ind. Appl.*, vol. 36, no. 2, pp. 540–548, 2000.

[NAK12] N. Nakao and K. Akatsu, “Simple unipolar excitations for SR motors considering fundamental component of self-inductance distribution,” *15th International Conference on Electrical Machines and Systems (ICEMS2012)*, no. 1, pp. 1 – 6, 2012.

[NAK13] N. Nakao and K. Akatsu, “A simple unipolar excitation strategy for switched reluctance motors by using PWM current control,” *5th IEEE Energy Conversion Congress and Exhibition in Asia (ECCE Asia 2013)*, pp. 1111–1117, 2013.

[NAK14] N. Nakao and K. Akatsu, “Vector control specialized for switched reluctance motor drives,” *XXIst Int. Conf. on Elect. Mach. (ICEM2014)*, pp. 937–943, Sep. 2014.

[NAM10] K. Nam, *AC Motor Control and Electric Vehicle Applications*. CRC Press, 2010.

[NEL74] R. H. Nelson and P. C. Krause, “Induction machine analysis for arbitrary displacement between multiple winding sets,” *IEEE Trans. Power Apparatus and Systems*, vol. PAS-93, no. 3, pp. 841–848, May 1974.

[OWE10] R. L. Owen, Z. Q. Zhu, and G. W. Jewell, “Hybrid-excited flux-switching permanent-magnet machines with iron flux bridges,” *IEEE Trans. Magn.*, vol. 46, no. 6, pp. 1726–1729, Jun. 2010.

[OWE11] R. Owen, Z. Q. Zhu, J. Wang, D. A. Stone, and I. Urquhart, “Review of variable-flux permanent magnet machines,” *presented at the Int. Conf. Electr. Mach. Syst.*, pp. 1–6, 2011.

[PAN14] D. Pan, F. Liang, Y. Wang, and T. A. Lipo, “Extension of the operating region of an IPM motor utilizing series compensation,” *IEEE Trans. Ind. Appl.*, vol. 50, no. 1, pp. 539–548, Jan./Feb. 2014.

[PAR29] R. H. Park, “Two-reaction theory of synchronous machines generalized method of analysis-part I,” *Transactions of the American Institute of Electrical Engineers,* vol. 48, no. 3, pp. 716–727, Jul. 1929.

[PAR00] S. J. Park, H. W. Park, M. H. Lee, and F. Harashima, “A new approach for minimum-torque-ripple maximum-efficiency control of BLDC motor,” *IEEE Trans. Ind. Electron.*, vol. 47, no. 1, pp. 109–114, Feb. 2000.

[PEL12] G. Pellegrino, A. Vagati, P. Guglielmi, and B. Boazzo, “Performance comparison between surface-mounted and interior PM motor drives for electric vehicle application,” *IEEE Trans. Ind. Electron.*, vol. 59, no. 2, pp. 803–811, Feb. 2012.

[POT15] N. Pothi, Z. Q. Zhu, I. A. A. Afinowi, B. Lee, and Y. Ren, “Control strategy for hybrid-excited switched-flux permanent magnet machines,” *IET Electric Power Applications*, vol. 9, no. 9, pp. 612–619, 2015.

[QIA04] W. Qian, S. Panda, and J. Xu, “Torque ripple minimization in PM synchronous motors using iterative learning control,” *IEEE Trans. Power Elec.*, vol. 19, no. 2, pp. 272–279, 2004.

[RAH00] K. M. Rahman, B. Fahimi, G. Suresh, A. V. Rajarathnam, and M. Ehsani, "Advantages of switched reluctance motor applications to EV and HEV: design and control issues," *IEEE Trans. Ind. Appl.*, vol. 36, pp. 111-121, 2000.

[RAH04] M. F. Rahman, Md. E. Haque, L. Tang, and L. Zhong, “Problems associated with the direct torque control of an interior permanent-magnet synchronous motor drive and their remedies,” *IEEE Trans. Ind. Electron.*, vol. 51, pp. 799–809, Aug. 2004.

[ROD01] M. Rodrigues, P. J. Costa Branco, and W. Suemitsu, "Fuzzy logic torque ripple reduction by turn-off angle compensation for switched reluctance motors," *IEEE Trans. Ind. Electron.*, vol. 48, pp. 711-715, 2001.

[RUS98] K. Russa, 1. Husain, and M. E. Elbuluk, "Torque-ripple minimization in switched reluctance machines over a wide speed range," *IEEE Trans. Ind. Appl.*, vol. 34, pp. 1105-1112, 1998.

[SAH01] N. C. Sahoo, J. X. Xu, and S. K. Panda, "Low torque ripple control of switched reluctance motors using iterative learning," *IEEE Trans. Energy Conv.*, vol. 16, pp. 318-326, 2001.

[SAN12] J. de Santiago, H. Bernhoff, B. Ekergard, S. Eriksson, S. Ferhatovic, R. Waters, and M. Leijon, "Electrical motor drivelines in commercial all-electric vehicles: A review," *IEEE Trans. Veh. Technol.*, vol. 61, no. 2, pp. 475–484, Feb. 2012.

[SAN13] A. P. Sandulescu, F. Meinguet, X. Kestelyn, E. Semail, and A. Bruyere, "Flux-weakening operation of open-end winding drive integrating a cost-effective high-power charger," *IET Electrical Systems in Transportation*, vol. 3, no. 1, pp. 10–21, Mar. 2013.

[SAN14] A. P. Sandulescu, F. Meinguet, X. Kestelyn, E. Semail, and A. Bruyere, "Control strategies for open-end winding drives operating in the flux-weakening region," *IEEE Trans. Power Elec.*, vol. 29, no. 9, pp. 4829–4842, Sep. 2014.

[SAR12] A. Sarikhani and O. A. Mohammed, "Demagnetization control for reliable flux weakening control in PM synchronous machine," *IEEE Trans. Energy Convers.*, vol. 27, no. 4, pp. 1046–1055, Dec. 2012.

[SHI07] S. Shinnaka and T. Sagawa, "New optimal current control methods for energy-efficient and wide speed-range operation of hybrid-field synchronous motor," *IEEE Trans. Ind. Electron.*, vol. 54, no. 5, pp. 2443–2450, Oct. 2007.

[SIN98] B. Singh, V. K. Sharma, and S. S. Murthy, "Performance analysis of adaptive fuzzy logic controller for switched reluctance motor drive system," *in Proc. Industry Applications Conference*, pp. 571-579, 1998.

[SIN05] G. K. Singh, D. K. P. Singh, K. Nam, and S. K. Lim, "A simple indirect field-oriented control scheme for multiconverter-fed induction motor," IEEE Trans. Ind. Electron., vol. 52, no. 6, pp. 1653–1659, Aug. 2005.

[SOM02] V. Somasekhar and K. Gopakumar, "A space vector modulation scheme for a dual two level inverter fed open-end winding induction motor drive for the elimination of zero sequence currents," *EPE Journal*, vol. 12, no. 2, pp. 26–36, Jun. 2002.

[SOM08a] V. T. Somasekhar, S. Srinivas, and K. K. Kumar, “Effect of zero-vector placement in a dual-inverter fed open-end winding induction motor drive with alternate sub-hexagonal center PWM switching scheme,” *IEEE Trans. Power Elec.*, vol. 23, no. 3, pp. 1584–1591, May 2008.

[SOM08b] V. T. Somasekhar, S. Srinivas, and K. K. Kumar, “Effect of zero-vector placement in a dual-inverter fed open-end winding induction-motor drive with a decoupled space-vector PWM strategy,” *IEEE Trans. Ind. Electron.*, vol. 55, no. 6, pp. 2497–2505, Jun. 2008.

[SOM13] A. Somani, R. K. Gupta, K. K. Mohapatra, and N. Mohan, “On the causes of circulating currents in PWM drives with open-end winding AC machines,” *IEEE Trans. Ind. Electron.*, vol. 60, no. 9, pp. 3670–3678, Sep. 2013.

[SOO95] W. L. Soong, D. A. Staton, T. J. E. Miller, “Design of a new axially laminated interior PM motor,” *IEEE Trans. Ind. Appl.*, vol.31, no.2, pp.358-367, 1995.

[SRI13] S. Srinivas and K. R. Sekhar, “Theoretical and experimental analysis for current in a dual-inverter-fed open-end winding induction motor drive with reduced switching PWM,” *IEEE Trans. Ind. Electron.*, vol. 60, no. 10, pp. 4318–4328, Oct. 2013.

[STA99] A. M. Stankovic, G. Tadmor, Z. J. Coric, and 1. Agirman, "On torque ripple reduction in current-fed switched reluctance motors," *IEEE Trans. Ind. Electron.*, vol. 46, pp. 177-183, 1999.

[STE93] H. Stemmler and P. Guggenbach, “Configurations of high-power voltage source inverter drives,” *in Proc. EPE’93 Conf.*, pp. 7–14, Sep. 1993.

[SWA06] M. M. Swamy, T. Kume, A. Maemura, & S. Morimoto, “Extended high-speed operation via electronic winding-change method for AC motors,” *IEEE Trans. Ind. Appl.*, vol.42, no.3, pp. 742-752, May-June 2006

[TAK89] I. Takahashi and Y. Ohmori, “High-performance direct torque control of an induction motor,” *IEEE Trans. Ind. Appl.*, vol. 25, no. 2, pp. 257–264, Mar./Apr. 1989.

[TAK12] M. Takeno, A. Chiba, N. Hoshi, S. Ogasawara, M. Takemoto, and M. A. Rahman, “Test results and torque improvement of the 50-kw switched reluctance motor designed for hybrid electric vehicles,” *IEEE Trans. Ind. Appl.*, vol. 48, no. 4, pp. 1327–1334, 2012.

[TAKI15] M. Takiguchi, H. Sugimoto, N. Kurihara, and A. Chiba, “Acoustic noise and vibration reduction of SRM by elimination of third harmonic component in sum of radial forces,” *IEEE Trans. Energy Conv.*, vol. 30, no. 3, pp. 883–891, Sep. 2015.

[TAN03] L. Tang , L. Zhong, M. F. Rahman, and Y. Hu “A novel direct torque control for interior permanent-magnet synchronous machine drive with low ripple in torque and flux-a speed-sensorless approach,” in *Proc. IEEE Trans. Ind. Appl.*, vol. 39, pp. 1748–1756, Nov./Dec. 2003.

[TUR10] M. Tursini, E. Chiricozzi, and R. Petrella, “Feedforward flux-weakening control of surface-mounted permanent-magnet synchronous motors accounting for resistive voltage drop,” *IEEE Trans. Ind. Electron.*, vol. 57, no. 1, pp. 440–448, 2010.

[VAG98] A. Vagati, M. Pastorelli, G. Franceschini, and S. C. Petrache, “Design of low-torque-ripple synchronous reluctance motors,” *IEEE Trans. Ind. Appl.*, vol. IA-34, no. 4, pp. 758–765, Jul./Aug. 1998.

[VAG10] A. Vagati, G. Pellegrino, and P. Guglielmi, “Comparison between SPM and IPM motor drives for EV application,” *in Proc. XIX Int. Conf. ICEM*, pp. 1–6, Sep. 2010.

[VIJ08] K. Vijayakumar, R. Karthikeyan, S. Paramasivam, R. Arumugam, and K. N. Srinivas, “Switched reluctance motor modeling, design, simulation, and analysis: A comprehensive review,” *IEEE Trans. Magn.*, vol. 44, no. 12, pp. 4605–4617, Dec. 2008.

[WAN05] S. Wang, Q. Zhan, Z. Ma, and L. Zhou, “Implementation of a 50-kW four-phase switched reluctance motor drive system for hybrid electric vehicle,” *IEEE Trans. Magn.*, vol. 41, no. 1, pp. 501–504, Jan. 2005.

[WAN12] Y. Wang, A. Member, Z. Deng, F. Machine, and D. C. Power, “Analysis of electromagnetic performance and control schemes of electrical excitation flux-switching machine for DC power systems,” *IEEE Trans. Energy Conv.*, vol. 27, no. 4, pp. 844–855, 2012.

[WU15] Z. Z. Wu, Z. Q. Zhu, and J. T. Shi, “Novel doubly salient permanent magnet machines with partitioned stator and iron pieces rotor,” *IEEE Trans. Magn.*, vol. 51, no. 5, May 2015.

[XIA15] C. Xia, B. Ji, and Y. Yan, “Smooth speed control for low-speed synchronous motor using proportional-integral-resonant controller,” *IEEE Trans. Ind. Electron.*, vol. 62, no. 4, pp. 2123–2134, Apr. 2015.

[YAN12] W. Yang, W. Xu, and X. Xiao, “Torque ripple reduction strategy of model based predictive torque control for doubly salient permanent magnet synchronous machines,” *IEEE Energy Conversion Congress and Exposition*, pp. 113–120, Sep. 2012.

[ZHA95] Y. Zhao and Lipo T. A., “Space vector PWM control of dual three-phase induction machine using vector space decomposition,” *IEEE Trans. Ind. Appl.*, vol. 31, no. 5, pp. 1100–1109, 1995.

[ZHA11] Y. Zhang, J. Zhu, W. Xu, and Y. Guo, “A simple method to reduce torque ripple in direct torque-controlled permanent-magnet synchronous motor by using vectors with variable amplitude and angle,” *IEEE Trans. Ind. Electron.*, vol. 58, no. 7, pp. 2848–2859, 2011.

[ZHA12] Z. Zhang, Y. Tao, and Y. Yan, “Investigation of a new topology of hybrid excitation doubly salient brushless DC generator,” *IEEE Trans. Ind. Electron.*, vol. 59, no. 6, pp. 2550–2556, Jun. 2012.

[ZHO15] Y. Zhou and H. Nian, “Zero-sequence current suppression strategy of open-winding PMSG system with common DC bus based on zero vector redistribution,” *IEEE Trans. Ind. Electron.*, vol. 62, no. 6, pp. 3399–3408, Jun. 2015.

[ZHU07] Z. Q. Zhu and D. Howe, “Electrical machines and drives for electric, hybrid and fuel cell vehicles,” *Proc. IEEE*, vol. 95, no. 4, pp. 746–765, Apr. 2007.

[ZHU09] X. Zhu, M. Cheng, K. T. Chau, and C. Yu, “Torque ripple minimization of flux-controllable stator-permanent-magnet brushless motors using harmonic current injection,” *Journal of Applied Physics*, vol. 105, no. 7, pp. 07F102:1–07F102:3, 2009.

[ZHU10] Z.Q.Zhu, and J.T.Chen, “Advanced flux-switching permanent magnet brushless machine,” *IEEE Trans. Magn.*, vol. 46, no. 6, pp. 1447–1452, Jun. 2010.

[ZHU11] Z. Q. Zhu, “Switched flux permanent magnet machines—Innovation continues,” *in Proc. Int. Conf. Elect. Mach. Syst. (ICEMS)*, pp. 1–10, Aug. 2011.

[ZHU12] H. Zhu, X. Xiao, and Y. Li, “Torque ripple reduction of the torque predictive control scheme for permanent-magnet synchronous motors,” *IEEE Trans. Ind. Electron.*, vol. 59, no. 2, pp. 871–877, Feb. 2012.

[ZHU14] Z. Q. Zhu and X. Liu, “Novel stator electrically field excited synchronous machines without rare-earth magnet,” *9th Int. Conf. on Ecological Vehicles and Renewable Energies (EVER2014)*, pp. 1–13, Mar. 2014.

[ZHU15a] Z. Q. Zhu, M. Al-Ani, X. Liu, and B. S. Lee, “Comparison of electromagnetic performance of switched flux permanent magnet machines with mechanical flux adjusters,” *IET Electrical Systems in Transportation*, no. 1, pp. 1–10, 2015.

[ZHU15b] Z. Q. Zhu, Y. J. Zhou, and J. T. Chen, “Electromagnetic performance of non-overlapping stator wound field synchronous machine with salient pole rotor,” *IEEE Trans. Magn.*, vol. 51, no. 11, p. 8110104, 2015.

[ZHU16a] Z. Q. Zhu, B. S. Lee, and X. Liu, “Integrated field and armature current control strategy for variable flux reluctance machine using open winding,” *IEEE Trans. Ind. Appl.*, vol. 52, no. 2, pp. 1519–1529, 2016.

[ZHU16b] Z. Q. Zhu and B. S. Lee, “Integrated field and armature current control for dual three-phase variable flux reluctance machine drives,” *IEEE Trans. Energy Conv., Accepted*, 2016.

[LEE16a] B. S. Lee and Z. Q. Zhu, "Torque ripple reduction for 6-stator/4-rotor-pole variable flux reluctance machines by using harmonic field current injection," *IEEE ECCE International Conference*, in publication, 2016

[ZHU16c] Z. Q. Zhu, B. S. Lee, L. Huang, and W. Chu, "Contribution of current harmonics to average torque and torque ripple in switched reluctance machines," *IEEE Trans. Mag., Accepted,* 2016.

[LEE16b] B. S. Lee and Z. Q. Zhu, "Comparative study of torque production and torque ripple reduction for variable flux reluctance machines," submitted to *IEEE Trans. Energy Conv.*, 2016.

Appendix

Figs. A.1-A.5 show the phase self-inductances waveforms and spectra under the five investigated the current waveforms and different magnitudes. In order to fully consider the influence of magnetic saturation, the inductances are calculated by the frozen permeability method [CHU13]. The zero rotor position is referred to the position shown in Fig. 3.2.

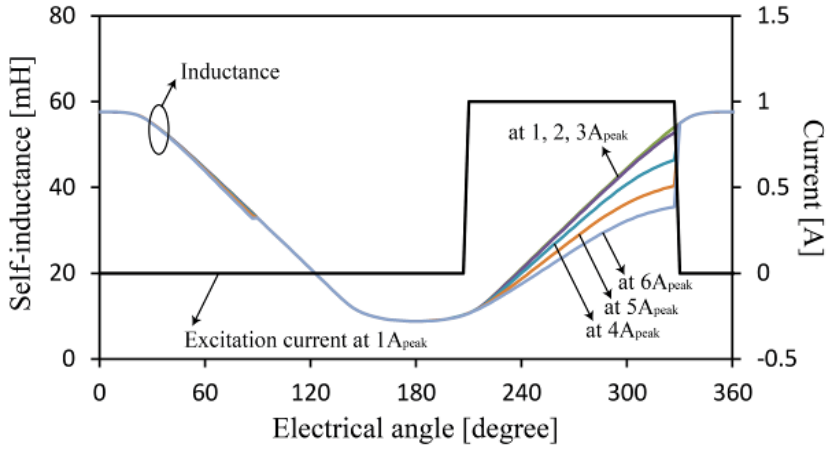

(a) Excitation current and *abc*-axis self-inductance

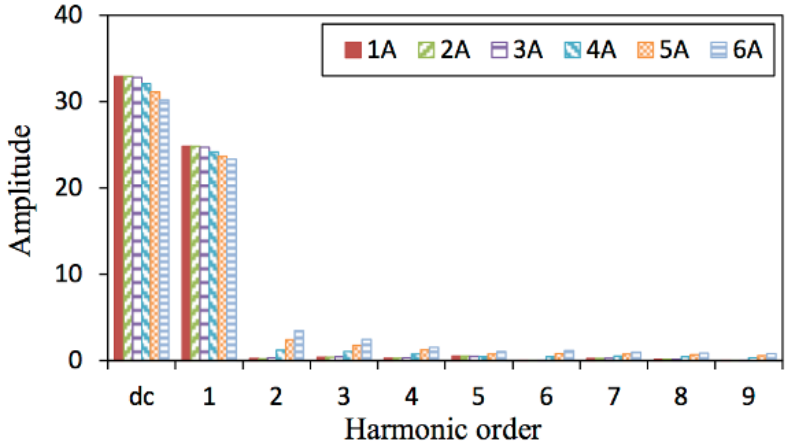

(b) Corresponding harmonics

Fig. A.1. Self-inductance calculated by frozen permeability under rectangular excitation.

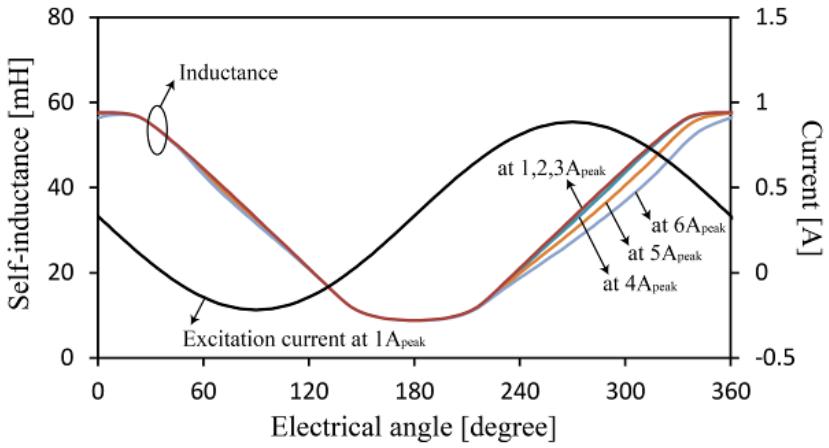

(a) Excitation current and *abc*-axis self-inductance

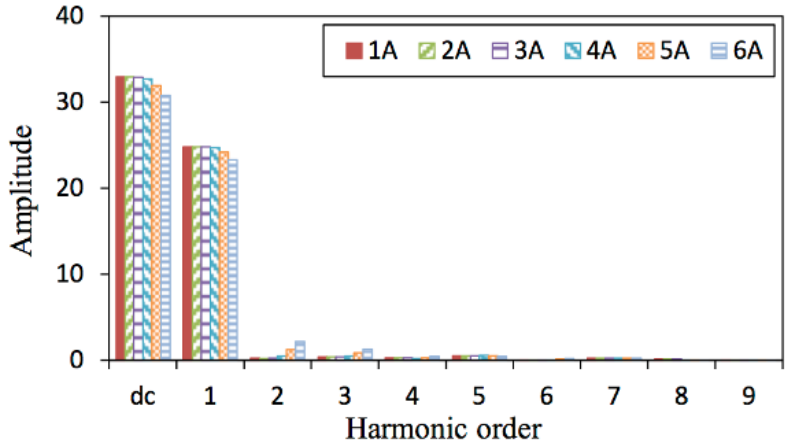

(b) Corresponding harmonics

Fig. A.2. Self-inductance calculated by frozen permeability under Case I excitation.

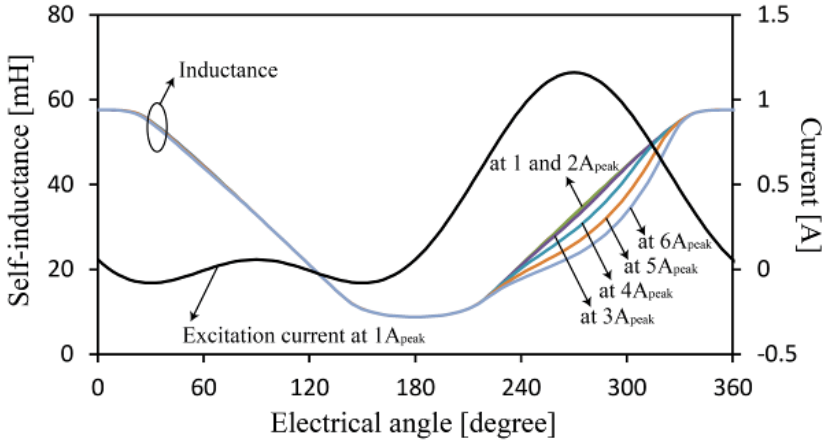

(a) Excitation current and *abc*-axis self-inductance

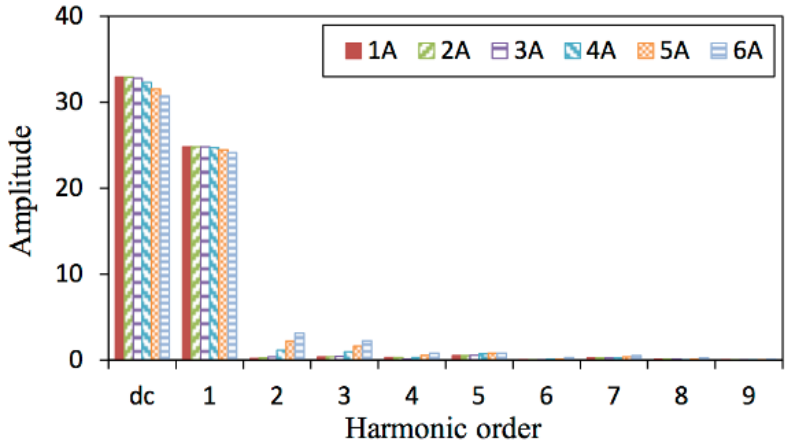

(b) Corresponding harmonics

Fig. A.3. Self-inductance calculated by frozen permeability under Case II excitation.

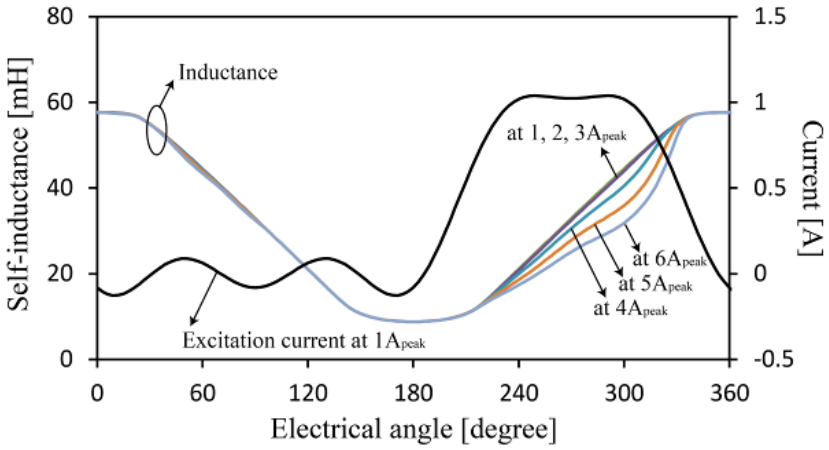

(a) Excitation current and *abc*-axis self-inductance

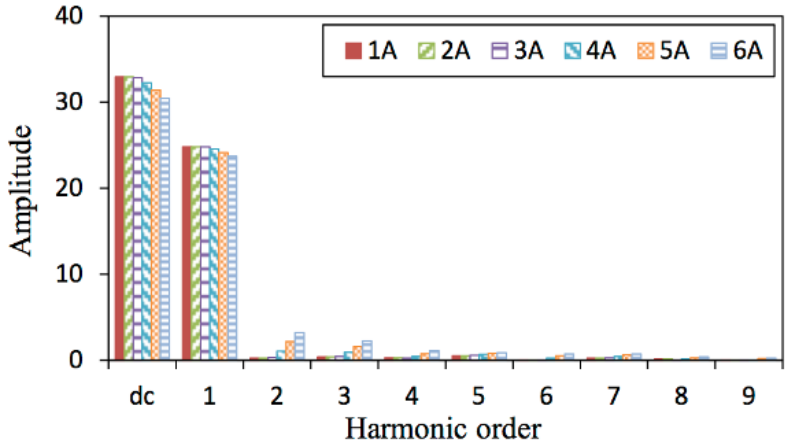

(b) Corresponding harmonics

Fig. A.4. Self-inductance calculated by frozen permeability under Case III excitation.

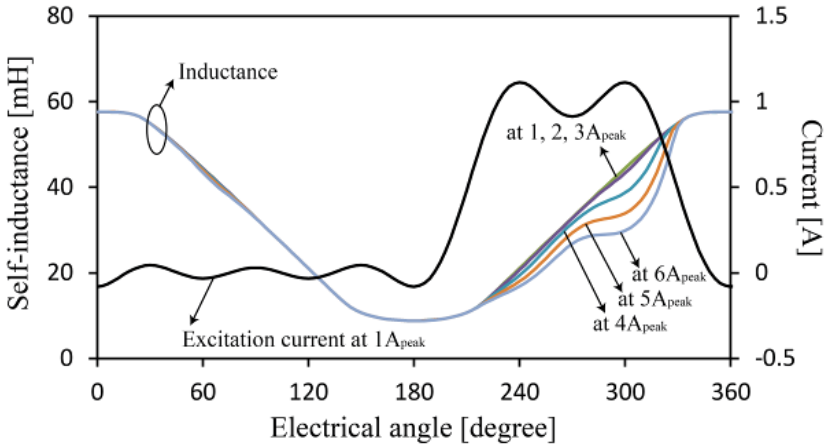

(a) Excitation current and *abc*-axis self-inductance

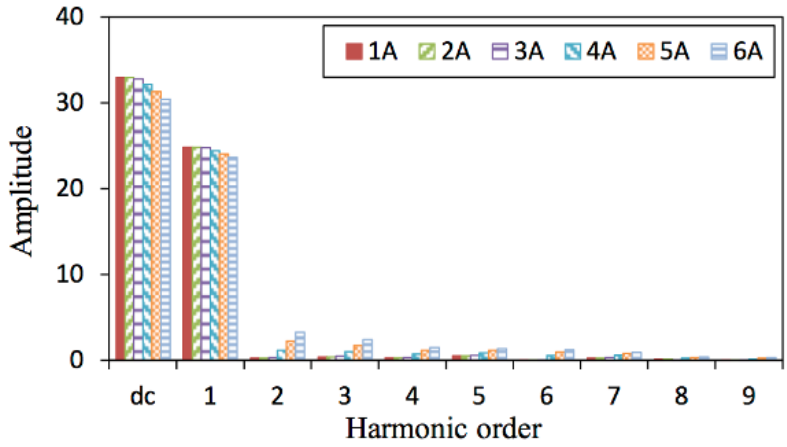

(b) Corresponding harmonics

Fig. A.5. Self-inductance calculated by frozen permeability under Case IV excitation.

Publications

Z. Q. Zhu, **B. S. Lee**, and X. Liu, "Integrated field and armature current control strategy for variable flux reluctance machine using open winding," *IEEE Trans. Ind. Appl*., vol. 52, no. 2, pp. 1519–1529, 2016. Z. Q. Zhu, **B. S. Lee**, and X. Liu, "Integrated field and armature current control strategy for variable flux reluctance machine using open winding," *Tenth International Conference on Ecological Vehicles and Renewable Energies (EVER2015)*, pp. 1–7, Apr. 2015, Best Paper Award and recommended for submission to *IEEE Trans. Ind. Appl*.

Z. Q. Zhu and **B. S. Lee**, "Integrated field and armature current control for dual three-phase variable flux reluctance machine drives," *IEEE Trans. Energy Conv.*, accepted, 2016.

B. S. Lee, Z. Q. Zhu, and D. Wu "On-load voltage distortion compensation method using disturbance observer for SPM machines with closed slot," *Chinese Journal of Electrical Engineering*, vol.1, no.1, pp. 58–69, 2016.

N. Pothi, Z. Q. Zhu, I. A. A. Afinowi, **B. S. Lee**, and Y. Ren, "Control strategy for hybrid-excited switched-flux permanent magnet machines," *IET Electric Power Applications*, vol. 9, no. 9, pp. 612–619, 2015.

Z. Q. Zhu, M. Al-Ani, **B. S. Lee**, and X. Liu, "Comparative study of the electromagnetic performance of switched flux permanent magnet machines," *IET Electric Power Applications*, vol. 9, no. 4, pp. 297–306, 2015.

Z. Q. Zhu, M. M. J. Al-Ani, X. Liu, and **B. S. Lee**, "A mechanical flux weakening method for switched flux permanent magnet machines," *IEEE Trans. Energy Conv.*, vol. 30, no. 2, pp. 806–815, Jun. 2015.

Z. Q. Zhu, M. Al-Ani, X. Liu, and **B. S. Lee**, "Comparison of electromagnetic performance of switched flux permanent magnet machines with mechanical flux adjusters," *IET Electrical Systems in Transportation*, no. 1, pp. 1–10, 2015.

B. S. Lee and Z. Q. Zhu, "Torque ripple reduction for 6-stator/4-rotor-pole variable flux reluctance machines by using harmonic field current injection," *IEEE ECCE International Conference*, in publication, 2016, and *IEEE Trans. on Industry Applications, under revision.*

B. S. Lee, N. Pothi, M. M. J. Al-Ani, and Z. Q. Zhu, "Experimental study of torque and flux weakening performance of alternative switched flux PM machines," *7th IET International Conference PEMD*, pp. 1–6, Apr. 2014.

Z. Q. Zhu, **B. S. Lee**, L. Huang, and W. Chu, "Contribution of current harmonics to average torque and torque ripple in switched reluctance machines," *IEEE Trans. Mag.*, 2016, accepted.

B. S. Lee and Z. Q. Zhu, "Comparative study of torque production and torque ripple reduction for variable flux reluctance machines," submitted to *IEEE Trans. Energy Conv.*, 2016.